THE FUNDAMENTALS OF THE OPERATION OF POLYMER ELECTROLYTE MEMBRANE FUEL CELLS UNDER DRY AND FLOODED CONDITIONS WITH AN EFFICIENT APPROACH TO THE MANAGEMENT OF LIQUID WATER

Erin E. Kimball

A DISSERTATION

PRESENTED TO THE FACULTY

OF PRINCETON UNIVERSITY

IN CANDIDACY FOR THE DEGREE

OF DOCTOR OF PHILOSOPHY

RECOMMENDED FOR ACCEPTANCE

BY THE DEPARTMENT OF

CHEMICAL ENGINEERING

Advisors: Jay Benziger and Yannis Kevrekidis

March 2010

Abstract

Polymer electrolyte membrane (PEM) fuel cells are power conversion devices that have the potential to become an important part of a distributed energy portfolio independent of fossil fuels. In order to improve their performance and make their mainstream use possible, the fundamental physics of PEM fuel cell operation must be thoroughly understood. Included in this is the effect of the water balance inside the fuel cell. Either too little water or an excess leading to liquid water accumulation can cause fuel cell failure. Several factors affect the water balance, some inherent in fuel cells and others determined by the system design.

The tool used to study fuel cell operation was the Segmented Anode Parallel Channel (SAPC) fuel cell. Transparent flow channels and a segmented anode allowed for direct visualization of liquid water and measurement of the current distribution along the flow channel. Under dry conditions, hydration fronts were observed to propagate along the flow channel as the fuel cell ignited or extinguished. Under wet conditions, liquid water accumulation observed in the flow channel created areas of local reactant starvation. Each segment of the SAPC fuel cell was modeled as a differential element, coupled together electrically and through the flux of the reaction components.

The design of the SAPC fuel cell was very simple. The fuel cell was allowed to operate autonomously without potentiostatic or galvanostatic controllers that hide much of the physics of fuel cell operation. The setup and experimental results elucidated the importance of flow pattern, temperature, load resistance, flow channel orientation with respect to gravity, gas diffusion layer material, flow rates, and flow field construction. Each of these factors changed how much water was removed as a vapor or how severely

liquid water hindered the fuel cell operation. It was shown that the design of the fuel cell can be tailored to maintain the fuel cell hydration while also effectively removing excess liquid water. The flow rates could be kept low, allowing for high fuel utilization and dry feeds. The need for extra peripheral equipment, such as humidifiers or feed recycling, was alleviated.

Acknowledgements

I would first like to thank my advisors, Prof. Yannis Kevrekidis and, in particular, Prof. Jay Benziger, for their guidance and support over the years. Graduate school was a struggle for me in the beginning, but I am grateful to have been given the chance to learn and succeed.

I also must thank the Benziger group members, both past and present, for their invaluable discussions and support. I am particularly grateful for the conversations with Barclay Satterfield and May Jean Cheah, which brightened many of the days in the lab.

During my years at Princeton, my peers have motivated me, inspired me, and introduced me to so many things. It is only through being surrounded by the caliber of people at Princeton that I have had such rich experiences.

The importance of the unwavering support of my family and friends is impossible to put into words. Thank you to my brothers, sisters, aunts and uncles, grandparents, closest friends, and Step-mom, Sherry. It is their encouragement that has always pulled me through the times of doubt and the long nights that often stretched into the next morning.

Finally, thank you to my parents, Cyndi Erickson and W. Scott Kimball. Throughout my childhood, college, and graduate school, they have guided me without lecturing, allowed me to learn and grow without punishment, and love me without conditions. My Mom, with her grace, strength, and amazing energy has been my greatest inspiration. My Dad, with his devotion, intelligence, ideals, and great sense of humor, is someone who I completely admire. Knowing that he is proud of me has been tremendously fulfilling. I love you both!

Table of Contents

List of Publications

Benziger, J., E. Kimball, R. Mejia-Ariza, and I.G. Kevrikidis, *Oxygen mass transport limitations at the cathode of polymer electrolyte membrane fuel cells.* **In preparation**, 2010.

Benziger, J., J.E. Chia, E. Kimball, and I.G. Kevrekidis, *Reaction dynamics in a parallel flow channel PEM fuel cell.* Journal of the Electrochemical Society, 2007. **154**(8): p. B835-B844.

de Decker, Y., J.B. Benziger, E. Kimball, I.G. Kevrekidis, *Multi-stability, nonlinear response and wave propagation in self-humidified PEM fuel cells.* Chemical Engineering Science, 2009. **Accepted**.

Kimball, E., J. Benziger, and I.G. Kevrekidis, *Effects of GDL structure with an efficient approach to the management of liquid water in PEM fuel cells.* Fuel Cells, 2010. **Accepted**.

Kimball, E., T. Whitaker, Y.G. Kevrekidis, and J.B. Benziger, *Drops, slugs, and flooding in polymer electrolyte membrane fuel cells.* AIChE Journal, 2008. **54**(5): p. 1313-1332.

List of Figures

List of Tables

1 Introduction

1.1 The case for fuel cells

The economic, environmental, and political implications of a dwindling supply of fossil fuels are immense and cannot be ignored. Sustaining the world's growing energy demands will require the development and widespread implementation of alternative energy sources. Fuel cells are electrochemical power conversion devices that have the potential to be key components of a distributed energy supply portfolio. The size, operating temperature, and fuel are varied over wide ranges that make fuel cells suitable for several applications ranging from large power plants to portable electronics.

Polymer electrolyte membrane (PEM) fuel cells take in hydrogen as the fuel and either pure oxygen or air as the oxidant. Their low temperature operation (25 – 100 ºC) makes them ideal for distributed stationary power supplies, portable applications, and as a part of an automotive system. PEM fuel cells have a high power density and can operate continuously, but their most significant advantages are their clean operation and utilization of hydrogen. The hydrogen and oxygen react to generate an electrical current with water as the only product. No harmful emissions result from the fuel cell operation, reducing the environmental impact compared to conventional power sources. The reactants are abundant everywhere on the planet, reducing economic effects of production changes and political control over large supplies.

1.2 Challenges to commercialization

Several issues have hindered the commercialization of fuel cells. Of these, perhaps the most complex is the production and storage of hydrogen. Hydrogen can be produced by several methods. Electrolysis of water is the preferred choice with moderate temperature requirements and no harmful by-products, but requires a high energy input. The water-gas shift reaction is the most common method, but new technologies that separate hydrogen from the flue gas of coal fired power plants (developed for the purpose of carbon dioxide capture and sequestration) may offer a better alternative in the future. For small scale production processes, hydrogen can be produced locally as needed; commercial scale production requires storage and transport of the hydrogen to the fuel cell site. The difficulty in storing the hydrogen is due to the need to balance the cost of materials, such as pipeline infrastructures or compressed gas tanks; with the density of the stored hydrogen, e.g. as a gas, liquid, or chemical compound; with the energy input into the process, e.g. to compress the gas or create the metal-hydride bonds. A substantial body of literature now focuses on this complex problem.[1-4]

The cost of the hydrogen production and storage is a significant contribution to the overall cost of fuel cell systems. Even without the consideration of hydrogen, though, the cost of the fuel cell alone is another barrier to commercialization. The key components of PEM fuel cells are the Nafion® membrane, platinum catalyst, and carbon fiber gas diffusion layer. These materials are expensive, but greatly improve the fuel cell performance compared to alternatives. A lot of effort is currently being put into using less material in the fuel cell, making the manufacturing costs cheaper, and, mostly, into finding materials that are cheaper but perform at least as well.

The high cost of the materials amplifies the importance of durability. Consumers are accustomed to very high reliability with the energy supply from the grid, combustion engines in their cars, and batteries in their laptops. With widespread use of fuel cells, temporary interruptions from material failures could be dealt with, but it would be hard for consumers to accept fixes that require very expensive replacement components. The problem of durability is not easy to define and study. The different materials degrade through various processes, each with a different cause and time scale. The severity of these processes is highly sensitive to the operating conditions, changes in the external load, and overall system design. A thorough understanding of degradation in the fuel cell and how best to increase the durability is still lacking in the literature.

1.3 Importance of water management

Intertwined with each of the challenges above is the issue of water management. The presence of water inside the fuel cell is necessary to hydrate the Nafion membrane. The various alternatives to Nafion that may be cheaper, more durable, or thinner still require hydration to operate well.[5] The fuel cell works by the membrane conducting protons from the anode to the cathode while driving electrons through the external circuit where they do useful work. The flow of electrons around the circuit is matched by the conduction of protons through the membrane. The conduction of protons is dependent on the water activity in the membrane, increasing by several orders of magnitude for Nafion from 1×10^{-7} S/cm with no water activity to 1×10^{-1} S/cm at saturated conditions, as shown in Figure 1.1.[6] When a fuel cell is designed and run at operating conditions that

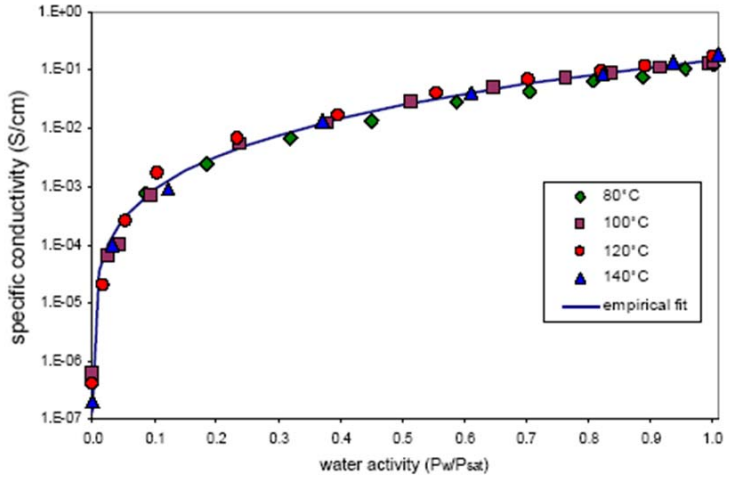

Figure 1.1 Taken from [1]. Conductivity of Nafion 115 as a function of water activity at temperatures from 80 to 140 ◦C. The empirical fit to the data is given by $\sigma = 1.3 \times 10^{-7} \exp(14(P_w/P_{sat})^{0.2})$ S/cm.

remove too much water from the system, external humidification of the feeds is necessary and increases the cost and complexity of the system.

With more careful system designs, extra humidification is not needed. The electrochemical reaction produces water that can be absorbed by the membrane. The water production can be substantial enough to saturate the fuel cell and cause accumulation of liquid water. The liquid water is problematic, as it can block the reactants from reaching the catalyst and hurt the fuel cell performance. Furthermore, very high potential gradients can be created with areas of local reactant starvation caused by liquid water blockages and are thought to accelerate the degradation of the catalyst material.

The most common solution to removing excess water is a large increase in the flow rates to simply blow it out of the flow channels. This requires much higher supplies of reactants, complicating the problem of hydrogen production and storage. Extra pumping, fuel recycling, and humidification are then required. The system cost and

complexity are again increased, along with the auxiliary power consumption and overall size.

Engineering the fuel cell design for effective water removal is a much better approach to the water management issue. Lower flow rates can be used that reduce the convective removal of water and eliminate the need for external humidification and recycling. This is a very complicated issue involving the material properties of the various components, the gravitational and shear forces that act on the liquid water, and the need to distribute the reactants evenly over a large active area. The ability to make clever improvements away from conventional fuel cell system design requires a thorough understanding of the fundamental physics of the operation under both saturated and drier conditions; this is the focus of the work presented in this document.

1.4 Basics of PEM fuel cells

A schematic of a PEM fuel cell is given in Figure 1.2 and shows the different layers of the fuel cell. The different paths for the protons and electrons from the anode to the cathode and the flow of reactants are also shown. Each layer has a specific purpose and very different structure, introducing multiple length scales into the system.

1.4.1 Nafion membrane

As mentioned before, the polymer electrolyte membrane is at the center of a PEM fuel cell. The most common membrane, Nafion, was developed by DuPont in 1968 and is still the industry standard. It is a polymer material made up of a polytetrafluoro-ethylene (PTFE; also known as Teflon) backbone with perfluorovinyl ether side chains terminated in sulfonate groups; the chemical structure is shown in Figure 1.3.

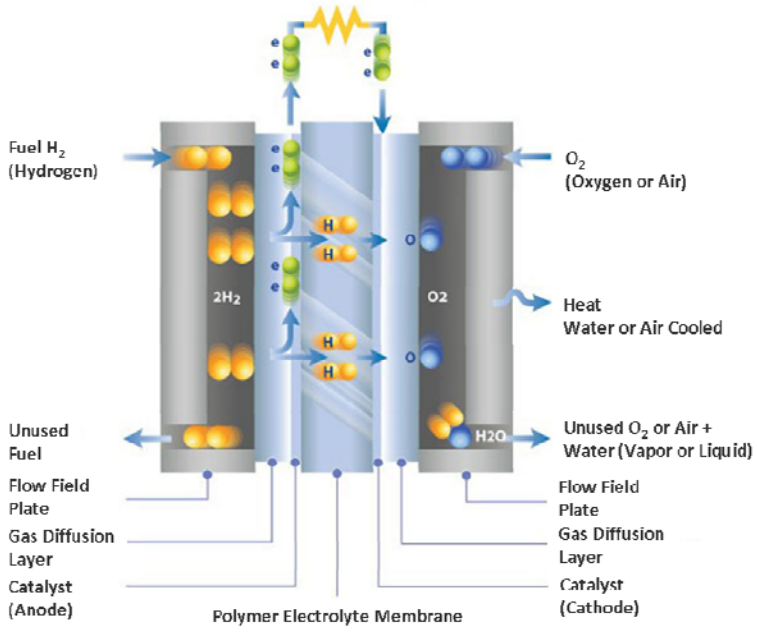

Figure 1.2 Taken from www.ballard.com. Schematic of a PEM fuel cell showing the polymer electrolyte membrane in the middle. The consecutive layers are the catalyst next to the membrane, the gas diffusion layer and the flow field plates. Hydrogen reacts at the anode and oxygen reacts at the cathode.

For Nafion, z = 1 and the ratio x/y gives the equivalent weight. A tradeoff is found between mechanical stability (larger equivalent weight) and conductivity (smaller equivalent weight).

The exact physical structure is still debated, especially how the structure changes as the membrane takes up water. The water molecules associate with the sulfonate groups, forming clusters that swell as more water is absorbed. The protons associate with the water molecules and hop between the clusters to move from the anode to the cathode. Eventually the clusters percolate between the PTFE matrix and the morphology becomes two continuous phases. The transport of protons becomes more like diffusion through bulk water and the conductivity is greatly increased.

The membrane must meet multiple requirements: high conduction of protons, very poor conduction of electrons, impermeable to gases, good mechanical stability, and

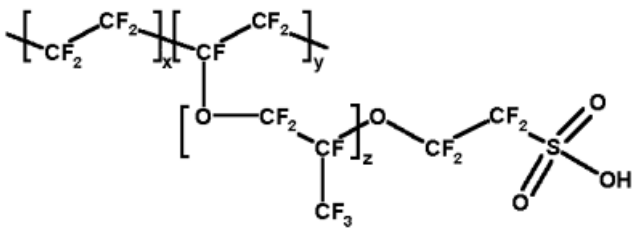

Figure 1.3 Chemical structure of Nafion, taken from http://en.wikipedia.org/wiki/Nafion. For Nafion, z = 1 and the x/y ratio gives the equivalent weight.

good chemical stability. Nafion is the material that meets these requirements the best and does so under a wide range of temperatures.

1.4.2 Catalyst layer

On both sides of the membrane is the catalyst layer. The standard catalyst is platinum nano-particles on a porous carbon support and coated with PTFE, shown in Figure 1.4. The loading of the catalyst is typically about 0.5 mg cm^{-2}. Both reducing the required catalyst loading or finding cheaper catalyst materials while maintaining the same performance of the fuel cell is an extensive area of research. So far, platinum is still the best catalyst for both the hydrogen oxidation reaction that happens at the anode,

$$H_2 \rightarrow 2H^+ + 2e^- \tag{1.1}$$

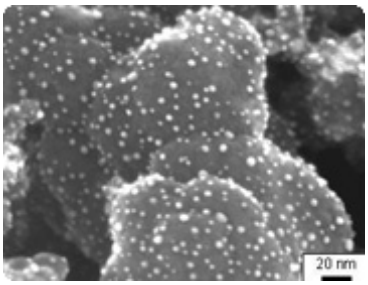

Figure 1.4 SEM photo of platinum catalyst nano-particles on a porous carbon support. Taken from http://www.tex.shinshu-u.ac.jp.

and the oxygen reduction reaction at the cathode,

$$\frac{1}{2}O_2 + 2H^+ + 2e^- \rightarrow H_2O \quad (1.2)$$

The structure of the catalyst layer tries to optimize the area of three-phase interface: the Nafion phase for the conduction of protons, the carbon support for the conduction of electrons, and the pore space for the mass transfer of the gaseous reactants. The porous nature of the carbon increases the surface area while the hydrophobic coating helps to expel liquid water that forms as a product of the reaction at the cathode. The accumulation of liquid water can block the supply of reactant to the catalyst particles. The catalyst layer is also impregnated with Nafion to provide better transport of the protons within more of the catalyst layer.

1.4.3 Gas diffusion layer

The next layer on the other side of each of the catalyst layers is the gas diffusion layer (GDL), another key component of fuel cells that serves multiple functions. The membrane, catalyst layers, and GDLs pressed together are what make up the membrane electrode assembly (MEA) that is often sold as a single component. The GDL is typically a carbon fiber material that is also coated with PTFE to increase its hydrophobicity.

Shown in Figure 1.5 are images of the two most common materials. In part (a) is carbon cloth, made from bundles of carbon fibers (each fiber ~10 μm in diameter) woven together. Part (b) shows carbon paper (at a higher magnification) made from the same fibers, but instead randomly oriented into a paper-like web. The major difference between the two materials is the resulting pore sizes from the construction. With the

carbon paper, large pores of ~140 μm are observed at the intersections of the fiber bundles with much smaller pores of ~10 μm between the fibers within the bundles. The pores of the carbon paper are much more uniform, with sizes in a smaller range of ~10 – 20 μm.

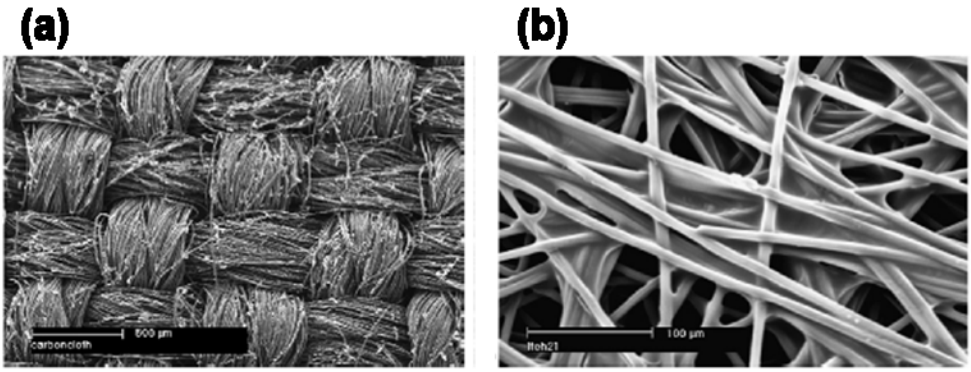

Figure 1.5 (a) SEM photo of a carbon cloth GDL. **(b)** SEM photo of a carbon paper GDL; magnification is ~10 times larger than in part (a). Taken from [7].

The pores of the GDL allow for the transport of the reactants from the flow channel to the catalyst. At the same time, water that is produced at the cathode catalyst or transported through the membrane to the anode must be able to get to the flow channels. When water is present only as a vapor, the transport is through diffusion; both the water and the reactants diffuse through the GDL pores driven by activity gradients. When liquid water is formed, the hydrophobicity of the GDL becomes important. The liquid water must build up until a high enough hydraulic pressure is created that can overcome the hydrophobic surface energy of the water entering the pore. The water breaks through at the largest pores first and can then flow through freely, even at a reduced pressure. The smaller pores are left open for the gas flow. The significance of the GDL structure and hydrophobicity is discussed in detail in Chapter 5.

While the pores of the GDL transport the reactants and water, the bulk of the GDL must conduct electrons. At the anode, the electrons are formed at the catalyst and are conducted through the GDL to the rest of the circuit. At the cathode, the electrons flow from the circuit, through the GDL, to the catalyst where they combine with the oxygen and protons to form water. The material of the GDL must be highly conductive while also durable under the various clamping pressures in assembled fuel cells.

1.4.4 Flow field plates

The outer layer on both sides of the fuel cell is the flow field plate. It must be a conductive material, like the GDL, and provides the conduction path from the GDL to the external circuit. The flow field plates are much thicker than the GDLs (millimeters compared to 100s of micrometers) so that their specific conductivity must be very high. Graphite is a common material for its high conductivity and low corrosion, but stainless steel and graphite composites (higher durability than graphite) are also used. In fuel cell stacks (often hundreds of fuel cells assembled in series), the thickness and weight of the flow field plates also become significant factors.

The flow channels for the reactants are carved out of the flow field plates. The ribs between the flow channels provide the contact to the GDL and are referred to as the "lands". The flow fields are often intricate serpentine patterns of one or more channels with the goal of dispersing the reactants evenly over the active area of the catalyst; a couple of examples are shown in Figure 1.6 The dimensions of the channels are ~1 mm for the depth and width, but into the tens and hundreds of mm for length. The flow channels can also be interdigitated to force convection through the GDL or modified in

shape along the length to maintain the linear velocity of the flow streams as the reactants are consumed.

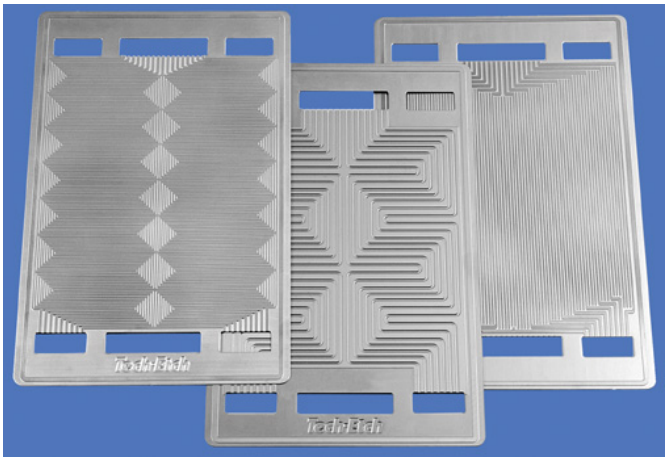

Figure 1.6 Examples of flow field plates for PEM fuel cells. Taken from www.tech-etch.com/photoetch/fcpr.html.

1.5 The Stirred-tank-reactor fuel cell

1.5.1 Rationale for design

As mentioned above, the flow fields of typical PEM fuel cells are intricate and consist of long, narrow channels. This usually requires higher flow rates and humidification of the feeds. More importantly for research purposes, the channels create substantial gradients in water activity and reactant concentrations over the active area. Measurements taken during experiments typically record the integrated response along the flow channels, making it difficult to determine the extent of the effects caused by a change in system or operating conditions. The typical data used to compare fuel cell operation consists of the measurements of the voltage across and current through a load resistance while sweeping the load resistance from open circuit (load resistance = ∞; V_{load}

≈1 V) to short circuit (load resistance = 0; $V_{load} \approx 0$) voltage. The voltage is plotted as a function of the current to give the standard polarization curve.

There are several issues with this approach to studying fuel cell operation. The first, as mentioned above, concerns the changes that occur along the flow channel as reactants are consumed and water is produced. The entire area is exposed to the same voltage, but with changing water activities, reactant concentrations, or other factors, some areas will produce a higher current than others. Often, an increase in current from one part of the fuel cell will cause a decrease in current at another part. The response of the total current will indicate a change of much smaller magnitude. As the total current is the measurement used in the analysis, this can mask the full implications of the experiment.

The second issue is the use of a potentiostat to control the voltage (or sometimes a galvanostat to control the current) when the independent parameter is actually the external load. The voltage of the fuel cell is the result of the activity gradient in hydrogen between the anode and cathode in series with the membrane and other internal resistances. The potential gradient drives the protons across the membrane and electrons through the external circuit, resulting in the measured current. Conservation of energy around the circuit (fuel cell and load) governs both the voltage and current. The only parameter that can be explicitly set is the external load. A potentiostat works by changing the load until the desired voltage is achieved, complicating the system and overshadowing the autonomous response of the fuel cell.

The last issue is the time over which polarization curves are taken. The different processes of an operating fuel cell occur on several different time scales. The electrochemical reactions are very fast, occurring over times of < 1 s, while the

membrane water uptake and transport is much slower, with time scales of 100 – 1000 s. The time scales for the transport of reactants and water within the GDLs and flow channels are intermediate. Increasing the current increases the rate of water production, but the time for water to accumulate and start affecting the fuel cell performance is usually much longer than the time between voltage steps. A change that causes the fuel cell to dry out and no longer operate can also take thousands of seconds to have an effect. The residual water is first removed before the membrane dehydrates and the total current decreases. A polarization curve taken soon after a change in the operating conditions does not show all of the implications.

The Stirred-Tank-Reactor (STR) fuel cell was developed in the Benziger group as a tool to study the fundamentals of fuel cell operation without the complications from gradients along the flow channel and external controllers.[8] The concept was borrowed from traditional chemical reactor engineering in which stirred-tank reactors (either mechanically stirred or through diffusive mixing) are assumed to have homogeneous reactant concentrations within the tank. The STR fuel cell consists of essentially two stirred tank reactors, one on the anode side and one on the cathode side, that are coupled by the electron flow through the external circuit, proton flow through the membrane, and water transport through the membrane. Instead of flow channels, the reactants were fed into open plenum chambers with only a few pillars contacting the GDL. The flow rates and volume of the plenums were chosen such that the residence time of the reactants in the plenums was greater than the characteristic diffusion time of the gases, as in equation (1.3),

$$\begin{aligned} \tau_R &> \tau_D \\ \frac{V_{gas}}{F} &> \frac{\left(V_{gas}\right)^{2/3}}{D_{gas}} \end{aligned} \tag{1.3}$$

where V_{gas} is the volume of the gas in the plenum, F is the flow rate of the gas through the plenum, and D_{gas} is the diffusivity of the gas. The STR fuel cell was typically operated with $\tau_R/\tau_D \sim 1-10$. The gases were thus well-mixed by diffusion and could be assumed to be homogeneous. The only gradients were in the transverse direction across the membrane, creating a one-dimensional system and greatly simplifying the analysis.

1.5.2 Experimental setup

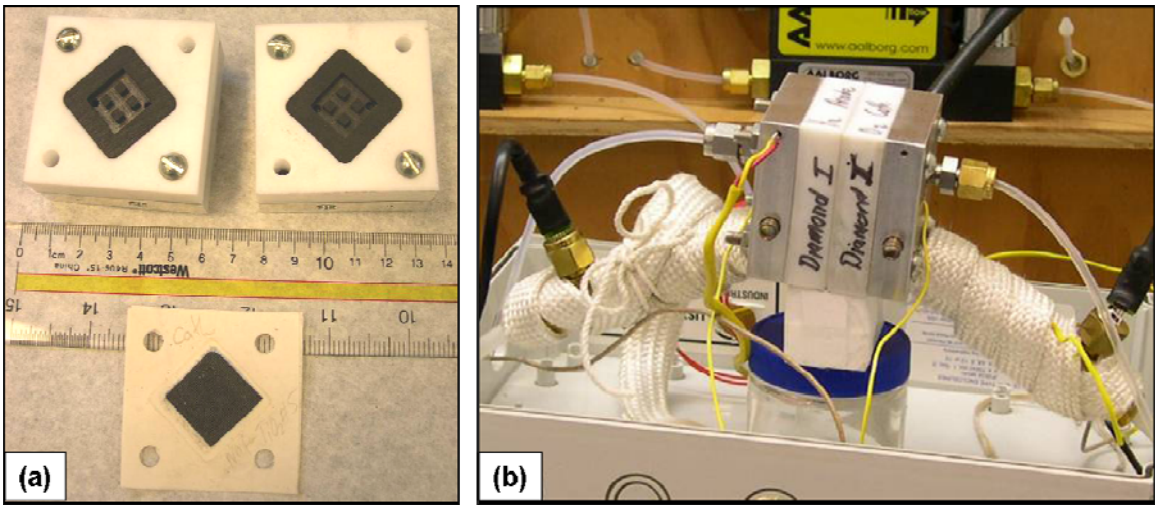

Figure 1.7 (a) Photo of the disassembled STR fuel cell. The flow field plates are shown at the top and the MEA is shown at the bottom. **(b)** Photo of the assembled STR system with the inlet tubes connected at the top and the outlets wrapped in heating tape with relative humidity sensors attached. Photos courtesy of Warren Hogarth.

A photo of a disassembled STR fuel cell is shown in Figure 1.7(a). The plenums are carved out of graphite plates to be 15 mm on each side. The four pillars contact the GDL and provide the electrical conduction path. The MEA is also shown with the gasket

material. Figure 1.7(b) shows the fully assembled fuel cell. Aluminum plates sandwich the fuel cell to provide compression and temperature control. The reactants are supplied from mass flow controllers through the inlets at the top of the fuel cell. The outlets are at the bottom of the fuel cell. Heating tape is wrapped around metal outlet fittings that allow for measurement of the outlet relative humidity at the fuel cell temperature.

The placement of the inlets at the top and outlets of the bottom makes the flows in the same direction as gravity. The diamond shape of the plenums and pillars eliminate areas that would trap any liquid water formed in the fuel cell. The combination of the downward flows, gravitational forces, and plenum design make the fuel cell self-draining; any liquid water leaves through the outlet tubes. Liquid water accumulation that can block the flow of reactants from the flow channels to the catalyst in conventional fuel cells is not a problem in the STR fuel cell. The data analysis is again simplified by the absence of complications from liquid water accumulation.

Another benefit of the well-mixed condition is the back-mixing of the water produced by the electrochemical reaction. The entire membrane will be well hydrated, even with dry feeds. In a conventional system with dry feeds and small channels, the water produced from the area near the inlets is evaporated into the flow streams and convected downstream. The velocities of the flow streams are high and do not allow for substantial back diffusion of water. Often the fuel cell is very dry near the inlets, but over-saturated near the outlets. The flow channel design creates the need for external humidification of the feeds and excessive flow rates to prevent liquid accumulation.

1.5.3 Insights from experimental results

The auto-humidified operation of the STR fuel cell was previously studied extensively in the Benziger group.[8-12] The simple 1-D design allowed for the calculation of several important parameters needed for the simulation of PEM fuel cell operation (the model equations are described in detail in Chapter 4). Allowing the fuel cell to run autonomously (under a constant load without potentiostatic or galvanostatic control) resulted in the observation of several phenomena not previously reported. These included multiple steady-states, ignition (a sharp increase in current) and extinction (a drop in the current to near zero), and sudden changes in the current and voltage without any change in operating conditions. The implications of these observations are discussed in more detail in the following chapters.

Just as important as the evidence of complex physics involved in fuel cell operation was the proof of operation with dry feeds. It is still commonly believed that at least one of the feed streams must be humidified. The results from the STR fuel cell showed that the need for humidification was a consequence of the flow field design reducing back mixing. The removal of excess liquid water could be achieved through system design instead of increased flow rates. With the self-draining and open plenum characteristics, fuel efficiency could be very high and still allow for stable operation.

Reactant distribution over the entire active area was not an issue at the small scale of the STR fuel cell. Maintaining the well-mixed condition would be more difficult with a large cell, as higher flow rates would be required to sustain a higher current. Furthermore, it was hard to connect the results with the STR design to what was being reported in the literature, dominated by results with different flow channel designs.

1.6 The Segmented anode parallel channel fuel cell

1.6.1 Rationale for design

The water activity and reactant concentrations change dramatically along the flow channels of PEM fuel cells. One approach was to eliminate the flow channels and gradients in order to study the fundamental physics of fuel cell operation with the 1-D STR fuel cell system. Another approach was to better understand the effects of the different gradients. This was done by segmenting the anode and taking measurements from several different points along the flow channel, instead of one integrated measurement. The simplest flow field design with flow channels was two-dimensional with a single straight channel, the inlets at one end, and the outlets at the other. This led to the segmented anode parallel channel (SAPC) fuel cell.

The dimensions of the flow channel (1.6 mm wide by 3.2 mm deep) were larger than most conventional flow channels (~1 mm dimensions). The first reason for the large channels was to allow for the section of the fuel cell at each segment to act like one small STR fuel cell. The flow channel volume and segment length were such that the residence time of the gas along one segment was greater than the characteristic diffusion time, just as in equation (1.3). The gases at each segment could be assumed to be homogeneous, simplifying the analysis. This condition was especially important for modeling purposes. Similar to the modeling of plug flow tubular reactors as several STRs in series, as in traditional chemical reactor engineering, each segment of the SAPC fuel cell could be modeled with the same 1-D model used with the STR fuel cell. The "tanks" of the model and the segments of the fuel cell were coupled through the flow streams and diffusion of water through the membrane.

Although the dimensions of the flow channel needed to allow diffusive mixing of the gases in the channel, the spacing between the segments and range of flow rates were chosen so that there was a clear separation between each segment. The dispersion of the gases was one consideration, as given by the Péclet number,

$$\mathrm{Pe} = \frac{l_{seg}}{D_{gas}} \times F \Big/ A_{channel} \tag{1.4}$$

where l_{seg} is the length of one segment and $A_{channel}$ is the cross-sectional area of the flow channel. Between segments, the typical Péclet number was ~2, indicating that convection was more important than diffusion and the dispersion was low between segments. The other consideration was that the separation between the segments (3.2 mm) had to be much larger than the thickness of the GDL (~0.5 mm) so that the transverse conduction of electrons through the GDL (between the lands and catalyst) was more than any lateral conduction between adjacent segments.

1.6.2 Experimental setup

The current design of the SAPC fuel cell was developed through a few iterations. A photo of the design used in the work presented here is shown in Figure 1.8(a) with a diagram of the system shown in part (b). The particular fuel cell used in the experiments presented here consisted of two polycarbonate plates with flow channels 1.6 mm wide x 3.2mm deep x 75 mm long. The design was such that the anode and cathode flow channels were in a single plane and terminated in a 90º angle that connected into a tube fitting adapted to 1/8" polyethylene tubing. Two stainless steel electrodes 6.4 mm wide x 54 mm long, lined the cathode flow channel. The anode consisted of six segments of stainless steel, 6.4 mm long and separated by 3.2 mm along the channel. The lead wires

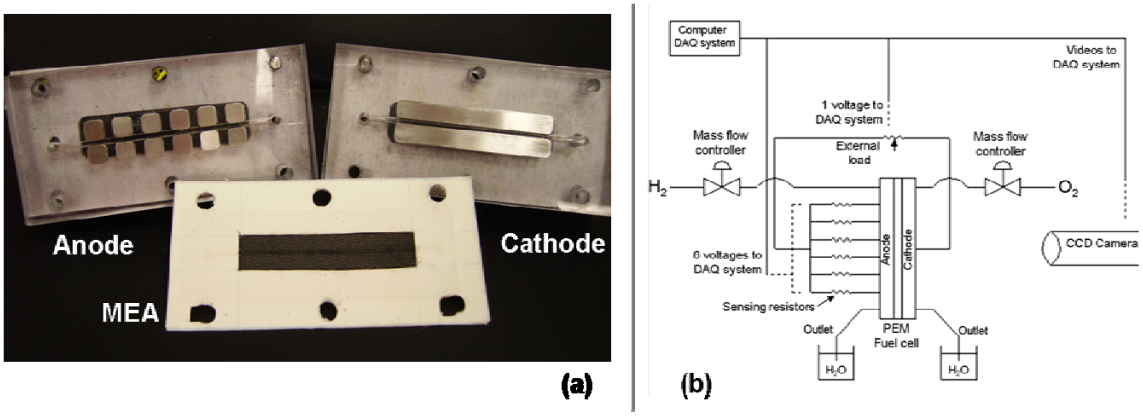

Figure 1.8 (a) Photo of the disassembled SAPC fuel cell showing the segmented anode flow field (top left), the cathode flow field (top right), and the MEA with gasket. **(b)** Diagram of the SAPC fuel cell system.

from each anode segment were connected individually to a 0.1 Ω sensing resistor. The six leads from sensing resistors at the anode were connected together, and the common lead was connected through a 0-20 Ω, 10-turn potentiometer to the cathode. The experiments were conducted with the load resistance > 0.5 Ω. The sensing resistors were a total resistance of 0.016 Ω so they contributed < 3% of the total external impedance. A CCD camera was positioned to view the cathode flow channel. (It was also possible to look at the anode flow channel, but all the interesting phenomena were observed at the cathode). Video images were collected and time stamped so they could be correlated with the current and voltage measurements.

A computer DAQ board, interfaced through LabVIEW, read the voltage drops across the potentiometer (that served as the load resistance) and those across each of the sensing resistors. Data samples were read from the board at 20 Hz and then conditioned to mitigate the noise in the measurements. When data was being saved to a file at 1 data set per second, each input was sampled at 16 Hz and 16 values were averaged. For longer term experiments, 1024 samples were read from the board, averaged, and written

to the file at 1 data point per minute. With this, the fluctuations in the data from noise were kept acceptably low at no more than ±0.0001 A.

The tubing from the gas flow channel outlets was bent down and bled into 10 mL graduated cylinders with a small hydrostatic head (~2-3 cm H_2O), so that the cell pressure was effectively 1 bar. Liquid in the cylinders kept air from back diffusing into the flow channels; the total liquid water leaving from both the anode and cathode could be measured. It was also possible to see gas bubbles leaving the anode and the cathode, which helped identify the extent of reactant conversion in the fuel cell. This setup allowed for the flows at the anode and cathode to be either co-current or counter-current. Data were collected at temperatures from 20-80°C. Experiments at the higher temperatures were used to identify ignition/extinction phenomena in the SAPC, where water was only present as water vapor. To study the effects of liquid water on fuel cell performance, the fuel cell was operated at 20-25ºC; the vapor pressure of water was sufficiently low (~0.025 bar) so that convection of water vapor was negligible and almost all the water transport was by liquid flow.

The MEAs were constructed in the lab from a Nafion 115 membrane, carbon cloth or carbon paper GDLs, and silicon gaskets. The GDLs were ELAT V2.1 obtained from E-TEK with the catalyst, 0.5 mg/cm^2 of 20% Platinum on Vulcan XC-72, applied to one side. The dimensions of the electrodes were 5.72 cm long by 1.43 cm wide to give a total area of 8.17 cm^2. (Only 10%, 0.91 cm^2, of the MEA was exposed to the gas channel, the other 90% of the MEA was under the stainless steel electrodes).

1.6.3 Advantages of the design

The design of the SAPC fuel cell was unique from what was found in the literature. Other groups had built cells with transparent flow channels for liquid water visualization[13-15] while others incorporated segmented electrodes[16-19], but the SAPC fuel cell was the first to combine the two. The movement of liquid water in the flow channels could be correlated with fluctuations in the local currents for the first time. The ability to change the orientation of the fuel cell with respect to gravity gave further insights into the implications of liquid water accumulation. This is discussed in detail in Chapter 3.

The single flow channel, low flow rates, and dry feeds greatly simplified the system and analysis. Operating with a constant load resistance without any external controllers showed how the current from each segment responded to system changes and adjusted to reach an autonomous steady-state. Even with a relatively short flow channel, large differences were observed in the local currents along the flow channel. Results are analyzed in detail in the following chapters.

1.7 Overview of dissertation

This dissertation is organized in two main parts. The first part, Chapters 2 – 4, focuses on factors inherent in fuel cell systems. The importance of the water balance and the multiple steady-states that are observed are investigated in Chapter 2. The SAPC fuel cell is used with the flows both co-current and counter-current to highlight the effects of water convection in the flow channels and diffusion in the membrane. The importance of gravity, a factor that is usually disregarded but always present in terrestrial fuel cell

systems, is discussed in the context of large amounts of liquid water accumulation in Chapter 3. The insights gained from the experiments in Chapters 2 and 3 helped in developing the mathematical model described in Chapter 4. Simulation results without any free parameters are compared to experimental data and allow for prediction of critical operating parameters.

The second main part, Chapters 5 and 6, focus on the engineering of fuel cell designs. The factors of gravity and material properties can be exploited to improve performance. Most designs take the flow field geometry and material properties as given parameters and try to find models that fit the data. The work presented here shows that the flow field and GDL properties can be used as design parameters to improve fuel cell performance. Chapter 5 investigates the effects of the structure of the GDL on the accumulation of liquid water. Modifications to the standard GDL materials are made and offer a way to design fuel cells for specific applications. Chapter 6 looks at the effects of the flow field properties. The dimensions of the flow channels, spacing between channels, surface properties of the lands contacting the GDL, and surface properties of the flow channels are all studied. The choice of using oxygen or air changes the optimal flow field design.

The final chapter, Chapter 7, gives a summary of the conclusions from the dissertation and offers suggestions for future work. The SAPC fuel cell design led to several important realizations about PEM fuel cell operation, but new systems and experiments are needed to offer more concrete proof of how the different aspects of a fuel cell design impact the operation and can be tailored to achieve the optimal performance.

1.8 References

1. Brown, L.F., *A comparative study of fuels for on-board hydrogen production for fuel-cell-powered automobiles.* International Journal of Hydrogen Energy, 2001. **26**(4): p. 381-397.

2. Dillon, A.C. and M.J. Heben, *Hydrogen storage using carbon adsorbents: past, present and future.* Applied Physics A-Materials Science & Processing, 2001. **72**(2): p. 133-142.

3. Grochala, W. and P.P. Edwards, *Thermal decomposition of the non-interstitial hydrides for the storage and production of hydrogen.* Chemical Reviews, 2004. **104**(3): p. 1283-1315.

4. Ogden, J.M., M.M. Steinbugler, and T.G. Kreutz, *A comparison of hydrogen, methanal and gasoline as fuels for fuel cell vehicles: implications for vehicle design and infrastructure development.* Journal of Power Sources, 1999. **79**(2): p. 143-168.

5. Mehta, V. and J.S. Cooper, *Review and analysis of PEM fuel cell design and manufacturing.* Journal of Power Sources, 2003. **114**(1): p. 32-53.

6. Yang, C., S. Srinivasan, A.B. Bocarsly, S. Tulyani, and J.B. Benziger, *A comparison of physical properties and fuel cell performance of Nafion and zirconium phosphate/Nafion composite membranes.* Journal of Membrane Science, 2004. **237**(1-2): p. 145-161.

7. Wang, Y., C.Y. Wang, and K.S. Chen, *Elucidating differences between carbon paper and carbon cloth in polymer electrolyte fuel cells.* Electrochimica Acta, 2007. **52**(12): p. 3965-3975.

8. Moxley, J.F., S. Tulyani, and J.B. Benziger, *Steady-state multiplicity in the autohumidification polymer electrolyte membrane fuel cell.* Chemical Engineering Science, 2003. **58**(20): p. 4705-4708.

9. Benziger, J., E. Chia, E. Karnas, J. Moxley, C. Teuscher, and I.G. Kevrekidis, *The stirred tank reactor polymer electrolyte membrane fuel cell.* AIChE Journal, 2004. **50**(8): p. 1889-1900.

10. Chia, E.S.J., J.B. Benziger, and I.G. Kevrekidis, *Water balance and multiplicity in a polymer electrolyte membrane fuel cell.* AIChE Journal, 2004. **50**(9): p. 2320-2324.

11. Hogarth, W.H.J. and J.B. Benziger, *Dynamics of autohumidifed PEM fuel cell operation.* Journal of the Electrochemical Society, 2006. **153**(11): p. A2139-A2146.

12. Hogarth, W.H.J. and J.B. Benziger, *Operation of polymer electrolyte membrane fuel cells with dry feeds: Design and operating strategies.* Journal of Power Sources, 2006. **159**(2): p. 968-978.

13. Tuber, K., D. Pocza, and C. Hebling, *Visualization of water buildup in the cathode of a transparent PEM fuel cell.* Journal of Power Sources, 2003. **124**(2): p. 403-414.

14. Yang, X.G., F.Y. Zhang, A.L. Lubawy, and C.Y. Wang, *Visualization of liquid water transport in a PEFC.* Electrochemical and Solid State Letters, 2004. **7**(11): p. A408-A411.

15. Weng, F.-B., A. Su, C.-Y. Hsu, and C.-Y. Lee, *Study of water-flooding behaviour in cathode channel of a transparent proton-exchange membrane fuel cell.* Journal of Power Sources, 2006. **157**(2): p. 674-680.

16. Berg, P., K. Promislow, J. Stumper, and B. Wetton, *Discharge of a segmented polymer electrolyte membrane fuel cell.* Journal of Fuel Cell Science and Technology, 2005. **2**(2): p. 111-120.

17. Hakenjos, A. and C. Hebling, *Spatially resolved measurement of PEM fuel cells.* Journal of Power Sources, 2005. **145**(2): p. 307-311.

18. Natarajan, D. and T. Van Nguyen, *Current distribution in PEM fuel cells. Part 1: Oxygen and fuel flow rate effects.* AIChE Journal, 2005. **51**(9): p. 2587-2598.

19. Nishikawa, H., R. Kurihara, S. Sukemori, T. Sugawara, H. Kobayasi, S. Abe, T. Aoki, Y. Ogami, and A. Matsunaga, *Measurements of humidity and current distribution in a PEFC.* Journal of Power Sources, 2006. **155**(2): p. 213-218.

2 Hydration fronts

2.1 Introduction

The stable operation of a PEM fuel cell requires maintaining the correct balance between the water produced by the electrochemical reaction and the water removed through convection. This is especially important during the start-up of the fuel cell; at first, the current is controlled by the initial hydration of the membrane, but changes quickly as the fuel cell responds to the operating conditions. When starting from dry conditions (i.e. the membrane is not fully hydrated) and with the water production greater than the water removal, the fuel cell current output evolves to a high current or "ignited" steady-state. A positive feedback between the water produced and the increasing conductivity of the membrane allows for a sharp increase in the current. If more water is removed than produced, the current decreases to a very low current or "extinguished" steady-state. All of the system operating parameters—flow rates, cell temperature, load resistance—affect the water balance to varying degrees by changing either how much water is removed through the flow streams or the rate of water production. There are critical values for each parameter below which the fuel cell ignites and above which the fuel cell extinguishes. The STR fuel cell described earlier in section 1.5 is an ideal system for studying ignition and extinction, due to the absence of gradients in directions other than transverse through the membrane.

Previous work in the Benziger group showed the importance of the initial hydration state of the membrane in determining whether the fuel cell ignited or extinguished for the one-dimensional STR fuel cell.[1] Figure 2.1 shows the fuel cell current vs. time results when starting the fuel cell with varying initial water contents,

denoted by λ (molecules of water per sulfonic acid group in the membrane). If the initial membrane water activity was below a critical value, the fuel cell current was too low so that the rate of water production was less than the rate of water removal. The fuel cell operation evolved to the dry extinguished steady-state. Above that value, the fuel cell ignited, so that the current increased dramatically and the ignited steady-state was obtained. The current for the ignited state was several orders of magnitude higher than that of the extinguished state.

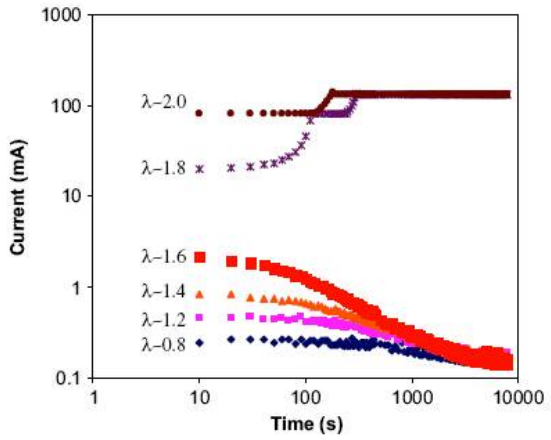

Figure 2.1 (taken from Moxley, et al.[1]) Start-up of an autohumidification PEM fuel cell with different initial water contents (= # H_2O/SO_3). The fuel cell was operated at 50 ℃ with a 5 Ω load resistance. The current through the external load resistance is shown as a function of time. The current was recorded every 10 s for a period of 6 h.

The parameters listed above were varied with the STR fuel cell to cause a switch between the ignited and extinguished steady-states with the same initial water content. Figure 2.2 shows that with settings of 2 Ω for the load resistance, 8/4 ml min^{-1} H_2/O_2 for the flow rates, and 60 °C for the temperature, the current ignites and reaches a final value of ~300 mA/cm^2 (curve a). Increasing the load resistance to 5 Ω (curve b), increasing the flow rates to 12/6 ml min^{-1} H_2/O_2 (curve c), or increasing the temperature to 70 °C (curve d) all caused the fuel cell to extinguish to a miniscule current production of only ~1

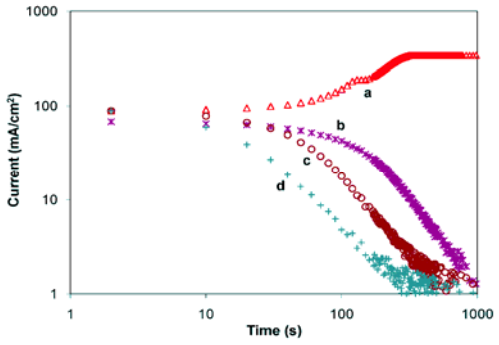

Figure 2.2 (taken from Moxley, et al.[1]) STR PEM fuel cell start-up after injecting 1.0 mg/cm^2 of water into a 1 cm^2 dry fuel cell. (a) Cell temperature – 60 °C, feed flows: anode - 8 mL/min of H_2 cathode - 4 mL/min O_2, load resistance - 2 Ω. (b) Cell temperature - 60ºC, feed flows: anode - 8 mL/min of H_2 cathode - 4 mL/min O2, load resistance - 5 Ω. (c) Cell temperature - 60ºC, feed flows: anode - 12 mL/min of H2 cathode - 6 mL/min O2, load resistance - 2 Ω. (d) Cell temperature - 70ºC, feed flows: anode - 8 mL/min of H2 cathode - 4 mL/min O2, load resistance - 2 Ω.

mA/cm^2. In the well-mixed system, the decline in current was gradual and took hundreds of seconds to reach the steady-state.

A standard fuel cell has flow channels, often very long and narrow, and is not well mixed. The water content varies drastically over the active area of the MEA. The local current density is dependent on the local water content and any local variations in the internal resistance (including the membrane resistance). The flow rates also change as the reactants are consumed by the electrochemical reaction and water is evaporated into the flow channels. Lateral diffusion in the flow channels and membrane becomes important and helps to smooth out the gradients in water activity. The interaction of these factors with each other as they change gradually causes hydration fronts to propagate along the flow channel. Ignition of the current at one point in the flow channel initiates a propagating ignition front that can then allow the entire fuel cell to reach the high current steady-state. Alternatively, the extinction of one area can cause the entire fuel cell to dry out and fail. These phenomena could not be studied with the one-

dimensional STR fuel cell. The SAPC fuel cell was the simplest two-dimensional system that could be designed and led to several insights into the physics of ignition and extinction.

The original purpose of the SAPC fuel cell design was to study the propagation of hydration fronts along the flow channel during ignition and extinction. With the segmentation of the anode, it was possible to observe the dynamics of the propagation along the flow channel as the current from each segment of the anode responded sequentially to the change in the operating conditions. The SAPC fuel cell allowed for the observations of where the front started, how quickly it propagated, and whether it moved down the entire length of the flow channel or stopped part way. In later experiments, the SAPC also proved to be valuable in studying flooding, or the blockage of the reactants by liquid water. Those results are discussed in the next chapter while all the results presented in this chapter are for the case when liquid water is not present in the fuel cell.

Several factors influence the appearance of ignition and extinction fronts. Many of these either cannot be controlled explicitly—such as the local current density, reactant partial pressures, and water activity in the membrane—or are pre-determined by the system design—such as the channel dimensions and flow field geometry. The parameters that could be controlled and set to a certain value with the SAPC fuel cell were the same as those found to be important with the STR fuel cell experiments—feed flow rates, load resistance, and temperature. The initial hydration state of the membrane was also very important, but was hard to control to a precise value. Additionally, with the flow channels, the choice of flow pattern—co-current or counter-current—had a large

influence on the appearance and movement of the hydration fronts. All of these factors were investigated thoroughly and gave much more insight than what would be possible from the integrated measurements and I-V curve results from traditional fuel cell systems.

The following chapter gives experimental results from the SAPC fuel cell showing both ignition and extinction front propagation with several sets of operating conditions. A simple numerical model is described and used to predict conditions that lead to fuel cell ignition.

2.2 Ignition

2.2.1 Co-current vs. counter-current flow pattern

The SAPC fuel cell allowed for both co-current and counter-current flows. The choice of flow pattern changed the local membrane hydration and current density distribution along the flow channel. With co-current flows, the water was convected from the inlets to the outlets through the feed streams at both the anode and cathode sides of the fuel cell. The water activity and membrane proton conductivity increased farther downstream and allowed for higher currents closer to the outlets. The change in flows to counter-current operation convected more water to the middle of the flow channel. The water was convected in one direction on the cathode side, transported across the membrane and convected in the other direction at the anode side, creating a "cyclic" convection pattern that introduced some convective mixing into the system. With dry feeds on both sides, counter-current flows gave a current distribution that was higher in the middle of the flow channel.

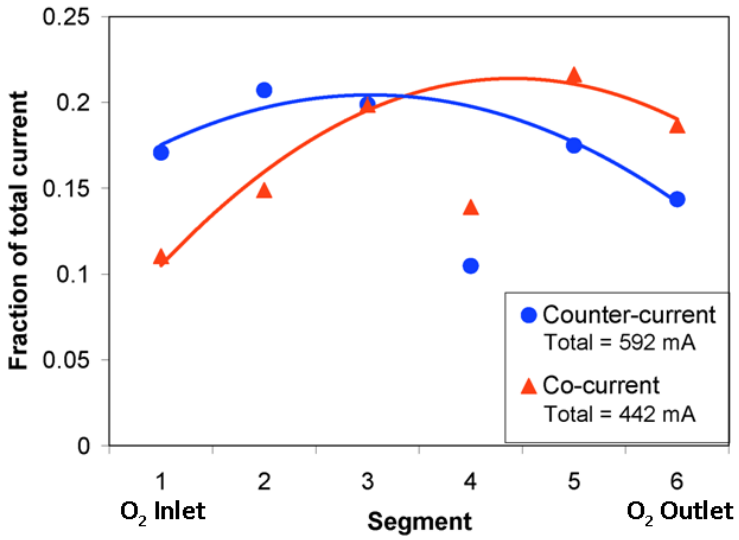

Figure 2.3 Typical steady-state current profiles for the SAPC fuel cell with both co-current (triangles) and counter-current (circles) flows. Segment 1 is always defined as that closest to the oxygen inlet; with co-current flows, the hydrogen inlet is also at segment 1 and with counter-current flows, the hydrogen inlet is at segment 6. The unusually low currents at segment 4 were due to a faulty electrical connection and were disregarded when calculating the trendlines. Operating conditions: flow rates = 6/3 ml min^{-1} H_2/O_2, load resistance = 0.5 Ω, temperature = 25 °C.

Figure 2.3 shows the steady-state "current profiles," or the fraction of total current from each of the six segments along the flow channel, for two typical experiments, one with co-current and one with counter-current flows (polynomial-fit trendlines are given for visual clarity). In Figure 2.3, and in the rest of this chapter, segment 1 is always defined as closest to the oxygen inlet. With co-current flows, the hydrogen inlet is also at segment 1 and with counter-current flows, the hydrogen inlet is at segment 6.

The local current density is lowest where the flow streams are driest and highest where the flow streams are the most humidified. The co-current profile (triangles) shows a maximum at segment 5 with a relatively steep decline to segment 1 and a small decrease at segment 6. The flows on both sides become more humidified closer to the outlets, but the partial pressure of the reactants also decreases due to consumption by the reaction. The counter-current profile (circles) has a maximum at segment 3 with only

gradual declines to either direction. The convection from both ends of the flow channel (through the hydrogen on the anode side and the oxygen on the cathode side) causes the membrane to be the most hydrated and the local current density to be highest in the middle of the channel. The unusually low currents from segment 4 are a result of a faulty electrical connection giving a higher internal resistance at that location and were disregarded when calculating the trendlines.

The total steady-state current with counter-current flows of 592 mA is higher than the total current of 442 mA with co-current flows for the data shown in Figure 2.3. Some of the difference can be attributed to degradation of the MEA and other changes in the internal resistance when reassembling the fuel cell. However, the ratio of the total current for counter-current flows relative to co-current flows was consistently greater than 1, indicating that the cyclic convection of water with counter-current flows was an important factor. With low flows of 6/3 ml min^{-1} H_2/O_2, as in Figure 2.3, the average ratio of the total current with counter-current flows relative to co-current flows was 1.3. Under conditions with higher total currents (due to better fuel cell construction) the average ratio decreased to 1.1, even with higher flow rates of 12/6 ml min^{-1} H_2/O_2. The increased water production locally hydrated the membrane to a greater degree, making convection of water in the flow channels less of a factor in determining the current distribution. Increasing the temperature from 25 °C, as in Figure 2.3, to 60 °C increased the ratio to 1.5. The increased vapor pressure of water made the convection in the flow channels and the convective mixing with counter-current flows much more important.

Figure 2.4 further shows the significance of the choice of flow pattern at elevated temperatures. The temperature was increased from 25 to 60 ºC over the first ~1000 s.

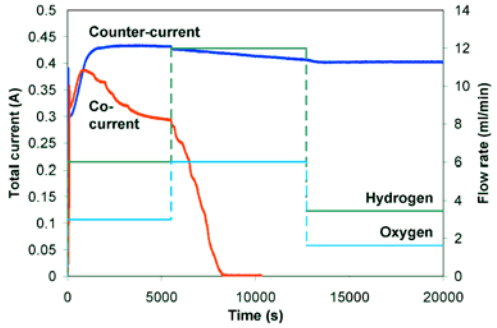

Figure 2.4 Results of the total current produced by the fuel cell with time for operation with both co-current and counter-current flows. The temperature was increased from 25 °C at time 0 to 60 °C at ~1000 s to increase the importance of water transport through convection in the flow streams. The flow rates of hydrogen on the anode side and oxygen on the cathode side are shown on the secondary axis and have a heightened effect on the fuel cell operation.

With counter-current flows, the total current is slightly decreasing with the higher flow rates and stable with reduced flows. When part of the membrane started to dry out near the cathode flow channel inlet, water from the anode side flow channel was absorbed into the membrane due to the increased water partial pressure in the hydrogen. Even though only dry feeds were used, the anode flow stream was humidified from upstream evaporation of water (the area of the fuel cell near the cathode outlet). The proton conductivity and current was sustained for a much longer time. The results with co-current flows show an initial ignition, due to the initially lower temperature and the membrane being hydrated before the experiment was started. As the temperature reaches 60 ºC, the current starts to decline with the increased water evaporation and decreased membrane hydration. The increase in flow rates at ~5500 s (shown on the secondary axis in the figure) causes the fuel cell to completely extinguish. With co-current flows, the anode flow stream could not be more humidified than the cathode flow stream, so the rehydration of the membrane did not occur.

2.2.2 Dependence on initial conditions

The initial water content of the membrane can be difficult to control, especially with commercial systems that cannot be taken apart and reassembled easily. Excess water in the flow channels can be purged with a sharp increase in the gas flows, but the dynamics of water absorption and desorption in the membrane are slow enough[2] that the time scales for pre-conditioning a system would be infeasible for mainstream use. This could be problematic for intermittent use of fuel cell systems as significantly different behavior is observed with a membrane that is already hydrated when the flows are started in comparison to when the membrane is dry. Also, when the membrane is dry, it can be uniformly dry, but still allow for the fuel cell to ignite, or it can be very dry at some points and slightly hydrated at others, such that only part of the fuel cell ignites and is able to contribute to the total current and power output.

2.2.2.1 Hydrated startup

When the membrane is well hydrated, two different ignition fronts are observed. The first is fast and causes a peak in the currents on a time scale of about 100 s. This peak corresponds to the start of the flow of hydrogen from the anode inlet and along the flow channel. The second ignition front occurs over longer time scales as the membrane takes up water. The proton conductivity of the membrane increases, allowing the current to increase until a steady-state is obtained. Figure 2.5 shows the spatio-temporal data leading to the steady-state profiles shown in Figure 2.3. With co-current flows (part a), the current from the area closer to the inlets, where the membrane was slightly more hydrated, starts increasing with the second ignition first. A front then propagates down the channel and the currents evolve to be higher towards the outlets, as discussed

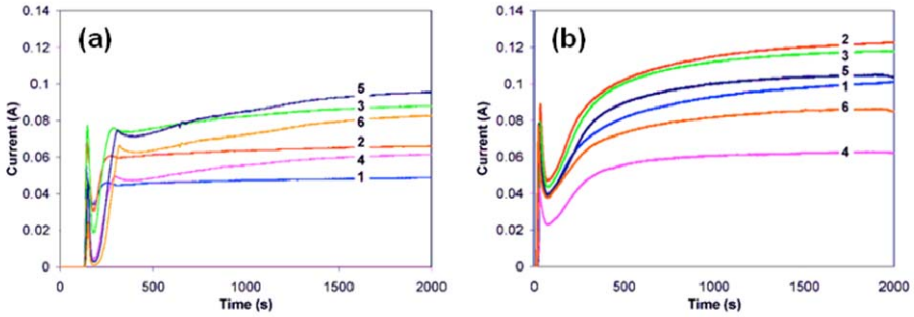

Figure 2.5 Spatio-temporal data from each of the six segments of the SAPC fuel cell (numbered 1 – 6) for the experiments leading to the steady-state profiles in Figure 2.3 with (a) co-current and (b) counter-current flows. Segment 1 is always defined to be at the oxygen inlet. Two ignition fronts are observed: the peaks occurring over ~100 s correspond to the flow of hydrogen (see Figure 2.6) while the more gradual increase to the steady-state corresponds to the water feedback loop. Operating conditions: flow rates = 6/3 ml min^{-1} H_2/O_2, load resistance = 0.5 Ω, temperature = 25 °C.

previously. With counter-current flows (part b), the membrane was more uniformly hydrated and the currents from the six different segments start increasing with the second ignition at about the same time, eventually reaching the steady-state with the currents highest in the middle of the channel.

The initial hydration uniformity of the membrane is indicated by the relative magnitudes of the fast peaks mentioned above. Figure 2.6 zooms in on the peaks from Figure 2.5, again for both co-current flows (part a) and counter-current flows (part b). The local currents peak in the order of the segments' exposure to the hydrogen flow. With a flow rate of 6 ml min^{-1} and channel dimensions of 1/8" x 1/16", one would expect there to be about 0.32 s between each peak based on the time for convection between segments, but the actual times were much longer, ~1-2 s. This indicates other transport processes, such as diffusion through the GDL, are dominating the current evolution on that time scale. The current distribution will evolve to the steady-state, but the process will take much longer when the initial state is far from the steady-state.

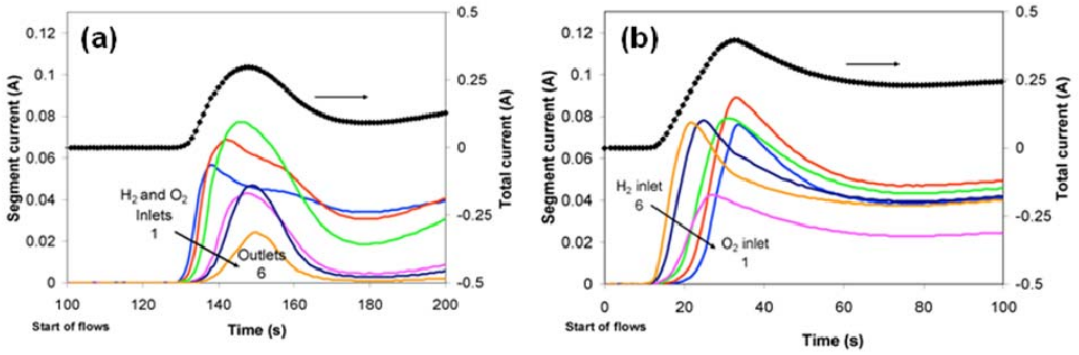

Figure 2.6 Zoom in on the fast peaks from Figure 2.5 with (a) co-current flows and (b) counter-current flows. The currents from the segments peak in the order of exposure to hydrogen flow while the relative magnitudes give an indication of the initial hydration state of the membrane (colors correspond to the segments as in Figure 2.5). The total current is also given on the secondary axis to show the integrated response of the fuel cell.

The initial peaks are also important due to the difficulties they could cause with controlling a fuel cell system. The total current changes by as much as 30 mA/s and then drops off at a slower rate of ~10 mA/s. These values are not large, but would be significantly amplified for commercial systems that are much larger than the SAPC fuel cell. The flows are in excess (more reactants are supplied than consumed) while the current is changing rapidly; a change in flows that continues to provide any excess reactants would not have a large impact. Also, the time scale over which the current is changing is small enough that the water content in the membrane does not change significantly; changing the humidification of the feeds would also not cause the peaks to disappear. Therefore, for the current to be controlled, the external load would be varied, but would also change the voltage output of the fuel cell. Figure 2.7 shows the rate of the change in power for the same data shown in Figure 2.6(b). The power, the product of the current and voltage, is the variable that must be maintained and creates high process gains with respect to the load resistance that would be difficult to regulate with quick

changes from positive to negative. With the much more gradual current increases with the second ignition front, the rate of power change is over an order of magnitude lower and would be much easier to compensate for. This indicates a tradeoff for system design: the more hydrated initial state of the membrane allows the fuel cell to equilibrate faster (also see the following section), but the peaks that occur just after the flows are started must be expected in the controller design.

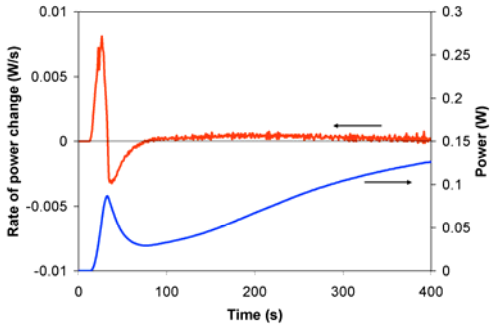

Figure 2.7 The power output and rate of change of the power for the peaks shown in Figure 2.6(b). The power change quickly increases and then quickly drops during the peak in the power. During the more gradual increase of the second hydration front, the rate of power change is almost an order of magnitude less, and would be much easier to control.

2.2.2.2 Dry startup

Starting the fuel cell with the membrane very dry (but still above the critical water content for the given parameter set) gave very different results than the case with a hydrated membrane. With dry conditions, no peaks are observed corresponding to the start of the hydrogen flow and the ignition profile is determined by the convection of water. With co-current flow, the segments closer to the outlets ignite first due to the convection of water downstream. The hydration front then propagates up the channel as diffusion of water allows for ignition and increasing current upstream. With counter-current flow, the cyclic convection of water causes the ignition to start in the middle of

the flow channel and propagate both towards the inlets and the outlets. The time scales for the ignition to occur are much longer than when starting the fuel cell with a hydrated membrane.

Figure 2.8 shows typical spatio-temporal data for dry startup with both co-current (part a) and counter-current (part b) flows. With co-current flows, the local currents at segments 5 and 6 start to ignite within a few hundred seconds, followed by the currents from the other segments in order up the channel. There are very long delays between each segment ignition as water must back diffuse up the channel against convection; the current from segment 1 does not increase significantly until about 15,000 s, over four hours after the flows are started. With counter-current flows, the ignition order is very different, but still occurs over a time scale on the order of 10,000 s. The current from segment 2 ignites first, followed by the current from segments 1 and 3 at about the same time, after about 1000 s. The currents from segments 4, 5, and 6 then ignite sequentially over the next ~8000 s. It might be expected that the current from segment 6 would ignite first as water is produced on the cathode side and so would be more readily transported into the cathode flow stream and downstream to segment 6. However, water diffusion through the membrane is comparable to water diffusion in the gases[3], allowing for a significant amount of water to be transported to the anode side, where it is convected back towards the oxygen inlet. The stoichiometric ratio of 2:1 was used to set the flow rate of H_2 relative to the flow rate of O_2, so convection on the anode side of the fuel cell was a larger factor than convection on the cathode side.

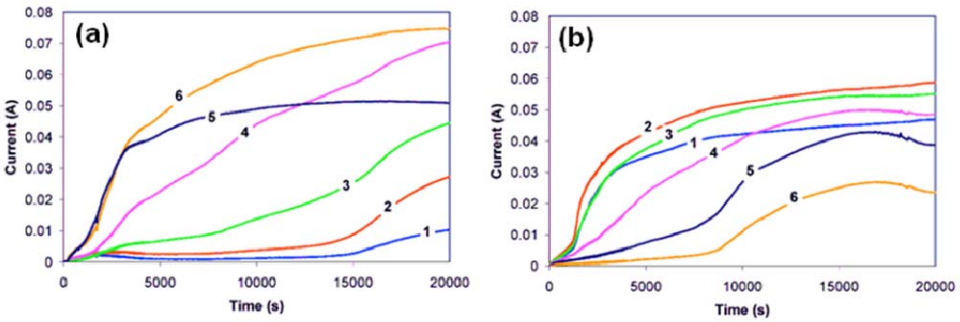

Figure 2.8 Spatio-temporal data from each of the six segments (segment 1 at the oxygen inlet) for startup from dry conditions with (a) co-current and (b) counter-current flows. With co-current flow, the currents from the segments at the outlets ignited first and a front propagates back up the channel. With counter-current flows, the middle of the channel ignites first (closer to the hydrogen outlet) and the front propagates outwards from both directions. The time scales are much longer than those for startup from hydrated conditions (see Figure 2.5). Operating conditions: flow rates = 3/1.5 ml min^{-1} H_2/O_2, load resistance = 0.5 Ω, temperature = 25 °C.

The absolute times for ignition were hard to quantify due to the difficulty in precisely controlling the initial water content of the membrane and internal resistances of the fuel cell. The membrane could be dried at a given temperature for a given amount of time, but how much water was absorbed in the membrane at the beginning of the drying, its spatial distribution, and how much water was taken up due to ambient humidity after the drying all influenced the hydration state. It should be noted that although the membrane was the important factor in determining the initial water content, the drying and rehydrating always took place with the membrane pressed with the catalyst and gas diffusion layers in the assembled MEA. It was not possible to take the MEA apart, treat the membrane and reassemble the MEA. The other consideration was with changes in the internal resistances of the fuel cell (other than that of the membrane). Any degradation of the MEA, either during the previous experiment or drying process, or increase in contact resistance when putting the fuel cell together would increase the total

internal resistance. For a constant load resistance and given voltage, this would decrease the current and water production, resulting in longer times for ignition and startup.

Simply drying out the membrane completely in order to always start from the same initial condition was not a possibility due to the presence of the extinguished steady-state. The membrane could be dried completely, ensuring uniformity, but the fuel cell would always be at the extinguished steady-state regardless of the different operating parameters. The initial water content of the membrane had to be above a critical value for ignition to occur. With the differential STR fuel cell used for the experiments previously completed in the Benziger group, the composition of the gases in the plenums could be assumed to be homogeneous. With the SAPC fuel cell, the flow channel and segmented anode showed that with non-uniform initial conditions, part of the membrane could be below the critical water content while another part could be above. If the current ignited near the outlets and the operating parameters were set such that convection was a greater factor than diffusion, then the ignition front would not propagate back up the full length of the flow channel. Only a fraction of the fuel cell would be operating and contributing to the power output.

An example of this situation is shown in Figure 2.9. The MEA was left in the fuel cell after an experiment in which the flow rates, load resistance, and temperature were all increased to cause the fuel cell to completely extinguish. The flows were co-current during the previous experiment (and for the results in Figure 2.9) so that more water evaporated into the flow streams closer to the inlets and was convected towards the outlets. The currents at segment 1 extinguished first, followed sequentially by the other segments down the channel (extinction fronts are discussed in more detail in section 2.3).

Each segment extinguished when the water content of the membrane was too low to allow a measurable current production, but residual water in the membrane and GDL continued to be evaporated while the flows were on. Only when the entire fuel cell was extinguished were the flows stopped. During the experiment, the temperature was increased to 80 °C so that the evaporation of water was increased. This caused the membrane to be extremely dry near the inlets while being very dry, but just below the critical water content, near the outlets.

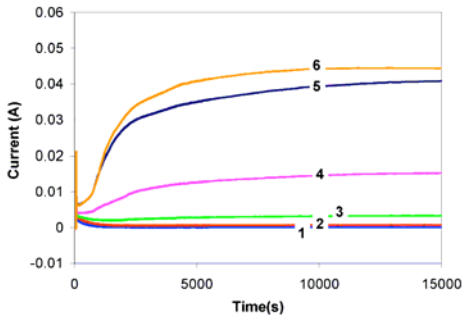

Figure 2.9 Spatio-temporal data from each of the six segments (segment 1 at the inlets) for startup with co-current flows from non-uniformly dry conditions, leading to only partial ignition. The membrane was slightly more hydrated closer to the outlets (at segment 6) than at the inlets (at segment 1). The membrane was too dry at the inlets for back diffusion to allow the entire fuel cell to ignite. Operating conditions: flow rates = 6/3 ml min^{-1} H_2/O_2, load resistance = 0.5 Ω, temperature = 25 °C.

Before the data in Figure 2.9 was taken, the fuel cell outlets were closed and the cell was allowed to cool from 80 °C back to room temperature over ~3.5 hours. As the temperature decreased, any small amount of water in the flow streams increased in activity due to the decrease in water vapor pressure with the cell cooling. The membrane absorbed a small amount of water until the water activities in the membrane and flow channel were equilibrated. Near the outlets, where the membrane was not as dry, this allowed the water content to become above the critical level. With the restart of the flows (at time $t = 0$ in Figure 2.9), the fuel cell ignited. All of the segments show a small,

but measurable current at first, but the currents from segments 1 and 2 are only ~1 mA after 500 s. The current from segment 3 also remains very low at ~3 mA. The small amount of product water then fed into the water balance at segment 4. The current from segment 4 reaches 15 mA, producing significantly more water. The increases continue to segments 5 and 6 with segment 6 reaching a maximum of ~45 mA.

Even though water could diffuse upstream in the membrane, it did not cause ignition during the duration of the experiment because of downstream convection. The membrane was too dry near the inlets and could not absorb enough water to reach the critical water content. It should be noted that how the hydration of the membrane affects water diffusion, possibly making it slower when the membrane is very dry, is not well understood. Structural changes in the membrane occur as water is absorbed and could also be a contributing factor in determining the critical water content. It should also be possible to reach a partially-ignited steady-state independent of the initial condition. Changing the water balance by changing the flow rates, temperature, and load resistance can result in an ignition profile anywhere from fully extinguished to fully ignited. Experimentally, the range of operating parameters leading to partial ignition is very narrow and was not reproducible from a uniform initial condition.

A final consideration with startup from a dry membrane is ignition through water injection. Previous work in the Benziger group showed ignition after a small amount of water, 100 µl, was injected into the anode feed stream of the STR fuel cell.[4] The current showed an initial sharp increase followed by a gradual increase over hundreds of thousands of seconds. A similar experiment was done with the SAPC fuel cell, shown in Figure 2.10. 50 µl of water were injected into the anode feed at time $t = 0$. The diffusive

mixing was much less in the flow channel of the SAPC fuel cell than in the open plenum of the STR fuel cell, but the small amount of water that was taken up by the membrane was enough to put the water content above the critical level required for ignition.

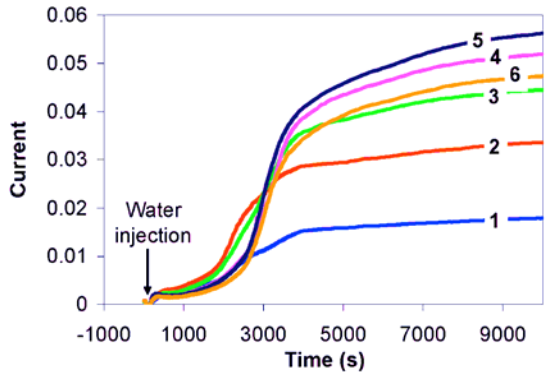

Figure 2.10 Spatio-temporal data from the six segments (segment 1 at the inlets) for startup with co-current flows and water injection. At time t = 0, 50 µl water were injected, starting the ignition front. With co-current flows, the current distribution evolves to be higher closer to the outlets. Operating conditions: flow rates = 3/1.5 ml min^{-1} H_2/O_2, load resistance = 0.5 Ω, temperature = 25 °C.

The currents showed a small jump just after the water injection and then increased more gradually with a hydration front over the next ~10,000 s. Again, because of the difficulty in controlling the initial state of the membrane, the necessary volume of the water injection or flow rate limit was not studied with the SAPC fuel cell (the STR fuel cell design was much more well suited for those studies; see Hogarth, et al.[4]). However, the dominant factor should be the time the injected water spends in the flow channel, as opposed to the volume of water. Due to the hydrophobicity of the GDL, water only reaches the membrane and can be absorbed after evaporating and diffusing through the pores of the GDL to the catalyst/membrane interface. That amount of water is limited by the rate of evaporation and transport through the GDL.

It should be noted that the proton conduction in the membrane is only through the most conductive part. The protons are not transported across the resistive part and will

move laterally in the membrane if the transverse gradient is too high. Although the transverse water profile in the membrane during fuel cell operation has not been studied in our system, one would expect the membrane to be driest and most resistive closer to the anode side. Water is produced at the cathode side and only reaches the anode side of the membrane by transverse diffusion across the membrane or transport through the anode side gas stream from a more hydrated part of the fuel cell. Injecting water into the cathode side would be less effective than the injection into the anode side.

2.2.3 Temperature dependence

Increasing the temperature of the fuel cell has several effects on its operation. The carbon monoxide poisoning of the catalyst is reduced, especially for temperatures above 100 °C. The kinetics of the electrochemical reactions are enhanced. For the work discussed here, the most important consideration is the increase in the vapor pressure of water with increasing temperature. More water evaporates into the flow streams with higher temperatures. This can be beneficial, as extra water is carried more quickly to drier parts of the fuel cell and can allow the membrane to be more uniformly hydrated. Also, extra water that would condense and cause flooding at lower temperatures would instead be removed as a vapor through convection. On the other hand, if the rate of water production is not high enough and too much water evaporates from the membrane, the membrane resistance will increase, decreasing the current and further lowering the water production. Eventually the fuel cell will dry out and fail. Although several references can be found in the literature that state that operation of a fuel cell with dry feeds is impossible above 60 °C[5], this is only true when the right balance of water removal and water production is not achieved.

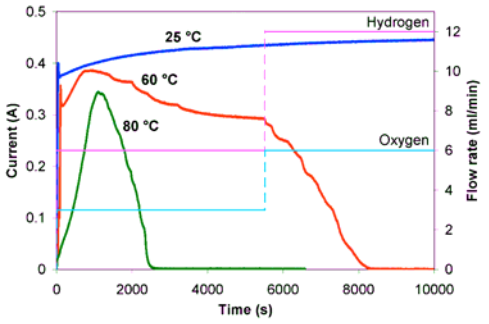

Figure 2.11 Results of the total current produced with time for three different temperatures—25, 60, and 80 °C. The temperature is increased from 25 °C to the setpoint over the first ~1000 s. As the water vapor pressure increases exponentially with increasing temperature, more water is removed through convection and the operation becomes highly dependent on the flow rates (shown on the secondary axis). Operating conditions: co-current flows, load resistance = 0.5 Ω.

Figure 2.11 shows the total current from the SAPC fuel cell versus time with co-current flows, for three different temperatures—25, 60, and 80 °C—and with two different flow rates—6/3 and 12/6 ml min^{-1} H_2/O_2. The MEA was well hydrated before being put into the fuel cell, giving the peaks just after the flows were started. The temperature of the cell was increased from room temperature to the indicated value over ~1000 s (for the results at 60 and 80 °C; temperature vs. time data not shown for visual clarity). The MEA used in the experiments had a low total active area (3/16" x 2 ¼") so that the total current was relatively low. At 25 °C, the current ignites and the fuel cell runs with stable operation at both sets of flow rates. At 60 °C, the saturation vapor pressure of water is dramatically increased from 0.03 bar at 25°C to 0.20 bar, almost an order of magnitude increase. The convection of water out of the fuel cell is then also greatly increased. At the lower flow rates, the current ignites, but decreases as the temperature increases. Still, the fuel cell operates and stabilizes at an ignited, but lower, total current compared to the 25 °C case. The increase in flow rates at ~5500 s makes convection more important and the water removal exceeds the water production at 60 °C;

the current drops off to complete extinction of the fuel cell. Further increasing the cell temperature to 80 °C, a 33 % increase, increases the saturation vapor pressure to 0.47 bar, an increase of almost 250% from the vapor pressure at 60 °C. The fuel cell starts to ignite with the start of the flows, initial hydration, and initially low temperature, but then quickly fails as the cell temperature reaches the 80 °C setpoint.

The large increases in the water saturation vapor pressure in the range where most PEM fuel cells operate (60-80 °C) makes the system much more sensitive to the other adjustable parameters—flow rates, load resistance, and flow pattern. With the higher water content in the flow streams at the higher temperatures, convective effects are greatly amplified. The load must be at a level that allows for a high enough water production rate. With the SAPC fuel cell, an equivalent way to control the water production over the entire length of the flow channel is to change the width of the MEA under the lands (the ribs on either side of the flow channel that contact the GDL; see section 1.6). This changes the active area of the MEA by the same factor for each segment along the flow channel. Several experiments were done with varying the width of the MEA with widths ranging from 3/16" to 9/16" (originally to investigate lateral transport of the reactants under the lands). The flows were either co-current or counter-current and the temperature was set to 25, 60, or 80 °C.

Although experiments should be done with much more refined changes in the different parameters, the rough parameter space diagram of Figure 2.12 shows clear regions where the SAPC fuel cell can operate. With high active areas, more water is produced and the fuel cell can operate at higher temperatures with both co- and counter-current flows and with low or high flow rates (6/3 or 12/6 ml min^{-1} H_2/O_2), designated as

region I. At high temperatures and with decreasing active area, a point is reached where the fuel cell can only operate with the lower flow rates with both co- and counter-current flows, designated as region II. Further decreasing the active area requires counter-current flows to operate at elevated temperatures and high flows, designated as region III and similar to the results discussed with Figure 2.4. Finally, for low active areas and high temperatures up to 80 °C, the fuel cell could only operate with low flows (6/3 ml min^{-1} H_2/O_2) and only if the flows were counter-current, shown as region IV.

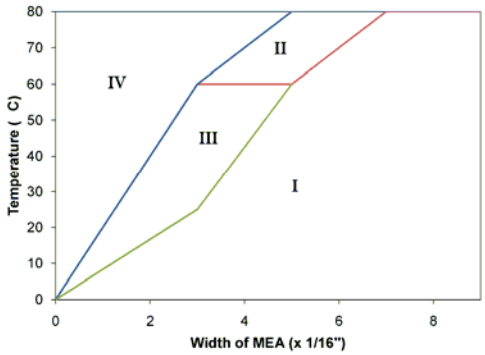

Figure 2.12 Parameter space diagram giving critical conditions for fuel cell operation with varying MEA active areas and temperatures. Region I designates operation with either co- or counter-current flows and either low or high flow rates (6/3 or 12/6 ml min^{-1} H_2/O_2). Region II is defined by where the fuel cell can operate with either co- or counter-current flows but only at the low flow rates. At lower active areas, counter-current operation is required for operation with the higher flows, designated as region III. Finally, the fuel could operate only at the low flow rates and with counter-current flows at high temperatures and low active areas, designated as region IV.

The results in Figure 2.12 are only applicable for a specific fuel cell design. Changing the flow field geometry, flow channel dimensions, GDL material, oxidant (air instead of oxygen), or other aspects of the system design will change the water balance. The water balance is affected by either changing the convective removal of water from the cell or by changing how well the fuel cell operates, giving a lower or higher current and water production rate. The data used to make Figure 2.12 was also taken starting with a well hydrated membrane. Starting from a dry state would decrease the areas

where the fuel cell could ignite and operate (this is investigated further through simulations, described in Chapter 4). Although Figure 2.12 is only applicable to a specific system—the SAPC fuel cell, carbon cloth GDLs, hydrated initial conditions—it is still very useful as it shows the possibility to operate with dry feeds at elevated temperatures. Fuel cell failure is the result of not carefully choosing the operating parameters. At a given temperature, the fuel cell will operate in one of the four regions and the parameters should be adjusted based on the system requirements to ensure stable operation.

2.3 Extinction

Extinction in the SAPC fuel cell occurs when the removal of water from the fuel cell exceeds the water production and the membrane becomes dehydrated. The water balance must be achieved locally in order for the local membrane proton conductivity to remain high. When one area of the fuel cell begins to dry out, it no longer produces water that can feed into the water balance and help hydrate other areas of the fuel cell. If the fuel cell continues to extinguish, a drying front propagates from the driest areas along the flow channels to eventually extinguish the entire fuel cell. Here a distinction is made between a fuel cell not being able to ignite, such as in the high temperature cases of Figure 2.11, and a fuel cell "extinguishing", or failing with the change of one or more system parameters after showing long-term stable operation at an ignited steady-state.

2.3.1 Co-current extinction

Figure 2.13 shows typical results of an extinction front propagating along the flow channel with co-current flows. The important factors are the same as those discussed

above for determining how the fuel cell ignites. To obtain the data in Figure 2.13, the fuel cell was started with co-current flows (inlets at segment 1) and conditions that would allow it to ignite and run with stable operation for a long time period. After several hours, the temperature and load resistance were increased so that the water removal exceeded the water production. An extinction front is observed to propagate down the flow channel from the inlets to the outlets until the entire fuel cell fails and the current production is essentially zero.

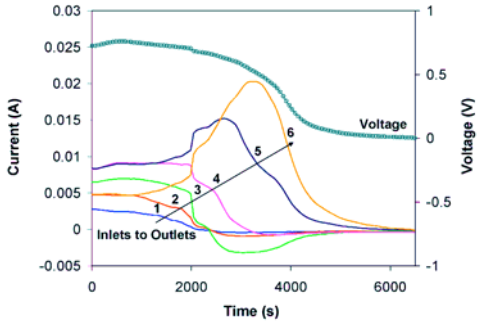

Figure 2.13 Spatio-temporal data of the six segment currents and the voltage showing the propagation of an extinction front with co-current flows. At time $t = 0$, the flows were set at 6/3 ml min^{-1} H_2/O_2, the load resistance was set at 20 Ω, and the temperature was increased to 80 °C. The negative currents at segment 3 and the peaks in the currents from segments 5 and 6 were initially unexpected. The voltage only decreases slightly until the last segment begins to extinguish. Both inlets are at segment 1.

There are a two interesting features to note in Figure 2.13 that were not originally expected. The first is the negative current at segment 3 that occurs around 3000 s. At that point, the currents from segments 1 and 2 are extinguished and the current from segment 3 drops off sharply, levels off at about zero, then becomes negative. The area of the fuel cell downstream of segment 3—segments 4, 5, and 6—is still operating and producing a current. Some of the electrons from those areas are driven to segment 3 through the external circuit (again, the segments are connected electrically in parallel), where they can react with protons to evolve hydrogen. This phenomenon is not yet well

understood, but must be driven by significant lateral potential gradients along the flow channel. The fuel cell voltage, the variable commonly measured in fuel cell experiments, decreases only very slightly during this time period and gives no indication of the large changes in the current distribution or the locally negative currents. This is further evidence of the importance of understanding the physics of the fuel cell on a local level and not relying on measurements integrated over an entire active area.

The second feature in Figure 2.13 is related to the first in that, as the currents from the segments closer to the inlets extinguish, the currents from the downstream segments increase. The fuel cell voltage only decreases slightly until the last segment extinguishes and the entire fuel cell fails. The catalyst at the extinguished segments is still active and a large enough activity gradient can still drive the hydrogen oxidation reaction. The resistance of the dry membrane at the extinguished segments is too high to conduct the evolved protons, but they can be transported laterally along the flow channel. This increases the hydrogen activity downstream and causes the currents to increase where the protons can still be conducted across the membrane to form water at the cathode. As more and more of the fuel cell extinguishes, the effect is amplified at the areas still operating, resulting in the large peak at segment 5 and the even higher peak at segment 6, the last segment to extinguish. Accounting for the lateral flow of protons is important for predicting the extinction front, but also for predicting responses to changes in load resistance and flow rates and when considering degradation of the MEA. This is discussed further in Chapter 4 describing the "Tanks-in-series" mathematical model.

2.3.2 Counter-current extinction

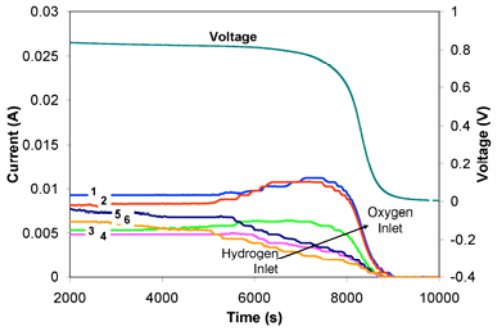

Figure 2.14 Spatio-temporal data of the six segment currents and the voltage showing the propagation of an extinction front with counter-current flows. At time $t = 0$, the flows were set at 6/3 ml min^{-1} H_2/O_2, the load resistance was set at 20 Ω, and the temperature was increased to 80 °C. The currents extinguish much more gradually than with co-current flows. The peaks are not as large and negative currents are not observed. Again, the voltage only decreases slightly until the last segment begins to extinguish. The oxygen inlet is at segment 1 and the hydrogen inlet is at segment 6.

When the flows were switched to counter-current, many of the same features discussed above were still observed, but with some significant differences. Figure 2.14 shows typical results for the propagation of the extinction front with counter-current flows. At time $t = 0$, the temperature started to increase to 80 °C and the load resistance was increased to 20 Ω, equivalent to the conditions for the data in Figure 2.13. The first difference between Figures 2.13 and 2.14 is the time between when the temperature and load resistance was increased and when the first segments start to extinguish. With co-current flows, the currents start to decline significantly about 1000 s after the temperature begins to be increased. With counter-current flows, no change is observed for about 5000s. The difference arises from the cyclic transport of water towards one end of the fuel cell on the cathode side and towards the other end on the anode side, the same factor that lead to the results in Figure 2.4. Water is transported within the fuel cell more and

removed through the flow streams less, allowing for water to continue to be produced by the reaction for a longer period of time and slowing the extinction propagation.

When the extinction does start, the changes in the currents are less dramatic than with co-current flows. Negative currents are not observed at any of the segments. Also, the magnitudes of the peaks from the currents that extinguish last are not as large. The currents that extinguish first do so much more gradually and only reach zero just before the entire fuel cell is extinguished. Again, this is because the cyclic transport of water keeps the membrane more uniformly hydrated. As long as water is being produced somewhere along the channel, water will be convected through one of the flow streams to the other areas of the fuel cell. The lateral potential gradients are lessened with the more uniform hydration.

Finally, switching to counter-current flows separates the hydrogen and oxygen inlets, showing that the currents from the segments closer to the hydrogen inlet extinguish first. Segment 1 is always defined as that closest to the oxygen inlet; segment 6 is closest to the hydrogen inlet with counter-current flows and extinguishes first. Under non-saturated conditions at a particular distance from the respective inlet, the flow stream on the anode side will be drier than the flow stream on the cathode side. Water is produced on the cathode side and must diffuse across the membrane before evaporating into the anode flow stream. The mass transfer resistance creates an activity gradient across the membrane so that the membrane is drier on the anode side in general. With dry feeds, the driving force for evaporation of water into the flow streams is greatest at the inlets. The driest area, where the fuel cell extinguishes first, is closest to the hydrogen inlet.

2.3.3 Dependence on load resistance

Increasing the flow rates increases the convection of water out of the cell; not as much water evaporated upstream can be absorbed by the membrane downstream and the fuel cell extinguishes faster. Changing the temperature has a more dramatic effect as the water saturation vapor pressure increases greatly with only small increases in temperature; the driving force for evaporation into the flow streams is increased and the fuel cell extinguishes for a much wider range of operating conditions. Increasing the load resistance has a more subtle effect by decreasing the current and rate of water production, with the largest changes at lower loads. Changing the load resistance affects the entire area of the fuel cell in the same way whereas increasing the flow rates or temperature has the greatest effect at the driest parts of the fuel cell. The segments are connected electrically in parallel so that the currents from each segment are driven by the same potential difference across the external load.

The data shown in Figure 2.13 is with a load resistance of 20 Ω. In Figure 2.15 all of the operating conditions are the same as in Figure 2.13, but with the load resistance set to only 10 Ω instead of 20 Ω. The higher currents, relative to those in Figure 2.13, have several effects. The time for the first segment to extinguish is much longer, ~4800 s compared to ~1000 s, but the time for the front to propagate all the way down the channel to completely extinguish the fuel cell is comparable, ~4000 s. The currents from segments 1-4 decline more gradually and the peaks in the currents from segments 5 and 6 are much broader than in Figure 2.13. The higher currents throughout the fuel cell allow for more water to diffuse back up the channel. At the drier parts of the fuel cell, though,

the water is evaporated very quickly into the flow streams. With less severe lateral potentials, negative currents are not observed at any point.

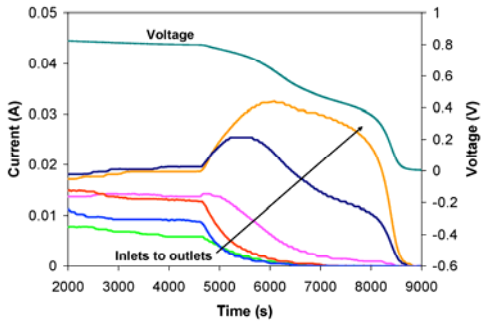

Figure 2.15 Spatio-temporal data of the six segment currents and the voltage showing the propagation of an extinction front with a load resistance of 10 Ω. The other operating conditions were equivalent to those for Figure 2.13 (co-current flows, flows of 6/3 ml min^{-1} H_2/O_2 and temperature increased to 80 °C at time t = 0). The extinction front propagates much more slowly, the peaks at segments 5 and 6 are much broader, and negative currents are not observed. Both inlets are at segment 1.

Further decreasing the load resistance for the extinction to 5 Ω gives the results shown in Figure 2.16. The time for the first segment to extinguish is still around 5000 s, but the extinction front stops part way down the channel, giving a partial extinction similar to the partial ignition shown in Figure 2.9. As the currents from segments 1-3 drop off, the currents from segments 4-6 increase to a maximum, as expected. But then with the increased current and water production, the local membrane hydration remains sufficiently high to stay at the ignited steady state. At around 20,000 s, the back diffusion of water in the flow channels and membrane allows the currents to partially recover. The currents from segments 4 and 5 increase to a higher current, ignited steady-state. The current from segment 6 decreases with the decrease in lateral proton conduction. The fully extinguished currents—at segments 1, 2, and 3—show a slight increase, but are not able to reignite. The currents remain at the new steady-state for the duration of the experiment (> 60,000 s; the full time scale is not shown).

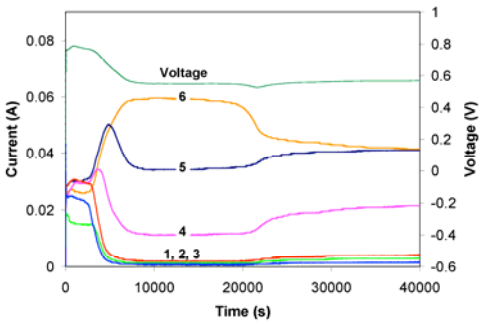

Figure 2.16 Spatio-temporal data of the six segment currents and the voltage showing the propagation of an extinction front with co-current flows and a load resistance of 5 Ω. The other operating conditions were equivalent to those for Figure 2.13 (flows of 6/3 ml min^{-1} H_2/O_2 and temperature increased to 80 °C at time t = 0). The extinction front starts at segment 1 and propagates through segment 3, but as the currents increase downstream, the water production is increased and the front stops. The fuel cell recovers to a partially ignited stead-state, similar to Figure 2.9. Both inlets are at segment 1.

2.4 Predicting ignition and extinction

2.4.1 Analytic prediction

With the orders of magnitude difference between the two stable steady-states, ignited or extinguished, it is necessary to be able to predict how the current will evolve for a given cell design and set of operating conditions. The simplest way to predict fuel cell ignition is by a steady-state mass balance of the water removed through convection with the water produced by the electrochemical reaction without considering any spatial variations, given in equation (2.1),

$$\frac{F_A P_{w,A} + F_C P_{w,C}}{RT} = \frac{V}{R_L + R_{mem}} \cdot \frac{1}{2\mathfrak{F}} \tag{2.1}$$

Here, F_A and F_C are the flow rates at the outlets of the anode and cathode sides, respectively; $P_{w,A}$ and $P_{w,C}$ are the partial pressures of water in the flow streams on the anode and cathode sides, respectively; R is the universal gas constant; T is the

temperature of the fuel cell; V is the voltage across the external load; R_L is the external load resistance; R_{mem} is the proton resistance of the membrane; and $\mathcal{F}$ is Faraday's constant. Assuming that the water activity is equilibrated in the transverse direction, the partial pressure of water in the flow streams can be written as a function of the water activity as $a_w \cdot P_w^{sat}$, where a_w is the water activity and P_w^{sat} is the saturation vapor pressure at the given temperature. The membrane resistance is also dependent on the water activity, as given by equation (2.2)

$$10^7 \cdot \exp(-14 \cdot a_w^{0.2}) \cdot \frac{t_{mem}}{A_{mem}} \tag{2.2}$$

where t_{mem} is the thickness of the membrane in centimeters and A_{mem} is the area of the membrane in cm^2.

Plots of the water removal (LHS of equation (2.1)) versus the water production (RHS of equation (2.1)) will intersect at the steady-states of the fuel cell operation, as shown in Figure 2.17. The exponential dependence of the membrane resistance on the water activity leads to the sigmoidal shape of the water production curve. The water removal curve is a straight line with a linear dependence of the water partial pressure on the water activity. With the conditions used for Figure 2.17, there are three steady-states: the extinguished steady-state at very low water activity, the unstable-steady state, and the ignited steady-state at a water activity of about 0.84.

Equation (2.1) is useful in predicting the initial water content needed for the fuel cell to ignite. If the water content is above the unstable steady-state, the water production is greater than the water removal and the current will increase until the ignited steady-state is reached. Below the unstable steady-state, the water removal is greater and the

fuel cell will extinguish. The equation does not take into account any spatial variations in water activity or other parameters. As the results discussed above show, the local water content can vary greatly, leading to differences in the local membrane resistance and current density. Also, as the feeds are consumed by the reaction and water is evaporated into the flow streams, the partial pressure of the water in the flow channels changes along the channel. Finally, the water removal will be decreased through back-diffusion in both the flow streams and the membrane.

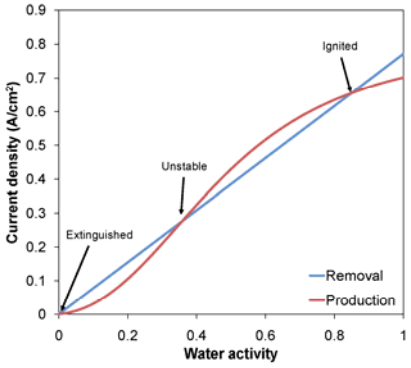

Figure 2.17 Numerical prediction of the steady-states based on equation 2.1. The water removal depends on water activity through the water partial pressure, giving a linear dependence. The water production depends on water activity through the membrane resistance, with the exponential dependence leading to a sigmoidal shape. Model parameters: flow rates = 2/1.3 ml min^{-1} H_2/O_2, temperature = 25 ºC, load resistance = 0.75 Ω.

Describing the change in water activity along the length of the flow channel is much more complex than the simple mass balance of equation (2.1). Neglecting diffusion simplifies the calculation drastically so that relations can be written and solved analytically. This gives a first approximation of whether the fuel cell will ignite or extinguish and what the water activity profile along the flow channel might look like. The local flux of water is similar to the LHS of equation (2.1),

$$J = \frac{F_A + F_C}{A_{ch}} \cdot \frac{P_w}{RT} = \frac{F_A + F_C}{A_{ch}} \cdot \frac{P_w^{sat}}{RT} \cdot a_w \qquad (2.3)$$

where J is the flux of water in mol s^{-1} per unit area, A_{ch} is the cross sectional area of the flow channel, and the other symbols are the same as before. In using equation (2.3), it is assumed that the water activity is equilibrated in the transverse direction, or that the water activity is the same in the anode flow stream, membrane, and cathode flow stream at a given position along the channel. For this assumption to be true, transverse water transport within the membrane, across the membrane interfaces, and into the flow channels must be fast compared to convective transport. This is dependent on several properties including the structure of the GDL and morphology of the membrane interface.[6]

Using Fick's Second Law, the change in flux along the flow channel can be correlated with the local change in water concentration with time,

$$\frac{\partial c_w}{\partial t} = \frac{\partial J}{\partial z} = \frac{F_A + F_C}{A_{ch}} \cdot \frac{P_w^{sat}}{RT} \frac{\partial a_w}{\partial z} \tag{2.4}$$

where c_w is the concentration of water in moles per unit volume. Excess flows are assumed such that the flow rates are approximately constant with z. The water production also contributes to the change in concentration with time,

$$A_{ch} \cdot \frac{\partial c_w}{\partial t} = \frac{j}{2\mathfrak{F}} \cdot w_{gdl} \tag{2.5}$$

where j is the current density and w_{gdl} is the "effective" width of the GDL. The width on the RHS of equation (2.5) is specified as an effective width because all of the catalyst layer may not be utilized. Depending on the width of the lands and the lateral transport of the reactants under the lands, there may be a part of the catalyst that is not exposed to the reactants and so does not contribute to the current production. On the LHS side of equation (2.5), the water concentration is scaled by the flow channel area because the set

of equations (2.4) and (2.5) is neglecting diffusion and only accounting for lateral water transport through the flow streams.

At steady-state, the flux will equal the production rate. Setting equations (2.4) and (2.5) equal to each other allows for the calculation of the change in water activity along the flow channel,

$$\frac{da_w}{dz} = \frac{\frac{j}{2\mathfrak{F}} \cdot w_{gdl}}{\left(F_A + F_C\right) \cdot \frac{P_w^{sat}}{RT}} \tag{2.6}$$

Using values corresponding to the SAPC fuel cell, a constant value for the current density of 1 A cm^{-2}, and typical flow rates of 6/3 ml min^{-1} H_2/O_2, the water activity gradient is 2.5 cm^{-1} at 25 °C, decreasing to 0.46 cm^{-1} at 60 °C. The water activity decreases from outlet to the inlet; neglecting back diffusion the water activity in the SAPC fuel cell reaches 1, indicating saturated conditions, at 0.4 cm from the inlet at 25 °C and with dry feeds. At 60 °C, the length for saturation increases to 2 cm, but the majority of the flow channel will still be exposed to saturated flow streams.

2.4.2 Numerical prediction

Assuming a constant current density in equation (2.6) predicts ignition for conditions where the actual fuel cell would extinguish. If any part of the fuel cell is extinguished, it will not be producing water to help hydrate the rest of the cell. Allowing the current density to be a function of water activity is better suited for a numerical solution. First, the change in j with increasing a_w is calculated using Kirchhoff's laws. For a fuel cell connected to a constant external load, as with the SAPC fuel cell experiments, the voltage across the load, V (also equal to $j \cdot R_L \cdot A_{mem}$), must be balanced

by the battery voltage resulting from the difference in hydrogen activity across the membrane and the voltage contribution from the membrane resistance,

$$V - V_b + j \cdot R_{mem} \cdot A_{mem} = 0 \tag{2.7}$$

The membrane resistance is a function of water activity, as given in equation (2.2). The effective fuel cell voltage, V_b, is also a function of water activity as follows,

$$V_b = V_o - V_T \ln\left(\frac{j \cdot A_{mem}}{I_o} + 1\right) + \frac{RT}{4\mathfrak{F}} \ln\left[\frac{\left(a_H^{cat}\right)^2 \left(a_O^{cat}\right)}{\left(a_w\right)^2}\right] \tag{2.8}$$

The derivation of equation (2.8) is discussed in detail in Chapter 4, but a brief description is given here. V_o is the standard thermodynamic potential for the formation of water. The second term represents the voltage losses from the energy needed to initiate the reactions with the catalyst layers modeled as diodes. V_T is the diode threshold voltage and I_o is the diode saturation current. The third term is the potential resulting from the activity gradient of hydrogen across the membrane. The hydrogen at the cathode is assumed to be in equilibrium with the oxygen and water at the cathode, where a_H^{cat} and a_O^{cat} are the activities of hydrogen at the anode catalyst layer and oxygen at the cathode catalyst layer, respectively. For a given a_w, the current density, j, can be solved for numerically.

To calculate the water activity profile along the flow channel, an inlet condition and the other operating conditions (temperature, flow rates, load resistance, etc.) need to be specified. For small enough steps, the water activity at $z + \Delta z$ can be calculated from equation (2.6) as,

$$a_w\big|_{z+\Delta z} = a_w\big|_z + \left[\frac{\frac{j\big|_{z+\Delta z}}{2\mathfrak{F}} \cdot w_{ch}}{\left(F_A + F_C\right) \cdot \frac{P_w^{sat}}{RT}} \right] \cdot \Delta z \tag{2.9}$$

The current density, j, in equation (2.9) is calculated using simple linear interpolation between points of the numerical solution of $j = f\left(a_w\right)$ obtained from equations (2.7) and (2.8) at the given temperature for the full range of water activity, $0 \le a_w \le 1$. The results are solutions for the water activity and current density profiles at several points along the flow channel. The water activity is constrained to be no greater than 1 in the calculations. In an operating fuel cell, after the water activity reaches 1, any addition of water condenses as a liquid. In that case, the fuel cell would be fully ignited and any changes in the current distribution would be the result of liquid water blocking the flow of reactants into the GDL. These considerations are discussed in the next chapter; the analysis given here is only for cases with no liquid water present.

The inlet and operating conditions are changed to predict whether or not ignition will occur and where it occurs first. The results give the steady-state prediction while neglecting diffusion. After ignition occurs at the point predicted by the calculations, water diffusion in the membrane and flow channels would allow an ignition front to propagate upstream over time, at least part way. Figure 2.18 shows results of the calculations for conditions that lead to ignition in the middle of the channel. The same sigmoidal shape of the water production curve from Figure 2.17 appears in the current density curve. The $j(z)$ curve increases slowly at moderate water activities, but then reaches an inflection point where both the current density and water activity increase much more quickly. The appearance of the inflection point gives a way to quantitatively

define “ignition”; if the inflection point appears before the end of the channel, the fuel cell ignites, otherwise, the current remains very low and the fuel cell is extinguished. After the inflection point, the water content is much higher and there is a substantial water activity gradient created across the inflection point. In an operating fuel cell, the gradient would drive diffusion that would allow more of the fuel cell to ignite, provided the water removal was not too great. The appearance of the inflection point is similar to temperature runaway in an adiabatic plug flow reactor.[7] The inflection point in the temperature profile indicates a condition where the rate of reaction and temperature increases dramatically and can lead to instabilities without an upper limit, analogous to the increase in water activity across the inflection point allowing for much higher currents in a fuel cell.

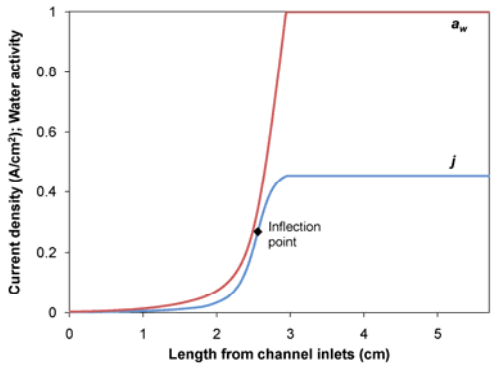

Figure 2.18 Results of the calculations with equations (2.7)-(2.9). After calculating the *j(z)* curve, the inflection point can be found to quantitatively define “ignition”. If the inflection point occurs before the end of the flow channel, a dramatic increase in water activity and current is observed and the fuel cell can be said to be ignited.

Even though the above equations neglect diffusion, they are still useful in predicting how changes in the different parameters will affect the fuel cell startup. Figure 2.19 shows examples of how the water activity profile along the flow channel shifts with changes in the different parameters. Increasing the inlet water activity from 2.5×10^{-3} to

0.01 (curve a) shifts the activity profile towards the inlets; more water is added to the fuel cell and causes the ignition to start earlier in the channel. Increasing the load resistance from 2 to 6 Ω (curve b) has the opposite effect and pushes the profile towards the outlets; the water removal is the same, but the water production is decreased at a higher load. The effect of increasing the convection of water out of the cell is more dramatic, either by increasing the flow rates (from 6/3 to 12/6 ml min^{-1} H_2/O_2; curve c) or increasing the temperature (from 25 to 50 °C; curve d). The ignition point can be shifted beyond the end of the flow channel and the water activity remains very low.

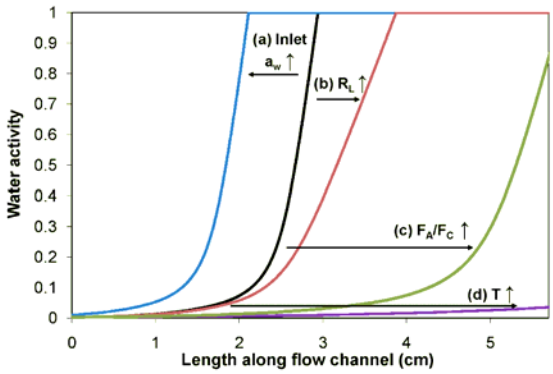

Figure 2.19 Shift in the water activity profile with a change in the parameters. **(a)** An increase in the inlet water activity from 2.5×10^{-3} to 0.01 shifts the profile towards the outlets. **(b)** An increase in the load resistance from 2 to 6 Ω shifts the profile towards the outlets. **(c)** An increase in the flow rates from 6/3 to 12/6 ml min^{-1} H_2/O_2 shifts the profile much farther towards the outlets. **(d)** An increase in the temperature from 25 to 50 °C pushes the ignition point past the end of the flow channel.

The fuel cell is particularly sensitive to the temperature, due to the exponential dependence of the water vapor pressure on temperature, and to the inlet water activity, due to the exponential dependence of the membrane proton conductivity on water activity. Figure 2.20 shows results of predicting the fuel cell ignition by finding the inflection point in the $j(z)$ curve, as described above, for varying inlet water activities and temperatures.

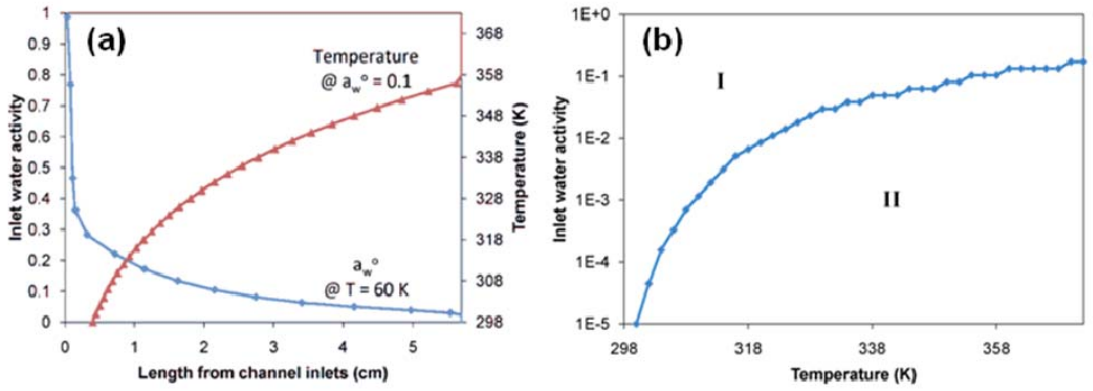

Figure 2.20 Results from equations (2.7)-(2.9) showing the location of the calculated inflection point of the *j(z)* curve, indicating when and where ignition is predicted to occur. **(a)** The different parameters can be varied to see their influence on the location where the ignition front starts. Strong dependences are observed for the initial water activity and the temperature. **(b)** Parameter space diagram based on the calculations showing combinations of the initial water activity and temperature that result in ignition (region I) or extinction (region II).

In part (a), results are given for the location of the ignition (where the inflection point occurs) along the flow channel for varying the inlet water content at a constant temperature (T = 60 °C; blue curve) and for varying the temperatures at a constant water content ($a_w^o = 0.1$; red curve). The steep negative slope of the blue curve shows that at a constant temperature of 60 ºC, the fuel cell ignites quickly for water activities greater than about 0.3. Below that value, the appearance of the ignition front starts getting pushed much farther down the channel. Substantial back diffusion or counter-current flows would be necessary for the entire active area to ignite and contribute to the fuel cell operation. The more gradual slope of the red curve shows that with an inlet water activity of 0.1, the start of the ignition front gets pushed farther down the channel with increasing temperatures. At high enough temperatures, above about 356 K, the ignition point is pushed beyond the end of the flow channel, indicating a temperature limit for ignition with the specified conditions.

Similar calculations to those resulting in the data in part (a) can be done for a range of temperatures and inlet water activities. The critical inlet water activity that allows for ignition before the end of the flow channel can be found for a range of temperatures. Keeping all other parameters constant, it is then possible to construct a parameter space diagram indicating for what sets of temperatures and initial water activities ignition will occur, as shown in part (b) of Figure 2.20. The curve shows the critical inlets water activity for ignition at the given temperature. Above the curve, designated as region I, the fuel cell ignites at least partially. Below the curve, the fuel cell will be extinguished. As expected, with increasing temperature, higher initial water activities are required to initiate ignition.

The results shown in Figure 2.20 can also be compared to ignition criteria with an STR fuel cell system. The same expressions from equations (2.7) and (2.8) are used to calculate the current for a given initial water activity. With no flow channel or lateral gradients, the criterion for ignition is the point where the water production is equal to the water removal and the initial water content is above the critical value (see section 2.1). The water production is determined by the current and has an exponential dependence on the water activity through the membrane resistance. The water removal is determined by the flow rates and has an exponential dependence on the temperature through the water saturation vapor pressure. The result using the same operating parameters as used for Figure 2.20 is shown in Figure 2.21(a). It is significantly different then the result with a flow channel, reproduced as part (b). With the flow channel, the inlet water activity is the important parameter; water is convected downstream and eventually initiates the ignition. Without a flow channel, the water activity is equilibrated over the active area

and the initial hydration is the important parameter. With the flow channel, the critical water activity increases sharply at lower temperatures and levels off at about 0.1 at higher temperatures, as discussed above. With the STR system, ignition is predicted up to temperatures of about 340 K for the entire range of water activities tested, indicating an improvement over the flow channel system. Between 340 and 368 K, the curve is not monotonic. The fuel cell should ignite for very low water activities and higher activities of about 0.1. The shape of the curve is due to the exponential dependences on both sides of the water balance. This could cause difficulties for engineering a system, and the times for ignition could be drastically different. At temperatures above 368 K, ignition is only predicted for water activities of ~1×10^{-5}. Depending on the ease of preconditioning the system, either a flow channel or an STR design of the fuel cell could be the better choice at higher temperatures.

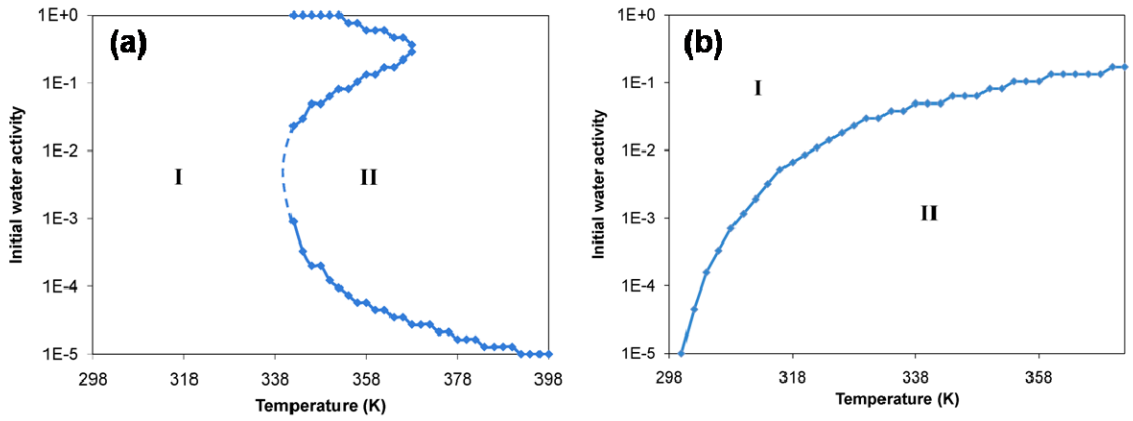

Figure 2.21 Comparison of critical conditions for ignition between (a) an STR fuel cell and (b) a fuel cell with a simple flow channel. With a flow channel (same chart as Figure 2.20(b)), higher temperatures require higher inlet water activities for ignition. With a channel-less STR design, ignition is predicted for the full range of initial water activities at temperatures below ~340 K, indicated as region I. Above 368 K, ignition is predicted only for very low water activities and the cell extinguishes for most of the water activities tested, indicated as region II. Between 340 and 368 K, the curve is not monotonic and both ignition and extinction are predicted for moderate water activities.

2.5 Conclusions

The operation of PEM fuel cells is highly dependent on maintaining the correct balance between water removal and water production. With conditions where liquid water does not condense, water is removed though the flow streams as a vapor. The rate of removal depends on the flow rates and water vapor pressure, which is very sensitive to the cell temperature. Water is produced by the electrochemical reactions. The rate of water production depends on the current, which depends on the external load and the membrane and internal resistances. The flow channels of standard fuel cell designs and the SAPC fuel cell make it necessary to consider the water balance on a local scale. Water is convected downstream through the flow streams and diffuses through both the flow streams and the membrane. The convection and diffusion of water couples different areas of the membrane to each other so that changes in the water activity propagate along the flow channels. When the local water balance is such that the water produced plus the water transported from other areas of the fuel cell is greater than the water removed through convection or diffusion to areas with lower water activity, the local current evolves to an ignited high current steady-state. Otherwise, the membrane resistance increases with decreasing water activity and the local current extinguishes to essentially zero.

The SAPC fuel cell was ideal for studying the propagation of ignition and extinction fronts along the flow channels. Changing the flow pattern, flow rates, initial water content, load resistance, and temperature all had large effects on whether ignition or extinction fronts started and how far they propagated along the channel. Systems need to be designed carefully for a given set of operating conditions to ensure the ignited

steady-state is achieved over the entire active area of the fuel cell. Mass balances and numerical solutions can be used to predict whether the fuel cell will ignite or not and to give insight into which parameters the operation is most sensitive to, such as the initial water activity and temperature.

2.6 References

1. Moxley, J.F., S. Tulyani, and J.B. Benziger, *Steady-state multiplicity in the autohumidification polymer electrolyte membrane fuel cell.* Chemical Engineering Science, 2003. **58**(20): p. 4705-4708.

2. Satterfield, M.B. and J.B. Benziger, *Non-fickian water vapor sorption dynamics by nafion membranes.* Journal of Physical Chemistry B, 2008. **112**(12): p. 3693-3704.

3. Majsztrik, P.W., M.B. Satterfield, A.B. Bocarsly, and J.B. Benziger, *Water sorption, desorption and transport in Nafion membranes.* Journal of Membrane Science, 2007. **301**(1-2): p. 93-106.

4. Hogarth, W.H.J. and J.B. Benziger, *Dynamics of autohumidifed PEM fuel cell operation.* Journal of the Electrochemical Society, 2006. **153**(11): p. A2139-A2146.

5. Larminie, J. and A. Dicks, *Fuel cell systems explained*. 2nd ed. 2003, Chichester, West Sussex: J. Wiley.

6. Majsztrik, P., A. Bocarsly, and J. Benziger, *Water permeation through Nafion membranes: The role of water activity.* Journal of Physical Chemistry B, 2008. **112**(51): p. 16280-16289.

7. Balakotaiah, V., D. Kodra, and D. Nguyen, *Runaway limits for homogeneous and catalytic reactors.* Chemical Engineering Science, 1995. **50**(7): p. 1149-1171.

3 Influence of Gravity

3.1 Introduction

The previous chapter described the operation of PEM fuel cells under conditions where water is only present as a vapor and liquid does not accumulate. The analysis was especially applicable to controlling the start-up of the fuel cell and operating at elevated temperatures. The best choice of operating conditions was determined by the ability to maintain the balance between water production and water removal on a local scale within the fuel cell. The major factor was the exponential dependence of the membrane proton conductivity on the water activity. In order for a PEM fuel cell to provide a significant power output for any substantial amount of time, it is a requirement that the membrane remains hydrated. It is not possible to design a system that can stably operate with conditions where the water removal is greater than the water production. This issue can be circumvented by passing the feeds through an external humidification system, but it is a very inefficient solution that results from poor system design.

More commonly, fuel cells operate at the other end of the water balance, when the water production is much higher than the water removal and the fuel cell becomes saturated with water. Perhaps the greatest challenge facing PEM fuel cells is the difficulty in maintaining stable operation and control due to flooding by liquid water. The build-up of water produced at the membrane/cathode interface is known to limit the current output from PEM fuel cells. This issue has been minimized by increasing the flow rates to highly excessive levels that blow any liquid out of the channel. The stability of the fuel cell operation is improved, but the overall efficiency is decreased, as a recycling system must be added to keep the fuel utilization reasonable. Also, the

increased water evaporation from the high flow rates makes humidification of the feeds a requirement. Again, the overall system cost, complexity and power requirement is increased.

The mechanism of water transport from the cathode where it is produced to the outlets of the fuel cell is still widely debated in the literature. Liquid water has been observed to accumulate in the gas flow channels, which has spawned the development of models for two-phase gas/liquid flow in the flow channels. Several researchers have built visualization fuel cells, making use of neutron or optical imaging. Neutron imaging has been used to study water distribution in operating fuel cells, usually with serpentine channels and accumulation of water at the corners.[1-5] Optical imaging of transparent fuel cells has shown droplet growth and detachment, sometimes at preferential locations, or the formation of a film of liquid water.[6-11] Modeling efforts have focused on the transport of bulk water in the channels[12, 13] or the conditions necessary to push liquid droplets along the surface of the GDL[14-17], while others assumed the liquid droplets are suspended in the gas as a mist and carried out in the gas flow.[16] Another approach has been to build fuel cells with segmented electrodes to gain information about the current distribution over the active area of the MEA.[18-22] In one case the flow channels were transparent, so that condensation was observed in conjunction with distribution measurements.[20] Still, although it has been inferred that differences in the local currents are due to liquid water effects, direct correlations between liquid water build-up and dynamic current data have not been reported. The SAPC fuel cell was ideal for providing insights into the effects of liquid water and how systems can be more cleverly designed.

In this chapter it is shown that liquid water in the cathode flow channel is responsible for inhibiting mass transport to the membrane/cathode interface. Gravity or shearing action from the gas flow overcomes the surface adhesion of the drop emerging into the flow channel to the water in the pore, detaching the drop and allowing the water to move along the GDL surface. The drops accumulate and form slugs in the cathode gas flow channel. How and where this occurs in the cathode flow channel depends on the orientation of the fuel cell with respect to gravity. Changing the orientation and the direction of gas flows relative to gravity controls where liquid water accumulates and alters the local current in PEM fuel cells. Investigation of these effects has led to observations of a variety of complex dynamic current outputs from a PEM fuel cell.

3.2 Experimental setup

The SAPC fuel cell system described previously in section 1.6 was used for this study. Pure hydrogen and oxygen were supplied from commercial cylinders through mass flow controllers at flow rates of 1-20 ml min^{-1}. The computer DAQ system was used to read and control the gas flow rates. There were also relative humidity sensors placed in the outlets from the gas flow channels and the RH could be logged. In the experiments reported here liquid water was always present in the flow channels and the relative humidities in both the anode and cathode outlets were always 100%.

Most of the experiments were done with fixed flow rates of 6/3 ml min^{-1} H_2/O_2, or 12/6 ml min^{-1} H_2/O_2. Through a series of tests, it was observed that with a load resistance of 0.5 Ω and flow rates less than 6/3 ml min^{-1} H_2/O_2, no gas bubbles were seen when the outlets of the anode and cathode were placed in vials of water. This indicated that all of the gas was consumed by the reaction, commonly referred to as a "stoichiometry" (ξ) of

1, where the stoichiometry is defined to be the ratio of gas supplied through the feed to that consumed by the fuel cell with the given current (the ratio of H_2 to O_2 is kept constant at 2:1). When the flow rates were increased to 7/3.5 ml min^{-1} H_2/O_2 or greater, gas bubbles were seen from the outlets of the anode and cathode. The inlet flow rates of 6/3 ml min^{-1} H_2/O_2 will be referred to as ξ_1, and 12/6 ml min^{-1} H_2/O_2 as ξ_2. The maximum total current from the SAPC fuel cell driving a 0.5 Ω load impedance at 25ºC and 1 bar total pressure was ~0.8-0.9 A. Variability in the internal resistance of about 10% was found from MEA to MEA, corresponding to a variability in the total current. The flow rates corresponding to ξ_1 limited the maximum current to 0.8 A with complete conversion of the reactants. Increasing the either of the reactant feed rates beyond ξ_1 did not result in any substantial increase in the maximum total current from the SAPC fuel cell. Although it has been reported that severe degradation of the catalyst can occur under starved conditions[23-25], effects of degradation were not observed through consecutive experiments with the same MEA. An auto-humidified self-draining fuel cell was also run under anode starved conditions for > 1000 hours with negligible change in the MEA performance.[26] This was perhaps due to the choice to let the fuel cell run autonomously under a constant load resistance without the addition of potentiostatic or galvanostatic controllers.

The experiments summarized here consist of a vast array of data. A typical data set consists of the six current measurements for the six anode segments, the voltage drop across the load, anode and cathode flow rates, and the relative humidity in the anode and cathode effluent. This data is recorded with a time stamp at a frequency of between 0.1 to 1 Hz and stored as a data array. A typical experiment runs from 15,000 s to 172,800 s. It

is impossible to summarize all the information contained in experiments in a few simple graphs. Certain features of the data have been highlighted. A database of Excel files containing all of the vetted data (currently consisting of ~100 files with an average size of 20 MB) are available for viewing at the Benziger group web site. Video images were selectively recorded at various times during operation. The video images were time stamped and can be correlated with the Excel data files. The video images are also available. (Website URL: http://pemfc.princeton.edu/data.html)

3.3 Fuel Cell Operation

The data from the SAPC fuel cell are complex and not easily summarized. The focus here is on the general trends associated with changing cell orientation, flow rate, and flow direction. It is also possible with the SAPC fuel cell set-up to switch between co- and counter-current flows and change the temperature of the fuel cell. The work reported in this chapter consistently utilized co-current operation.

All of the experiments were performed with a fixed load at 25ºC and one of the two sets of flow rates (ξ_1 or ξ_2). There are five different physical orientations (three horizontal and two vertical) of the SAPC fuel cell which are defined by the effect that gravity has on liquid accumulation in the gas flow channel. For this relatively simple fuel cell with a very limited set of operating parameters (only one load, only one temperature and two sets of flow rates) there are twenty different experimental systems under investigation. Of these twenty, only two can be characterized as having stable (time invariant) steady states. The other eighteen configurations give rise to complex spatio-temporal patterns of current density. All the experimental systems have been examined

multiple times. The results presented here are representative, but the reader is referred to the data files available on the Benziger group website to see the full extent of spatio-temporal current density patterns.

The total area of each of the fuel cell flow channels was 1.2 cm^2 with a volume of 0.38 cm^3. The maximum current obtained with the MEAs made in the lab was 0.85-0.9 A (current density of 0.94-0.99 A/cm^2, based on the exposed MEA surface in the flow channels) with an external load of 0.5 Ω. At a current of 0.9 A, the time required for liquid water to fill the cathode flow channel was 4000 s. All tests were run for periods that lasted more than 10,000 s to make sure the liquid content in the flow channel had time to equilibrate.

The data is presented in three formats. The most general presentation consists of the currents in each electrode segment as a function of time. This consists of a set of line graphs, often truncated to represent a limited time period. Many of the experiments ran for over 100,000 s and the local current variations occur on time scales from $1\text{-}10^4$ s; time slices are chosen to highlight specific characteristics of the current density patterns. These figures also show the inlet flow rates to the anode and cathode, so it is possible to associate changes in the spatio-temporal current patterns with changes in flow. A second presentation of the data consists of the current distribution profiles along the length of the flow channel. Because of the time varying nature of the current density these would typically be snapshots at a fixed moment in time. The current profiles are represented as a steady-state with error bars to denote the time varying component. The third type of data presentation is a correlation of current density as a function of time along with a photographic sequence of water within the flow channel.

3.4 Effects of orientation

3.4.1 Horizontal configuration

Three different horizontal configurations of the SAPC PEM fuel cell are possible. They are defined by the effect that gravity has on liquid accumulation in the gas flow channel. Illustrated in Figure 3.1 are two of the horizontal configurations: (a) "cathode down," with the cathode below the anode so that liquid water at the cathode falls away from the GDL by gravity, and (b) "cathode up," with the cathode above the anode such that liquid water accumulates on the surface of the GDL.

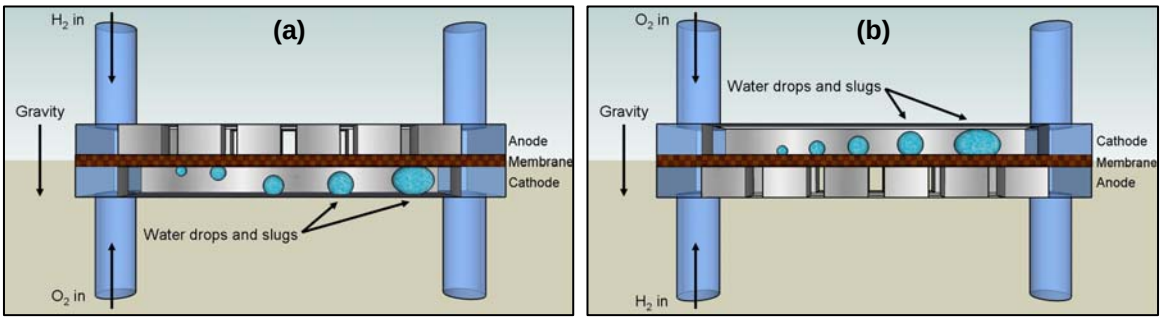

Figure 3.1 Schematic of the fuel cell in two of the three possible horizontal orientations. **(a)** "cathode down"; the cathode faces down and droplets grow on the GDL until they detach and fall to the back of the channel. The droplets continue to grow as they are pushed along the channel. **(b)** "cathode up"; the cathode faces up so that droplets sit on top of the GDL and grow as they are pushed along the channel.

The third horizontal configuration, "in-plane," is with the anode and cathode in the same horizontal plane such that liquid water accumulating in the cathode flow channel will fall onto the side walls of the channel and only partially block oxygen access to the GDL. The results from the experiments with the "in-plane" orientation were qualitatively the same as those with the "cathode down" orientation, and so will not be discussed further. With each configuration, the fuel cell was operated with the load resistance fixed at 0.5 Ω, dry H_2 and O_2 feeds, and at a temperature of 25ºC. By convention, electrode segment

1 is defined as that nearest the oxygen inlet. For co-current flow, as with the data presented here, the hydrogen feed is also at electrode segment 1. During operation, the feed flow rates were adjusted while the current and the voltage measurements continued to be recorded. Visual observations of any liquid water in the anode and cathode were intermittently recorded. Video clips of liquid water motion in the cathode flow channel were recorded during "steady-state" operation. The steady-state results from these tests are summarized in Table 3.1. A summary of all the tests conducted for this study is provided in the Appendix.

Table 3.1 Summary of horizontal fuel cell opertation.

			Segment current (mA; position 1 is at the oxygen inlet)						
Configuration		**ξ***	**1**	**2**	**3**	**4**	**5**	**6**	**ΔVload**
"cathode down"	co-current	1	146	179	158	160	90	61	.446
	co-current	2	124	151	146	180	166	173	.525
	counter-current	1	107	129	182	159	126	87	.383
	counter-current	2	145	154	186	148	114	80	.415
"cathode up"	co-current	1	160	203	180	131	64	40	.388
	co-current	2	118	158	170	175	142	140	.455
	counter-current	1	194	138	124	70	30	17	.287
	counter-current	2	164	167	185	134	122	90	.430
"in-plane"	co-current	1	154	214	183	122	57	31	.383
	co-current	2	102	155	166	172	158	155	.454
	counter-current	1	108	128	139	145	142	126	.453
	counter-current	2	170	170	175	149	114	81	.420

*ξ=1 corresponds to 6/3 ml min^{-1} H_2/O_2, ξ=2 corresponds to 12/6 ml min^{-1} H_2/O_2

3.4.1.1 Horizontal Configuration: Cathode Down

The time-dependent currents in all the electrode segments at stoichiometry ξ_1 and ξ_2 for the "cathode down" orientation are shown in Figure 3.2. It is evident that the currents show no fluctuations for 20,000 s at the higher stoichiometry of ξ_2. Gas bubbles were seen leaving the outlet tubes at both the anode and cathode, and the relative humidity of the gas effluents was 100%. Collection of the liquid water pushed out of the

outlets showed greater than 90% recovery of the water produced by the fuel cell reaction, with the rest taken up by the membrane, trapped in parts of the GDLs and flow channels, or carried off as water vapor in the anode and cathode effluents. Furthermore, it was possible to routinely run the SAPC fuel cell in this configuration indefinitely with stable operation.

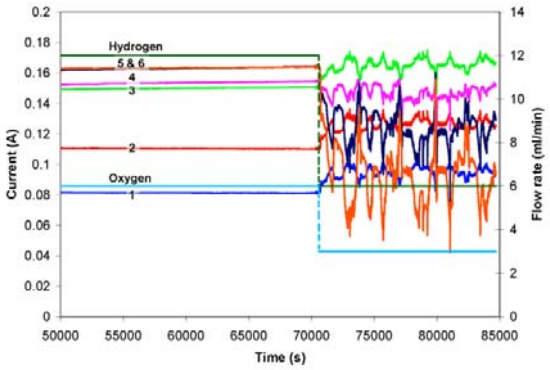

Figure 3.2 Spatio-temporal data from the six segments and the two flow rates for the SAPC fuel cell in the horizontal "cathode down" orientation. "Steady-states" are shown with both ξ_1 (fluctuating) and ξ_2 (stable). The feed flow rates were decreased at 70,000 s, leading to the large fluctuations in the current. The electrode segment is indicated by number with the oxygen inlet upstream of segment 1.

When the flow rates are reduced to ξ_1, the electrode currents immediately begin to show significant local current fluctuations, with the largest fluctuations seen at the electrode segments furthest downstream. These erratic fluctuations persisted indefinitely. Observations of the cathode flow channel showed that a liquid water slug was blocking the end of the channel when the current in segment 6 was low. When the slug was pushed into the effluent tube, the current increased. No gas bubbles were observed from the outlet tubes of the anode and the cathode, indicating that all the feeds were consumed. The distribution of the current along the flow channel also shows a significant change with the flow reduction. The currents decrease in electrode segments 5 and 6, as expected, because of depletion of the reactants downstream in the flow channel. The

surprising result is that the currents increase in segments 1 and 2 near the inlet to the flow channel. The response to the change in the inlet flow rate occurred almost immediately and was reversible. This suggests that these changes in current distribution were produced from local variations in concentrations of hydrogen and oxygen and were not directly related to local water content in the GDL or membrane. In-plane currents resulting from local variations in a fuel cell system have been observed in the bipolar plates of fuel cell stacks[27, 28] and in a cell with segmented electrodes that were connected through a bipolar plate.[29] The large redistribution that was observed was not expected in the SAPC fuel cell, though, because the segments are electrically isolated except through contact with the GDL. This was further studied through simulations and will be discussed in Chapter 4.

3.4.1.2 Horizontal Configuration: Cathode Up

Flipping the fuel cell so that the cathode faced up and was above the anode, the "cathode up" orientation, resulted in distinctly different behavior. In contrast to the stable currents with a stoichiometric excess of the feeds, as was observed for the "cathode down" orientation, the local current densities for "cathode up" show fluctuations at both low and high stoichiometries, ξ_1 and ξ_2. Shown in Figure 3.3 are the spatio-temporal current data for the "cathode up" orientation. With ξ_2, corresponding to the time period 5000-80,000 s in Figure 3.3, the currents in every electrode segment show fluctuations. The fluctuations resemble regular square wave oscillations with time periods of about 3000-4000 s and are most pronounced in segments 4, 5, and 6. In some runs, the amplitude of the oscillations grew with time or only occurred in the current from segment

6. Water droplets were observed to form on top of the GDL, close to the oxygen inlet where the current density was the highest.

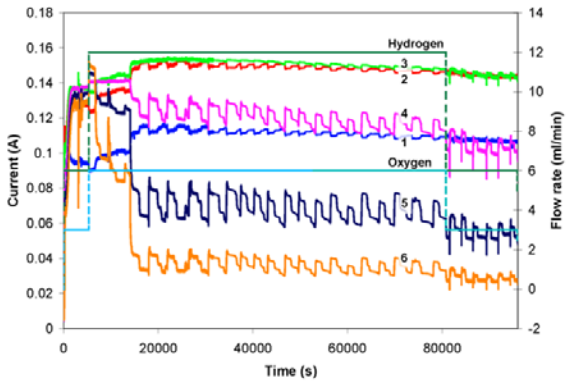

Figure 3.3 Spatio-temporal data from the six segments and two feed flow rates for the SAPC fuel cell in the horizontal configuration with the cathode facing up above the anode, "cathode up". Oscillations with periods of 3000-4000 s are seen with the greatest amplitude in the segments closest to the outlets. The electrode segment is indicated by number with the oxygen inlet upstream of segment 1.

Figure 3.4 shows one such image, corresponding to a time of 80,674 s in Figure 3.3. The droplets grow to a critical size, at which point they detach, are pushed along the GDL, and coalesce with other droplets until they form a slug that spans the channel. This blocks the flow of oxygen to the segments closer to the outlet and causes the instabilities both up- and down-stream of the slug.

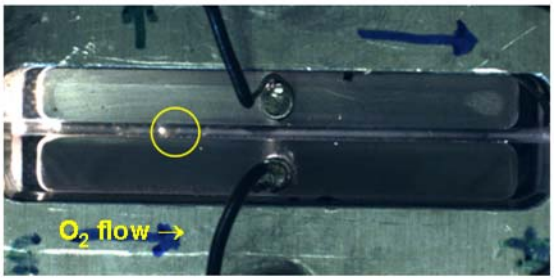

Figure 3.4 Photo of SAPC fuel cell in the "cathode up" orientation corresponding to time 80,674 s in Figure 3.3. Droplets are seen forming and sitting on top of the GDL.

The current density profile at ξ_2 for the "cathode up" orientation is slightly different than for "cathode down," as shown in Figure 3.5. Comparing the profiles gives more evidence of the importance of gravity with flooding in the flow channels. The current increases from electrode segment 1 to 3 for both orientations of the cathode. When the cathode is facing down, the current increases sharply upstream and then levels off downstream at segments 4, 5, and 6; however, in comparison, when the cathode faces up the current is significantly lower downstream in segments 3 through 6. When the flow rates were increased from ξ_1 to ξ_2, the current profile redistributed along the channel for both orientations. At the higher flow rate, ξ_2, the current was lowest at segment 1 and continuously increased to be highest at segment 6 for both orientations. With the "cathode down", the currents in all segments lined out to stable steady-state values after the flow rate was increased to ξ_2. In contrast, with the "cathode up" orientation, a second current redistribution occurred after about 1300 s after increasing the flow rate to ξ_2 and took about 10,200 s to reach the oscillating "steady-state" evident in Figure 3.3. The oscillating current profiles for the "cathode up" orientation were qualitatively similar for ξ_1 and ξ_2, but the magnitude of the current fluctuations were larger at the lower stoichiometry. As there was an excess of fuel at ξ_2, it must be the case that the liquid water in the flow channel was collecting on top of the GDL close to the outlets. When water is produced at the catalyst layer, it flows through the largest pores to the flow channel, leaving smaller pores open for gas flow. However, when water is already in the flow channel and droplets are pushed along the GDL, the water blocks all of the pores and creates a much greater resistance for the mass transfer of oxygen to the catalyst.

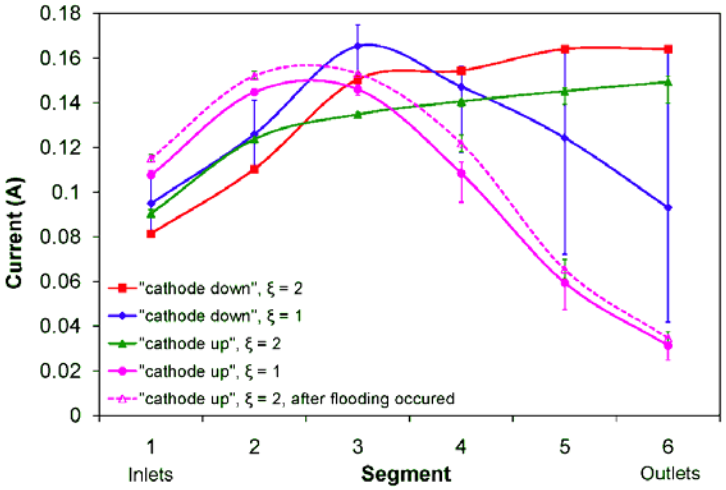

Figure 3.5 Steady state current density profiles for the SAPC H_2/O_2 fuel cell in four horizontal configurations: the "cathode down" and "cathode up" orientations and two feed stoichiometries, ξ_1 and ξ_2. The oxygen inlet is always upstream of electrode segment 1. With ξ_2, the currents are high all along the channel before flooding occurs. After flooding, the local currents are slightly higher towards the inlets and dramatically lower closer to the outlets. The same trends are observed with ξ_1. The error bars represent the fluctuations in the current.

The dynamic response was also examined when the reactant flows were reduced from ξ_2 to ξ_1 with both orientations. With the "cathode up", as the liquid water had already caused a large redistribution and fluctuations in the local currents, the flow reduction does not qualitatively change the current profile. The most notable change is an increase in the magnitude of the fluctuations, as seen by the larger error bars for "cathode up" and ξ_1 in Figure 3.5. For "cathode down", erratic fluctuations followed a redistribution in the currents with the decrease in reactant flows, as seen in Figure 3.2 and highlighted by the large error bars in Figure 3.5. The decrease in the local currents in the downstream section of the fuel cell is less with the "cathode down" orientation, due to the assistance from gravity in removing liquid water from the cathode flow channel.

Comparing the different fuel cell configurations indicates that gravity-assisted drainage of liquid from the cathode gas flow channel was the key factor. When water

drainage is assisted by gravity and there is a stoichiometric excess of reactant feed, the fuel cell operates stably. When the reactant feed is reduced to the point where water slugs build up in the cathode flow channel, the local current density fluctuates because the water in the flow channel blocks reactants from getting to the membrane/electrode interface. The current distributions for the two horizontal flow configurations discussed are summarized in Table 3.1. These are time averaged currents over periods of 5000-10000 s. Included in Table 3.1 are data for the same configurations, but with counter-current flows. The currents tend to be higher towards the middle of the channel when the flows are counter-current, but the same effects from flooding are still evident.

3.4.2 Vertical configuration

Two distinct vertical configurations of the SAPC fuel cell were examined based on the direction of gas flow at the cathode relative to gravity. The cathode flow could be in the direction of gravity, the "inlets up" orientation, or it could be against gravity, the "inlets down" orientation. When the cathode flows are in the direction of gravity, water drainage is gravity assisted. Oxygen flow counter to gravity requires the gas to lift the liquid up the channel for it to be removed from the cell. Counter-current flows were examined, but yielded qualitatively similar results; data for counter-current flows are available on the web. The same set of operating conditions was used as for the horizontal flow: a load impedance of 0.5 Ω, flow rates with stoichiometry ξ_1 or ξ_2, and a temperature of 25ºC. Table 3.2 summarizes the time-averaged "steady-state" current profiles for the six different tests for the vertically oriented SAPC fuel cell (data for counter-current flow, with the oxygen flow against gravity ("inlets down" orientation) has also been included in Table 3.2).

Table 3.2 Summary of vertical fuel cell operation

Configuration		ξ*	Segment current (mA; position 1 is at the oxygen inlet) 1	2	3	4	5	6	ΔVload
"inlets down"	co-current	1	87	121	129	143	121	93	0.388
	co-current	2	86	120	129	147	132	106	0.407
"inlets up"	co-current	1	193	242	200	86	29	17	0.432
	co-current	2	116	161	173	170	144	147	0.520
	counter-current	1	145	156	197	153	98	54	0.448
	counter-current	2	173	164	163	152	107	79	0.476

*ξ=1 corresponds to 6/3 ml min^{-1} H_2/O_2, ξ=2 corresponds to 12/6 ml min^{-1} H_2/O_2

3.4.2.1 Vertical Configuration: Inlets up

The flow of liquid water with the vertical SAPC fuel cell in the "inlets up" orientations was assisted by both the gas flow and gravity. Liquid drops consistently formed in the cathode flow channel and grew until they nearly spanned the flow channel, then detached and fell rapidly down the length of the flow channel. The process repeated itself with a frequency of ~100 s. There were small fluctuations in the current from the segment nearest to where the drop formed; the current would decrease by 5-10% while the drop was forming and then rise after the drop fell. The currents in the segments distant from the where the drop formed appeared to be quite stable. Evidence for the mechanism of water transport through and detachment from the GDL in a setup analogous to the "inlets up" orientation of the SAPC fuel cell is discussed further in Chapter 5.

3.4.2.2 Vertical Configuration: Inlets down

The current densities for the vertical SAPC fuel cell with co-current flows going against gravity, the "inlets down" orientation, are much more complex in nature. The current density profiles do not appear to be well described by simple deterministic models; for the same set of operating conditions the current density could be stable, show

regular periodic oscillations or show random fluctuations. All types of behaviors were observed in multiple studies. Periodic oscillations could be induced in the current density, but the fuel cell could not be shut down and restarted and guaranteed to be restored to the same state of operation.

Figures 3.6 and 3.7 show one example of how the current profile can evolve throughout the course of an experiment with the "inlets down" orientation. Figure 3.6 tracks the current density in the SAPC fuel cell as a function of time after the feed flow rates are reduced from ξ_2 to ξ_1. At the high flow rates, the currents in each segment are stable. Liquid was seen to accumulate in the cathode flow channel just below the active area of the MEA and periodically a liquid slug rose rapidly through the flow channel. The slugs were approximately 10 mm long and rose up the channel at a frequency of one slug every 10-12 s. They traveled through the column in 1 s, approximately equal to the gas velocity in the cathode.

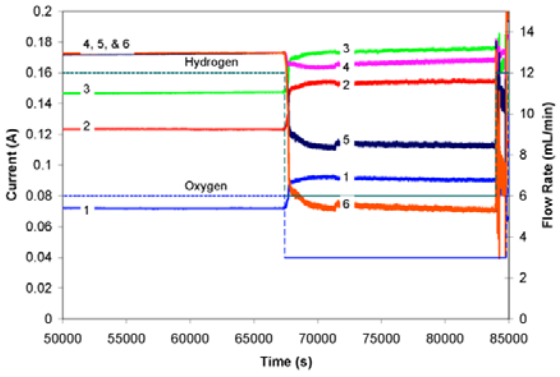

Figure 3.6 Spatio-temporal data for the six segments and two feed flow rates for the SAPC fuel cell in the vertical "inlets down" orientation. The flow rates were changed at 67,500 s, which resulted in a redistribution of the current. At 84,000 s, the inlet flow rate at the anode was increased while the cathode flow rate was kept constant. The electrode segment is indicated by number with the oxygen inlet upstream of segment 1. A blowup of the current distribution after the flow rate change at 84,000 s is shown in Figure 3.7.

When the gas flow rate is reduced from ξ_2 to ξ_1 the current redistributed as seen previously with the horizontal configurations. The current density increases near the gas inlet and decreases downstream of the inlets. Fluctuations in the current densities also started with the reduced flow. After increasing only the anode flow to ξ_2 at 84,000 s, the stability of the currents changes dramatically, as shown in Figure 3.7. Changes in the current distribution and stability were not expected, because the oxygen flow at the cathode was still fixed, but instead increasing the anode flow appeared to induce large fluctuations in the currents. Figure 3.7 shows that the current takes about 350 s to move to a steady-state, with very large fluctuations in the current over that time period. The new "steady-state" is periodic oscillations at the downstream electrode segments located at the top of the flow channels.

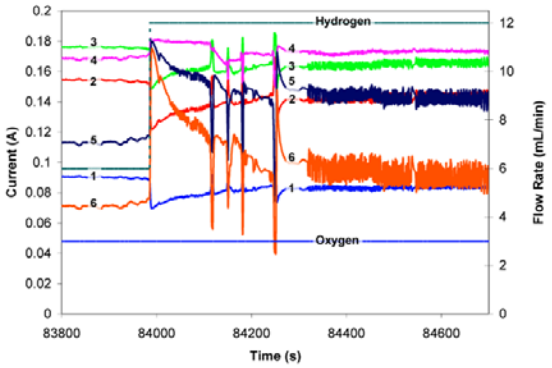

Figure 3.7 Blow up of the current response of the vertical SAPC fuel cell with the gas flows rising against gravity, in the "inlets down" orientation. At 84,000 s the inlet flow rates were changed from ξ_1 for both the hydrogen and oxygen feeds to ξ_1 for oxygen and ξ_2 for hydrogen. The electrode segment is indicated by number with the oxygen inlet upstream of segment 1.

3.4.2.3 Vertical Configuration: Effect of Reactant Flow Rate

In most cases with the "inlets down" orientation, stable current density profiles were found at higher gas flow rates, where both hydrogen and oxygen were fed in stoichiometric excess of the current (more reactants supplied than consumed). If the

auto-humidified SAPC fuel cell current was allowed to self-ignite with inlet flow rates of 7 – 20 ml min^{-1} H_2 and 3.5 – 12 ml min^{-1} O_2, the SAPC fuel cell would eventually operate with a stable current density profile. Gas bubbles were seen exiting from both the anode and cathode outlets going into water reservoirs. Liquid slugs of volume 2 – 3 μl were also seen in the tube from the exit of the cathode. They were pushed through the tube with the excess oxygen that was collected in the water reservoir. For inlet flow rates ≤ 6/3 ml min^{-1} H_2/O_2, the reactants were completely reacted to water in the fuel cell. No gas bubbles were seen to exit from either the anode or cathode when the H_2/O_2 feed ratio was 2; if one reactant was in excess, gas bubbles were observed. At the low inlet flow rates, different patterns of current density and liquid movement were observed. If the inlet flow rates were reduced below 6/3 ml min^{-1} H_2/O_2 and sufficient time was allowed to pass (this could be as long as 100,000 s in some cases), the system would eventually evolve to a cathode flow channel partially flooded by slugs at the bottom. The liquid slugs would grow at the bottom and be periodically pushed up through the flow channel. This would result in current oscillations.

The current profiles for co-current flows at ξ_1 and ξ_2 are shown in Figure 3.8. These current density profiles are similar to those seen with horizontal flows. The most distinguishing feature is the large decrease in current downstream of the inlet for ξ_1. Liquid slugs in the flow channel appear to have exacerbated the starvation of the reactants to the downstream electrode segments. The error bars seen for ξ_1 show the magnitude of the oscillations.

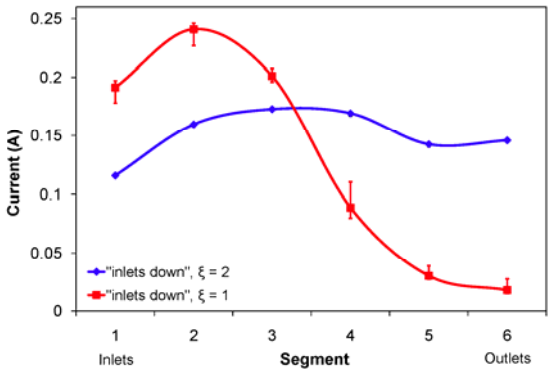

Figure 3.8 Steady state current density profiles for the vertical SAPC fuel cell with the flows against gravity, in the "inlets down" orientation, and two different feed stoichiometries: ξ_1 and ξ_2. The oxygen inlet is always upstream of electrode segment 1. With ξ_2 the currents are high all along the channel with only small deviations from segment to segment. With ξ_1 the currents are higher towards the inlets and dramatically lower towards the outlets due to liquid water exacerbating the starvation effects. The error bars represent the fluctuations in the current.

In some cases, the oscillatory behavior began immediately after a flow reduction to $\xi = 1$; however, it was not a deterministic process. In one case, the oscillations began only after the oxygen flow was decreased to 1.5 ml min^{-1}, or $\xi = 0.5$. The fuel cell was allowed to self ignite and equilibrate with flows of 7 and 3.5, just above $\xi = 1$. After about 14 hours with stable operation, the H_2 flow was increased to 12 ml min^{-1} so that starvation at the anode was not a factor, and the O_2 flow was decreased by 0.5 ml min^{-1} every 5000 s, as shown in Figure 3.9(a). Surprisingly, the currents remained stable with only small irregular fluctuations until the O_2 flow was reduced to 1.5 ml min^{-1} at 111,400s. The current profile leveled off for about 1000 s after the initial decrease in total current. Then, at 112,400 s, the currents spontaneously began to oscillate, as shown in Figure 3.9(b). As the local current densities close to the inlets dropped, those closer to the outlets rose, so that the average total current remained about constant. The oscillations persisted for the duration of the experiment, about 2000 s, with a period of 5 seconds.

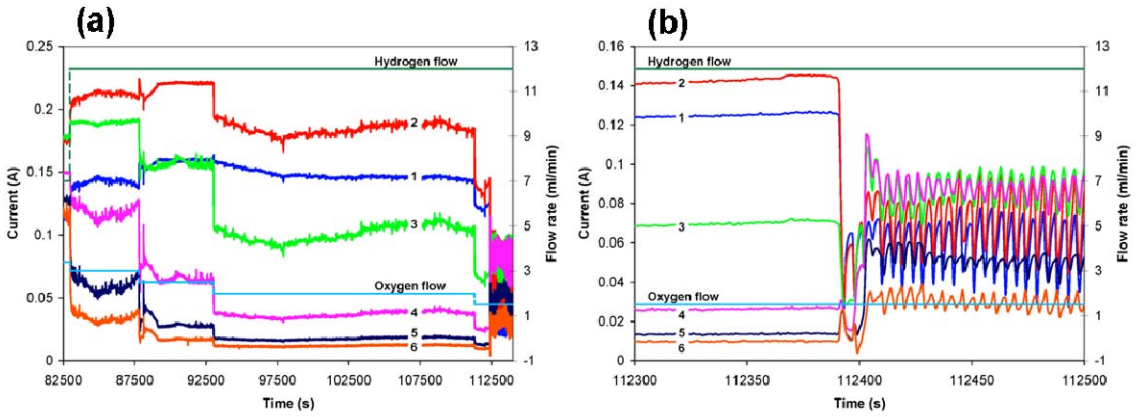

Figure 3.9 Spatio-temporal current profiles with the SAPC fuel cell in the vertical "inlets down" orientation. **(a)** Long-term data. The flows were run just above ξ_1 for 50,000 s with only small fluctuations in the currents. At 83,000 s, the oxygen flow started being reduced until regular periodic oscillations started at about 112,400 s. **(b)** Zoom in on the time period 112,300 – 112,500 s from part (a). The currents redistribute with those near the inlets dropping dramatically while those closer to the inlets increase. All of the currents start fluctuating with quick periodic oscillations. The electrode segment is indicated by number with the oxygen inlet upstream of segment 1.

With the fuel cell starved, the effects of the slug motion were most prominent near the inlets. Figure 3.10 shows the detail of the current oscillations along with images of the cathode flow channel from a video that we captured. The oscillations correlate very well with the movement of the water slugs in the channel. New slugs form around the middle of segment 1, blocking the flow of oxygen and causing the currents to drop by as much as 70%! As the slug is pushed up the channel, the gas begins to break through the slug and water falls back down the channel. The currents recover in the lower segments as oxygen is blocked from reaching the higher segments. For the same reason, small drops in the currents are seen from the segments close to the outlets. The water falling back down the flow channel combines with droplets emerging from the GDL to form a new slug in the same location and the oscillations continue.

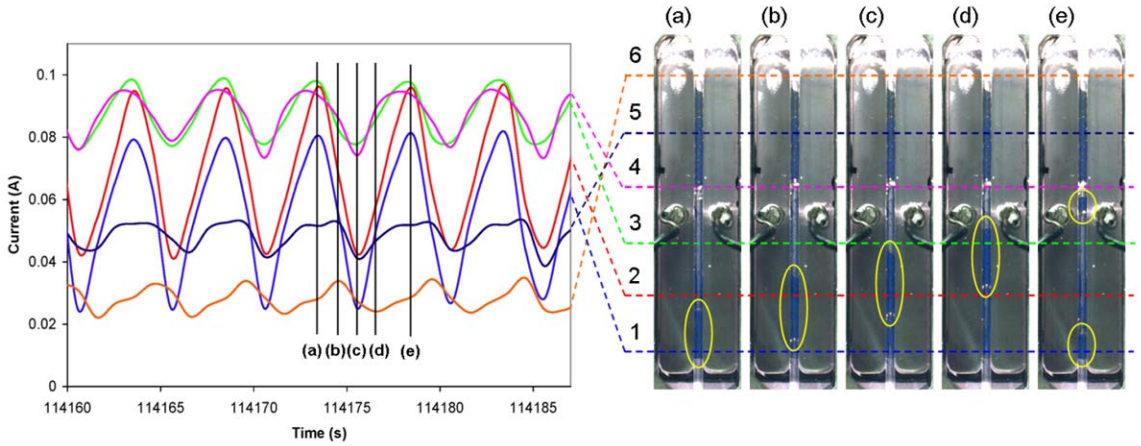

Figure 3.10 Spatio-temporal correlation of local current and water slugs in the vertical SAPC fuel cell with the flows against gravity, in the "inlets down" orientation. The current measurements are from the continuation of the data shown in Figure 3.9. Slugs form near the bottom of the MEA and are pushed part-way up the channel before falling back down to help create a new slug in the same location.

Figures 3.2, 3.3, and 3.6 all show different "steady-state" spatio-temporal current profiles in the SAPC fuel cell operated at the same conditions. Several different current profiles were observed but all appeared to be variations of the three basic types shown above. The currents are either steady, show regular oscillations that correlate with the periodic formation and movement of slugs, or fluctuate randomly with random slug movement. More than 25 tests were carried out for the SAPC fuel cell in the vertical orientation (corresponding to over 1000 hours of testing) and an operating trajectory that led to a specific spatio-temporal current profile was not identified. It was found that by reducing the inlet flow rates it is possible to induce the regular oscillations where the slugs accumulate at the bottom of the cathode channel. But the opposite effect was also observed where oscillations started about 8000 s after an increase in flows from $\xi = 1$ to $\xi = 1.3$, shown in Figure 3.11.

The spatio-temporal current distribution in the vertical SAPC fuel cell with the gas flows upwards was complex and did not appear to be deterministic. At the same feed

flow rates, load impedance, and temperature, the steady state settled into different spatio-temporal patterns including: (i) stable current with a constant current density profile along the length of the flow channel, (ii) oscillating currents with periods of 10-400 s that correlated with water slug motion along the channel, or (iii) irregularly fluctuating currents.

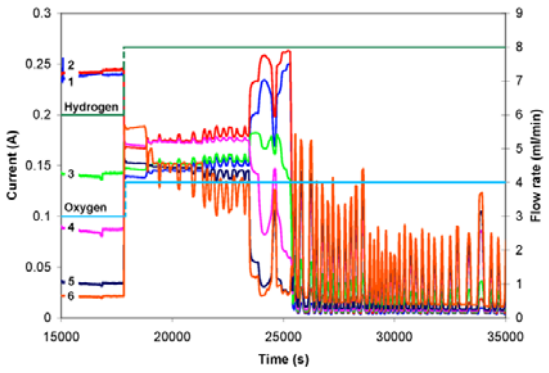

Figure 3.11 Spatio-temporal current profiles with the SAPC fuel cell in the vertical "inlets down" orientation. The inlet flows were increased from ξ=1 to ξ=1.3 at 17,000 s. The current redistributed and then grew unstable. Shortly after 25,000 s the fuel cell currents dropped dramatically and very regular oscillations were observed. The electrode segment is indicated by number with the oxygen inlet upstream of segment 1.

3.5 Analysis of flooding

The results presented here suggest a significantly different physical basis for water transport in PEM fuel cells compared to the common approaches found in the literature. This was one of the first studies to correlate flow visualization with local current density measurements. This work was also the first to directly observe the importance of orientation and gravity on flooding in PEM fuel cells.

A number of models have been proposed for water transport through the GDL. Most models employ Darcy's law to describe two phase flow in porous media[15, 16, 30-

33], as was done with some of the earliest published fuel cell models, such as that by Bernardi and Verbrugge.[34] Often, the models also include capillary condensation of water in the GDL.[15, 31-33, 35, 36] Based on these assumptions, it is usually concluded that flooding causes all of the pores of the GDL to fill with water and any liquid that reaches the channel is either removed as mist in the gas streams or wicks onto the hydrophilic channel walls. The data from the SAPC fuel cell suggests a different interpretation of "flooding" in PEM fuel cells. Liquid water must be transported across the GDL due to a hydrostatic pressure gradient between the cathode catalyst/membrane interface and the cathode gas flow channel. A good GDL should be hydrophobic to inhibit capillary condensation of water. Liquid water only enters the largest pores in the GDL so that only a small number of pores are blocked to gas flow (this is discussed further in Chapter 5).

Once the water breaks through the GDL to the flow channel, the observations again suggest different physical phenomena govern the motion of liquid water than those found in the PEM fuel cell literature. Often, the surface tension between the liquid drops and the GDL surface is considered to be the most important force[11], with gravity being neglected if mentioned at all. Assuming that the liquid drops are held to the GDL by the GDL/water surface tension, a few groups have examined how water droplets or films held to the GDL move along the channels and onto the channel walls. The interfacial energy of water with the GDL and the channel walls are the key system parameters for those models.[11, 13, 17] These numerical studies have also shown that hydrophilic channel walls are desirable, with the flow of water along the corners of the channel being an important mechanism for water removal. Other studies have focused on the

deformation and movement of droplets attached to the GDL under different operating conditions.[8, 15, 17] It is thought that the surface tension forces are balanced by the drag force from the gas flow, while the droplet deforms until it finally detaches. The important factors affecting how the droplets moved down the channel and interacted with the channel walls were found to be the gas flow, hydrophilicity/hydrophobicity of the channel walls, GDL surface, and temperature. In some cases it was concluded that the droplets that sat on top of the GDL blocked the flow of oxygen and could even form a film over the GDL. The results presented here suggest that drop detachment is the result of gravity or shearing forces overcoming the cohesive forces between the water in the GDL pore and the water drop on the surface of the GDL.

The results obtained from the experiments with the SAPC fuel cell paint a conceptually different physical picture of water transport and flooding than what has conventionally been assumed. It was shown that when placing the fuel cell with the cathode facing down there is no evidence of current reductions due to flooding even in the presence of liquid water in the gas flow channel. No flooding occurs when gravity assists in keeping liquid water away from the GDL surface, indicating that flooding is not the result of capillary condensation in the GDL, but rather liquid blocking oxygen transport across the gas flow channel/GDL interface. It was also shown that drops are held in place due to the surface tension of water in the GDL pore, and gravity plays an important role in how the water drops detach. The SAPC fuel cell experiments lead to four important conclusions about how water is transported and is the cause of flooding in PEM fuel cells:

1. The current reduction due to flooding in PEM fuel cells is the result of water slugs in the cathode flow channel.
2. Drops grow until gravity or the shearing force from gas flow overcomes surface tension and detaches the drop.
3. The detached drops coalesce and grow into slugs in the cathode gas flow channel.
4. Slug motion is critically dependent on the orientation of the flow channels.

The data suggest it is impossible to give a complete description of the spatio-temporal current density in the simplest of two-dimensional fuel cells – a fuel cell with a single straight channel. Very complex behavior has been observed that depends on two critical parameters: (i) the orientation of the fuel cell with respect to gravity, and (ii) the stoichiometry of the inlet feeds. The simplified model fuel cell has helped to isolate the key physics of water transport in a way previous investigators have not been able to. Some general conclusions can be drawn from the data presented here, but this is only the beginning of identifying the essential physics that properly describe fuel cell operation.

3.5.1 Water Drop Detachment

As the water flows through the GDL, it forms a drop at the surface of the GDL exposed to the flow channel. Since the GDL surface is hydrophobic, there is no cohesive force holding a drop to the GDL surface. In the experimental data reported here, the drops must be held in place by the cohesive force between the water in the drop and the water in pore. The drops grow until the force of gravity on the drop exceeds the surface tension holding the drop in place; the force balance for the critical drop size for detachment is given by equation (3.1).

$$2\pi\gamma_{water}r_{pore} = \frac{4}{3}\pi r_{drop}^{3}\rho_{water}g \tag{3.1}$$

The water at the membrane/electrode interface accumulates as it forms. Since it is in a confined space, the accumulating water will build up the hydrostatic pressure necessary to push the liquid through the largest pores. The pores in the GDL are interconnected within the plane and so the liquid water will search for the path of least resistance to push through to the gas flow channel. Other investigators that have seen droplets on the surface of the GDL ascribe the resistance to motion as resulting from the interfacial energy between the GDL and the droplet. Our results suggest that water drops move along the hydrophobic GDL surface with little force from the gas flow. It is the surface tension between the drop and the water in the GDL pore that holds the drops in place and must be overcome.

3.5.2 Mechanism of Cathode Flooding

If liquid water does not flood the pores of the GDL what is the mechanism of flooding in PEM fuel cells? The results from the SAPC fuel cell in different orientations show that the current in the fuel cell only drops when liquid water accumulates in the cathode gas flow channel in a way that inhibits oxygen transport into the GDL. When the flow channel is horizontal with the cathode facing downward or when the flow channel is vertical with the gas flow going in the direction of gravity, there was no evidence of any current reduction from flooding by liquid water unless the oxygen feed was completely consumed by reaction. In both of these configurations liquid water drainage is assisted by gravity.

When the gas flow rate to the cathode was reduced so that the oxygen feed was totally consumed, there was only gravity to assist in the liquid water removal. This resulted in the "periodic" spikes in the current shown in Figure 3.2 for ξ_1. The water would build up near the outlet of the flow channel. This caused a reduction in current in electrode segment 6, resulting in a slight excess of oxygen in the feed. The oxygen pressure would build up until it pushed a water slug out of the gas outlet of the fuel cell. The same phenomenon was observed with the fuel cell oriented vertically with the gas flows going downward. It might have been expected that the water would drain from the fuel cell just by gravity. However, the stainless steel electrodes along the sides of the flow channel are slightly hydrophilic and hold drops in place near the bottom of the flow channel in the absence of any gas flow. This gives rise to similar behavior as that seen in Figure 3.2.

Placing the SAPC fuel cell horizontal with the cathode facing up or placing the fuel cell vertical with the cathode flow going upwards, counter to gravity, both create situations where gravity plays a much greater role in the flooding. With the horizontal orientation, the water drops form on the GDL but it is only the shearing force from the gas flow that can detach the drops and force them to move. If the drops are sufficiently small so they don't significantly disrupt the gas flow field, the critical drop size can be found by balancing the shear force from the gas multiplied by the area of the drop with the surface energy holding the drop to the pore in the GDL,

$$\left(\frac{4\mu_{gas}Q_{gas}}{\pi r_{channel}^3}\right)\left(\pi r_{drop}^2\right) > 2\pi r_{pore}\gamma_{water} \tag{3.2}$$

A critical drop size for detachment can be identified from the force balance. At the flow rates in the SAPC fuel cell (Q = 0.1 cm^3/s, v = 100 cm/s) the critical drop size is

2 cm, which is larger than the flow channel. This implies that simple shearing action is not sufficient for the drop detachment. Rather what must happen is the drop will grow until it spans the gas flow channel and blocks the gas flow. The gas pressure will increase until it is sufficient to detach the drop; the required pressure for drop detachment is given by equation (3.3).

$$\Delta P = \frac{\rho_{gas} Q_{gas}^2}{2\pi^2 r_{channel}^4} > \frac{2 r_{pore} \gamma_{water}}{r_{channel}^2} \tag{3.3}$$

In the SAPC fuel cell ($r_{channel}$ = 1 mm) the required pressure to detach the drops that span the channel is 10 Pa. In large fuel cells where the gas flow rates and velocities in the small channels are much larger, the shearing force of the gas can become sufficient to detach liquid drops from the pores. For a 1000 cm^2 H_2/O_2 fuel cell operating at 0.5 A/cm^2 with ξ_2, the cathode flow rate is 50 cm^3/s, v = 50,000 cm/s, and the critical radius for drop detachment is 0.3 mm. However, when the cell size decreases to 100 cm^2, the gas velocities are no longer sufficient to cause drop detachment by shearing action and water drops that span the flow channels will be observed.

After drops detach from the anchoring pore, they require little force to move and so they are pushed to the end of the cathode gas flow channel. In the SAPC fuel cell, the flow channel turns 90º to exit. In the horizontal orientation with the cathode facing up, the exit flow points up against gravity. Because of the configuration of the fuel cell and exit tube, liquid water forms drops that, after detachment, are pushed towards the outlet of the flow channel. The drops are held up until the pressure is sufficient to push the water up against gravity into the exit tube. The drops tend to accumulate at the exit end of the flow channel and coalesce to form larger drops and slugs. The data in Figure 3.3

shows that the slugs grow and inhibit oxygen transport to the membrane/electrode interface near the outlet of the flow channel. The slug growth blocks the gas flow so a pressure builds up and eventually pushes the slug out of the channel. The slug growth and push out is evident in Figure 3.3 where the currents in electrode segments 4, 5, and 6 fluctuate the most, but the currents are almost constant in the upstream electrode segments.

The effect of gravity is most dramatic for the SAPC fuel cell vertically oriented with the cathode flow rising upwards against gravity. As shown above, the gas flow rate is insufficient to cause the drops to detach as they grow at the surface of the GDL, so drops instead will fall due to gravity. The most commonly observed behavior is that the drops fall to the bottom of the cathode gas flow channel, where they coalesce to form slugs. When the slugs first form, they are sufficiently small and the gas can deform them and flow past. As the slugs get larger, the pressure drop associated with slug deformation becomes too great and the slugs span the channel, blocking gas from moving up the channel. The gas pressure builds up and pushes the slug up the column. The gas pressure must overcome the gravitational force associated with the slug, as given by equation (3.4).

$$\Delta P = \frac{\rho_{gas} Q_{gas}^2}{2\pi^2 r_{channel}^4} > L_{slug} \rho_{water} g \tag{3.4}$$

At the top of the cathode gas flow channel, the flow encounters a 90º angle. The slugs break apart at the top so that a smaller slug of water is pushed out of the exit tube, and the rest of the water flows back down the channel and is incorporated into forming a new liquid slug.

3.5.3 Slug Formation and Motion

The details of the process of slug formation, motion and the gas flow are hard to predict quantitatively, but certain trends are evident. At sufficiently high gas flow rates, the slugs are continually formed and pushed up the channel with little or no change in the currents from the six electrode segments. This appears to correspond to the slugs moving up the channel over a short period of time, where the liquid does not remain in any position long enough to hinder oxygen transport to the membrane/electrode interface. Reducing the oxygen flow rate where there is little stoichiometric excess results in the slugs temporarily blocking the oxygen flow and causing large current fluctuations. Figure 3.10 shows that just after the slug forms and blocks the gas flow, the currents start to drop in all the electrode segments. The local current turns on as the slug moves up the channel. The currents continue to rise until the next slug has grown sufficiently large to block the flow channel and the process repeats itself.

The process of slug formation and rising in the vertical cathode flow channel occurs over a period of 10-30 s. The typical slug as shown in Figure 3.10 is 0.025 cm^3. The rate of water formation in Figure 3.9 is 5-10 cm^3/s, so it should take 2500 s to form a slug from just the water produced by reaction. Slug formation is much faster. This is clear evidence of slug breakup within the flow channel as 90% of the water in the slug must rain back down the flow channel to form a new slug. Slug formation and breakup is common in gas-solid fluidized beds, which seems most analogous to the liquid water motion in the vertical SAPC fuel cell.

Many complex water distributions were observed that gave rise to highly variable dynamic current distribution patterns. For example, stopping the reactant flows to the

horizontal SAPC fuel cell with the cathode facing up for several minutes resulted in a water film spreading across the entire GDL. When the reactant feeds were restarted, the currents in all electrode segments were reduced by more than an order of magnitude and it took several hours before fuel cell operation returned to its pre-shutdown performance.

The complexity of behavior is partially captured in Figures 3.2, 3.3, 3.6, and 3.9. The intention was to illustrate the basic physics that affect water transport and flooding in PEM fuel cells; models that can capture all the complexities are far from being realized. Detachment of drops and movement of slugs is a function of gas flow rate; drops will coalesce as they move along the flow channel and will grow and make slugs. Smaller drops and slugs move faster than larger ones so that the small ones will overtake the larger ones and combine to make even larger slugs. Additionally, the gas velocity decreases from the inlet to the outlet, depending on the current, as per equation (3.5).

$$Q_{gas}(x) = Q_{gas}^{inlet}\left(1 - \frac{w_{ch}}{4\mathcal{F}}\int_{inlet}^{x} j(x)\,dx\right) \tag{3.5}$$

The decrease in the gas velocity along the length of the cathode gas flow channel will result in slugs slowing down as they approach the outlet and grow to block the gas from getting to the membrane/electrode interface. This is what was reported for the SAPC fuel cell in the horizontal configuration with the cathode facing up. The water slugs build up at the end of the flow channel and cause a current drop in the electrode segments near the outlet.

A secondary effect of the inlet flow rates observed in the SAPC fuel cell was the redistribution of the current. Reducing the inlet gas flow rates caused the current density to increase at the upstream electrode segments and decrease at the downstream electrode segments. The decrease at the downstream segments was anticipated because the

depletion of the reactants would reduce the chemical potential driving force for the current. However, the increase in the current density at the upstream electrode segments was unexpected. The current redistribution is due to lateral currents that result from the changes in the potential distribution associated with the depletion of the reactants.[27-29] When the reactant flows were reduced to partially starve the fuel cell, the upstream electrode segments are at higher potential differences than the downstream electrode segments. This causes the currents to be concentrated in the upstream electrode segments. The effects of the lateral currents were observed during extinction of the fuel cell, discussed in Chapter 2, and have been incorporated into simulations, as discussed in Chapter 4.

3.5.4 Implications for Fuel Cell Design and Operation

The PEM fuel cell literature is still deficient in understanding the physics of liquid motion in PEM fuel cells. Yet, with these results, we can start to think about how to improve the designs of fuel cell systems and materials. One consideration is the GDL. The best GDL material will have a bimodal pore distribution – large pores to carry water from the membrane/electrode interface into the gas flow channel and small pores to carry oxygen from the gas flow channel to the membrane/electrode interface. Liquid drops form on the surface of the GDL as water emerges from the largest pores. The flow channels should be designed so that slug and drop motion to remove the liquid water can be facilitated by gas flow or gravity.

In practice, there are a variety of approaches that have been proposed to deal with flooding in PEM fuel cells. The most common approach is to employ excess reactant flows so the gas velocities are sufficiently high to blow liquid water out of the flow

channels. A variety of flow channel configurations are available commercially and others are reported in the literature; most being variations on serpentine flow channels.[37-41] It appears that the required flow rates to remove liquid water have been determined through operational experience—no models for multiphase flow have been found that predict the required flow rates. Other approaches to manage liquid water include porous electrodes to wick liquid water from the cathode flow channel, and controlled temperature gradients along the flow channels to increase water vapor flow.[42, 43]

The standard fuel cell design employing serpentine flow channels may be best for fuel cells operating in the "zero-G" environments of space vehicles[44], but they may not be a good design for operation on earth. The results presented here point out that the orientation of the flow fields with respect to gravity plays an important role in fuel cell flooding. Previous students in the Benziger group introduced the self-draining channel-less PEM fuel cell that could operate with Nafion membranes utilizing dry feeds.[45] By removing the flow channels they could permit liquid water exiting the GDL to drain by gravity. They found no evidence of flooding in the self-draining fuel cell for current densities > 2 A/cm^2 at temperatures of 25-80ºC with H_2/O_2 feeds at exact stoichiometry of hydrogen and stoichiometric excess of 30% oxygen.[26] Recently Honda introduced gravity assisted draining in their new parallel flow channel fuel cell design[46], but there are no details of its operating characteristics.

Besides channel orientation, the gas flow rate also plays an important role in the motion of liquid drops and slugs in flow channels of fuel cells. This has important implications in control of the cathode feed rate for load following. As the power output

(or current output) is reduced, the feed rate is generally reduced in direct proportion to the current. This keeps the volume fraction of liquid drops and slugs constant. However, as shown above, the speed of the detachment of drops and motion of the slugs depends on the gas flow rate or gas flow rate squared; so reducing the gas flow rate with reduced current can result in more coalescence of drops and slugs leading to current fluctuations. Flow control for load following must take into account the problem of slug motion in the flow channels. It should be noted that flooding and cathode inlet feed control is less of a problem with air than with oxygen. The large amount of nitrogen associated with air causes a large increase in the gas flow rate, and much less decrease in the flow rate along the length of the flow channel, both of which improve the removal of liquid slugs. On the negative side – the higher flow rate of the air also acts to dry the membrane, which may require greater humidification of the cathode feed. The implications are that the optimal fuel cell flow system design and control may be different for the H_2/O_2 and H_2/air fuel cells, and the design should make that distinction.

3.6 Conclusions

Experiments have been presented that illuminate the physics of liquid water transport in PEM fuel cells. These key experimental results are:

1. Liquid water enters the largest pores of the GDL and flows from the membrane/electrode interface to the cathode gas flow channel.
2. Water drops form on the surface of the GDL, which are held in place by cohesive forces with water in the pores. The drops detach when gravity or shear forces overcome the cohesive forces.

3. After a water drop detaches, it moves freely along the surfaces in the gas flow channel, running into other drops and combining to form liquid slugs.
4. Liquid slugs grow until they hinder the gas flow in the cathode flow channel.
5. Flooding occurs when liquid water slugs hinder the gas transport downstream and cause the starvation of the reactants to the membrane/electrode interface.
6. The motion of liquid slugs is gravity dependent.
    a. If the fuel cell is oriented such that gravity assists the removal of liquid from the cathode gas flow channel, the fuel cell will operate stably.
    b. When the fuel cell is oriented such that the gas flow must push the liquid slugs against gravity, reactant gas flow is temporarily blocked, resulting in large current density fluctuations.

The results presented in this chapter suggest that new models for PEM fuel cells are needed. Standard computational fluid dynamic models that are being pursued extensively for PEM fuel cell design are not adequate to capture the physics associated with flooding. The water transport pores in the GDL are randomly distributed and the gas flow decreases along the length of the gas flow channels due to reaction. CFD models are not able to deal with two phase flow systems where the relative fraction of the two phases is changing as a function of time and position. It is more likely that probabilistic models can more successfully capture the complexity associated with multiphase flow in PEM fuel cells.

3.7 References

1. Hickner, M.A., N.P. Siegel, K.S. Chen, D.N. McBrayer, D.S. Hussey, D.L. Jacobson, and M. Arif, *Real-time imaging of liquid water in an operating proton exchange membrane fuel cell.* Journal of the Electrochemical Society, 2006. **153**(5): p. A902-A908.

2. Owejan, J.P., T.A. Trabold, D.L. Jacobson, D.R. Baker, D.S. Hussey, and M. Arif, *In situ investigation of water transport in an operating PEM fuel cell using neutron radiography: Part 2 - Transient water accumulation in an interdigitated cathode flow field.* International Journal of Heat and Mass Transfer, 2006. **49**(25-26): p. 4721-4731.

3. Pekula, N., K. Heller, P.A. Chuang, A. Turhan, M.M. Mench, J.S. Brenizer, and K. Unlu, *Study of water distribution and transport in a polymer electrolyte fuel cell using neutron imaging.* Nuclear Instruments & Methods in Physics Research Section A-Accelerators Spectrometers Detectors and Associated Equipment, 2005. **542**(1-3): p. 134-141.

4. Trabold, T.A., J.P. Owejan, D.L. Jacobson, M. Arif, and P.R. Huffman, *In situ investigation of water transport in an operating PEM fuel cell using neutron radiography: Part 1 - Experimental method and serpentine flow field results.* International Journal of Heat and Mass Transfer, 2006. **49**(25-26): p. 4712-4720.

5. Turhan, A., K. Heller, J.S. Brenizer, and M.M. Mench, *Quantification of liquid water accumulation and distribution in a polymer electrolyte fuel cell using neutron imaging.* Journal of Power Sources, 2006. **160**(2): p. 1195-1203.

6. Liu, X., H. Guo, and C.F. Ma, *Water flooding and two-phase flow in cathode channels of proton exchange membrane fuel cells.* Journal of Power Sources, 2006. **156**(2): p. 267-280.

7. Ma, H.P., H.M. Zhang, J. Hu, Y.H. Cai, and B.L. Yi, *Diagnostic tool to detect liquid water removal in the cathode channels of proton exchange membrane fuel cells.* Journal of Power Sources, 2006. **162**(1): p. 469-473.

8. Theodorakakos, A., T. Ous, A. Gavaises, J.M. Nouri, N. Nikolopoulos, and H. Yanagihara, *Dynamics of water droplets detached from porous surfaces of relevance to PEM fuel cells.* Journal of Colloid and Interface Science, 2006. **300**(2): p. 673-687.

9. Tuber, K., D. Pocza, and C. Hebling, *Visualization of water buildup in the cathode of a transparent PEM fuel cell.* Journal of Power Sources, 2003. **124**(2): p. 403-414.

10. Yang, X.G., F.Y. Zhang, A.L. Lubawy, and C.Y. Wang, *Visualization of liquid water transport in a PEFC.* Electrochemical and Solid State Letters, 2004. **7**(11): p. A408-A411.

11. Zhang, F.Y., X.G. Yang, and C.Y. Wang, *Liquid water removal from a polymer electrolyte fuel cell.* Journal of the Electrochemical Society, 2006. **153**(2): p. A225-A232.

12. Jiao, K., B. Zhou, and P. Quan, *Liquid water transport in straight micro-parallel-channels with manifolds for PEM fuel cell cathode.* Journal of Power Sources, 2006. **157**(1): p. 226-243.

13. Quan, P. and M.C. Lai, *Numerical study of water management in the air flow channel of a PEM fuel cell cathode.* Journal of Power Sources, 2007. **164**(1): p. 222-237.

14. Cai, Y.H., J. Hu, H.P. Ma, B.L. Yi, and H.M. Zhang, *Effects of hydrophilic/hydrophobic properties on the water behavior in the micro-channels of a proton exchange membrane fuel cell.* Journal of Power Sources, 2006. **161**(2): p. 843-848.

15. He, G.L., P.W. Ming, Z.C. Zhao, A. Abudula, and Y. Xiao, *A two-fluid model for two-phase flow in PEMFCs.* Journal of Power Sources, 2007. **163**(2): p. 864-873.

16. Meng, H. and C.Y. Wang, *Model of two-phase flow and flooding dynamics in polymer electrolyte fuel cells.* Journal of the Electrochemical Society, 2005. **152**(9): p. A1733-A1741.

17. Zhan, Z.G., J.S. Xiao, M. Pan, and R.Z. Yuan, *Characteristics of droplet and film water motion in the flow channels of polymer electrolyte membrane fuel cells.* Journal of Power Sources, 2006. **160**(1): p. 1-9.

18. Araki, T., H. Koori, T. Taniuchi, and K. Onda, *Simulation of the current density distribution for a PEMFC by using measured electrochemical and physical properties of the membrane.* Journal of Power Sources, 2005. **152**(1): p. 60-66.

19. Buchi, F.N., A.B. Geiger, and R.P. Neto, *Dependence of current distribution on water management in PEFC of technical size.* Journal of Power Sources, 2005. **145**(1): p. 62-67.

20. Hakenjos, A. and C. Hebling, *Spatially resolved measurement of PEM fuel cells.* Journal of Power Sources, 2005. **145**(2): p. 307-311.

21. Natarajan, D. and T. Van Nguyen, *Current distribution in PEM fuel cells. Part 1: Oxygen and fuel flow rate effects.* AIChE Journal, 2005. **51**(9): p. 2587-2598.

22. Nishikawa, H., R. Kurihara, S. Sukemori, T. Sugawara, H. Kobayasi, S. Abe, T. Aoki, Y. Ogami, and A. Matsunaga, *Measurements of humidity and current distribution in a PEFC.* Journal of Power Sources, 2006. **155**(2): p. 213-218.

23. Patterson, T.W. and R.M. Darling, *Damage to the cathode catalyst of a PEM fuel cell caused by localized fuel starvation.* Electrochemical and Solid State Letters, 2006. **9**(4): p. A183-A185.

24. Reiser, C.A., L. Bregoli, T.W. Patterson, J.S. Yi, J.D.L. Yang, M.L. Perry, and T.D. Jarvi, *A reverse-current decay mechanism for fuel cells.* Electrochemical and Solid State Letters, 2005. **8**(6): p. A273-A276.

25. Taniguchi, A., T. Akita, K. Yasuda, and Y. Miyazaki, *Analysis of electrocatalyst degradation in PEMFC caused by cell reversal during fuel starvation.* Journal of Power Sources, 2004. **130**(1-2): p. 42-49.

26. Woo, C.H. and J.B. Benziger, *PEM fuel cell current regulation by fuel feed control.* Chemical Engineering Science, 2007. **62**(4): p. 957-968.

27. Kulikovsky, A.A., *Voltage loss in bipolar plates in a fuel cell stack.* Journal of Power Sources, 2006. **160**(1): p. 431-435.

28. Santis, M., S.A. Freunberger, M. Papra, A. Wokaun, and F.N. Buchi, *Experimental investigation of coupling phenomena in polymer electrolyte fuel cell stacks.* Journal of Power Sources, 2006. **161**(2): p. 1076-1083.

29. Berg, P., K. Promislow, J. Stumper, and B. Wetton, *Discharge of a segmented polymer electrolyte membrane fuel cell.* Journal of Fuel Cell Science and Technology, 2005. **2**(2): p. 111-120.

30. Lin, G.Y., W.S. He, and T. Van Nguyen, *Modeling liquid water effects in the gas diffusion and catalyst layers of the cathode of a PEM fuel cell.* Journal of the Electrochemical Society, 2004. **151**(12): p. A1999-A2006.

31. Pasaogullari, U. and C.Y. Wang, *Liquid water transport in gas diffusion layer of polymer electrolyte fuel cells.* Journal of the Electrochemical Society, 2004. **151**(3): p. A399-A406.

32. Wang, Z.H., C.Y. Wang, and K.S. Chen, *Two-phase flow and transport in the air cathode of proton exchange membrane fuel cells.* Journal of Power Sources, 2001. **94**(1): p. 40-50.

33. Weber, A.Z., R.M. Darling, and J. Newman, *Modeling two-phase behavior in PEFCs.* Journal of the Electrochemical Society, 2004. **151**(10): p. A1715-A1727.

34. Bernardi, D.M. and M.W. Verbrugge, *A Mathematical-Model Of The Solid-Polymer-Electrolyte Fuel-Cell.* Journal of the Electrochemical Society, 1992. **139**(9): p. 2477-2491.

35. Liu, Z.X., Z.Q. Mao, and C. Wang, *A two dimensional partial flooding model for PEMFC.* Journal of Power Sources, 2006. **158**(2): p. 1229-1239.

36. Natarajan, D. and T. Van Nguyen, *Three-dimensional effects of liquid water flooding in the cathode of a PEM fuel cell.* Journal of Power Sources, 2003. **115**(1): p. 66-80.

37. Xu, C. and T.S. Zhao, *A new flow field design for polymer electrolyte-based fuel cells.* Electrochemistry Communications, 2007. **9**(3): p. 497-503.

38. Kitta, S., T. Okumoto, H. Uchida, and M. Watanabe, *New metal separators coated with carbon/resin composite layers for PEFCs.* Electrochemistry, 2007. **75**(2): p. 213-216.

39. Kumar, A. and R.G. Reddy, *Effect of gas flow-field design in the bipolar/end plates on the steady and transient state performance of polymer electrolyte membrane fuel cells.* Journal of Power Sources, 2006. **155**(2): p. 264-271.

40. Nikam, V.V. and R.G. Reddy, *Corrugated bipolar sheets as fuel distributors in PEMFC.* International Journal of Hydrogen Energy, 2006. **31**(13): p. 1863-1873.

41. Yan, W.M., C.H. Yang, C.Y. Soong, F.L. Chen, and S.C. Mei, *Experimental studies on optimal operating conditions for different flow field designs of PEM fuel cells.* Journal of Power Sources, 2006. **160**(1): p. 284-292.

42. Dufner, B.F., M.L. Perry, J.C. Trocciola, D. Yang, and J.S. Yi, *Bi-zone water transport plate for a fuel cell* U.S.P.a.T. Office, Editor. 2003, UTC Fuel Cells, LLC: United States.

43. Voss, H.H., D.P. Wilkinson, and D.S. Watkins, *Method and apparatus for removing water from electrochemical fuel cells by controlling the temperature and pressure of the reactant streams* U.S.P.a.T. Office, Editor. 1995, Ballard Power Systems Inc. : United States.

44. Sone, Y., M. Ueno, H. Naito, and S. Kuwajima, *One kilowatt-class fuel cell system for the aerospace applications in a micro-gravitational and closed environment.* Journal of Power Sources, 2006. **157**(2): p. 886-892.

45. Hogarth, W.H.J. and J.B. Benziger, *Operation of polymer electrolyte membrane fuel cells with dry feeds: Design and operating strategies.* Journal of Power Sources, 2006. **159**(2): p. 968-978.

46. Komura, T., T. Moriya, S. Isobe, and T. Ushiro, *Fuel cell system and draining method for the same* in *US Patent & Trademark Office, Patent Full Text and Image Database*, U.S.P.a.T. Office, Editor. 2001, Honda Giken Kogyo Kabushiki Kaisha: United States.

4 Model and simulations

4.1 Introduction

The successful simulation of PEM fuel cell operation is extremely valuable in improving system designs and ensuring reliability. It is often difficult to measure a system variable while the fuel cell is running without making modifications to the system that could have an effect on the results. Also, experimental data can be misinterpreted, with the actual cause of an observation obscured by integrated measurements or experimental system artifacts. The complexities of PEM fuel cell experiments are well known, shifting much of the attention of research groups to developing mathematical models.

The amount of effort put into simulating the operation of PEM fuel cells has grown exponentially in recent years.[1] The complexity spans the range from empirical fits[2, 3] to full three-dimensional, non-isothermal models solved with computational fluid dynamics (CFD) programs.[4, 5] The scale of the system being simulated can be from microscopic[6, 7], as in looking at the morphology of the catalyst layer[8], to a full power station, incorporating a large fuel cell stack with peripheral components such as humidifiers and power conditioning units.[9, 10] Each level of modeling is important and serves a worthwhile purpose in continuing to improve the operation of fuel cells. From an engineering perspective, however, understanding the fundamental physics of the operation of a PEM fuel cell is a primary goal.

With this goal in mind, a one-dimensional model was developed in the Benziger group, mostly through the work of E. Joanne Chia.[11] The model was validated and parameter values were calculated based on experimental results from the one-dimensional

STR fuel cell, described in section 1.5. Drawing analogies from traditional chemical reactor design and simulation, the 1-D model was extended to two dimensions through a "tanks-in-series" approach, similar to the modeling of a plug-flow reactor by several stirred-tank reactors in series.[12] The data from the SAPC fuel cell experiments was then coupled with results from the tanks-in-series simulations to give further insight.

4.2 One-dimensional "Stirred tank reactor" model

The 1-D design of the experimental STR fuel cell dramatically simplifies the mass balances and constitutive equations that describe the system. The fuel cell is essentially two reactors—the anode and cathode plenums—coupled through proton transport across the membrane, electron transport through the external circuit, and water transport between the different layers. The electrochemical reactions drive a current through an external circuit, for which the independent parameter that can be manipulated is the load resistance. The other parameters that are set explicitly are the design specifications, such as the flow channel dimensions and MEA active area; the inlet flow rates; the cell temperature (assumed constant for the small systems used in this work); and the total cell pressure. The other variables respond to changes in these system parameters and must be calculated as described below.

4.2.1 Circuit representation

The most basic circuit involving a fuel cell is illustrated in Figure 4.1. The fuel cell contributes to the circuit through a few components in series. The first is the battery voltage, V_b, resulting from the chemical potential difference of hydrogen between the

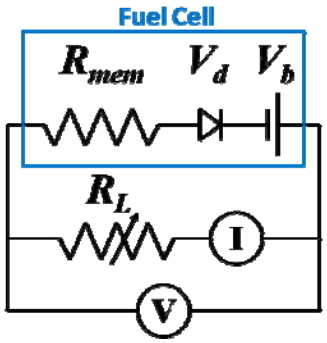

Figure 4.1 Diagram of basic circuit involving a fuel cell. The fuel cell can be broken up into different components: the internal resistance primarily from the membrane, R_{mem}, the voltage drop from the rectifying junction at the catalyst layer, V_d, and the voltage from the difference in hydrogen chemical potential between the anode and cathode, V_b. The independent parameter that can be changed is the external load resistance, R_L. The fuel cell responds to the load and the resulting current and voltage must be measured.

anode and cathode, as given by equation (4.1),

$$V_b = \frac{RT}{2\mathfrak{F}} \ln\left(\frac{a_H^{anode}}{a_H^{cathode}}\right) \tag{4.1}$$

where R is the universal gas constant, T is the cell temperature, the 2 denotes the number of electrons evolved by the reaction of one molecule of hydrogen, $\mathfrak{F}$ is Faraday's constant, and a_H^{anode} and $a_H^{cathode}$ are the activities of hydrogen at the anode and cathode catalyst layers, respectively. The very fast time scales of the electrochemical reactions relative to the other dynamic processes during fuel cell operation allow the activity of hydrogen at the cathode to be calculated from the assumption of reactive equilibrium of the hydrogen with water and oxygen at the cathode,

$$K_w = \frac{\left(a_w^{cathode}\right)^2}{\left(a_H^{cathode}\right)^2 \left(a_O^{cathode}\right)} \quad \Rightarrow \quad a_H^{cathode} = \frac{\left(a_w^{cathode}\right)}{\left(K_w\right)^{1/2} \left(a_O^{cathode}\right)^{1/2}} \tag{4.2}$$

The equilibrium constant, K_w, can equivalently be written for the formation of water as

$$K_w = \exp\left(\frac{-\Delta G^o}{RT}\right) \tag{4.3}$$

where ΔG^o is the Gibbs free energy of formation, equal to -237 kJ mol^{-1} for liquid water at 25 °C. Substituting equations (4.2) and (4.3) into (4.1) gives the standard thermodynamic expression for the fuel cell voltage,

$$V_b = \frac{-\Delta G^o}{4\mathfrak{F}} + \frac{RT}{4\mathfrak{F}} \ln\left[\frac{\left(a_H^{anode}\right)^2 a_O^{cathode}}{\left(a_w^{cathode}\right)^2}\right] \tag{4.4}$$

The internal resistance of the fuel cell, primarily due to the resistance of the membrane and denoted as R_{mem}, acts in series with the battery voltage. The expression for 1100 equivalent weight (EW) Nafion was determined empirically in the Benziger group to be (also equation (2.2))[13]

$$R_{mem} = 10^7 \cdot \exp(-14 \cdot a_w^{0.2}) \cdot \frac{t_{mem}}{A_{mem}} \tag{4.5}$$

where t_{mem} and A_{mem} are the thickness and in-plane area of the membrane, respectively, in centimeters. Equation (4.5) was used in the model as all of the experiments in this work utilized MEAs constructed with 1100 EW Nafion. The resistance of other polymer electrolytes are expected to have analogous dependences on water activity. The contact resistances between the different electrical connections for the SAPC fuel cell were measured and found to be only ~0.2 Ω; they did not add a significant contribution to the total internal resistance. The importance of the contact resistance between the GDL and lands is still debated in the literature with widely varying values[14-16] and is not considered here.

The final component of the fuel cell part of Figure 4.1 is the diode, causing the voltage drop V_d. The catalyst layers are rectifying junctions for the electrons carried by the external circuit and the protons carried through the membrane. The kinetics are equivalent to Butler-Volmer kinetics and can be modeled as a diode with a threshold voltage V_T and saturation current I_o.[12] The voltage drop due to the diode effect is given by equation (4.6),

$$V_d = V_T \ln\left(\frac{i}{I_o} + 1\right) \tag{4.6}$$

By Kirchhoff's loop rule, the sum of the voltage drops around the complete circuit must be equal to 0. This gives an expression to calculate the current, i,

$$i = \frac{V_b - V_d}{R_{mem} + R_L} \tag{4.7}$$

4.2.2 Mass balances

The simplicity of the STR fuel cell system allows for basic mass balances to be incorporated into the model that can then be validated by the experimental data. The reactants are consumed by the electrochemical reactions at a rate given by the current. At the same time, water is generated. The balances for the flow rates at the anode and cathode sides are given by equations (4.8) and (4.9), respectively,

$$F_A = \left[F_A^{in} \cdot \frac{P_{tot}}{RT^{in}} + k_{w,1} A_{mem} \left(a_w - \frac{P_{w,A}}{P_w^{sat}} \right) - \frac{i}{\mathfrak{F}} \left(k_w^{eo} + 1/2 \right) \right] \cdot \frac{RT}{P_{tot}} \tag{4.8}$$

$$F_C = \left[F_C^{in} \cdot \frac{P_{tot}}{RT^{in}} + k_{w,2} A_{mem} \left(a_w^{gdl} - \frac{P_{w,C}}{P_w^{sat}} \right) - \frac{i}{4\mathfrak{F}} \right] \cdot \frac{RT}{P_{tot}} \tag{4.9}$$

The first term of the RHS of each equation is the inlet rate in mol s^{-1}. The second terms describe the transport of water into the flow channel, based on gradients in water activity.

In equation (4.8), $k_{w,1}$ is a lumped parameter mass transfer coefficient with units of mol s^{-1} cm^{-2} that describes the transport of water into the anode flow channel. The coefficient $k_{w,1}$ accounts for the water transport across the membrane, the interfacial transport of the water into the fluid phase at the anode catalyst/membrane interface, and the water transport from the catalyst layer through the GDL to the flow channel. Considering each process individually would introduce several ill-defined adjustable parameters into the model. The lumped parameter approach minimized the number of parameters and allowed for the values of the coefficients to be determined from a fits with experimental data. The water transport was based on the difference between the membrane water activity, a_w, and the water activity in the anode flow channel, given by the partial pressure of water in the anode flow stream over the water saturation vapor pressure, $P_{w,A}/P_w^{sat}$.

The parameter $k_{w,2}$ in equation (4.9) is similar to $k_{w,1}$ and also has units of mol s^{-1} cm^{-2}, but only describes the transport of water from the cathode catalyst layer across the cathode GDL. The transport is driven by the gradient between the water activity in the cathode flow channel, $P_{w,C}/P_w^{sat}$, and the water activity at the cathode catalyst/GDL interface, a_w^{gdl}. The value for the water activity at the catalyst/GDL interface is calculated separately from the membrane water activity because the water is produced between the two layers. Water is then either absorbed into the membrane or transported

through the GDL. The different dynamics of the two transport processes make it so that the two activities are not always in equilibrium.

The values for the mass transfer coefficients were calculated from experiments with the STR fuel cell, described in section 1.5. The value of $k_{w,1}$ that best fit the data was found to be 1.3×10^{-6} mol s^{-1} cm^{-2}. The value for $k_{w,2}$ was slightly larger at 1.6×10^{-6} mol s^{-1} cm^{-2}. The calculated values for the coefficients are expected to be dependent on the details of the catalyst layers and GDL and the local water activity. In contrast to most other models reported in the literature, the water diffusion across the membrane has not been included as a significant transport resistance. Other work in the Benziger group showed that water transport in Nafion is limited by interfacial transport; diffusion within the membrane is much faster.[17] Both coefficients are dependent on the transport through the GDL, but $k_{w,1}$ is smaller, as it is also dependent on the transport across the membrane interface. If diffusion through the membrane was the limiting factor for membrane water transport, it would be expected that $k_{w,1}$ would be much smaller and dependent on the membrane thickness.

The third term in each equation accounts for the consumption of reactants by the electrochemical reactions. For each mole of electrons emitted at a rate of $i/\mathcal{F}$, 0.5 mol of hydrogen and 0.25 mol of oxygen is consumed. The extra factor k_w^{eo} in equation (4.8) describes the moles of water transported across the membrane away from the anode by electro-osmotic drag. The value of k_w^{eo} is calculated based on experimental observations[18-20] as

$$k_w^{eo} = 2\left(\frac{P_{w,A}}{P_w^{sat}}\right)^4 \tag{4.10}$$

The factor k_w^{eo} is multiplied by the current as it is accounts for the number of water molecules associated with the protons that are formed by the hydrogen oxidation reaction and transported across the membrane at a rate of $i/\mathcal{F}$. It should be noted that very recent work in the Benziger group has provided evidence against the significance of electro-osmotic drag. It is thought that the extra transport of water from the anode to the cathode is not the result of electro-osmotic drag, but is driven by a concentration gradient created from a higher depletion of reactants and increasing water partial pressure at the anode. If this is verified, the model equations can be updated, but for the results discussed here, electro-osmotic drag is assumed to be important and described by equation (4.10).

As the current evolves dynamically, the flow rates change. The partial pressures of the reactants change in the flow channels and at the catalyst layers. The product water is absorbed into the membrane or is transported through the GDLs and into the flow channels. The changes in the hydrogen partial pressure in the anode flow channel and the oxygen partial pressure in the cathode flow channel are given by the following mass balances

$$\frac{dP_H}{dt} = \left[F_A^{in} \cdot \frac{P_H^{in}}{RT} - F_A \cdot \frac{P_H}{RT} - \frac{i}{2\mathcal{F}}\right]\frac{RT}{V_A^{gas}} \tag{4.11}$$

$$\frac{dP_O}{dt} = \left[F_C^{in} \cdot \frac{P_O^{in}}{RT} - F_C \cdot \frac{P_O}{RT} - \frac{i}{4\mathcal{F}}\right]\frac{RT}{V_C^{gas}} \tag{4.12}$$

where the terms are simply the rates of moles in minus the moles out minus the moles consumed by reaction. The factors RT/V_A^{gas} and RT/V_C^{gas} convert the rates in mol s^{-1} to the

rate of pressure change (bar s^{-1}) where V_A^{gas} and V_C^{gas} are the volumes of the anode and cathode flow channels (or plenums), respectively. Once liquid water condenses in the channels, the flow streams are saturated and the partial pressures are constant. The effect of the consumption of the reactants is a change in the flow rates.

The change in moles of water in the membrane is described based on the change of water activity in the membrane, a_w, with the following mass balance

$$N_{SO_3}\frac{d\lambda}{da_w}\frac{da_w}{dt} = k_{w,3}A_{mem}\left(a_w^{gdl} - a_w\right) - k_{w,1}A_{mem}\left(a_w - \frac{P_{w,A}}{P_w^{sat}}\right) \tag{4.13}$$

The first factor on the LHS, N_{SO_3}, is the moles of sulfonic acid groups in the Nafion membrane. For Nafion 115, the equivalent weight (grams of Nafion per mole of sulfonic acid groups) is 1100. With a dry density, ρ_{nafion}, of 2 g cm^{-3}, the moles of sulfonic acid groups is calculated as

$$N_{SO_3} = \frac{\rho_{nafion}t_{mem}A_{mem}}{1100} \tag{4.14}$$

where t_{mem} and A_{mem} are again the thickness and in-plane area of the membrane, respectively. The second factor gives the change in water molecules associated with each sulfonic acid group, λ, with changing water activity. This is calculated based on the empirical fit[13]

$$\lambda = 14.9a_w - 44.7\left(a_w\right)^2 + 70.0\left(a_w\right)^3 - 29.5\left(a_w\right)^4 - 0.446\left(a_w\right)^5 \tag{4.15}$$

The two terms on the RHS side give the rate of transport between the membrane and cathode side GDL and between the membrane and anode flow channel, respectively, based on the lumped parameter mass transfer coefficients $k_{w,3}$ and $k_{w,1}$, both with units of

mol s^{-1} cm^{-2}. The value for $k_{w,3}$ of 5.6×10^{-6} mol s^{-1} cm^{-2} was also calculated from experiments with the STR fuel cell. The value is higher than the other mass transfer coefficients as the transport is only across the cathode membrane/catalyst interface.

The final mass balance describes the change in the amount of water in the cathode side GDL. As water is produced, it is either taken up by the membrane or transported through the cathode GDL and into the flow channel. If the gas in the GDL pores becomes saturated, liquid water begins to condense and the water activity equals 1. With the saturation vapor pressure and pore volume known, the maximum number of moles of water vapor and liquid water can be calculated. When the number of moles of water in the GDL, n_w^{gdl}, is below the saturation value, $n_{w,\max}^{gdl}$, the water activity in the GDL is calculated as $a_w^{gdl} = n_w^{gdl} \big/ n_{w,\max}^{gdl}$. Above the saturation value, $a_w^{gdl} = 1$. The change in the moles of water is calculated by the balance

$$\frac{dn_w^{gdl}}{dt} = k_{w,3} A_{mem} \left(a_w^{gdl} - a_w \right) - k_{w,2} A_{mem} \left(a_w^{gdl} - \frac{P_{w,C}}{P_w^{sat}} \right) + \frac{i}{\mathcal{F}} \left(k_w^{eo} + 1/2 \right) \qquad (4.16)$$

The first two terms on the RHS have been discussed with other mass balances; the first term is also in equation (4.13) while the second is in equation (4.9). The third term is similar to the last term of equation (4.8), except that electro-osmotic drag and the electrochemical reaction add water to the GDL.

4.2.3 Mass transfer relations

In order to close the set of equations described in the previous two sections, the partial pressures of the reactants at the catalyst layers must be related to the partial pressures in the flow channels. The porous structure of the GDL adds a mass transfer

resistance to the flow of reactants from the flow channel to the catalyst layers. The transport of reactants through the GDL is much slower than the electrochemical reactions so that a balance can be assumed between the reactants reaching the catalyst layer and the reactants being consumed by the reaction. This is described by the following equations for hydrogen at the anode catalyst and oxygen at the cathode catalyst, respectively,

$$k_H A_{mem}\left(P_H - P_H^{anode}\right) = \frac{i}{2\mathfrak{F}} \tag{4.17}$$

$$k_O A_{mem}\left(P_O - P_O^{cathode}\right) = \frac{i}{4\mathfrak{F}} \tag{4.18}$$

where k_H and k_O are the lumped parameter mass transfer coefficients for the transport of hydrogen and oxygen through the GDL, respectively. To a first approximation, the two mass transfer coefficients k_H and k_O can be calculated from the diffusion coefficient corrected for the influence of the porous structure as

$$k = \frac{\varepsilon D}{\tau t_{gdl}} \tag{4.19}$$

where ε is the porosity of the GDL, D is the gas diffusivity, τ is the tortuosity of the GDL pores, and t_{gdl} is the thickness of the GDL.

With many sets of operating conditions, especially with the low flow rates and temperatures that have been studied in this work, a significant amount of liquid water forms at the cathode (water can also condense at the anode, but to a much smaller degree). This affects the operation of the fuel cell by creating a higher mass transfer resistance for the oxygen to reach the catalyst layer from the flow channel. The results in the previous chapter showed that it is the liquid water in the flow channels that blocks the pore openings from the gas flow and hurts the fuel cell performance. Liquid water is

only found inside the largest pores where it is easiest for the water to overcome the hydrophobic surface energy of the GDL material; most of the pores are still open for gas flow. Prior to this work, the most common view was that liquid water formed by capillary condensation in the pores, so that as more liquid formed, less pore space was open to the gas flow and the fuel cell performance was reduced. The latter effect is much easier to predict in a mathematical model. It is also what was believed when the model discussed here was developed in the Benziger and Kevrekidis groups. The effect was captured by the following modification to the calculation of k_O

$$k_O = \frac{k_O^{\max}}{1 + \frac{n_{w,liq}^{gdl}}{n_{w,\max}^{gdl}} \left(\frac{k_O^{\max} - k_O^{\min}}{k_O^{\min}} \right)} \tag{4.20}$$

Equation (4.20) is a scaling between the maximum value for the mass transfer, $k_O^{\max}$, when no liquid water is present (the number of moles of liquid water in the GDL, $n_{w,liq}^{gdl}$, is equal to zero) and the minimum value, $k_O^{\min}$, when the GDL pores are filled with liquid ($n_{w,liq}^{gdl} = n_{w,\max}^{gdl}$). For $k_O^{\max}$, the gas phase diffusivity of 0.2 $cm^2\ s^{-1}$ is used in equation (4.20) and for $k_O^{\min}$, the much lower liquid diffusivity of 2×10^{-5} $cm^2\ s^{-1}$ is used instead.

The decrease in k_O with liquid water buildup is shown in Figure 4.2. The largest effects are seen with the start of condensation as only a small layer of water is needed to dramatically reduce the mass transport. Although that small layer is predicted to be inside the pores, the effect is the same as if a small layer of liquid or a droplet was covering the opening of the pore at the surface. For this reason, the model still predicts some of the flooding behavior that was observed experimentally. The movement of liquid water in the flow channels and its removal from the fuel cell are not captured here

and impose limits for operating conditions that can be simulated. The simulation of liquid in the flow channels is beyond the scope of this work, but is the subject of continuing research in the Benziger and Kevrekidis groups.

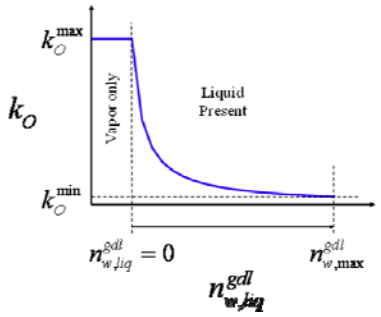

Figure 4.2 Change in k_O with increasing liquid water in the cathode GDL. The largest effects are when liquid first starts to condense. Only a small amount of water is needed to create a much higher mass transfer resistance.

In order to close the model, the activity in the gas phase at low temperatures and pressures can be calculated as the partial pressure over the total pressure. Equations (4.17) and (4.18) can then be substituted into equation (4.4) to give

$$V_b = \frac{-\Delta G^o}{4\mathfrak{F}} + \frac{RT}{4\mathfrak{F}} \ln\left[\frac{\left(P_H - \frac{i}{2\mathfrak{F}} \cdot \frac{1}{k_H A_{mem}}\right)^2 \left(P_O - \frac{i}{4\mathfrak{F}} \cdot \frac{1}{k_O A_{mem}}\right)}{\left(a_w^{gdl}\right)^2 \left(P_{tot}\right)^3}\right] \tag{4.21}$$

4.3 "Tanks-in-series" extension

The above equations of the STR model simulate the dynamic operation of a one-dimensional PEM fuel cell while predicting multiple steady-states and effects of flooding. The results from the model[21] fit well with experimental data from the STR fuel cell described in section 1.5 and allowed for the calculation of several parameters of the

model. To make the model more applicable to the usually much larger systems employing long and narrow flow channels, the model was extended to the "tanks-in-series" (TIS) model. The concept was taken from analogy with traditional chemical reactor engineering, where a plug flow reactor can be modeled as several stirred tank reactors in series. The equations described in section 4.2 were solved for each element of the fuel cell, or "tank". A tank was defined by the length of flow channel for which diffusive mixing was faster than the residence time of the gas and the flow streams could be assumed to be homogeneous. The tanks were coupled in series through the flow streams and membrane water diffusion. Electrically, the tanks were connected in parallel. An additional coupling of lateral protonic currents through consecutive tanks was added based on observations from the SAPC fuel cell experiments.

4.3.1 Circuit representation

The anode segments of the SAPC fuel cell are electrically connected in parallel. This was incorporated into the model equations by modifying equation (4.7) to calculate the current from one tank as

$$i_{(j)} = \frac{V_{b(j)} - V_{d(j)} - V}{R_{mem(j)}} \tag{4.22}$$

where $V_{b(j)}$ and $V_{d(j)}$ are the same as in equations (4.21) and (4.6) with the local current, $i_{(j)}$, used in the calculations. V is the voltage measured across the external load and is calculated as

$$V = R_L \sum_{j=1}^{N} i_{(j)} \tag{4.23}$$

where N is the number of tanks in the model.

4.3.2 Mass balances

The mass balances are calculated separately for each tank. The activities, partial pressures, and water content in the GDL are calculated as before using the values for the specific tank, denoted by the subscript (j). The first coupling of the tanks is through the flow streams. The feed flow rates are used to calculate the moles entering the first tank on each side. For co-current flows, the inlets are to tank 1 on each side; for counter-current flows, the hydrogen inlet is at tank 1 and the oxygen inlet is at tank N. After the first tank, the calculated flow rate from the previous tank is used as the inlet flow rate to tank (j). This gives the following equations for the flow rates

$$F_{A(j)} = \left[F_{A(j-1)} \cdot \frac{P_{tot}}{RT} + k_{w,1} A_{mem} \left(a_{w(j)} - \frac{P_{w,A(j)}}{P_w^{sat}} \right) - \frac{i_{(j)}}{\mathfrak{F}} \left(k_{w(j)}^{eo} + 1/2 \right) \right] \cdot \frac{RT}{P_{tot}} \tag{4.24}$$

$$F_{C(j)} = \left[F_{C(j\pm1)} \cdot \frac{P_{tot}}{RT} + k_{w,2} A_{mem} \left(a_{w(j)}^{gdl} - \frac{P_{w,C(j)}}{P_w^{sat}} \right) - \frac{i_{(j)}}{4\mathfrak{F}} \right] \cdot \frac{RT}{P_{tot}} \tag{4.25}$$

where the index of the upstream tank is denoted by $(j-1)$ on both sides for co-current flows, and by $(j-1)$ on the anode side and $(j+1)$ on the cathode side for counter-current flows.

The second coupling of the tanks is through water diffusion in the membrane and changes the calculation of a_w to

$$\begin{aligned} & N_{SO_3} \frac{d\lambda}{da_{w(j)}} \frac{da_{w(j)}}{dt} = \\ & k_{w,3} A_{mem} \left(a_{w(j)}^{gdl} - a_{w(j)} \right) - k_{w,1} A_{mem} \left(a_{w(j)} - \frac{P_{w,A(j)}}{P_w^{sat}} \right) + \\ & k_{mem} A_{mem}^{trans} \left(a_{w(j-1)} - a_{w(j)} \right) - k_{mem} A_{mem}^{trans} \left(a_{w(j)} - a_{w(j+1)} \right) \end{aligned} \tag{4.26}$$

Equation (4.26) is equivalent to equation (4.13) with the addition of the last two terms on the RHS. The two terms account for water diffusion between consecutive tanks based on the membrane water activity gradient, the cross sectional area of the membrane, A_{mem}^{trans}, and the mass transfer coefficient, k_{mem}. A value of 5×10^{-5} mol s^{-1} cm^{-2} is used for k_{mem}, resulting from ex-situ experiments of water permeation through Nafion.

4.3.3 Lateral currents

The equations in the previous sections were developed previously in the Benziger and Kevrekidis groups, primarily by E. Joanne Chia.[12] The model predicted much of the physics that were observed experimentally, such as multiple steady-states and hydration front propagation, but did not capture the dramatic changes in the current distribution that were observed in the more recent experiments. The first example of this was with experiments studying extinction fronts along the flow channel. As described in Chapter 2, when the local currents began to drop off at the feed inlets with the drying of the membrane, the local currents towards the outlets, where the membrane was still well-hydrated, increased dramatically. These currents reached a peak before dropping off as the extinction front propagated to the end of the channel. The total voltage of the fuel cell remained nearly constant until the last segment began to extinguish.

Another example of the current redistribution was with changes in the flow rates between starved conditions and excess reactants. When the reactants were fed to the fuel cell at a level such that they were completely consumed, the currents were lower near the outlets where the flow of reactants was near zero. With an increase in flows, the currents from the segments near the outlets increased, as expected. But at the same time, the

currents from the segments near the inlets decreased. The changes were almost instantaneous with the flow increase and so were not due to changes in water content in the membrane. The inverse was also observed; a decrease in flows from excess reactants to starved conditions caused the expected decrease in the currents towards the outlets, but then also an increase from the currents closer to the inlets. When decreasing the flow rates, the response of the currents was more gradual, due to the flow channels and outlet tubes acting as small reactant reservoirs.

These experimental observations from the SAPC fuel cell indicated the presence of lateral currents between segments of the fuel cell. The hydrogen oxidation reaction is driven by a difference in chemical potential of hydrogen across some finite resistance. In a fuel cell, the largest difference is across the membrane, leading to the expression for the fuel cell voltage in equation (4.1). A secondary resistance exists, though, through the catalyst layer and GDL. A diagram of the resistances to proton conduction between the different areas of the fuel cell is shown in Figure 4.3 as they were captured in the model.

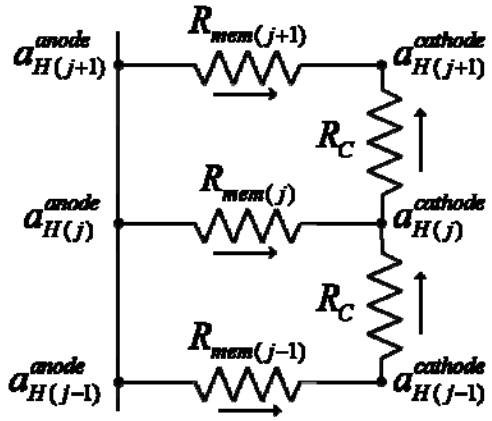

Figure 4.3 Diagram of resistances to proton conduction in the TIS model. Lateral currents between tanks at the cathode were added to better predict phenomena seen in experiments.

The arrows show the direction of positive protonic current defined in the model. The lateral resistance at the anode is not shown because it was not incorporated into the model. The lateral currents were first added at the anode to match the design of the SAPC fuel cell, but the calculated magnitudes of the lateral currents at the cathode were much larger, even with the same value for the lateral resistance on both sides. The addition of lateral currents at the anode did not change the simulation results for the parameter set matching the SAPC fuel cell setup. This indicated that effects at the anode were captured through activity gradients at the cathode and were not included for simplicity. The higher gradients in water activity, accumulation of liquid water, and lower flow rates at the cathode contributed to higher hydrogen activity gradients at the cathode versus the anode. Conditions causing the hydrogen activity gradients to be higher at the anode could make lateral currents at the anode more significant, but this was not observed for the parameter space investigated in the work presented here.

The finite protonic resistance of the GDL/catalyst layer creates lateral potential gradients that can also drive the hydrogen oxidation reaction. The liberation of 2 electrons for each molecule of hydrogen that is oxidized leads to the following expression for the lateral protonic current between adjacent segments,

$$i_{C(j)} = \frac{RT}{2\mathcal{F}} \ln\left(\frac{a_{H(j+1)}^{cathode}}{a_{H(j)}^{cathode}}\right) \cdot \frac{1}{R_C} \tag{4.27}$$

where an ohmic relation ($V_C = i_C R_C$) has been assumed to relate the potential from the activity gradient to the resulting current. The variable R_C is the protonic resistance through the GDL and catalyst layer. The activity of hydrogen at the catalyst is determined by the potential across the membrane as well as the lateral potentials. The

gradient in hydrogen activity across the GDL (calculated in terms of partial pressures) is balanced by the conduction of protons away from the catalyst. Using conservation of mass (also essentially Kirchhoff's Junction Rule), the total protonic current at a given segment is calculated as

$$i_{H(j)} = i_{C(j)} - i_{C(j+1)} - i_{(j)} \tag{4.28}$$

The value of $i_{H(j)}$ is then used in determining the partial pressure of oxygen at the cathode catalyst layer. The final set of equations is given at the end of this section.

The value for the lateral resistivity of the GDL/catalyst layer was taken from the literature [22, 23] to be about 100 Ω-cm at fully hydrated conditions. This value is an order of magnitude larger than the resistivity of a membrane equilibrated at a water activity of 1, about 10 Ω-cm. If the lateral transport is though the catalyst layer, it would be expected that the lateral resistivity would be higher than the transverse resistivity as the Nafion is impregnated between the catalyst particles. If lateral transport can also occur through the bulk membrane, differences in the structure of the membrane in the lateral and transverse directions could have an effect. It is not clear whether the lateral protonic currents flow through the catalyst layer or through the membrane at the interface. Experiments specifically designed to measure the lateral currents are needed to give a better understanding. Still, using the value of 100 Ω-cm for the resistivity allowed for the model predictions to fit well with experimental data. The value may change with hydration of the fuel cell, but was assumed to be constant in the TIS model.

The lateral currents are driven through the resistance when the difference in hydrogen activity between two parts of the fuel cell becomes comparable to the activity

gradient across the membrane. This can occur for a couple different reasons, diagramed in Figure 4.4.

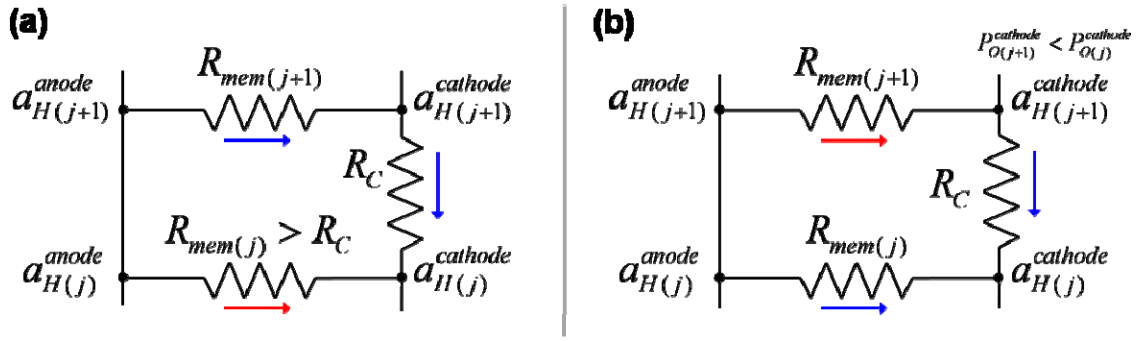

Figure 4.4 Circuit diagrams showing the redistribution of the currents. **(a)** Increased resistance of the membrane at tank *(j)* decreases the current across the membrane and the hydrogen activity at the cathode of *(j)*. The lateral current from tank *(j+1)* to tank *(j)* is increased and increases the current across the membrane at tank *(j+1)*. **(b)** Decreased oxygen activity at tank *(j+1)* increases the hydrogen activity at *(j+1)*. The lateral current from *(j+1)* to *(j)* is increased, more water is formed, the membrane at *(j)* becomes more hydrated, and more current flows across the membrane at *(j)*.

The first is when an area of the membrane begins to dry out, shown as tank *(j)* in part (a). The resistance across the membrane increases so that it becomes more favorable for the protons to flow through a more hydrated part of the membrane and then laterally across the cathode. The red arrow in the diagram shows where the current decreases with the drying of the membrane, across the membrane of tank *(j)*. The activity of hydrogen at the cathode, $a^{cathode}_{H(j)}$, is decreased and drives lateral currents from adjacent areas of the fuel cell, indicated by the blue arrow from $a^{cathode}_{H(j+1)}$ to $a^{cathode}_{H(j)}$. The activity, $a^{cathode}_{H(j+1)}$, is decreased and drives a higher current across the membrane at tank *(j+1)*, indicated by the blue arrow from $a^{anode}_{H(j+1)}$ to $a^{cathode}_{H(j+1)}$. The current measured at tank *(j)* decreases while the current at tank *(j+1)* increases, as observed experimentally.

Starvation of reactants, either by high reactant utilization or liquid water blockage, also induces lateral currents, as diagrammed in part (b) of Figure 4.4. If oxygen is starved at the cathode, shown at tank *(j+1)* in the diagram, protons transported across the membrane do not react and the hydrogen activity, $a_{H(j+1)}^{cathode}$, increases. Lateral currents flow, as indicated by the blue arrow from $a_{H(j+1)}^{cathode}$ to $a_{H(j)}^{cathode}$. The increased activity of hydrogen at tank *(j)* decreases the activity of oxygen but also increases the activity of water. The membrane becomes more hydrated, $R_{mem(j)}$ decreases, and the current measured at tank *(j)* increases. Starvation of hydrogen in the anode flow channel has a similar effect. More hydrogen will react upstream where the fuel is plentiful; lateral currents will flow downstream to areas where the hydrogen activity is decreased by the starvation. Accounting for these effects was found to be significant in the simulations, discussed in Section 4.4.

4.3.4 Final TIS Model with lateral currents

Equations (4.29) and (4.30) describe the change in the membrane water activity and moles of water in the cathode GDL, respectively, with time,

$$N_{SO_3}\frac{d\lambda}{da_{w(j)}}\frac{da_{w(j)}}{dt} = k_{w,3}A_{mem}\left(a_{w(j)}^{gdl}-a_{w(j)}\right)-k_{w,1}A_{mem}\left(a_{w(j)}-\frac{P_{w,A(j)}}{P_w^{sat}}\right)+ k_{mem}A_{mem}^{trans}\left(a_{w(j-1)}-a_{w(j)}\right)-k_{mem}A_{mem}^{trans}\left(a_{w(j)}-a_{w(j+1)}\right) \quad (4.29)$$

$$\frac{dn_{w(j)}^{gdl}}{dt} = k_{w,3}A_{mem}\left(a_{w(j)}^{gdl}-a_{w(j)}\right)-k_{w,2}A_{mem}\left(a_{w(j)}^{gdl}-\frac{P_{w,C(j)}}{P_w^{sat}}\right)+\frac{i_{(j)}}{\mathcal{F}}\left(k_{w(j)}^{eo}+1/2\right) \quad (4.30)$$

Equations (4.31) and (4.32) describe the change in the partial pressure of hydrogen in the anode flow channel and oxygen in the cathode flow channel, respectively, with time,

$$\frac{dP_{H(j)}}{dt} = \left[F_{A(j-1)} \cdot \frac{P_{H(j-1)}}{RT} - F_{A(j)} \cdot \frac{P_{H(j)}}{RT} - \frac{i_{(j)}}{2\mathfrak{F}} \right] \frac{RT}{V_A^{gas}} \tag{4.31}$$

$$\frac{dP_{O(j)}}{dt} = \left[F_{C(j\pm1)} \cdot \frac{P_{O(j\pm1)}}{RT} - F_{C(j)} \cdot \frac{P_{O(j)}}{RT} - \frac{i_{H(j)}}{4\mathfrak{F}} \right] \frac{RT}{V_C^{gas}} \tag{4.32}$$

Equations (4.33) and (4.34) give the total flow rates in the anode and cathode flow channels, respectively,

$$F_{A(j)} = \left[F_{A(j-1)} \cdot \frac{P_{tot}}{RT} + k_{w,1} A_{mem} \left(a_{w(j)} - \frac{P_{w,A(j)}}{P_w^{sat}} \right) - \frac{i_{(j)}}{\mathfrak{F}} \left(k_{w(j)}^{eo} + 1/2 \right) \right] \cdot \frac{RT}{P_{tot}} \tag{4.33}$$

$$F_{C(j)} = \left[F_{C(j\pm1)} \cdot \frac{P_{tot}}{RT} + k_{w,2} A_{mem} \left(a_{w(j)}^{gdl} - \frac{P_{w,C(j)}}{P_w^{sat}} \right) - \frac{i_{H(j)}}{4\mathfrak{F}} \right] \cdot \frac{RT}{P_{tot}} \tag{4.34}$$

Equations (4.35) – (4.38) describe the currents and voltages of the system,

$$V_{b(j)} = \frac{-\Delta G^o}{4\mathfrak{F}} + \frac{RT}{4\mathfrak{F}} \ln \left[\frac{\left(P_{H(j)} - \frac{i_{(j)}}{2\mathfrak{F}} \cdot \frac{1}{k_H A_{mem}} \right)^2 \left(P_{O(j)} - \frac{i_{H(j)}}{4\mathfrak{F}} \cdot \frac{1}{k_{O(j)} A_{mem}} \right)}{\left(a_{w(j)}^{gdl} \right)^2 \left(P_{tot} \right)^3} \right] \tag{4.35}$$

$$V_{d(j)} = V_T \ln \left(\frac{i_{(j)}}{I_o} + 1 \right) \tag{4.36}$$

$$i_{(j)} = \frac{V_{b(j)} - V_{d(j)} - V}{R_{mem(j)}} \tag{4.37}$$

$$V = R_L \sum_{j=1}^{N} i_{(j)} \tag{4.38}$$

4.4 Simulation results

The SAPC fuel cell was constructed for the purpose of studying the dynamics of the current distribution along the flow channel for both wet and dry conditions. The dimensions of the flow channel were about 2 – 3 times larger than what is commonly seen in commercial systems and the small active area allowed for low flow rates. Each segment could be modeled as one "tank" based on the criteria discussed above: that the diffusive mixing was substantial over the length of one segment (1/4" for the SAPC fuel cell). Much of the interesting results from the SAPC fuel cell were due to the transport of liquid water to and through the flow channels. These effects are not currently captured with the TIS model, but there are still many comparisons that can be made between simulation results and experimental data from the SAPC fuel cell.

4.4.1 Ignition

Simulating the operation of a fuel cell is especially useful when considering start-up conditions. The very basic equations for water removal and water production at steady-state predicted multiple steady states. The full set of equations that make up the dynamic TIS model are able to predict how the current evolves from an initial condition to either an ignited to extinguished steady-state along a flow channel. Differences in the fuel cell ignition with different operating parameters and initial conditions can be compared.

The first comparison here is between co-current and counter-current flows, as shown in Figure 4.5. The set of operating parameters—flow rates = 12/6 ml min^{-1} H_2/O_2, load resistance = 2.5 Ω, temperature = 343 K—allowed the fuel cell to ignite, but flooding did not occur. Starting from dry conditions (initial membrane water activity of

0.005), the current distribution evolves differently between the two flow patterns although the total current at steady-state only changes by 1.5 %. Based on experimental observations, such as that shown in Figure 2.8, the sharper ignition at tank 1 and peaks at tanks 1 and 6 with co-current flows should not be predicted. This was due to the assumption of a constant resistance to lateral currents at the cathode. The membrane was very dry initially and the transverse resistance was much higher than the value of 100 Ω used for the lateral resistance. The simulation predicted lateral currents to flow from tank 1 to tank 2, creating a higher activity gradient and over-predicting the current across the membrane at tank 1. Lateral currents were also predicted to flow from tank 6 to tank 5 as the membrane was hydrated more quickly at tank 6 due to the convection of water in the flow streams (refer to Figure 4.4(a)).

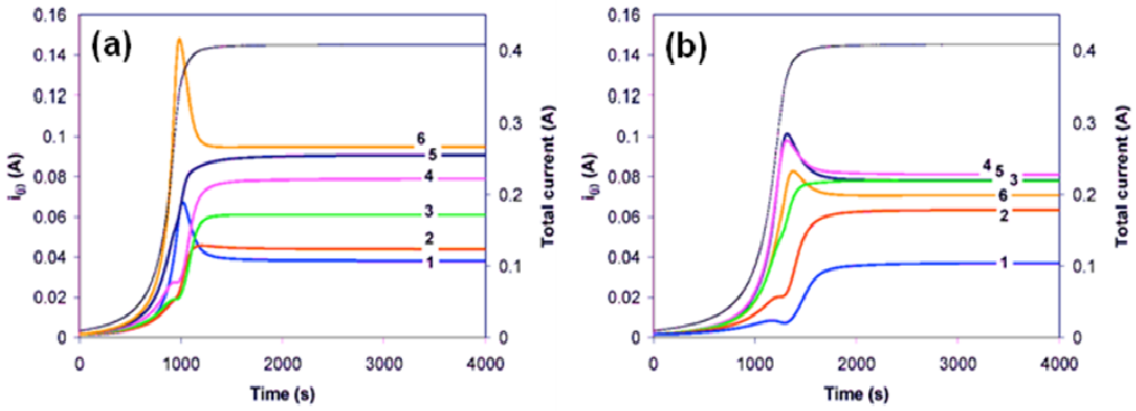

Figure 4.5 TIS simulation of startup from dry conditions (initial membrane water activity of 0.005). The simulated currents from the six tanks are shown with the oxygen inlet upstream of tank 1. **(a)** Ignition with co-current flows (hydrogen inlet also upstream of tank 1). The convection of water from the inlets to the outlets at both the anode and cathode cause the currents to ignite after ~800 s with significantly higher currents towards the outlets. **(b)** Ignition with counter-current flows (hydrogen inlet upstream of tank 6). The convection of water in opposite directions at the anode and cathode causes the currents to ignite more gradually after ~1200 s, but be more uniform and higher at the middle tanks. Model parameters: F_A/F_C = 12/6 ml min^{-1}, R_L = 2.5 Ω, T = 343 K.

The final current distribution in Figure 4.5(a) was as expected. With dry feeds, as in both the simulations and experiments, the membrane is driest at the inlets and increases in water activity down the flow channel. With no effects from flooding, the currents are lowest at the inlets and highest closer to the outlets. As discussed in Chapter 2, the time for ignition is difficult to compare with experiments as the initial water content of the membrane cannot be controlled precisely in a fuel cell.

The ignition with counter-current flows shown in Figure 4.5(b) occurs on a similar time scale as with co-current flows, but is much more uniform across the different tanks. The tanks ignite in the middle of the channel first, with ignition fronts propagating quickly towards the hydrogen inlet at tank 6 and slower towards the oxygen inlet at tank 1, consistent with experimental data. With experiments, the part of the fuel cell closer to the hydrogen inlet ignited much later than the part near the oxygen inlet (see Figure 2.8(b)). The delay was due to the time for the transport of water across the membrane from the cathode to the anode. The segment would not ignite until the full thickness of the membrane was sufficiently hydrated. This was not captured in the simulations as the membrane was assumed to have a uniform water activity. Recent experimental data investigating the permeation of water through the membrane could be used to predict the water activity gradient across the membrane, but this has not been incorporated into the work discussed here.

Changing the temperature, load resistance, and flow rates all have an effect on the time scales for ignition and final current distribution. The choice of flow pattern changes the effects of each parameter. Figure 4.6 shows how the currents change with different load resistances. Part (a) shows the ignition of the total current for both co-current (blue)

and counter-current (orange) flows and for three different load resistances—2.5, 5, and 10 Ω. As expected, the lower load resistances allow the current to ignite faster; more water is produced by the higher current and feeds into the positive feedback loop with the membrane hydration faster. The differences between co- and counter-current flows are small, being only slightly more pronounced at the lower load. Part (b) shows the steady-state "current profiles," or the fraction of the total current from each tank along the flow channel.

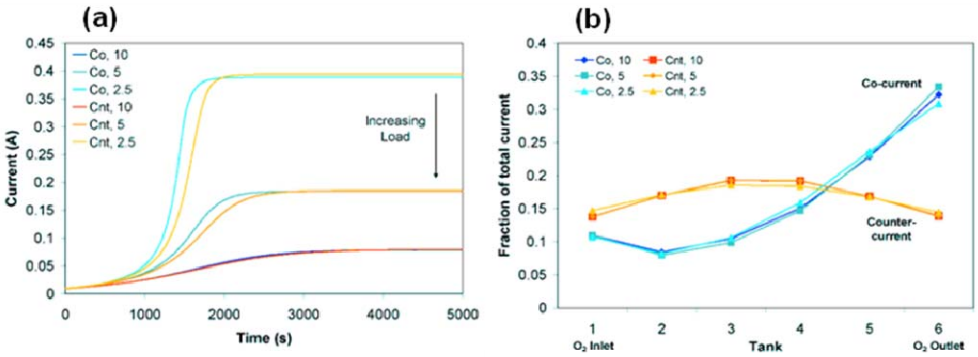

Figure 4.6 Effect of changing load resistance on ignition. **(a)** The change in ignition dynamics with changing load resistance for both co-current ("co") and counter-current flows ("cnt"). As the load is increased, the current and water production is decreased. The ignition is more gradual and the difference between co-current and counter-current flows is decreased with increasing load. **(b)** Steady-state current profiles after ignition for varying load resistance and both flow patterns. The total current decreases with increasing load, but the distribution of the current along the flow channel is unaffected. No flooding or drying occurs with these conditions. Constant model parameters: F_A/F_C = 12/6 ml min^{-1}, T = 358 K.

For each of the load resistances shown, the current ignites and the fuel cell does not flood. The profiles do not change significantly between the different loads, but show the significance of the choice of flow pattern. With co-current flows, the profile increases from the inlets to the outlets as more water is convected downstream. The profile is highest at the middle tanks for counter-current flows as water is convected from tank 1 to 6 on the cathode side and tank 6 to 1 on the anode side. Changing the load

affects each tank in the same way; the flows and temperature are unchanged, so that the importance of convection and flow pattern remain constant.

Changing the flow rates shows more of the differences between co-current and counter-current flows, as in Figure 4.7. The total current vs. time curves are given in part (a) for both co-current (blue) and counter-current (orange) flows and for oxygen flow rates ranging from 3 to 12 ml/min (stoichiometric ratio of H_2:O_2 held constant at 2 and flows always in excess). The simulations show increasing differences between the different flow patterns with increasing flows. For both flow patterns, with higher flow rates, the fuel cell takes longer to ignite; the convection of water out of the cell is increased so that the water uptake by the membrane is more gradual. The effect is more pronounced for counter-current flows than with co-current flows. The activity gradients that drive the transport of water into the flow streams are higher on average with counter-current flows and a dry stream at each end of the flow channel. For very high flow rates, the fuel cell extinguishes with both flow patterns.

Although the fuel cell takes longer to ignite with counter-current flows, part (b) of Figure 4.7 shows that counter-current flows may still be the better choice for fuel cell operation. With co-current flows, the increase in current from the inlets to the outlets becomes steeper with higher flows, but then at lower flows, the fuel cell begins to flood, causing the current to drop off at the outlets and redistribute back up the channel. The possible benefits of counter-current flows are seen with the much flatter profile curves, indicating a much more uniform current distribution. With the higher flows, the current near the oxygen inlet decreases while the current near the hydrogen inlet increases slightly. The uniformity of the current distribution is decreased from the moderate flow

rates, but is still much flatter than any of the curves with co-current flows. With the lower flow rates and counter-current flows, the current distribution is even more uniform. The more even transport of water along the flow channel has a second advantage in that flooding does not occur with flows of 6/3 ml min^{-1} H_2/O_2, as it did with co-current flows. Further decreasing the flow rates would cause flooding with counter-current flows and the currents would drop off where liquid water began to accumulate, but the range of flow rates where flooding does not occur is larger with counter-current flows than with co-current flows.

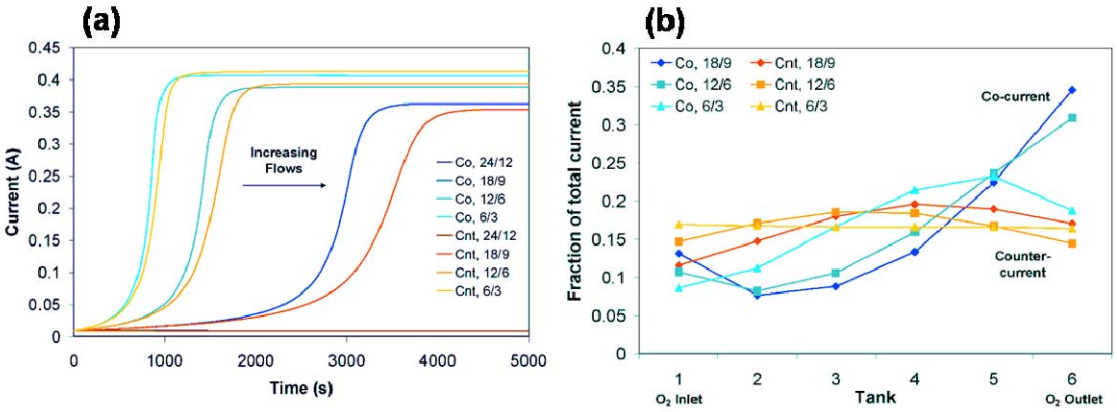

Figure 4.7 Effect of changing flow rates on ignition. The data series are labeled with the flow pattern ("co" for co-current and "cnt" for counter-current flows) and the flow rates of the reactants in ml min^{-1} (H_2/O_2). **(a)** The change in ignition dynamics with changing flow rates for both co-current and counter-current flows. The time for ignition is greater for higher flow rates, with the effect amplified with counter-current flows. **(b)** Steady-state current profiles after ignition for varying flow rates and both flow patterns. With co-current flows, flooding occurs at the lowest flow rates, causing the current at tank 6 to be lower. The currents increase more towards the outlets with higher flows until the entire fuel cell extinguishes. With counter-current flows, the currents are very uniform with the lower flows. The currents increase at the middle tanks and decrease at the oxygen inlet with higher flows until the fuel cell extinguishes. Constant model parameters: $R_L = 2.5\ \Omega$, $T = 358$ K.

Increasing the temperature has a similar effect to increasing the flow rates, as shown in Figure 4.8; the saturation vapor pressure of water increases with increasing temperature and causes convection to become more important. As with the previous two figures, the ignition of the total current is shown in part (a) for both co-current (blue) and

counter-current (orange) flows for a range of temperatures from 338 to 378 K. At the lower temperatures, very little difference is seen in the time for ignition for the two flow patterns. The decreased convection of water through the flow streams removes less water, allowing the fuel cell to ignite quickly, and lessens the effect of the choice of flow pattern. At higher temperatures, the fuel cell ignites more slowly in general. A more dramatic effect is observed with counter-current flows for the same reasons as discussed above with increasing flow rates. At a temperature of 378 K (80ºC), the fuel cell extinguishes with both flow patterns. The saturation vapor pressure of water has an exponential dependence on temperature. The fuel cell operation is the most sensitive to changes in temperature and times as long as ~8000 s are predicted for fuel cell ignition.

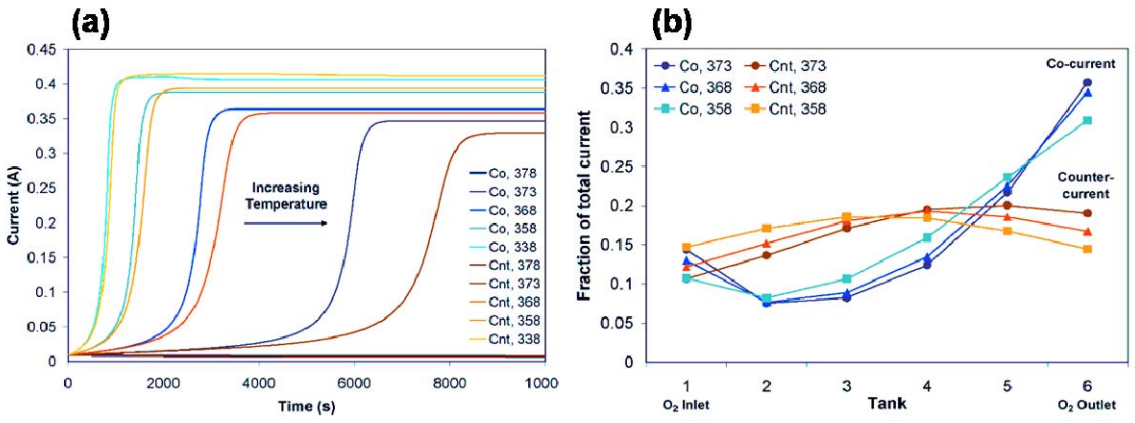

Figure 4.8 Effect of changing temperature on ignition. The data series are labeled with the flow pattern ("co" for co-current and "cnt" for counter-current flows) and the flow rates of the reactants in ml min^{-1} (H_2/O_2). **(a)** The change in ignition dynamics with changing temperature for both co-current and counter-current flows. As the temperature is increased, the water saturation vapor pressure is increased and more water is convected through the flow streams and removed from the fuel cell. The time for ignition is greater for higher temperatures, with the effect amplified with counter-current flows. **(b)** Steady-state current profiles after ignition for varying temperatures and both flow patterns. With co-current flows, the increase in the currents from the inlets to the outlets becomes steeper with increasing temperature until the fuel cell extinguishes. With counter-current flows, the currents decrease at the oxygen inlet and increase at the hydrogen inlet until the fuel cell extinguishes. No flooding occurs in the cases shown in part (b). Constant model parameters: F_A/F_C = 12/6 ml min^{-1}, R_L = 2.5 Ω.

The changes in the current distribution profiles with increasing temperature, shown in part (b), are also similar to how the profiles changed with increasing flow rates. With co-current flows, the increase from the inlets to the outlets becomes very steep at higher temperatures before the fuel cell extinguishes (profile not shown for a temperature of 378 K). With counter-current flows and increasing temperature, the current decreases at the oxygen inlet and increases at the hydrogen inlet. More water is evaporated into the cathode flow stream than the anode flow stream so that, for dry conditions, the convection from the oxygen inlet to the oxygen outlet is the most important for determining the current distribution. At the lower temperature of 338 K, the fuel cell floods with both flow patterns. Flooding is discussed in more detail in a later section; the profile curves for T = 338 K are not shown in part (b) for visual clarity.

4.4.2 Extinction

In the previous section, simulation results were shown for cases starting from a dry initial condition with the currents either igniting or decreasing to the extinguished steady-state. It may also be the case that the fuel cell is started from a well hydrated state or running at the ignited state and then a change in one or more of the operating parameters causes the water removal to become greater than the water production. An extinction front propagates along the flow channel as the membrane of each tank dries out and the currents fall to the low current extinguished steady-state. In the experiments with the SAPC fuel cell, the temperature was increased to 80 ºC and the load was increased to between 5 and 20 Ω (see Chapter 2). Experiments were conducted with both co-current and counter-current flows. Changing the load changed the time for the fuel cell to become completely extinguished or caused only part of the fuel cell to extinguish.

Simulating the extinction of the fuel cell matched well with experimental observations for both co-current and counter-current flows. For conciseness, only one example from the simulations is shown here

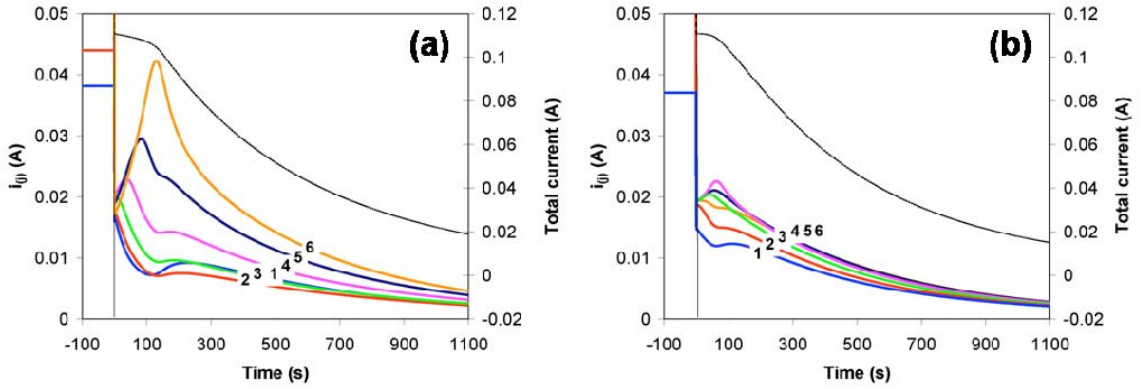

Figure 4.9 Extinction front propagation with an increase in load resistance from 2.5 to 10 Ω and an increase in temperature from 343 to 393 K. **(a)** Co-current flows. The fuel cell extinguishes at the inlets first. The currents at the outlets first increase then also decrease. **(b)** Counter-current flows. The fuel cell extinguishes at the oxygen inlet, then at the hydrogen inlet, and then in the middle of the flow channels. The currents in the middle of the channel increase only slightly then also decrease. Other model parameters: F_A/F_C = 12/6 ml min^{-1}, O_2 inlet at tank 1

The initial condition was set from the steady-state values after ignition with the set of parameters used to generate Figure 4.5 (flow rates = 12/6 ml min^{-1} H_2/O_2, load resistance = 2.5 Ω, temperature = 343 K). Figure 4.9 shows how the fuel cell extinguishes after an increase in the load resistance to 10 Ω and an increase in temperature to 393 K (all other parameters held constant) with both co-current (part (a)) and counter-current (part (b)) flows. With the moderate load and flow rates, the high temperature was required to cause the fuel cell to extinguish. With co-current flows, the results of the simulations were similar to experimental observations in the propagation of the extinction front from the inlets to the outlets. The feeds were driest and evaporated the most water at tank 1. The tanks then extinguished in order down the channel as less

water was produced and convected downstream. The same peaks in the currents near the outlets seen in experiments were predicted due to the lateral currents between the anodes of consecutive tanks (see Figure 4.4(a)). As the currents from tanks 1-3 drop off, the currents from tanks 5 and 6 increase dramatically by as much as 100%.

Inconsistencies between the simulations and experiments are seen in the time scales over which the extinction front starts and propagates along the channel. In the experiments, the currents responded immediately to the change in load, but did not start to drop off for about 1000 s; the simulations show an almost immediate initiation of the extinction front with the changes in load and temperature. At least part of the reason for the delay in the experimental data is the gradual increase in temperature. The temperature set-point was changed at time $t = 0$, but the fuel cell took about 1000 s to heat up completely. Errors in the time scales could also be the result of the values for the mass transfer coefficients that determine how quickly water is transported between the different layers of the fuel cell in the calculations. Also not captured in the simulations are the very sharp drops in the currents closer to the inlets and the negative currents at the middle of the channel.

The issue of accurately choosing the values for the mass transfer coefficients is seen more clearly in the results with counter-current flows, shown in part (b) of Figure 4.9. In experiments (see Figure 2.14), the extinction front starts at segment 6, closest to the hydrogen inlet, and propagates down the channel so that segment 1, at the oxygen inlet, extinguishes last. This was expected, as the hydrogen flow was always twice as high as the oxygen flow and the membrane was driest at the anode side. The simulations predict a much different pattern with the tanks closest to the oxygen inlet, 1 and 2,

extinguishing first followed by tank 6 at the hydrogen inlet, and finally tanks 3, 4, and 5. The difference in the front propagation between the simulations and experiments indicates an under-prediction of the transport of water on the anode side. An increase in the value for the mass transfer coefficient for the transport of water between the membrane and anode flow channel, $k_{w,1}$, increases the importance of water convection on the anode side. This would have the simulation predict the single extinction front starting at the hydrogen inlet seen in experiments and is discussed further in a later section. Even with the significant differences with counter-current flows, the comparison between the results with the two different flow patterns does show similarities with experiments. The magnitude of the peaks in the currents at the last tanks to extinguish are much less with counter-current flows. The fuel cell extinguishes more evenly with counter-current flows compared to the steeper drop offs with co-current flows.

4.4.3 Parametric studies

The difference in the times required for extinction between co-current and counter-current flows suggest conditions for which the fuel cell will extinguish with counter-current but not with co-current flows. This can easily be studied with the simulations to map out parameter spaces for which the fuel cell will extinguish from a high current state or ignite from a dry state. Figure 4.10 shows a mapping of these conditions with varying flow rates and temperature at a constant load resistance of 2.5 Ω. The first two curves from the left show the critical temperature for ignition from dry conditions (initial membrane water activity of 0.005) as a function of flow rate for co-current flows (light blue) and counter-current flows (orange). Ignition was defined by the total current increasing to a value with an order of magnitude of 100 mA with each tank

current on the order of 10 – 100 mA. When the fuel cell did not ignite (below the critical temperature), the total current dropped below the initial total current of ~10 mA. Conditions where the fuel cell only partially ignited (high currents at only some of the tanks) were not found for the model parameters discussed here. Simulations with various initial conditions could lead to part ignited/part extinguished steady-states, as was observed experimentally, but the range of parameters would be very narrow. Also, the total currents were comparable between the two flow patterns, as discussed in Figures 4.6 – 4.8.

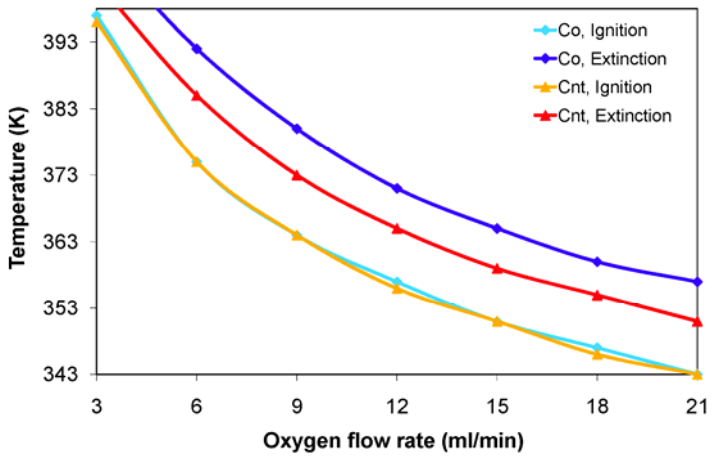

Figure 4.10 Parameter map for temperature and flow rates at a constant load of 2.5 Ω showing critical conditions for ignition and extinction with both co-current ("co") and counter-current flows ("cnt"). Simulations were done with the TIS model and a constant stoichiometric ratio of 2:1 was used for the H_2:O_2 flow rates. A hysteresis is observed between the results for ignition and extinction. The effect is more pronounced for co-current flows due to less convective mixing.

Below the ignition curves, the fuel cell will ignite; above the curves, the fuel cell extinguishes. As the flow rates are increased, the temperature must be lower to balance the increased convection by a decrease in water saturation vapor pressure. The curves for the two flow patterns are almost identical, with no more than a degree difference in the critical temperature at a given flow rate. This indicates that the critical state for ignition

is independent of flow pattern. The analysis from the STR fuel cell is applicable even with the flow channel; the initial water content and the diffusion of water within the cell are the important factors that lead to current ignition.

The two curves to the right show the critical temperature for extinction from an ignited steady-state versus flow rate, again for co-current (blue) and counter-current flows (red). Extinction was defined as the parameter value when each of the tank currents dropped below 2 mA to give a drop in the total current to less than 2% of the initial total current. Below the critical temperature for extinction, the fuel cell will continue to run at the ignited steady-state; above the critical temperature, the currents will drop off and the fuel cell will extinguish. A significant difference is seen between the two flow patterns; co-current flows allow for total currents about 5% higher and for operation at temperatures about 6 degrees higher than with counter-current flows. With co-current flows, the fuel cell acts more like a plug flow reactor during extinction; the rate of removal of water in the flow streams is the important factor, causing the extinction front instead of the back diffusion of water that allowed for the propagation of the ignition front. This results in a hysteresis so that the fuel cell can operate with a given set of flow rates and temperatures if already ignited, but will not reach the ignited state if starting from the dry state. The same hysteresis is seen with counter-current flows, but to a lesser degree. The counter-current flow pattern introduces some convective mixing into the system so that the characteristics are between those of a stirred-tank system and plug flow reactor during extinction.

Understanding when a fuel cell will ignite or extinguish is important for system design and control. The differences between co-current and counter-current flows are

significant when considering operating parameters, but also when considering the dynamic response of the system to a change in one or more of the parameters. This was shown in the previous two sections for both ignition and extinction front propagation. Counter-current flows caused the fuel cell to take longer to reach the final steady-state then with co-current flows. Another factor not shown in the parameter space in Figure 4.10 was the current distribution at a given set of operating parameters. Counter-current flows usually gave a more uniform distribution than co-current flows. The best choice for the flow pattern is a balance between the area of the parameter space allowing for operation, the dynamics of the front propagation, and the uniformity of the current distribution. Changes in the current distribution were very dramatic in several of the SAPC experiments and so were studied in more detail with the simulations, as discussed in the following section.

4.4.4 Current distribution

The current distribution can change dramatically with a change in an operating parameter. With the SAPC fuel cell, lateral protonic currents were observed to flow between segments of the fuel cell and could cause the current distribution to change dramatically on time scales on the order of seconds. Local reactant starvation caused by liquid water accumulation or decreased reactant feed created protonic currents from those segments towards areas of the fuel cell with sufficient reactant flow to the catalyst layer. Local drying of the membrane had a similar effect with currents from the more hydrated areas increasing and flowing laterally to the drier segments. In order to correctly predict the current distribution and fuel cell response, lateral protonic currents were added to the TIS model as an additional coupling between the cathodes of consecutive tanks, as

discussed in section 4.3.3. This allowed the model to more accurately predict some of the initially unexpected experimental observations from the SAPC fuel cell.

4.4.4.1 Change in flows

The first of these was the redistribution of the currents with a change in flow rates between excess and starved conditions. Figure 4.11 shows comparisons between experimental and simulation results for a flow increase (parts (a) and (b)) and a flow decrease (parts (c) and (d)). In the experiments, it was expected that an increase in flows from high utilization to supplying excess reactants would cause the increase in the currents from the segment closer to the outlets seen in Figure 4.11(a). Mass transfer limitations were heightened as most of the reactants were consumed at that point in the flow channel. However, at the same time, a decrease in currents from the segments close to the inlets is observed. The decrease in currents was caused by the lateral currents, as discussed with Figure 4.4(b). The time scales for the redistribution were fast enough that the change could not be attributed to changes in the water activity in the membrane.

Figure 4.11(b) shows the simulation results for an increase in flows. An initial decrease in the currents from tanks 1 and 2 coincides with increases at tanks 3 – 6. As the currents continue to increase closer to the outlets, those from the middle tanks level off and decrease. The final distribution is much narrower than with the lower flow rates. The currents are lower at the inlets where the membrane is drier and increase towards the outlets, similar to the experimental results in part (a).

The most significant difference between parts (a) and (b) of Figure 4.11 is the much slower rate of change predicted by the simulation versus the almost instantaneous redistribution seen in the experimental data. The model fails at very low reactant partial

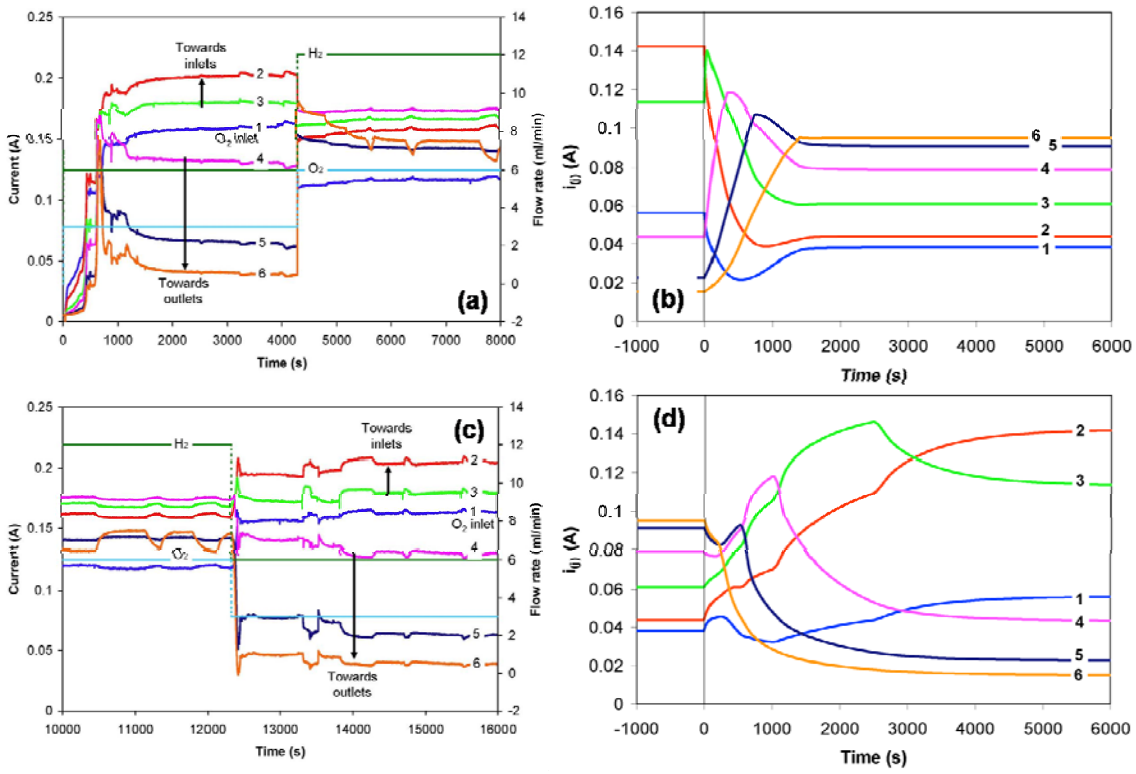

Figure 4.11 Changes in the segment/tank currents with changes in flows between excess and starved conditions. The segments and tanks are numbered 1 – 6; the flows are co-current with inlets always upstream of segment/tank 1. **(a)** Experimental results from the SAPC fuel cell. Flows increased from 6/3 to 12/6 ml min^{-1} H_2/O_2 at 4300 s. The currents redistribute immediately after the flow change. **(b)** Simulation results for a flow increase from 6/3 to 12/6 ml min^{-1} H_2/O_2 at 0 s. The currents redistribute over ~1500 s. **(c)** Experimental results for the flows decreased from 12/6 to 6/3 ml min^{-1} H_2/O_2 at 12300 s. The currents redistribute over the next ~150 s. **(d)** Simulation results for a flow decrease from 12/6 to 6/3 ml min^{-1} H_2/O_2 at 0 s. The currents redistribute quickly then change gradually over the next 3000 s as the fuel cell floods. Experimental parameters: $R_L = 0.5\ \Omega$, $T = 298$ K. Model parameters: $R_L = 2.5\ \Omega$, $T = 343$ K.

pressures, so that starvation conditions cannot be simulated to the degree that is accessible in experiments, where a vacuum can actually be created. In experiments, the increase in flows immediately increases the partial pressure of the reactants all along the flow channel and the currents respond quickly. In the simulations, the very low currents at the tanks near the outlets are the result of the model prediction of liquid water accumulation in the GDL. Liquid water is predicted to fill in the pores of the GDL on the cathode side as it condenses, increasing the mass transfer resistance for the reactants to

reach the catalyst layer. The result is a drop in the currents similar to that seen in experiments as the reactant partial pressure is reduced at the catalyst layer in both cases. With the simulation, the water must be driven out of the GDL by the increased flows before the currents respond, which occurs on a much longer time scale.

The results for decreasing flows, parts (c) and (d), show the same similarities and differences. The current distribution becomes much wider with the lower flow rates in both the experiment and simulation data. The currents near the outlets decrease, as expected, due to the decrease in reactant partial pressure. The currents near the inlets increase, initially unexpected, but due to the lateral currents at the cathode. The times for the currents to adjust are longer in both cases relative to those for the flow increase. In the experiment, this was due to a reservoir effect, as excess reactants were present in the outlet tubes and were consumed to some degree before the currents finished decreasing. In the simulation, the delay was due to the build-up of liquid water in the GDL. The different physics of the two different processes in parts (c) and (d), just as in parts (a) and (b), lead to a much longer time scale for the current redistribution predicted by the simulation versus what was observed experimentally.

4.4.4.2 Flooding

The experiments that were described in Chapter 3 clarified the mechanism of flooding. Flooding is the accumulation of liquid water in the flow channels that blocks the reactants from entering the GDL and reaching the catalyst layer. As the liquid water moved in the flow channels, by either shear force from the gas flow or gravity, the current distribution changed dramatically over time scales of only seconds. Modeling the movement of the liquid water is very difficult due to the different surfaces of the flow

channel and the changing flow rate with reactant consumption. This is the subject of continuing work in the Benziger and Kevrekidis groups. Although the TIS model incorrectly models flooding as the build-up of liquid water in the GDL, it is still useful for investigating how the current distribution can change when the mass transfer resistance to the flow of reactants is increased.

Figure 4.12 shows the change in the current distribution as the degree of flooding increases with decreasing temperature. Part (a) gives the results with co-current flows. At a temperature of 358 K, no flooding occurs and the currents increase from the inlets to the outlets with the convection of water in both flow streams. The currents from the tanks at the outlets start to decrease at temperatures of 348 and 338 as liquid water starts to build up. Further decreasing the temperature to 333 and then 328 K causes the currents at the outlets to drop off dramatically. Lateral currents are induced that cause the currents to increase towards the outlets and give the same peaks in the current profiles seen in experiments.

Part (b) of Figure 4.12 gives the results for counter-current flows. Most of the experiments done to study flooding in the SAPC fuel cell used co-current flows, but the model prediction of the current distribution is not what would be expected in an operating fuel cell. In the simulation, the water is convected towards the middle of the channel so that liquid water first condenses at tanks 3 and 4. The currents towards the ends of the flow channel increase and the product water continues to be convected towards the middle tanks and the profile curve has a parabolic shape. Treating the liquid water as contained in the GDL makes it unaffected by shear forces from the gas flows. This would not be expected in experiments, because the liquid water would be pushed through

the cathode-side GDL and into the flow channel. The oxygen flow would then push the liquid water along the flow channel towards the cathode outlet, where it would continue to accumulate and cause a decrease in the currents around segments 5 and 6, similar to part (a) of Figure 4.12. Liquid water has been observed to condense on the anode side in experiments, but the amount is much less than that on the cathode side; slugs do not form that could block the reactant flow.

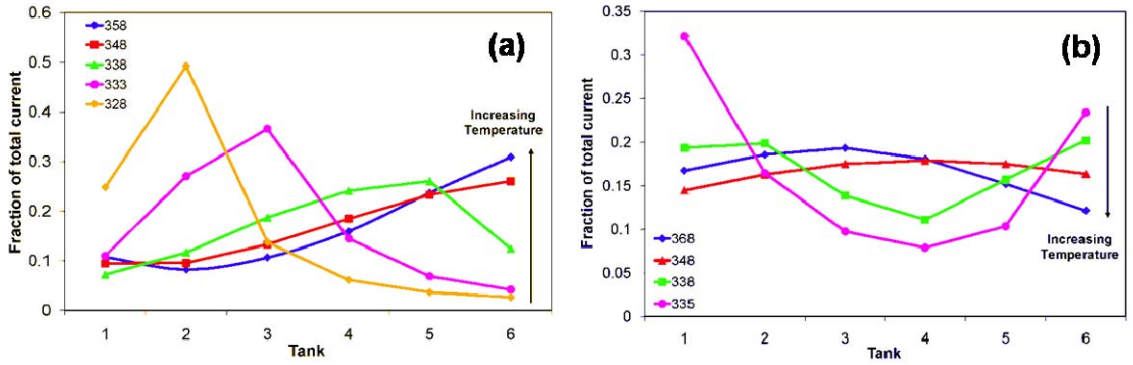

Figure 4.12 Change in current distribution caused by increased flooding with decreasing temperature. The series are labeled by the temperature (K); the oxygen inlet is upstream of tank 1 in both cases. **(a)** Results with co-current flows. Water builds up at the outlets first, causing the currents to decrease at the outlets and redistribute towards the outlets. At lower temperatures, more of the tanks closer to the outlets become flooded. **(b)** Results with counter-current flows. Water builds up in the middle of the channel, decreasing the currents and increasing the currents from the tanks at the ends of the channel. Constant model parameters: F_A/F_C = 12/6 ml min^{-1}; R_L = 2.5 Ω.

Even with the inaccuracy in the prediction of liquid water build-up, conditions where liquid water is or is not a large factor can still be compared. Figure 4.13 shows a good agreement between two experiments and simulations, based on the steady-state current distributions. The blue curves are for conditions that led to a large degree of flooding. In the experimental data, the fuel cell was in the orientation with the cathode facing up and the flow rates were reduced to a stoichiometry of about 1, both causing a large amount of liquid water build-up at the outlets, and resulting in the peak shape for

the distribution profile. For the simulation, the flow rates and load resistance were moderate, but the temperature was low. The tanks at the outlets flooded and the currents redistributed towards the inlets. The red curves are for conditions where liquid water was not a factor in the current distribution. For the experimental data, the fuel cell was rotated so that the flow channel was vertical with the inlets at the top. Gravity and the gas flow both helped remove liquid water so that it did not accumulate and cause significant flooding. The gas flows were also higher so that starvation effects were not a factor. For the simulation, the temperature was increased just high enough so that the amount of water in the GDL did not reach the saturation level that would cause liquid water to condense. At the same time, the temperature was not too high to cause drying of the membrane.

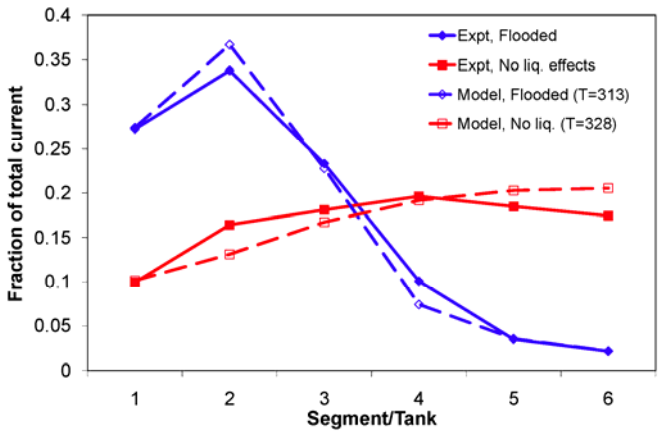

Figure 4.13 Comparison of the current profiles between experiments and simulations for conditions with a large degree of flooding (blue curves) and with minimized effects of liquid water (red curves). The flows are co-current with the inlets upstream of segment/tank 1 in every case. Experimental conditions: F_A/F_C = 6/3 ml min^{-1}, R_L = 0.5 Ω, T = 298 K, "cathode up" orientation for flooding and "inlets up" orientation for no flooding. Model parameters: F_A/F_C = 12/6 ml min^{-1}, R_L = 2.5 Ω, T = 313 K for flooding and T = 328 for no flooding.

One of the strengths of the TIS model is the reduced number of free parameters that must be fit to experimental data. The current distribution curves give one possibility for comparing experimental data and simulation results. The model is only semi-quantitative due to the difficulty in accurately determining several parameters and the necessity of making simplifying assumptions. The total currents are very different between the experiments and simulations due to the semi-quantitative nature of the model. The shapes of the current profiles are a better measure of the physics of the fuel cell operation and are in remarkably good agreement given no fitting parameters in the model.

4.4.4.3 Mass transfer coefficients

Several mass transfer coefficients are used in the model as lumped parameters describing the transport of reactants from the flow channel to the catalyst layer, the transport of water from the catalyst layer into the membrane, the transport of water into each of the flow channels, and the transport of water in the membrane between consecutive tanks. The values for the coefficients describing the gas flow are based on known diffusion coefficients and properties of the GDL, including the thickness, porosity, and tortuosity. The transport of water between the different layers of the fuel cell involved different phases and interfaces and was much more complex. First principles relations, like that of equation (4.19) could not be written. Instead, the values used in the model were derived from fits with the STR fuel cell data and were subject to the greatest uncertainty.[24]

The effect of uncertainty in the water transport coefficients is shown in Figure 4.14. Each of the coefficients describing water transport across the different interfaces

were both decreased and increased by an order of magnitude and the simulation was run from the same dry initial condition used before. The same base case of parameters was also used—flow rates of 12/6 ml min^{-1} H_2/O_2, a load resistance of 2.5 Ω, and a temperature of 358 K. No flooding occurred in any of the simulations; all of the changes were due to the changing balance between water production, diffusion, and removal. Only the results for changing the coefficients for the water transport into each of the flow channels are shown. Both increasing and decreasing the value of $k_{w,3}$, describing the transport of water from the cathode catalyst layer into the membrane, had very little effect on the final current distribution.

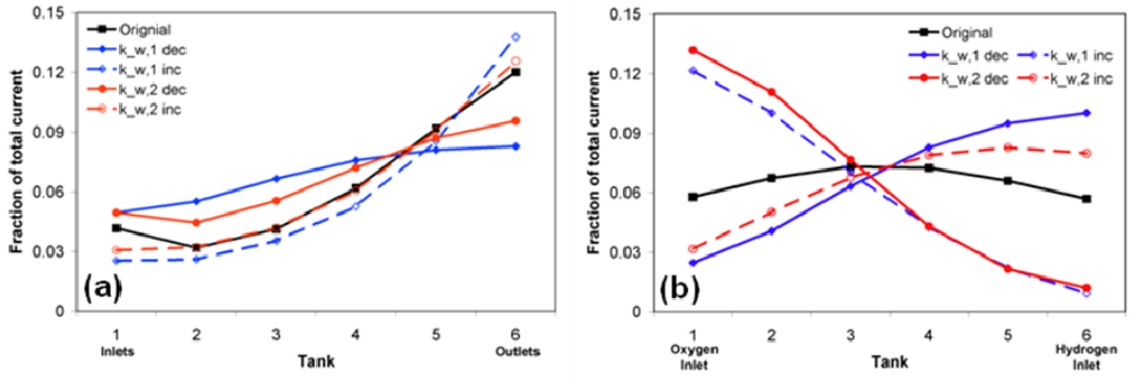

Figure 4.14 Effect of changing the values of the mass transfer coefficients for water transport into the anode flow channel, $k_{w,1}$, and into the cathode flow channel, $k_{w,2}$. The coefficients were either decreased by an order of magnitude ("dec"), decreasing the rate of transport into the flow channel, or increased by an order of magnitude ("inc"), increasing the rate of transport into the flow channel. **(a)** Results for co-current flows. Increasing either of the coefficients slightly increases the slope of the current profile curves. Decreasing the coefficients flattens out the profiles, indicating a more uniform current distribution. **(b)** Results with counter-current flows. Decreasing $k_{w,1}$ or increasing $k_{w,2}$ allows for more water in the cathode flow stream and the currents increase from the oxygen inlet to the hydrogen inlet. Increasing $k_{w,1}$ or decreasing $k_{w,2}$ allows for more water in the anode flow stream and the currents decrease from the oxygen to the hydrogen inlet. Original values: $k_{w,1} = 1.3\times10^{-6}$ mol s^{-1} cm^{-2}, $k_{w,2} = 1.3\times10^{-6}$ mol s^{-1} cm^{-2}. Model parameters: F_A/F_C = 12/6 ml min^{-1}, R_L = 2.5 Ω, T = 358 K.

Part (a) of Figure 4.14 shows the results with co-current flows for changing $k_{w,1}$, the coefficient for water transport from the membrane to the anode flow channel, and $k_{w,2}$, the coefficient for water transport from the cathode catalyst layer to the flow channel. Decreasing the coefficients by an order of magnitude makes the currents along the channel much more uniform. Not as much water evaporates into the flow streams, but instead diffuses through the membrane to even out the membrane water activities. The effect is more significant for the anode side coefficient due to the higher flow rate at the anode side. As expected, increasing the coefficients has the opposite effect, again with a more pronounced effect at the anode.

The effects of changing the mass transfer coefficients are more dramatic for counter-current flows, as shown in part (b) of Figure 4.14. Decreasing $k_{w,1}$ and increasing $k_{w,2}$ had similar effects; the convection of water on the cathode side is more important and the currents increase from the oxygen inlet to the oxygen outlet. Increasing $k_{w,1}$ and decreasing $k_{w,2}$ both make convection on the anode side more important and the currents decrease from the oxygen inlet to the oxygen outlet.

The large changes in Figure 4.14 show the sensitivity of the model predictions to different parameter values. Highly simplified experimental systems such as the STR and SAPC fuel cells are good tools for deducing values for model input. Experiments should be carefully designed to provide the right data to fit a certain parameter; fitting multiple parameters to a single polarization curve can easily lead to skewed conclusions.

4.5 Conclusions

The Stirred Tank Reactor and Tanks-in-Series models were developed previously in the Benziger and Kevrekidis groups. The SAPC fuel cell was designed and constructed to provide data that could be compared with simulations using the TIS model and offer further insights into the dynamics of fuel cell operation. The coupling of the tanks through lateral protonic currents at the cathode was added to better capture the physics observed with the SAPC fuel cell experiments. The TIS model was able to capture ignition and extinction fronts, the redistribution of the currents with changes in flows, and effects of flooding.

Several differences were observed between co-current and counter-current flows due to the convection of water through the flow streams. With co-current flows, the water is convected from tank 1, at the inlets, towards tank 6, at the outlets, on both the anode and cathode sides. With counter-current flows, the water is convected from tank 1 to tank 6 on the cathode side, but from tank 6 to tank 1 on the anode side. The resulting activity gradients driving water transport within the fuel cell caused the fuel cell to ignite faster under drier conditions (higher temperature, load resistance, or flow rates) with co-current flows than with counter-current flows. The steady-state current distributions were also very different between the two flow patterns. With co-current flows, the currents were lowest at the inlets and increased towards the outlets. Flooding occurred first at the outlets and caused the currents to redistribute back towards the inlets. With counter-current flows, the currents were highest at the middle of the channel and decreased towards each end. Flooding occurred at the middle first and caused the currents to increase at the ends so that the current distribution curve inverted in shape.

A significant difference was also observed between the two flow patterns for conditions that led to ignition and extinction. The operating conditions that allowed the fuel cell to ignite from dry conditions were almost identical for the two flow patterns, but a hysteresis was found for extinction from an ignited state. The ignition was initiated at the most hydrated part of the channel with the front propagation driven by back diffusion of water, without a large dependence on the flows. Extinction was different in that the fuel cell extinguished at the driest part along the flow channel; the front propagated as water was removed through the flow streams. The dependence on convection caused the fuel cell to extinguish for a narrower range of operating conditions with counter-current flows than with co-current flows.

Although the TIS model is only semi-quantitative, it was able to capture much of the physics observed from the SAPC fuel cell experiments. Good agreement was observed between the current profiles with conditions where liquid water accumulated and for conditions when it was not a significant factor. The physics of liquid water were not correctly incorporated in the model, but the effect of liquid water build-up was the same; future work will more accurately capture the presence of liquid water in the flow channel instead of just in the GDL. Being able to predict the change in current distribution with changing flows or liquid water accumulation is important when considering optimal operating conditions and possible degradation. Lateral currents and large potentials along the flow channel need to be understood for system design; the combination of data from the SAPC fuel cell and simulation results from the TIS model is a powerful tool and provides localized information. This is much more useful than the

standard polarization curve measurements commonly used in the field, that only provide information integrated over an entire, usually very large, active area.

4.6 References

1. Weber, A.Z. and J. Newman, *Modeling transport in polymer-electrolyte fuel cells.* Chemical Reviews, 2004. **104**(10): p. 4679-4726.

2. Fuller, T.F. and J. Newman, *Water and Thermal Management in Solid-Polymer-Electrolyte Fuel Cells.* Journal of the Electrochemical Society, 1993. **140**(5): p. 1218-1225.

3. Nguyen, T.V. and R.E. White, *A Water and Heat Management Model for Proton-Exchange-Membrane Fuel Cells.* Journal of the Electrochemical Society, 1993. **140**(8): p. 2178-2186.

4. Dutta, S., S. Shimpalee, and J.W. Van Zee, *Numerical prediction of mass-exchange between cathode and anode channels in a PEM fuel cell.* International Journal of Heat and Mass Transfer, 2001. **44**(11): p. 2029-2042.

5. Vladimir, G., L. Hongtan, and K. Sadik, *Two-dimensional model for proton exchange membrane fuel cells.* AIChE Journal, 1998. **44**(11): p. 2410-2422.

6. Weber, A.Z. and J. Newman, *Transport in Polymer-Electrolyte Membranes.* Journal of the Electrochemical Society, 2003. **150**(7): p. A1008-A1015.

7. Thampan, T., S. Malhotra, H. Tang, and R. Datta, *Modeling of Conductive Transport in Proton-Exchange Membranes for Fuel Cells.* Journal of the Electrochemical Society, 2000. **147**(9): p. 3242-3250.

8. Eikerling, M. and A.A. Kornyshev, *Modelling the performance of the cathode catalyst layer of polymer electrolyte fuel cells.* Journal of Electroanalytical Chemistry, 1998. **453**(1-2): p. 89-106.

9. Ahmed, S., J. Kopasz, R. Kumar, and M. Krumpelt, *Water balance in a polymer electrolyte fuel cell system.* Journal of Power Sources, 2002. **112**(2): p. 519-530.

10. Cownden, R., M. Nahon, and M.A. Rosen, *Modelling and analysis of a solid polymer fuel cell system for transportation applications.* International Journal of Hydrogen Energy, 2001. **26**(6): p. 615-623.

11. Benziger, J., E. Chia, E. Karnas, J. Moxley, C. Teuscher, and I.G. Kevrekidis, *The stirred tank reactor polymer electrolyte membrane fuel cell.* AIChE Journal, 2004. **50**(8): p. 1889-1900.

12. Chia, E.S.J., J.B. Benziger, and I.G. Kevrekidis, *STR-PEM fuel cell as a reactor building block.* Aiche Journal, 2006. **52**(11): p. 3902-3910.

13. Yang, C., S. Srinivasan, A.B. Bocarsly, S. Tulyani, and J.B. Benziger, *A comparison of physical properties and fuel cell performance of Nafion and zirconium phosphate/Nafion composite membranes.* Journal of Membrane Science, 2004. **237**(1-2): p. 145-161.

14. Meng, H. and C.Y. Wang, *Electron transport in PEFCs.* Journal of the Electrochemical Society, 2004. **151**(3): p. A358-A367.

15. Nitta, I., T. Hottinen, O. Himanen, and M. Mikkola, *Inhomogeneous compression of PEMFC gas diffusion layer Part I. Experimental.* Journal of Power Sources, 2007. **171**(1): p. 26-36.

16. Zhou, T.H. and H.T. Liu, *Effects of the electrical resistances of the GDL in a PEM fuel cell.* Journal of Power Sources, 2006. **161**(1): p. 444-453.

17. Satterfield, M.B. and J.B. Benziger, *Non-Fickian Water Vapor Sorption Dynamics by Nafion Membranes.* The Journal of Physical Chemistry B, 2008. **112**(12): p. 3693-3704.

18. Eikerling, M., Y.I. Kharkats, A.A. Kornyshev, and Y.M. Volfkovich, *Phenomenological theory of electro-osmotic effect and water management in polymer electrolyte proton-conducting membranes.* Journal of the Electrochemical Society, 1998. **145**(8): p. 2684-2699.

19. Springer, T.E., T.A. Zawodzinski, and S. Gottesfeld, *Polymer electrolyte fuel-cell model.* Journal of the Electrochemical Society, 1991. **138**(8): p. 2334-2342.

20. Zawodzinski, T.A., C. Derouin, S. Radzinski, R.J. Sherman, V.T. Smith, T.E. Springer, and S. Gottesfeld, *Water-uptake by and transport through Nafion® 117 membranes.* Journal Of The Electrochemical Society, 1993. **140**(4): p. 1041-1047.

21. Chia, E.S.J., J.B. Benziger, and I.G. Kevrekidis, *Water balance and multiplicity in a polymer electrolyte membrane fuel cell.* AIChE Journal, 2004. **50**(9): p. 2320-2324.

22. Boyer, C., S. Gamburzev, O. Velev, S. Srinivasan, and A.J. Appleby, *Measurements of proton conductivity in the active layer of PEM fuel cell gas diffusion electrodes.* Electrochimica Acta, 1998. **43**(24): p. 3703-3709.

23. O'Hayre, R., T. Fabian, S.-J. Lee, and F.B. Prinz, *Lateral Ionic Conduction in Planar Array Fuel Cells.* Journal of the Electrochemical Society, 2003. **150**(4): p. A430-A438.

24. Benziger, J., *Reactor Dynamics of PEM Fuel Cells*, in *Device and Materials Modeling in PEM Fuel Cells*. 2009, Springer-Verlag Berlin: Berlin. p. 91-122.

5 GDL structure

5.1 Introduction

The previous chapters have investigated the fundamentals of PEM fuel cell operation. The key physics inherent in fuel cell systems were highlighted and further studied through simulations. With unsaturated conditions, a positive feedback loop between the water produced by the electrochemical reaction and the proton conductivity of the membrane allows the fuel cell to ignite to a high-current steady-state, provided that the water produced is more than the water removed. If that condition is not met, the fuel cell dries out and the current falls to the extinguished steady-state. At the other end of operating regimes, the fuel cell is saturated and liquid water is present. Gravitational forces acting on the liquid water emerging in the flow channel can either assist or impede the removal of the water, depending on the configuration of the fuel cell. The dependence of the fuel cell operation on sufficient hydration of the membrane and effective removal of excess water is something that must be considered in the design of fuel cell systems. It is possible to attenuate the importance of these factors or their impact on the fuel cell performance, but the solutions commonly employed add unnecessary complexities and costs to the system and decrease the overall efficiency.

Fuel cell systems have traditionally been designed based on heuristics. Modifications are made that improve a fuel cell's performance and with enough consistent evidence—higher voltage at a given current or higher current at a given voltage—the modification is adopted as the standard. The measurement used for comparisons and analysis is typically the polarization curve, or a fast sweep through small steps in the voltage (controlled by a potentiostat) while measuring the current. This

measurement gives very limited information about the physics of the fuel cell operation, especially for larger systems with active areas on the order of hundreds of square centimeters. The composition of the flow streams, water content of the membrane, and liquid water accumulation changes dramatically along the length of the flow channel, as discussed in the previous chapters. How and where a system change makes an improvement is impossible to verify based on the integrated current vs. voltage measurements. Similarly, system failure with a given set of operating conditions can also be misinterpreted, so that the actual cause is overlooked.

A consequence of the lack of understanding of the physics of fuel cell operation is the inclusion of several inefficiencies in system designs. It has been known that the accumulation of liquid water decreases the performance. Without a thorough understanding, the engineering solution was to use high flow rates to remove liquid water through very high convective forces—to blow it all out. Often, the high flow rates removed too much water, especially near the flow channel inlets and at elevated temperatures; the evaporation was dramatically increased and not enough of the water produced by the electrochemical reaction could be absorbed by the membrane. The subsequent engineering solution was not to rethink the use of high flow rates to manage the liquid water, but instead to humidify the feeds upstream of the fuel cell in order to decrease evaporation. This solution required the addition of humidifiers and flow stream recycling to the fuel cell system, significantly adding to the complexity, cost, and power requirements.

The realization of better and more efficient designs requires a more in depth understanding of the basics of fuel cell operation, separate from the auxiliary components

and extra control. The basic specifications for the design of a system only include the flow channel dimensions, the flow field geometry and material, and the MEA construction. With the goal of investigating the transport of liquid water, the choice of GDL material in constructing the MEA was studied first. The water is produced at the cathode catalyst layer and must be transported through GDL in order to reach the flow channels and be removed. Once in the flow channels, the dimensions and surface properties of the flow channels and flow rates of the gas streams in combination with gravity determine how effectively the water is removed. Additional complexities are observed at the interface of the GDL surface and the lands. Under the channel, droplets emerge at the surface and are detached by the shear force from the gas flow and gravity, or span the flow channel to create a blocking slug. Under the land, however, the water emerges at the surface of the GDL and must be transported laterally along the interface until eventually reaching the corner of the GDL surface, land, and flow channel. In addition to the gas flow and gravity, the surface properties of the lands and morphology of the GDL are significant factors.

Liquid water transport through the GDL has been studied more extensively through numerical simulations in the context of flooding. Several models have been proposed to describe flooding in PEM fuel cells.[1-6] Most of these hypothesize that liquid water condenses in the pores of the gas diffusion layer (GDL) creating a mass transfer resistance for oxygen to get to the membrane/electrode interface as illustrated in Figure 5.1(a).

Previous work in the Benziger group examined water permeation through the GDL and obtained results that contradicted the previous hypotheses about liquid water

accumulation.[7] The GDL is a cloth or paper of carbon fibers that is treated with Teflon to increase its hydrophobicity. It was shown that water does not enter the GDL until a sufficient hydraulic pressure is applied to overcome the repulsive surface energy. The largest pores in the GDL are the first to permit water penetration, and once water penetrates the pores it can freely drain.

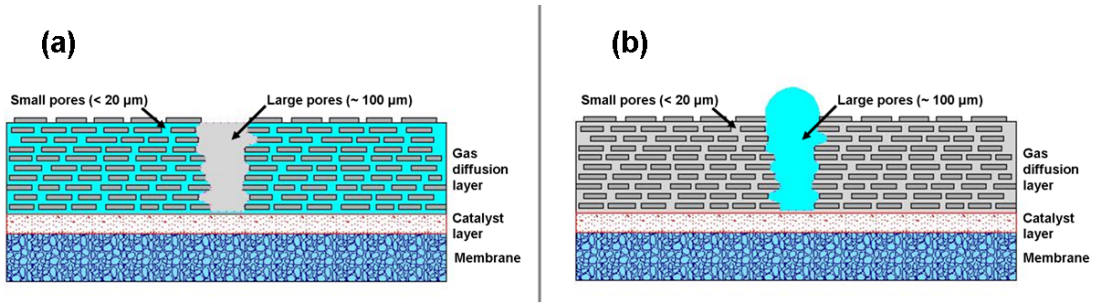

Figure 5.1 (a) Capillary condensation model of pore flooding in the GDL. This model assumes that liquid water condenses in the smallest pores of the GDL and sequentially fills the smallest pores and then the larger pores. When liquid water drops appear in the gas flow channel the entire GDL will be flooded. **(b)** Hydraulic driven flow model of liquid water flow in the GDL. The liquid water only enters the largest pores after the hydrophobic surface tension is overcome. The small pores remain unobstructed for gas transport. The small pores of the GDL only fill if the entire gas flow channel fills with liquid and pushes into the pores.

The results suggested a two highway system for liquid and gas transport through the GDL as illustrated in Figure 5.1(b). Liquid moves from the membrane/cathode interface through the largest pores driven by a hydraulic pressure, while gas moves from the gas flow channel to the membrane/cathode interface through smaller, but more plentiful, pores. Results that support these conclusions have also been reported using fluorescence microscopy to view the ex-situ transport of water through carbon paper.[8] Only a few models have been published recently that account for water flow through preferential pores even though this drastically changes the physics of how water is transported between the cathode catalyst layer and flow channel.[1-3, 8]

5.2 *Ex situ* visualization

The *ex situ* flow through different GDL media was tested in the Benziger group in the cell illustrated in Figure 5.2.[9] A 2.5 cm diameter piece of GDL media was mounted between two polycarbonate plates with 3 cm^3 plenums on either side of the GDL media. One plenum was connected to a liquid water reservoir. The reservoir was a beaker connected to the plenum with a Tygon tube and could be raised or lowered to a desired elevation relative to the cell. The plenum on the other side had an inlet for a slow stream of nitrogen at the top and an effluent out the bottom was collected in a beaker on a scale. The gas side was imaged with a Sony IEEE-1394 CCD camera.

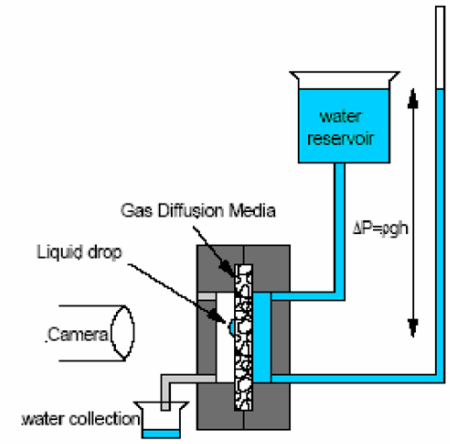

Figure 5.2 Schematic of the cell for measuring and visualizing flow through GDL media.

Before every experiment, the GDL media was dried by flowing nitrogen through both sides of the cell for 2 hours. The water reservoir was hooked up with it lying below the cell. The water reservoir was then raised to a desired height and held in position for 20 minutes, while recording the mass flow through the GDL media and obtaining video images of the water drops going through the GDL media. The two most commonly used

GDL materials were tested—Toray carbon paper and woven carbon cloth—with 20% Teflon treatments, both obtained from E-TEK (E-TEK Div. of De Nora N.A., Inc., 39 Veronica Ave, Somerset, NJ 08873-6800 USA).

No liquid water flows through the GDL media until a critical hydrostatic pressure head is applied by raising the water reservoir to an appropriate height. The required pressure head was ~15 cm water for the carbon cloth and ~ 60-80 cm water for the Toray paper. Once the critical hydrostatic head was exceeded, a continuous path of liquid water was established through the largest pores in the GDL media and liquid flow commenced with the water freely draining under the applied hydrostatic head. Water flow through the GDL material occurs with a few water drops (1-4) formed on the surface of the GDL. The drops grow to a critical size and then fall by gravity to the bottom of the plenum and drain from the cell. The process repeats itself with the water drops always forming at the same locations.

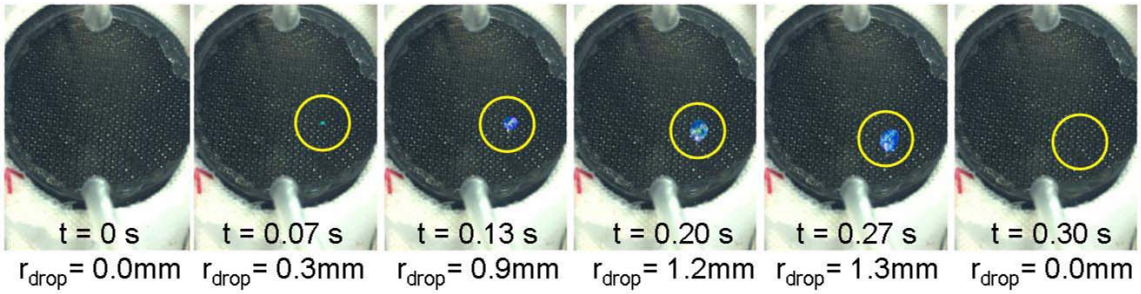

Figure 5.3 Series of photographs showing drop formation and detachment from the surface of a carbon cloth GDL under an applied hydraulic pressure of 170 mm H_2O.

Figure 5.3 shows a series of photographs of drops growing and the process repeating for the carbon cloth. The critical hydrostatic pressure head to initiate flow and the measured water flow rate for the first 2-3 minutes after flow was started are summarized in Table 5.1. The critical drop size before it falls by gravity was determined

from the videos and the critical radius is summarized in Table 5.1. The key results from these studies are that liquid flow is carried through a small number of the largest pores in the GDL. The Toray paper has smaller pores than carbon cloth so the critical pressure to initiate flow is greater and the flow through the smaller pores is less.

Table 5.1 Water permeation through GDL media

GDL Media	Required Head for Water Permeation (mm H2O)	Water Permeation Rate at Critical Hydraulic Pressure (g/min)	Critical Drop Radius for Detachment (μm)	Critical Pore Radius based on Initial Drop Formation (μm)
20% Teflon Treated Cloth	170	1.2	1250	140
20% Teflon Treated Toray Paper	600	0.22	600	21

5.3 SAPC fuel cell experiments

5.3.1 Fuel cell orientation

A major advantage of the SAPC fuel cell design (described in Chapter 1, section 6) was the ability to operate the fuel cell in one of several possible orientations. This was detailed in Chapter 3, but is briefly discussed again here. With the choice of co-current flow, there were five different physical orientations (three horizontal and two vertical) which were defined by the effect that gravity had on liquid accumulation in the gas flow channel. The horizontal configurations were with the cathode facing downward and the anode facing upwards ("cathode down"), the cathode facing upwards and the anode downwards ("cathode up"), and the cathode and anode in the same horizontal plane ("horizontal"). In the "cathode down" orientation, the force of gravity causes the droplets forming at the surface of the GDL to fall to the back of the flow channel. This occurs

when they grow large enough, so that the gravitational force overcomes the surface tension holding the drop to the water in the pore. The shear force from the gas flow must then push the droplets along the back of the flow channel to the outlets. The 90° bend at the outlet allows the drops to be easily removed, again with the help of gravity. The "horizontal" orientation is similar in that the droplets grow until they detach and fall, but then they are pushed along the side of the flow channel and can partially block the flow of reactants into the GDL. Also, at the outlet, the 90° bend does not change the orientation with respect to gravity and the liquid water must continue to be pushed by the gas flow to be removed. The third horizontal orientation, "cathode up", is opposite of "cathode down" in that gravity holds the drops to the surface of the GDL. The force from the gas flows must overcome the surface tension holding the drop to the pore and must then push the water out of the outlet against gravity after the 90° bend.

The two vertical orientations were with the inlets at the top of the flow channel, so that the gas flow was in the same direction as gravity ("inlets up"), and with the inlets at the bottom of the flow channel, so that gravity opposed the gas flow ("inlets down"). In the "inlets up" orientation, gravity assists in both detaching the drops and moving the water to the outlets. The gas flow must then push the water out after the 90° for it to be completely removed. With the "inlets down" orientation, the gas flow must also push the water after the bend at the outlet, but the water must first be pushed against gravity the entire way up the flow channel to reach the outlet. Gravity helps to detach the drops but they fall down the flow channel towards the inlets where they can cause excessive flooding.

Figure 5.4 shows schematics of one of the horizontal orientations, (a) "cathode down", and one of the vertical orientations, (b) "inlets up". The 90° bend at the outlets is shown clearly and water droplets are shown to demonstrate how they might grow as they move along the flow channel or detach and fall to the bottom.

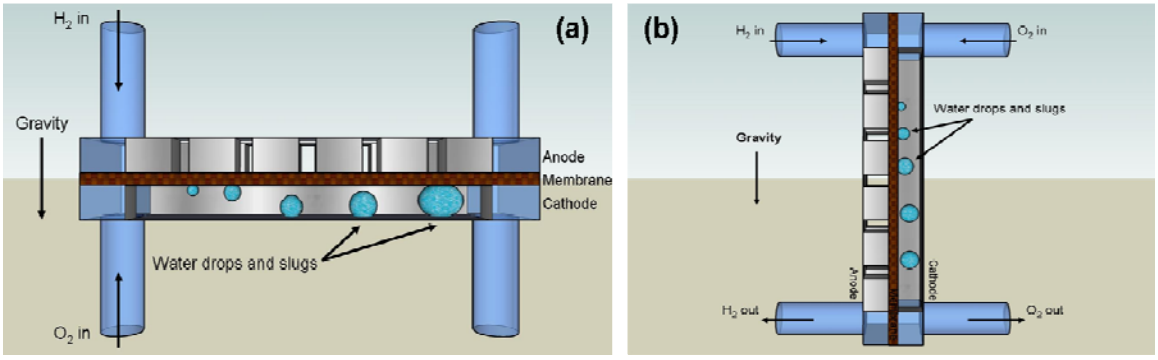

Figure 5.4 Diagrams of two of the five possible orientations of the SAPC Fuel Cell. There are three horizontal orientations: the cathode facing up, the cathode facing down (shown in (a)), and the anode and cathode in the same horizontal plane. There are also two vertical orientations: the inlets at the top of the flow channel (shown in (b)) and the inlets at the bottom of the flow channel.

5.3.2 Fuel Cell Operation

Hydrogen and oxygen were never humidified and were supplied directly from commercial cylinders through mass flow controllers at flow rates of 1-20 ml min^{-1}. There were also relative humidity sensors placed at the outlets of the gas flow channels to record any changes in the RH. In the experiments reported here, liquid water was always present in the flow channels and the RH in both the anode and cathode outlets was always 100% after a short start-up period.

The flow rates were chosen to understand the fuel cell operation under very high fuel conversion. This amplified the effects from gravitational forces and material properties relative to the effect of the shear force from gas flow. Furthermore, keeping the gas velocity in the flow channels low, while also keeping the temperature low,

reduced the convective flow of water vapor. At low convective flow rates for water in the flow channel, water diffusion in the membrane is sufficient to humidify the membrane and allow for operation with dry feeds. The maximum values the flow rates were fixed at were 12 ml/min^{-1} H_2 and 6 ml/min^{-1} O_2, corresponding to a stoichiometry (as defined in Chapter 3; the ratio of reactants supplied in the feed to reactants consumed) of about 2 for the SAPC fuel cell. Through a series of tests we observed that, with a load resistance of 0.5 Ω and a stoichiometry of 1 (flow rates of about 6/3 ml/min^{-1} H_2/O_2, varying slightly with the MEA and state of the system), no gas bubbles were seen from the outlets of the anode and cathode, indicating complete conversion of the reactants.

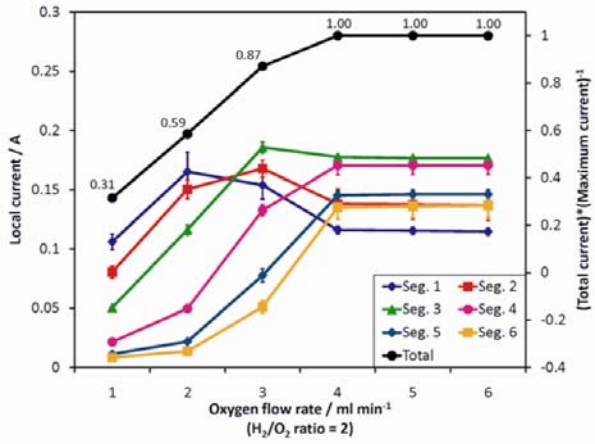

Figure 5.5 Local and total currents (relative to the maximum total current) vs. O_2 flow rate (H_2/O_2 ratio constant at 2). Above 3 ml min^{-1} O_2, the currents are independent of flow rate with a maximum total current of 0.88 A. At 3 ml min^{-1} O_2 and below, the reactants are completely consumed. The fuel cell was in the vertical "inlets up" orientation in order to minimize effects from liquid water accumulation. The data is the average from experiments with both increasing and decreasing the flow rates and starting from both dry and wet conditions. The error in the current measurements was very low at ±0.0001 A (see section 1.6) while the mass flow controllers had an acceptable level of accuracy at ±0.1 ml min^{-1}.

Figure 5.5 is a plot of the segmental currents and total fuel cell current as a function of O_2 flow rate with the H_2/O_2 flow rate ratio kept constant at 2. The maximum total current from the SAPC fuel cell driving a 0.5 Ω load impedance at 25ºC and 1 bar

total pressure was 0.88 A. For flow rates > 6/3 ml min^{-1} H_2/O_2 the total current was almost independent of flow rate. Decreasing the flow rate to 6/3 ml min^{-1} H_2/O_2 or lower resulted in a decrease in the total current delivered by the fuel cell, as evidenced by a change in slope of the current vs. flow rate curve. The net voltage changes at the same rate as the total current (with the constant load resistance of 0.5 Ω), however the absolute changes in the local currents indicate the local potential drops are not uniform along the electrodes.

5.3.3 Experimental protocol

A typical experiment consisted of 3 stages, (1) startup with low reactant flow rates, (2) "steady state" operation at excess stoichiometry and (3) "steady state" operation at a stoichiometry of 1. The fuel cell was started for one hour with dry feeds of 6/3 ml min^{-1} H_2/O_2; this was found to be sufficient to achieve a steady current in all six anode segments. After one hour the flows were increased to 12/6 ml min^{-1} H_2/O_2; this supplied the reactants at about a stoichiometry of 2 and is referred to here as ξ_2. The flows were kept at ξ_2 for two hours to allow the amount of water in the cell to equilibrate. At a current of about 0.9 A, the time for liquid water to fill the cathode flow channel was 4000 s; one hour is thus a critical time constant for the SAPC fuel cell operation and any characterization of fuel cell operation should extend for several time constants. Lastly, the flows were reduced to ξ_1, where all the reactants were consumed (~ 6/3 ml min^{-1} H_2/O_2), for four hours. This highlighted the effects of liquid water accumulation and how the parameters of the system affected its removal, including the influence of gravity.

During the entire experiment, the reactant flow rates, voltage drop across the load resistor, and the current measurements from the six different anode segments were logged every second, yielding raw data as shown in Figure 5.6(a). "Segment 1" was always

defined as the anode segment closest to the feed inlets and "segment 6" was always closest to the outlets, as shown in Figure 5.6(b). To mitigate the noise in the measurements, data samples were read from the data acquisition board at 16 Hz with the average over 16 samples saved to the data file at one point per second. With this, the fluctuations from noise in the data were kept acceptably low at no more than ±0.0001 A. (Typical current measurements for steady state operation was ~0.15 A per electrode segment, so the signal/noise ratio was >>100).

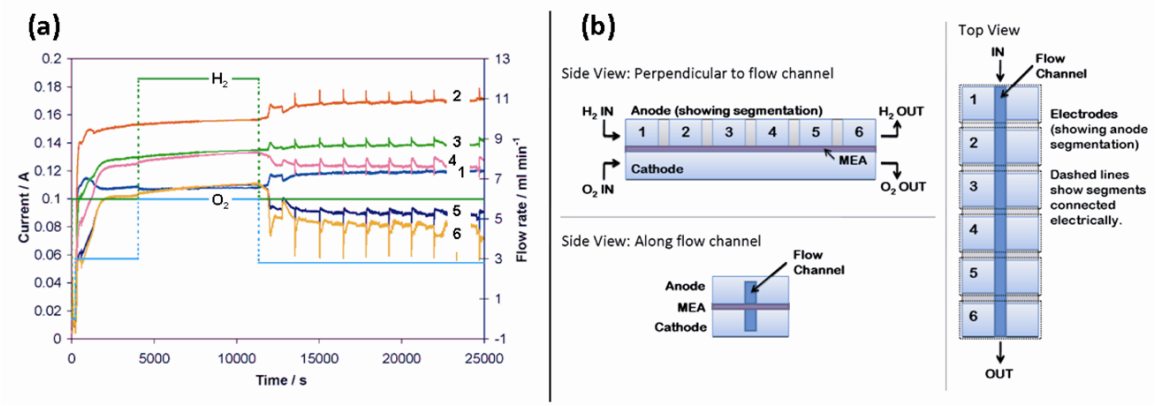

Figure 5.6 (a) Raw spatio-temporal data from a typical experiment with the SAPC FC. The segment is indicated by the numbers with the oxygen inlet at segment 1. The three stages are shown: start-up with low flow of 6/3 ml min^{-1} H_2/O_2, equilibration with 12/6 ml min^{-1} H_2/O_2, and starvation with complete consumption of reactants. Sharp fluctuations are observed when water slugs move through the flow channel. Parameters: cell temperature = 23 °C, load resistance = 0.5 Ω, orientation is horizontal "cathode down" (see part b). **(b)** Schematic of the SAPC fuel cell in the "cathode down" orientation (side views) showing the electrode segmentation. The flow channel is machined in the middle of the fuel cell such that the electrodes are electrically connected across the channel.

The data shown in Figure 5.6 was typical. After increasing the flow to ξ_2 the current measurements were stable, slowing increasing and finally leveling off. The current profile showed maximum current density at the center of the flow channel (between position 2 and 3). The fall off in current at the flow inlet and outlet is the result of an asymmetry in the lateral currents through the MEA. When the flow rates were

reduced to ξ_1, the currents showed some redistribution, with the currents near the inlet increasing modestly and the currents near the outlet decreasing. In most cases, the currents were stable between sharp periodic fluctuations caused by the movement of liquid water slugs (other cases showed continuously erratic fluctuations or sharp drop-offs in all of the currents).

The distribution of the currents along the flow channel during steady operation with both sets of flows rates, the frequency of fluctuations, and the magnitude of the fluctuations were all measures of how well excess water was removed from the fuel cell. These were influenced largely by the orientation of the fuel cell and structure of the GDL and will be analyzed in the following sections.

5.4 Effects of pore size

The most significant difference between carbon cloth and carbon paper GDLs relevant to fuel cell operation as described here is the pore size distribution. The largest pores, the ones through which liquid water will flow, are about 140 μm in carbon cloth (these occur at the intersection of the weave of the fiber bundles). The largest pores through carbon paper are about 20 μm.[7] The adhesive energy between water in the pores and the water drops on the GDL surface scales with the cross-sectional area of the pore [9] so that the force to detach drops from the GDL pore is much greater for carbon cloth then for carbon paper. It is more likely that droplets emerging from the carbon cloth will span the flow channel, forming a slug prior to detachment, whereas smaller drops emerging from the carbon paper may be detached as individual drops. The shear

force from the gas in the flow channel and the force from gravity both play a role in overcoming the surface energy to detach the droplets.

Very recent results from the Benziger group have shown that the difference in water flow under the lands between carbon cloth and carbon paper can also have a significant impact on the fuel cell performance. The more uniform surface of the carbon paper allows for more water transport between the lands and surface of the GDL.[10] These effects are also dependent on the surface properties of the lands and channel; this is discussed further in Chapter 6.

5.4.1 Experimental results

The coupling of the liquid water flow in the GDL and liquid flow in the flow channel was studied with the same two GDL materials discussed in section 2. Figure 5.7 shows current profiles for two different fuel cell orientations, one horizontal: "cathode down" (open symbols, dashed trendlines; shown in Figure 5.4(a)) and one vertical: "inlets down" (filled symbols, solid trendlines; opposite vertical orientation from that shown in Figure 5.4(b)). Results are given at stoichiometries ξ_2 (part a) and ξ_1 (part b) and with MEAs made with both carbon cloth (diamonds) and carbon paper (circles). The data points give the averages over multiple experiments while the linear best-fit trendlines are given to guide the eye.

When the fuel cell was operated with excess gas flow, ξ_2, the orientation had only a small effect on the local current distribution. The current profiles, given in Figure 5.7(a), are relatively flat and the curves essentially lie on top of one another, indicating a uniform current distribution and minimal flooding. (There are some variations due to reproducibility of preparing MEAs and putting the fuel cell together). When the feed

flow rates were reduced to ξ_1, the effects of gravity were amplified, as shown in Figure 5.7(b). With the horizontal "cathode down" configuration, there is little change between parts (a) and (b) and the dashed curves are relatively flat, indicating a uniform current distribution along the flow channel. Some starvation effects can be seen with the slight decrease in current at segments 5 and 6 (near the outlets), but the surface of the GDL is left open for the oxygen to flow to the catalyst layer and yield a high current density. It must be noted that there is a significant difference in the temporal dependence of the local currents between the high and low stoichiometries. As was reported previously, the currents are temporally stable for ξ_2, but show large fluctuations at ξ_1. However, the steady values do not vary significantly.

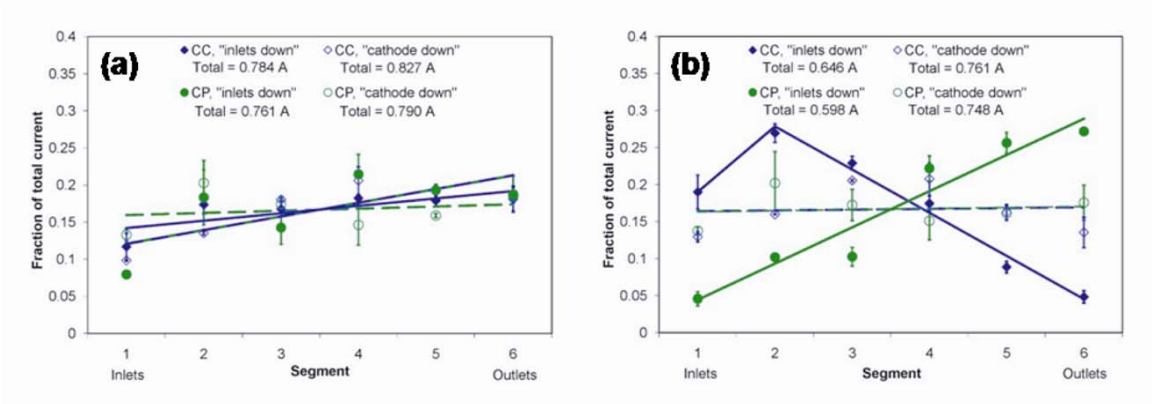

Figure 5.7 Current profiles from experiments with both carbon cloth ("CC"; diamonds) and carbon paper ("CP"; circles) used in making the MEA and with the fuel cell in two different orientations, "cathode down" (open symbols, dashed trendlines) and "inlets down" (filled symbols, solid trendlines). The data points give the averages over multiple experiments while the linear best-fit trendlines are given for clarity. The error bars denote the standard error over multiple experiments. **(a)** Reactants supplied at ξ_2 (flows of 12/6 ml min^{-1} of H_2/O_2) to give excess flows. **(b)** Reactants fully consumed with flows supplied at ξ_1 (~ 6/3 ml min^{-1} H_2/O_2). Parameters for each experiment: cell temperature = 23 °C, load resistance = 0.5 Ω. Refer to Figure 5.4 for descriptions of the different orientations.

In contrast, dramatic differences are seen in Figure 5.7(b) when gravity becomes more important and acts in the opposite direction of the gas flow; the current profiles for the carbon cloth are almost the inverse of that with the carbon paper. With the carbon

cloth GDL, the currents are much higher towards the inlets with a peak at segment 2 and a sharp drop off towards the outlets. The profile results from slugs of water getting stuck at the top of the flow channel. The pores were large enough that the adhesion of the drops to water in the pore caused the droplets to span the flow channel and form a slug before detaching from the GDL. As the gas pressure increased behind the slugs, the oxygen was reacted to a greater extent upstream so that it was almost completely consumed near segments 5 and 6 and could no longer push the water slugs up against gravity.

With the carbon paper GDL, the opposite trend was observed: low currents in the lower half of the channel and a sharp increase towards the upper segments. This resulted from water droplets detaching and falling to the bottom of the flow channel instead of forming slugs where the droplets emerged. The water collected at the bottom and blocked the flow of reactants to the segments closest to the inlets. The current redistributed towards the outlets as more oxygen was available to be consumed downstream.

5.4.2 Discussion

Droplets are detached from the surface of the GDL by overcoming the surface tension between the water in the droplet and the water in the pore. Both the shear force from the gas flow and gravity contribute to detachment, but only act in the same direction with one of the orientations, vertical “inlets up”. For the horizontal orientation “cathode down”, gravity assists in removing the drops from the GDL surface but the gas flow must push the liquid out of the flow channel. In the horizontal orientation “cathode up”, gravity acts to hold the drops on top of the surface of the GDL while the shear force acts

to detach the drops and push them along the flow channel. Finally, in the vertical orientation "inlets down", gravity and shear forces oppose each other with the flows going upwards and gravity pulling the droplets back towards the inlets. With these orientational dependences in mind, we can write the simple force balance for water drop detachment from the GDL (equation 1).

water surface tension = force from gravity $\pm$ shear force

$$2\pi r_{pore}\gamma_{water} = \frac{4}{3}\pi r_{drop}^3 \rho_{water} g \pm \left(\frac{4\mu_{gas}Q_{gas}}{\pi r_{channel}^3}\right)\left(\pi r_{drop}^2\right) \quad (1)$$

where r is the radius, γ is surface tension, μ is viscosity, Q is volumetric flow rate, ρ is density and g is the acceleration due to gravity. To fully capture the orientational effects, equation 1 should be written separately for each orientation as a three-dimensional vector equation, but here the ± symbol has simply been used to denote the different ways the two forces can act relative to each other.

When choosing a GDL material and designing flow channels, one wants to know if the water drops will span the flow channel and form slugs or remain as drops. Based on GDL pore diameters of 20 μm for carbon paper and 140 μm for carbon cloth, the predicted size for drop detachment due to gravity is 0.6 mm for carbon paper and 1.2 mm for carbon cloth. With the parameters of the SAPC FC ($Q_{gas} \sim 10^{-7}$ m^3 s^{-1}, $r_{channel} \sim 1$ mm), droplets will be detached before spanning the flow channel for both the carbon cloth and carbon paper in the vertical "inlets up" orientation, where the gas flow is assisted by gravity. When the flow channel orientation is horizontal "cathode down", gravity again will assist the detachment of the drops from the GDL. However, because gravity does not assist with pushing the drops along the flow channel, at low stoichiometry the drops will aggregate as they move along the flow channel and form

slugs near the outlet. In the horizontal "cathode up" orientation, the shear forces are insufficient to detach drops emerging from the carbon cloth GDL, resulting in slug formation at the location of the largest pores that blocks the gas flow. With a carbon paper GDL used in the horizontal "cathode up" orientation, the drops emerging from the GDL can be detached by the gas flow before spanning the channel, but they will aggregate with other drops as they move down the channel and form slugs near the outlet. The significance of this analysis is that without the force of gravity or the constraints of the channel walls, the droplets would grow to a radius exceeding the dimensions of the flow channel before the shear force would overcome the surface tension. In order to avoid slug formation, the fuel cell orientation must be chosen so that gravity assists in detaching the droplets from the water in the pores of the GDL.

The force balance in equation 1 assumed spherical droplets. As the droplets are deformed by the various forces or come into contact with the sides of the flow channel, this assumption is no longer valid. Furthermore, as the droplets grow and block a significant fraction of the channel cross-sectional area, the velocity of the gas will increase as it flows through a smaller cross-section and causes a greater deformation by shear force than what equation 1 predicts. These factors will change the calculation of when slugs are formed and have the added complexity of the possibility for water film formation, but is beyond the scope of the analysis presented here.

5.5 GDL modifications

The results in the previous sections helped in gaining a thorough understanding of how the properties of commercially available GDL materials affect water transport in the

fuel cell. The effects of the GDL hydrophobicity suggested that the pore sizes in the GDL could be exploited and actually used to control where and how the water emerges into the flow channels. To accomplish this, two carbon cloth GDLs were modified by creating a pore substantially larger than the intrinsic pores of the GDL (described below). It is thought that liquid water can move laterally between the GDL and catalyst layer seeking out the path of least resistance to flow, eventually leading to the largest pore. Water drops will emerge from the GDL at this large pore, with the dynamics of the fuel cell operation highly dependent on its location.

5.5.1 Experimental results

A single large pore was created in a carbon cloth GDL by poking a small pin all the way through the material. This created a pore with a diameter of about 400 μm, almost 3 times larger than the pores at the intersection of fiber bundle weave in carbon cloth that water would typically flow through.[7] The modified GDL was then used for the cathode side GDL in an MEA constructed as described in section 1.6. Figure 5.8 shows back-lit photos of GDLs with (a) the pore in a location that was under the channel and (b) the pore in a location that was under the land when the MEA was placed in the fuel cell. Overlays are given to show the relative location of the pores to the flow channel.

Figure 5.8(c) gives the diagram of the position of the pore along the flow channel, relative to the segmentation of the anode (also refer to Figure 5.6(b)). The pore was created 19 mm from one end of the GDL. If that end was closer to the inlets, the pore was across the membrane from the space between segments 2 and 3 of the anode. If the

pore was closer to the outlets, then it was across from the space between segments 4 and 5. The location of the pore proved to be very significant, as will be shown later.

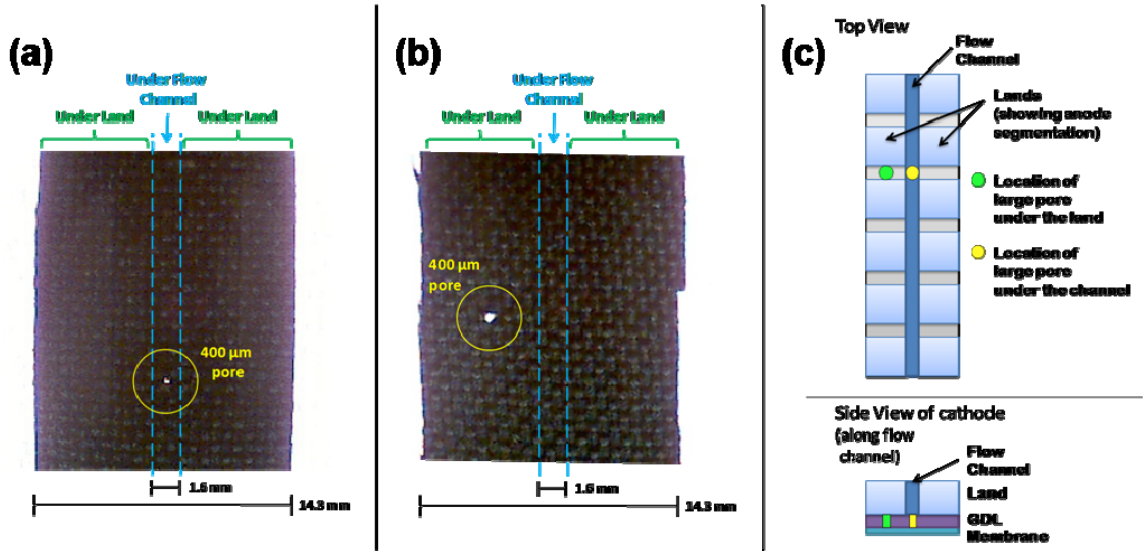

Figure 5.8 Photos and schematic of modifications to the GDLs. The large pore is forced to be either under the channel or under the land, and closer to the inlets or closer to the outlets. **(a)** Backlit photo of a carbon cloth GDL with a large pore (circled in yellow) created to be under the channel. Overlay is given to show the areas that would be under the lands and channel in the fuel cell. **(b)** Backlit photo of a carbon cloth GDL with a large pore (circled in yellow) created to be under the land. Overlay is given to show the areas that would be under the lands and channel in the fuel cell. **(c)** Schematic showing the location of the large pores relative to the segmentation of the anode when the large pore is under the channel (yellow dot) and under the land (green dot).

The results presented here are for a carbon cloth GDL, where a single large pore at the intersection of the fiber weave was easily opened up from 140 to 400 µm. When the large pore was under the channel, all of the liquid water emerged directly into the flow channel; interaction with the lands or channel walls occurred only after the emergent drop grew to span the channel. When the pore was under the land, the liquid water flowed through the GDL and entered the porous network between the GDL fiber weave and the flat stainless steel land. Liquid water moved along the interface between the GDL and land until it reached the flow channel, where it interacted with the surface of the stainless steel electrode making up one of the side walls of the channel. The stainless

steel land was hydrophilic (contact angle ~ 15°)[11], in contrast to the hydrophobic carbon GDL (contact angle > 100°)[7] so that the water wicked onto the channel side walls and left the surface of the GDL clear.

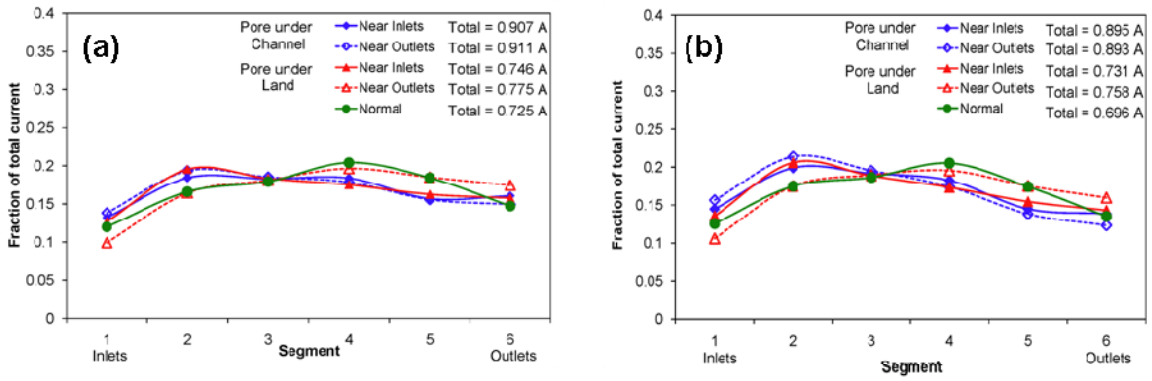

Figure 5.9 Current profiles for the five different configurations of the MEA with carbon cloth GDLs (see Figure 5.8). The fuel cell was in the "inlets up" orientation so that gravity assisted in removing the liquid water (see Figure 5.4(b)). The profiles are flat and lie on top of one another **(a)** with excess flows set at stoichiometry ξ_2 and **(b)** with complete utilization of the reactants with the flows set at stoichiometry ξ_1. Parameters for all experiments: cell temperature = 23 °C, load resistance = 0.5 Ω.

Changing the liquid drop–surface interaction altered the importance of gravity, creating dramatic differences in the local current distribution between the different fuel cell configurations. Figure 5.9 shows the results when gravity provided the most assistance in the removal of liquid water. The fuel cell was run in the "inlets up" orientation (as in Figure 5.4(b)), such that gravity assisted in removing the liquid water the entire length of the flow channel. Figure 5.9(a) gives the profiles of the current distribution with the flows at ξ_2. For each configuration of the MEA, the profiles are relatively flat and lie on top of one another. This indicates a uniform current distribution and minimal effects from liquid water accumulation. Figure 5.9(b) shows data from the same experiments shown in part (a), but after the flows were reduced to ξ_1 to give

complete consumption of the reactants. Still, the profiles remain flat, with a small decrease in the currents towards the outlets due to reactant starvation.

As with the results given in Figure 5.7, significant differences were observed in the temporal data for the experiments shown in Figure 5.9. With excess flows, the currents were stable, but with the flows at stoichiometry ξ_1, sharp fluctuations occurred due to the movement of liquid water slugs in the flow channel. The "steady" values (between the fluctuations) do not show significant differences, but the fluctuations themselves will be analyzed later in the following section. The full spatio-temporal data sets (showing the fluctuations) for all of the experiments presented in Figure 5.9 and the following Figure 5.10 can be viewed online at http://pemfc.princeton.edu.

Rotating the fuel cell to the horizontal "cathode up" orientation changed the influence of gravity so that it impeded liquid water removal, drastically changing the results. Figure 5.10 shows the steady-state current profiles for the fuel cell with the cathode facing up at stoichiometries ξ_2 and ξ_1 for different locations of the large pore. No steady state profile was obtained when the large pore was under the channel and near the inlet at ξ_1; this case will be reported separately. The current profiles at the higher flow rates, ξ_2, shown in Figure 5.10(a) are very similar to Figure 5.9(a). The flow of the excess reactants diminished the effects of gravity in the small fuel cell so that the current profiles are flat and overlapping. Very different results are shown in Figure 5.10(b): when the flows were reduced to ξ_1 with the "cathode up" orientation, the location of the large pore had a significant impact on the current profile. With the large pore placed under the land (triangles), either near the inlet or the outlet, the profiles were surprisingly flat. From visual observation, it appeared that as the water emerged into the channel at

the contact line between the GDL and land, it spread along the stainless steel delineating the side of the flow channel. There was minimal water accumulation on the surface of the GDL, which minimized the blockage of the pores at the surface of the GDL in the channel.

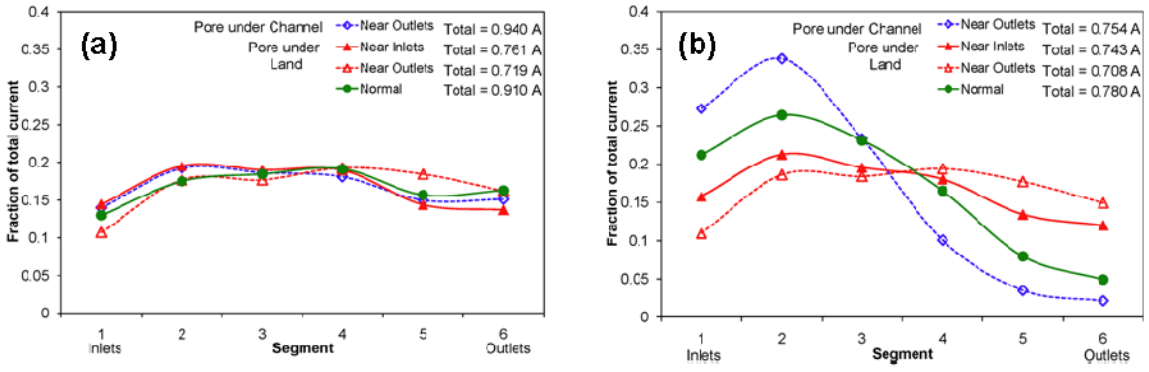

Figure 5.10 Current profiles for four different configurations of the MEA with carbon cloth GDLs (results with the large pore under the channel and closer to the inlets not shown). The fuel cell is in the "cathode up" orientation so that liquid water sits on the surface of the GDL as it is pushed along the flow channel and must be pushed against gravity to be removed through the outlets. **(a)** The profiles are flat and lie on top of one another with excess flows at ξ_2, but **(b)** dramatic differences are seen between the different configurations when the flows are reduced to ξ_1. Parameters for all the experiments: cell temperature = 23 °C, load resistance = 0.5 Ω.

Placing the large pore under the flow channel and near the outlets caused the water to emerge and form drops in the flow channel. Without the aid of gravity to assist in detachment, the drops grew and spanned the gas flow channel. With all of the water flowing out of the single location, it covered the surface of the GDL near the pore—around segments 4, 5, and 6—creating a much higher resistance for the transport of oxygen into the GDL and subsequently to the membrane cathode catalyst interface. The local currents were much lower in that region and redistributed towards the inlets to give the sharp peak seen in Figure 5.10(b) (diamonds). The unmodified GDL (circles) had multiple locations where water broke through due to local pressure variations and many

pores of similar sizes. Some water broke through under the land and some under the channel, indicated by how the profile curve lies right in between those for the two versions of modified GDLs.

The unusual results for the configuration with the horizontal "cathode up" orientation (same orientation as for the data shown in Figure 5.10) and a large pore under the channel and near the inlets are shown in Figure 5.11. The fuel cell progresses from start-up to a high current state, then the current almost completely shuts down, indicating a completely flooded state. After a period of time water vapor is convected out of the fuel cell, permitting oxygen to get from the flow channel to the membrane/catalyst interface and re-igniting the fuel cell current

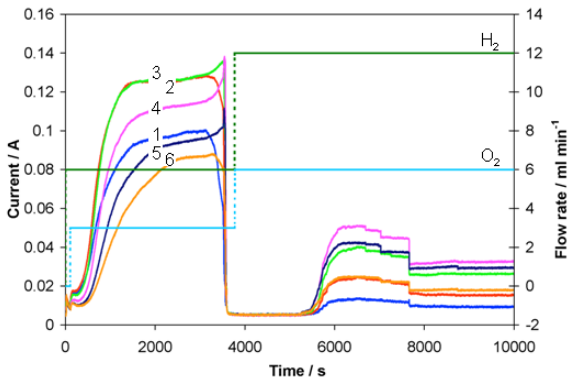

Figure 5.11 Spatio-temporal data of the current measurements from the six different anode segments with the fuel cell in the "cathode up" orientation and a large pore under the channel and closer to the inlets. Experiment parameters: cell temperature = 23 °C, load resistance = 0.5 Ω.

The flow rates were initially set low at 6/3 ml min^{-1} H_2/O_2 so that the convective flow of water vapor was reduced enough to permit the dry membrane to hydrate. The currents ignited quickly as a result of the positive feedback between higher water production and increased membrane conductivity.[12] However, after approximately one hour passed, the currents in the fuel cell totally extinguished. The liquid water

accumulated on the GDL surface, forming a slug and blocking the oxygen from getting into the GDL pores. The slug was pushed out of the flow channel but a film of liquid was left coating the walls, including the surface of the GDL. The oxygen flow to the cathode passed through the gas flow channel and never entered the GDL because of the liquid film. After one hour, the flows were increased to ξ_2, as done in all the other experiments. The fuel cell started to recover as the water film began to evaporate, but as more water was produced and pushed through the GDL, it added to the film at the surface and caused a secondary drop off in the currents, although not as severe as the initial failure. As the newly produced water emerged in the flow channel at a much slower rate than in a non-flooded fuel cell and accumulated with an already present film, slugs did not form to cause fluctuations as in the typical experiment. Instead, the thickness and coverage of the film changed until a balance was reached with the addition of product water into the film and the evaporation of water into the flow stream, as seen at about 7600 s in Figure 5.11. It is also possible that some liquid remained trapped between the GDL and the electrode (under the land) that reduced the diffusive oxygen transport laterally away from the flow channel, further contributing to the current production being unable to recover fully.

5.5.2 Analysis of fluctuations

Both the magnitude and frequency of the fluctuations can be compared for the different configurations of the SAPC fuel cell. Figure 5.12 compares the frequency of current fluctuations for three different orientations and the six configurations of the MEA discussed earlier (including a carbon paper GDL). The three orientations have varying degrees of influence from gravity: horizontal “cathode up”, such that water sits on top of the GDL and must be removed against gravity at the outlets (black); horizontal “cathode

down", such that gravity assists as the water droplets detach from the GDL and fall to the back of the flow channel but then must be pushed out by the gas flow (white); and vertical "inlets up", such that gravity assists in liquid water removal along the entire flow channel (gray). The boxes indicate the average frequency of fluctuations over at least 5 fluctuations, while the error bars indicate the maximum and minimum frequency between two fluctuations.

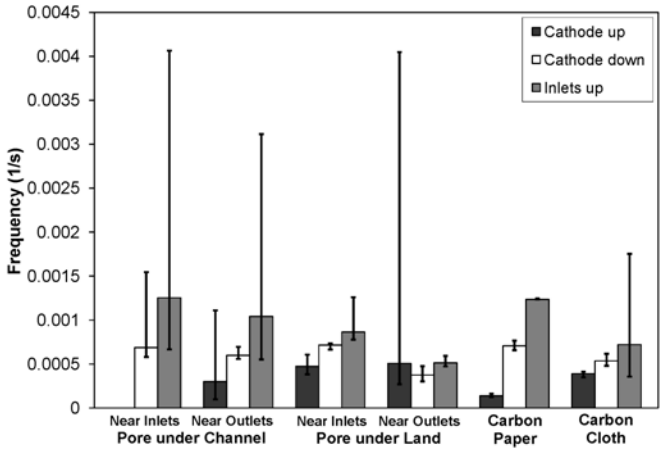

Figure 5.12 Comparison of the frequency of fluctuations with the fuel cell in three different orientations and with six different configurations of the MEA (including a carbon paper GDL). The average over several fluctuations is given with the error bars indicating the maximum and minimum frequency between two fluctuations.

With most of the configurations, as the assistance from gravity in removing water increases, so does the frequency of fluctuations. The vertical "inlets up" orientation, which has gravity acting in concert with the gas flow, has the highest frequencies. The horizontal "cathode down" has the next highest frequencies, where gravity assists in the removal of liquid from the surface of the GDL. The lowest frequencies were observed for the horizontal "cathode up" orientation. In the horizontal "cathode up" orientation, the outlet has a 90° angle from horizontal to vertical where water collects and causes a back-up in the gas flow before being removed from the fuel cell.

The large error bars with some of the configurations indicate more erratic fluctuations and inconsistent slug movement. With the "inlets up" orientation, gravity and the shear force from the gas flow acted in the same direction to deform the water droplets as they grew, changing how frequently they spanned the channel to form slugs. This effect was the most significant for the configurations with the large pore under the channel as the droplets were relatively large and formed directly in the channel. The deformation of the droplets could act to both help slugs form or elongate the droplets down the channel, causing the varied times between the fluctuations. Another factor was drop coalescence. Droplets forming higher in the channel, on the surface of the GDL or from condensation on the channel walls, were pushed down the channel by both gravity and shear forces and could coalesce with other droplets to irregularly increase the frequency of the fluctuations. With the carbon paper and the smaller droplets that formed at the surface, the converse was true; the smaller droplets were detached from the GDL much easier and were less affected by coalescing with other droplets, thus the variance bars are much smaller.

The other configuration with a large error bar is the one with the large pore under the land, closer to the outlets, and in the "cathode up" orientation. In that case, the water that emerged into the flow channel from under the land could accumulate with residual water not removed by previous slug movement. This could then form a slug in a shorter amount of time, causing fluctuations at higher frequencies. This effect was probably not observed when the large pore was under the land but near the inlets, as the water emerged earlier in the channel and spread out along the channel walls instead of forming a slug.

The frequency of the fluctuations is controlled by the time for water accumulation to form a slug; this was determined largely by the current, but was also affected by how much accumulated water was pushed out with each slug. The frequency of the fluctuations was ~10^{-3} Hz, approximately the time to fill a substantial fraction of the flow channel with liquid water. The fraction of the flow channel that was filled with liquid varied for the different configurations. Residual water after a slug was pushed out of the flow channel reduced the time necessary to form a new slug. Slugs would break up as they went around corners or through fittings, allowing the gas to flow by while pushing out only part of the water. In fuel cells with different flow field designs, this would be expected to happen around corners or at junctions where the geometry or diameter might change. Also, corners and junctions can change the orientation of the flow channel with respect to gravity, disrupting the flow of liquid water or creating areas where water can collect more easily, thus increasing the frequency of fluctuations.

The magnitude of the fluctuations was defined as the integrated deviation in the total current, averaged over several fluctuations. Figure 5.13 gives the magnitudes for the same orientations and configurations as shown in Figure 5.12. The magnitude generally varied inversely to the frequency – the product of frequency and magnitude was approximately constant to within a factor of 2.

Large variations in the magnitude of the fluctuations are seen between the different configurations and were larger for carbon cloth than carbon paper (noting the log scale on the vertical axis). The largest fluctuations were observed for the large pore under the flow channel with the cathode facing up; this corresponds to the situation where gravity was an impediment to slug removal. The most extreme case was the horizontal

"cathode up" orientation with the pore under the channel near the inlet; this situation resulted in the shutdown of the current when a liquid film was left behind, covering the GDL, that only eventually partially recovered (see Figure 5.11). When the large pore was situated under the land, the effects of orientation and location were minimized; the magnitudes are relatively constant across the different orientations. The channel walls were more hydrophilic than the surface of the GDL, so the water wicked onto the walls as it seeped out under the land and reached the channel. It could then flow along the walls spread out as a film and not hinder gas flow into the GDL, regardless of the orientation of the flow channels.

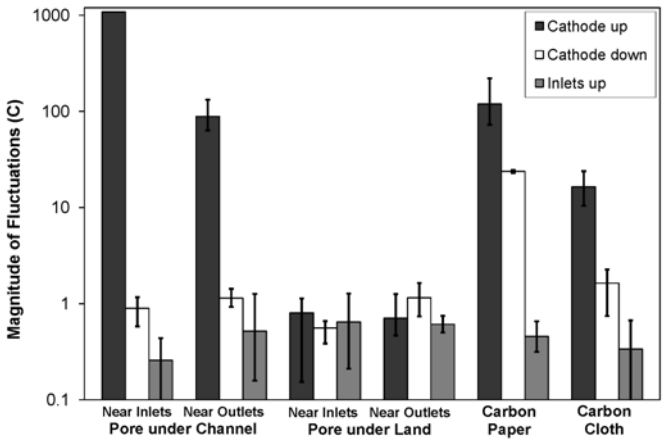

Figure 5.13 Comparison of the magnitude of the fluctuations with the fuel cell in three different orientations and with six different configurations of the MEA (including a carbon paper GDL). The average over several fluctuations is given with the error bars indicating the maximum and minimum magnitude.

5.6 Considerations for design

The trends in the frequency and magnitude between the different orientations have only been described semi-quantitatively. Neither the steady-state operation nor the fluctuations are deterministic. The spatio-temporal current patterns show variations from

the way in which water drops accumulate to form slugs and how the slugs move and break apart. Still, the results that have been discussed have implications for application-specific designs for PEM fuel cells, an issue not widely discussed in the literature. With some applications, such as portable power, the orientation of the fuel cell system might change suddenly (it could be dropped, kicked over, or the person wearing a fuel cell pack might fall over). An MEA configuration which is less sensitive to orientation would be very beneficial. Often, and most notably with the carbon paper, the magnitude of the fluctuations is very small in one orientation, but much larger in another. This could be very problematic when designing a controller for the fuel cell system if the configuration was chosen that minimized the fluctuations. If the system is only capable of compensating for very small changes, but then the orientation becomes one where large fluctuations occur, the entire system could fail. Other applications, automotive for example, will be much more stable with respect to the orientation, so that the system could be optimized with only minimum fluctuations expected.

The fluctuations and slug movement may also be further controlled by tailoring the pore size distribution with the application and fuel cell orientation in mind, allowing for slugs to form more or less frequently. For example, the data for the "inlets down" orientation in Figure 5.6(b) alludes to possible benefits of a "hybrid" GDL with larger pores in the lower half of the GDL, closer to the inlets, and smaller pores in the upper half, closer to the outlets. In that case, slugs should form at the bottom of the flow channel and clear drops of liquid water as they are pushed up and out of the flow channel in a predictable way.

As a final consideration, we have observed that defects in the flow channels caused water to build-up in a certain location. This causes larger slugs to form and the force needed to push the water past the defect is greater than that needed to push the water along a smooth channel. When the slug is finally removed, the resulting fluctuation may be much larger than expected. Another group has also reported results on water collecting at defects seen with MRI, but did not discuss the effects on the fuel cell performance.[13] Defects and other properties of the flow channels, such as the hydrophilicity or roughness of the channel walls, significantly influence the fuel cell performance and are the subjects of continuing work in our group.

5.7 Conclusions

The pore structure of the GDL directs the positions where water emerges into the gas flow channels. It was demonstrated for the first time that the pore structure of the GDL can be modified to force water to emerge at specific locations. The location of the emergent water with respect to the location in the channel or under the land, the local gas flow velocity, the orientation of the fuel cell with respect to gravity, and the surface properties of the gas flow channel determine how large drops or slugs form, whether drops span the flow channel, and what the local current density is in the fuel cell. The proper location of the water flow pores in the GDL can minimize the local current fluctuations in the fuel cell.

The differences between carbon cloth and carbon paper are significant and largely due to the differences in the sizes of the water droplets that emerge at the surface. With much larger pores, the droplets that form with the carbon cloth span the channel more

easily and form slugs that are then pushed along by the gas flow. With carbon paper, the droplets are smaller and more likely to detach from the GDL before spanning the flow channel. This can be exploited using straight flow channels oriented down where gravity assists the drainage; such designs have been adopted by Honda. The Honda design is not good for operation with dry feeds. When operating with dry feeds, where it is desirable to reduce the flow rate and have liquid in the cell mix with the reactants, carbon cloth will be better for stable operation.

Beyond examining how liquid water is transported through the GDL and into the cathode flow channel, it was shown that the GDL can be modified to direct the location of where liquid water will emerge from it. When water was directed to emerge into the flow channel, water slugs formed that spanned the channel and caused large fluctuations in the local current density. The magnitude of the fluctuations was reduced by locating the pores for liquid transport under the land. It is now possible to consider coupling the design of both the GDL and flow fields for specific applications.

5.8 References

1. He, G.L., P.W. Ming, Z.C. Zhao, A. Abudula, and Y. Xiao, *A two-fluid model for two-phase flow in PEMFCs.* Journal of Power Sources, 2007. **163**(2): p. 864-873.

2. Liu, Z.X., Z.Q. Mao, and C. Wang, *A two dimensional partial flooding model for PEMFC.* Journal of Power Sources, 2006. **158**(2): p. 1229-1239.

3. Meng, H. and C.Y. Wang, *Model of two-phase flow and flooding dynamics in polymer electrolyte fuel cells.* Journal of the Electrochemical Society, 2005. **152**(9): p. A1733-A1741.

4. Natarajan, D. and T. Van Nguyen, *Three-dimensional effects of liquid water flooding in the cathode of a PEM fuel cell.* Journal of Power Sources, 2003. **115**(1): p. 66-80.

5. Wang, Z.H., C.Y. Wang, and K.S. Chen, *Two-phase flow and transport in the air cathode of proton exchange membrane fuel cells.* Journal of Power Sources, 2001. **94**(1): p. 40-50.

6. Weber, A.Z., R.M. Darling, and J. Newman, *Modeling two-phase behavior in PEFCs.* Journal of the Electrochemical Society, 2004. **151**(10): p. A1715-A1727.

7. Benziger, J., J. Nehlsen, D. Blackwell, T. Brennan, and J. Itescu, *Water flow in the gas diffusion layer of PEM fuel cells.* Journal of Membrane Science, 2005. **261**(1-2): p. 98-106.

8. Litster, S., D. Sinton, and N. Djilali, *Ex situ visualization of liquid water transport in PEM fuel cell gas diffusion layers.* Journal of Power Sources, 2006. **154**(1): p. 95-105.

9. Kimball, E., T. Whitaker, Y.G. Kevrekidis, and J.B. Benziger, *Drops, slugs, and flooding in polymer electrolyte membrane fuel cells.* AIChE Journal, 2008. **54**(5): p. 1313-1332.

10. Gauthier, E., *Personal Communication*. 2009.

11. Givens, J.T., *Super-cleaning Stainless Steel*, in *Chemical Engineering*. 1999, Princeton University: Princeton. p. 64.

12. Benziger, J.B., E.S. Chia, Y. De Decker, and I.G. Kevrekidis, *Ignition and front propagation in polymer electrolyte membrane fuel cells.* Journal of Physical Chemistry C, 2007. **111**(5): p. 2330-2334.

13. Dunbar, Z.W. and R.I. Masel, *Magnetic resonance imaging investigation of water accumulation and transport in graphite flow fields in a polymer electrolyte membrane fuel cell: Do defects control transport?* Journal of Power Sources, 2008. **182**(1): p. 76-82.

6 Flow field design

6.1 Introduction

The flow of water from the catalyst layer, through the GDL, into the flow channels, and eventually to the outlets is one of the most important factors to understand about the operation of PEM fuel cells. The effects on local current density from liquid water accumulation are amplified when running the fuel cell near peak power. The effect of liquid water in a parallel flow channel fuel cell was covered extensively in the previous chapters. Gravity proved to have a huge influence on the fuel cell operation due to its effect on liquid water accumulation in the flow channels and removal through the outlets. The structure of the GDL controlled the flow of water from the catalyst layer to the flow channels and how the liquid water droplets emerged at the interface between the GDL and flow channel or land. This work elucidated much of the physics of fuel cell operation with liquid water present that was not previously understood. Much of the past literature has completely ignored any effects of gravity.[1, 2] Differences in GDL materials were known to change fuel cell performance, either improving or hurting performance depending on the choice of operating conditions, but a thorough understanding of the reasons was still lacking.[3, 4]

The designs of the flow fields described in the literature vary widely, without justification or systematic comparisons of designs. The development of extremely elaborate flow fields is often proprietary and most likely based on heuristics. Flow channel dimensions and properties are chosen based on the integrated measurements giving the usual polarization curve.[5, 6] The surface properties of the flow channel walls and lands are optimized by the cost and durability of the material and ease of

manufacturing.[7, 8] The approach taken in the Benziger group at Princeton was to build an understanding from the fundamental physics of fuel cell operation that is lacking in the literature. The SAPC fuel cell system was a tool well suited to fill in the gaps. Multiple modifications of the SAPC fuel cell design revealed that the properties of the flow channels and lands have a large influence on the performance of the fuel cell. The ability of the reactants to flow to the catalyst layer and the degree of removal of water away from the surface of the GDL were shown to be very important factors.

In addition to the effects from liquid water, the opposing flow of the gaseous reactants was also affected by the flow field design. The lateral flow of reactants under the lands was investigated by changing the width of the MEA and running experiments with both oxygen and air as the oxidant at the cathode. The dimensions of the flow channel and width of the lands should be chosen to optimize the liquid water removal from the fuel cell. The utilization of the catalyst under the lands, durability and manufacturability of the flow field plates, and weight of the plates should also be considered in the design.

Along with the dimensions of the flow channels and lands, the interaction between the flow field surfaces and liquid water must be understood to optimize fuel cell designs on a local scale. In this chapter, work is first presented on the flow of reactants under the lands. The driving force for lateral flow is shown to be different between using pure oxygen or air as the cathode feed. This is investigated by comparing the effects of changing the MEA width and load resistance. A simple mathematical model is also given to support the experimental findings. The complementary issue of liquid water flow under the lands is then discussed. Results are given from experiments in which the

surface properties of the lands were modified. Finally, the effects of changing the surface properties of the flow channel are shown. The results from the last two sections are not conclusive, but give important observations that offer a path for future work.

6.2 Lateral flow

The reactants are distributed over the active area usually through very long and narrow flow channels. The channels are machined into plates that contact the surface of the GDL at the lands, or ribs between the channels, and provide the conduction path for the electrons. The catalyst is distributed as a layer under both the channels and ribs. In order for all of the catalyst to be utilized, the channel and land dimensions must be such that the reactants are transported through the GDL, both transversely and laterally, fast enough to reach all of the catalyst before being consumed. It is common for the lands and the channels to simply be the same width; there has been surprisingly little research focused on finding optimal dimensions for a given fuel cell system.

The choice of feed, either oxygen or air, is also usually made arbitrarily. Often air is used in commercial systems for convenience, but this changes the flow of reactants through the GDL drastically. With oxygen, the lateral flow under the lands is driven by a pressure gradient. As the oxygen is consumed, a lower pressure is created at the catalyst layer and drives the flow from the channel through the GDL. With air, the inert nitrogen makes the pressure drop from oxygen consumption negligible. Instead, the concentration of the oxygen is decreased at the catalyst layer and drives diffusion of oxygen through the GDL.

6.2.1 Experimental results

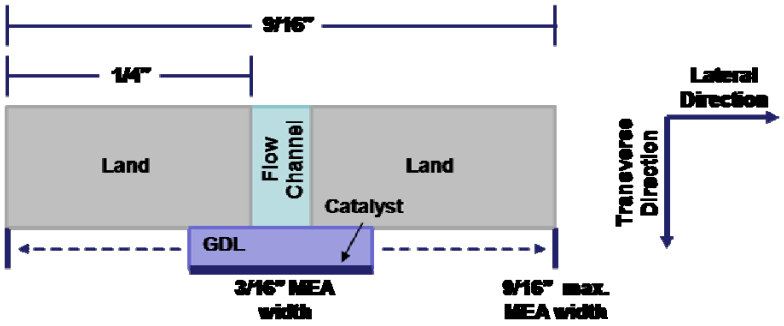

Figure 6.1 Schematic showing the cross section of one side of the SAPC fuel cell. The width of the MEA is increased from 3/16" (1/16" under the channel and 1/16" under each land) to 9/16" (1/16" under the channel and 1/4" under each land).

The SAPC fuel cell was used to study the lateral flow of reactants by changing the width of the MEA under the lands. Increasing the width of the MEA increased the active area by the same amount all along the flow channel. A schematic of the cross section of one side of the fuel cell is shown in Figure 6.1. The width of the MEA was varied from 3/16" (1/16" under the channel and 1/16" under each land) to 9/16" (1/16" under the channel and 1/4" under each land). With each increase in the width, the path from the flow channel to the additional catalyst was longer. An increase in MEA width without a corresponding increase in current indicated that oxygen was not reaching the edge of the MEA farthest from the flow channel and utilizing all of the catalyst. The single straight channel and wide land area greatly simplified the analysis compared to multi-channel and serpentine flow fields.

Figure 6.2 shows the change in the total current with different widths of the MEA under the land. Both oxygen (blue curves) and air (red curves) were used as the cathode feed. The temperature was kept at room temperature to keep the water vapor pressure low. The fuel cell was put in the vertical orientation with the inlets at the top to minimize

effects from liquid water. The experiments were conducted in the same way as in previous chapters—the fuel cell was started with low flows of 6/3 ml min^{-1} H_2/O_2, or 6/14.3 ml min^{-1} H_2/air, for one hour ("Startup"), then run with excess flows of 12/6 ml min^{-1} H_2/O_2, or 12/28.6 ml min^{-1} H_2/air, for two hours ("Excess"), then run under starved conditions with the flows set just below a stoichiometry of 1 ("Starved").

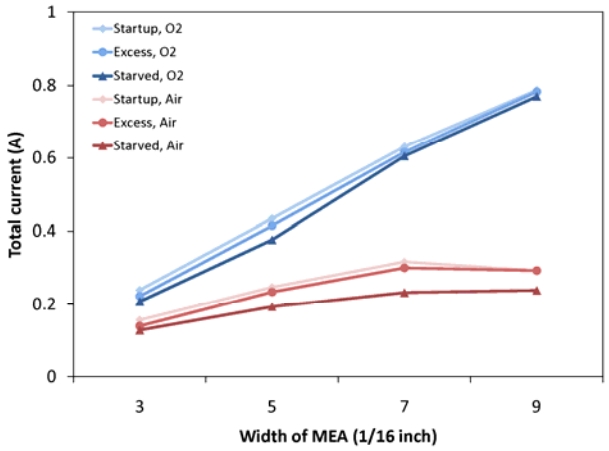

Figure 6.2 Change in current with increasing width of the MEA in the SAPC fuel cell with both oxygen (blue curves) and air (red curves) as the cathode feed. The current increases linearly with oxygen but is lower and levels off at the higher widths with air. Curves are given for each of the three stages of the experiments: "startup" with flow rates of 6/3 ml min^{-1} H_2/O_2, "excess" with flow rates of 12/6 ml min^{-1} H_2/O_2, and "starved" with flow rates set just below a stoichiometry of 1. Experiment parameters: load resistance = 0.5 Ω, temperature = 298 K, "inlets up" orientation, carbon cloth GDLs.

The results show clear differences between oxygen and air. With oxygen, the current continues to increase linearly with increasing MEA width and remains almost constant through the different stages of the experiment. With air, the current levels off as the MEA width is increased to 7/16" and 9/16". The currents are always lower with air than with oxygen with an amplified effect during the starvation stage. The decreased oxygen partial pressure with air, ~0.21 instead of ~1 with pure a pure oxygen feed, creates a decrease in the thermodynamic voltage across the membrane. The expected

change in current due to the change in voltage between oxygen and air is ~10 mA. This is an order of magnitude less than the observed change of ~100 mA, indicating that the mass transport of the oxygen appears to be a more important factor than the oxygen partial pressure in the flow channel.

The choice of reactant fed to the cathode—oxygen or air—changes the driving force for the flow through the GDL. With pure oxygen, the consumption by the electrochemical reaction creates a pressure drop that drives the flow of oxygen from the flow channels to the catalyst under the lands. The resistance to the flow of oxygen to the outer edge of the MEA is only due to the pore structure and tortuosity of the GDL. This does not completely impede the oxygen flow and the entire width of the catalyst layer is utilized. The physics are very different when air is used. The oxygen/nitrogen mixture fills in all of the pore space. With a minimum of 79% nitrogen in the pores, the concentration of nitrogen is lowest at the GDL/flow channel interface and increases towards the GDL/catalyst interface with the consumption of oxygen. The consumption of oxygen does not create a large pressure drop laterally through the GDL. Instead, oxygen must diffuse from the flow channel and within the pores through the nitrogen to the catalyst.

The concentration gradient driving the diffusion of oxygen through nitrogen is decreased with a decrease in current, accomplished by an increase in the external load resistance. With pure oxygen as the feed, the mass transport is less affected by a change in load resistance due to the absence of dilution by nitrogen. At higher temperatures, the vapor pressure of water is significant with both oxygen and air feeds. However, the vapor pressure is limited to a maximum of the saturation vapor pressure. Any excess

water after saturation condenses as liquid water in both the flow channel and at the catalyst layer. With liquid water present, there is no water activity gradient across the GDL and the partial pressure remains constant between the flow channel and catalyst layer. A small dilution effect will occur close to the inlets of the flow channel with dry feeds where the gas is not saturated, but this should not be a large factor and the following analysis is still applicable.

The pressure-driven flux of oxygen through the GDL is high enough to utilize all of the catalyst in every case tested. With air, the decreased consumption will allow the oxygen to diffuse farther under the land before being consumed. The difference between the fuel cell performance with oxygen or air feed is diminished with increasing load. At the same time, the effects are larger for increasing MEA width. This was shown by running the SAPC fuel cell with the same setup as before (vertical "inlets up" orientation and carbon cloth GDLs). The flows were set at 6 ml min^{-1} H_2 and either 3 ml min^{-1} O_2 or 14.3 ml min^{-1} air for one hour with a load resistance of 0.5 Ω. The membrane hydrated and the currents came to a stable steady-state. The load was increased to 2 Ω and the cell was run for 30 minutes to allow the currents to stabilize. The load was then increased to 5 Ω and the cell was run for another 30 minutes. The time between steps were kept low to avoid drying of the membrane with the large excesses of oxygen and air. Experiments were done with both O_2 and air feeds for each of the same four MEAs with varying widths and data was saved at the end of each step.

The results are shown in Figure 6.3 as the total current versus the load resistance for the different widths of the MEA and both oxygen (solid lines, closed symbols) and air (dashed lines, open symbols) feeds. The difference between the current with an oxygen

feed and the current with an air feed decreases with decreasing load resistance and with decreasing MEA width (9/16" width data not shown for clarity). The 3/16" wide MEA has the highest internal resistance (lowest cross-sectional area) and no difference between oxygen and air feeds is observed. It should be noted that the MEAs in these experiments consistently had higher internal resistances that those used in the experiments shown in Figure 6.2, indicated by the generally lower currents. This was most likely due to the manufacturing of the GDLs used for the experiments shown in Figure 6.3 (GDL material was purchased from a different supplier than with all other previous experiments).

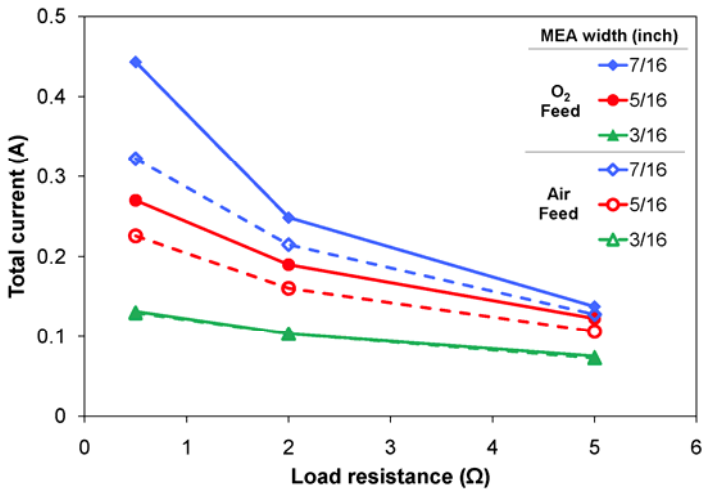

Figure 6.3 Total current versus load resistance for varying widths of the MEA and both oxygen and air feeds. The effect of changing the feed is diminished with decreasing load resistance and with decreasing MEA width.

Figure 6.4 gives the results from the same experiments shown in Figure 6.3 as the percent change in the current when switching from oxygen to air versus the width of the MEA for each of the three different loads. With the 3/16" and 5/16" wide MEAs, the load resistance has a negligible effect on the impact from switching feeds. The current decreases with the decreased partial pressure of oxygen when switching to air in each

case, but the effect doesn't change with increasing load. The MEAs are narrow enough that the oxygen reaches all of the catalyst even at the lowest load resistance, regardless of the feed. With the wider MEAs (7/16" and 9/16" wide), the decrease in current is much larger at the lowest load resistance as the catalyst is not fully utilized with air as the feed, as discussed above. The effect is the greatest for the widest MEA where there is the most unused catalyst with air. Increasing the load allows the oxygen to diffuse over more of the catalyst layer and the effect of the feed choice is diminished for the wider MEAs.

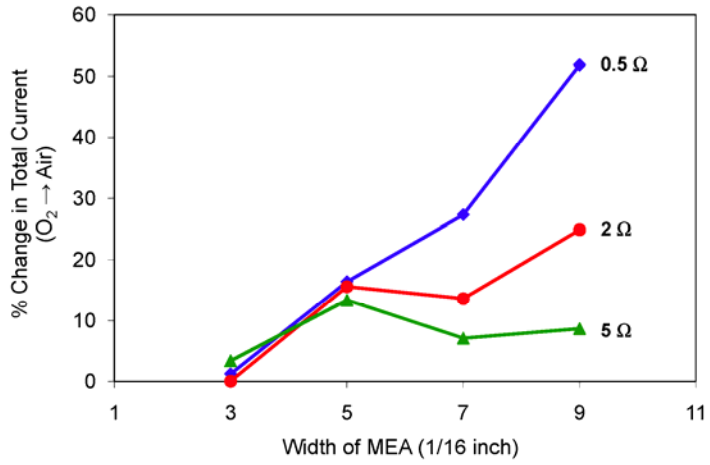

Figure 6.4 Effect of increasing load on the percent change in the total current when switching from an oxygen to an air feed for each of the widths of the MEA. The catalyst is always fully utilized with oxygen. When the catalyst is fully utilized with air, an increase in load does not have an effect. For wider MEAs, the oxygen in air does not reach all of the catalyst at lower loads, but reaches more as the load is increased.

The measurements from the SAPC fuel cell did not isolate the current production under the channel from the current production under the lands. The anisotropic structure of the GDL material causes the gas permeability to be higher in the transverse direction than in the lateral direction.[9, 10] It would thus be expected that the effects described above with changing load resistance are more significant under the land, where the resistance to mass transport is greater, than under the channel. This is something that

should be considered when choosing the dimensions of the channel and lands and can be investigated further with the simple mathematical model presented in the next section.

6.2.2 Mathematical modeling

The difference between the flow of oxygen and the flow of air under the land was examined with a simple mathematical model. As a first approximation, the GDL can be modeled in two dimensions, ignoring gradients along the flow channel, a valid simplification with excess reactants. The fuel cell was symmetric about the middle of the flow channel; only the area under half of the flow channel and one land was considered. A schematic of the model geometry is shown in Figure 6.5.

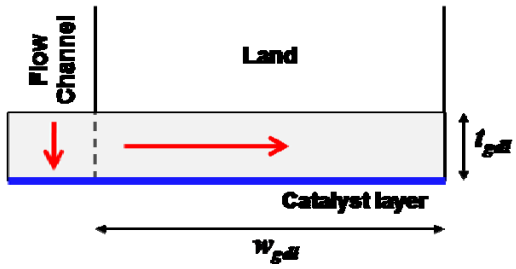

Figure 6.5 Schematic of the geometry used in modeling the flow of reactants under the lands. Only the area under half of the flow channel and one land was considered to take advantage of the symmetry of the system. The gray area indicates the GDL that was modeled. The red arrows indicate the directions of the gradients considered in each part of the GDL.

The flow through the GDL was considered in two parts: the flow under the channel, with the only gradient in the transverse direction, and the flow under the land, with the only gradient considered in the lateral direction along the width of the land. The directions of the gradients are indicated by the red arrows in Figure 6.5. At steady-state, the flux of reactants through the GDL is balanced by the rate of reactant consumption by the electrochemical reaction. With pure oxygen as the feed, the flow through the GDL is

driven by pressure gradients. With air as the feed, the flow of oxygen is limited by diffusion through the inert nitrogen. The rate of consumption is indicated by the current.

To find the current density from only the part of the MEA under the channel, where mass transfer limitations were minimal, the same experimental data from Figure 6.2 were used. For both pure oxygen and air feeds, the best fit line was found for the total current versus the width of the MEA under the land. With air, only the data from the 3/16" and 5/16" wide MEAs were used as the current starts to level off between the 5/16" and 7/16" data points. The y-intercept of the best fit lines (0 width under the lands) gave the contribution to the total current from only the part of the MEA under the channel. For both oxygen and air feeds, the current densities were found to be, respectively,

$$\begin{aligned} j_{O_2} &= 0.092 \text{ A cm}^{-2} \\ j_{air} &= 0.050 \text{ A cm}^{-2} \end{aligned} \tag{6.1}$$

In the absence of mass transfer limitations, the voltage difference due to the difference in partial pressure of oxygen between pure oxygen and air is 10 mV. With an internal resistance of ~0.2 ohms (a well-hydrated membrane), the current difference is ~50 mA, close to the difference in the calculated values in equation (6.1). The mass transfer limitations are minimized under the channel due to the anisotropic structure of the GDL and the order of magnitude difference between the thickness and width of the GDL.

The partial pressure at the catalyst layer under the channel was calculated simply by the balance of the flux through the GDL with the oxygen consumed by the reaction. With pure oxygen as the feed, the concentration does not change; the vapor pressure of water is negligible at 25 ºC (as in the experiments), no other gases are present, and the

entire fuel cell is at ambient pressure. As oxygen is consumed, the flux changes with the decrease in pressure at the catalyst layer. The flow through the porous GDL was modeled with Darcy's law to give the following balance,

$$\frac{\kappa \cdot (w_{ch} l_{gdl})}{\mu \cdot t_{gdl}} \left(P_{O_2}^{ch} - P_{O_2}^{cat} \right) = \frac{j_{O_2}}{4\mathcal{F}} \cdot \left(w_{ch} l_{gdl} \right) \cdot \frac{RT}{P_{O_2}^{cat}} \tag{6.2}$$

where $P_{O_2}^{cat}$ and $P_{O_2}^{ch}$ are the partial pressures of oxygen at the catalyst layer and in the channel, respectively. The $RT/P_{O_2}^{cat}$ term on the RHS of equation (6.2) is the density to keep the units consistent and account for changes in volume with changing pressure. The oxygen partial pressure at the catalyst was used as it was the relevant quantity for the current instead of the pressure in the channel. The temperature was chosen to be 298 K, as in the experiments, so that the vapor pressure of water was negligible and not considered. The ambient pressure and $P_{O_2}^{ch}$ were both equal to 1.013 bar. The definitions of the other variables and their values are given in Table 6.1. Solving for $P_{O_2}^{cat}$ numerically resulted in

$$P_{O_2}^{cat} = 1.013 \text{ bar} \tag{6.3}$$

and showed no change in the pressure within the significant figures.

For the case using air as the oxidant, the flux is through diffusion. The pores are filled with mostly nitrogen; the convective flow is negligible but the concentration of oxygen in the nitrogen changes and drives the diffusion. The partial pressure of oxygen in the channel, $P_{O_2,air}^{ch}$ (where the subscript *air* denotes the choice of feed), was reduced to 0.212 bar due to the inert nitrogen. The flux to the catalyst under the channel was modeled with Fick's law to give the following balance similar to equation (6.2),

Table 6.6.1 Variable definitions and values for the equations in Chapter 6. The subscripts O_2 and *air* denote the choice of feed to the cathode.

Variable	Definition	Value
$P_{O_2}^{ch} \big/ P_{O_2,air}^{ch}$	Partial pressure of oxygen in the flow channel with pure oxygen/air as the feed	1.013/0.213 bar
$P_{O_2}^{cat} \big/ P_{O_2,air}^{cat}$	Partial pressure of oxygen at the catalyst layer with pure oxygen/air as the feed	Function of distance under the lands
$j_{O_2} \big/ j_{air}$	Current density with pure oxygen/air as the feed	0.092/0.050 A cm^{-2}
F	Faraday's constant	96,485 C $(mol\ e^-)^{-1}$
R	Universal gas constant	83.145 cm^3 bar mol^{-1} K^{-1}
T	Temperature	298 K
w_{ch}	Flow channel width	0.159 cm
w_{gdl}	GDL width under the lands	0.635 cm
l_{gdl}	GDL length	5.72 cm
t_{gdl}	GDL thickness	0.0450 cm
κ	GDL permeability	10^{-8} cm^2
μ	Oxygen viscosity @ T	2×10^{-10} bar s
$D_{O_2,air}$	Diffusivity of oxygen in air	0.190 cm^2 s^{-1}
ε	GDL porosity	0.5
τ	GDL tortuosity	1.41

$$\frac{D_{eff} \cdot \left(w_{ch} l_{gdl} \right)}{RT \cdot t_{gdl}} \left(P_{O_2,air}^{ch} - P_{O_2,air}^{cat} \right) = \frac{j_{air}}{4\mathcal{F}} \cdot \left(w_{ch} l_{gdl} \right) \tag{6.4}$$

where the concentration of oxygen in the air is written in terms of the partial pressure as $P_{O_2,air} \big/ RT$. The effective diffusion coefficient, D_{eff}, is calculated by correcting the diffusion coefficient for oxygen in air, $D_{O_2,air} = 0.19\ cm^2\ s^{-1}$, for the porosity and tortuosity of the GDL as

$$D_{eff} = \frac{\varepsilon}{\tau} D_{O_2,air} \tag{6.5}$$

A common value of $\varepsilon = 0.5$ was used for the porosity and the Bruggeman relation, $\tau = \varepsilon^{-0.5}$, was used for the tortuosity.[10, 11] The result showed a small decrease in the oxygen partial pressure at the catalyst layer,

$$P_{O_2,air}^{cat} = 0.208 \text{ bar} \tag{6.6}$$

The calculations for the flow under the lands were slightly different as the oxygen was consumed along the entire width of the GDL, not just at the end as when considering the transverse flux under the channel. As the oxygen is consumed, the partial pressure of oxygen at the catalyst layer is decreased. The local current density is a function of the pressure above the catalyst and can be calculated with the same equations used in the STR model described in Chapter 4.

For these calculations, a 1 cm^2 area is assumed (allowing for the current and current density to be numerically interchangeable) and the oxygen partial pressure is assumed to be uniform over the area. In an actual fuel cell, the partial pressures and local current density varies over the active area. The voltage across the external load resistor is dependent on the total current, or the sum of the local currents over the entire area, as in the TIS model. The total current is dependent on the design of the fuel cell including the total area of catalyst being utilized and the decrease in oxygen partial pressure under the lands. For simplification, only the dependence of the local current density on the oxygen partial pressure without design considerations is given here. This does not effect the later calculations, as will be discussed below.

With the simplifications mentioned above, the battery voltage is a function of the reactant partial pressures as given by the following equation (equivalent to equation (4.4) where the gas phase activities are written as partial pressure over total pressure),

$$V_b = \frac{-\Delta G^o}{4\mathfrak{F}} + \frac{RT}{4\mathfrak{F}} \ln\left[\frac{\left(P_H^{anode}\right)^2 P_O^{cathode}}{\left(a_w^{cathode}\right)^2 \left(P_{tot}\right)^3}\right] \tag{6.7}.$$

For the purposes of this model, the hydrogen and water activities are assumed to be constant at 1. These assumptions are plausible as the experiments were run with the hydrogen in excess and with a well-hydrated membrane. The activity of oxygen can be written in terms of the oxygen partial pressure above the catalyst layer and the current density by assuming a steady balance between the oxygen transported to the catalyst and the oxygen consumed by the reaction (equivalent to equation (4.18)),

$$k_O\left(P_O - P_O^{cathode}\right) = \frac{j}{4\mathfrak{F}} \tag{6.8}$$

Substituting equation (6.8) into equation (6.7) gives the battery voltage in terms of the oxygen pressure and current density,

$$V_b = \frac{-\Delta G^o}{4\mathfrak{F}} + \frac{RT}{4\mathfrak{F}} \ln\left(\frac{P_O - \dfrac{j}{4\mathfrak{F} \cdot k_O}}{P_{tot}}\right) \tag{6.9}$$

The battery voltage and the current density are also related through the equivalent circuit (equivalent to equation (4.7); see Figure 4.1),

$$j = \frac{V_b - V_d}{\left(R_{mem} + R_L\right) \cdot 1\ \text{cm}^2} \tag{6.10}$$

Substituting equation (6.9) for the battery voltage and ignoring the diode voltage (for simplicity) leads to the final expression for the dependence of the current density on the oxygen partial pressure,

$$j = \frac{\frac{-\Delta G^o}{4\mathcal{F}} + \frac{RT}{4\mathcal{F}} \ln\left(P_O - \frac{j}{4\mathcal{F} \cdot k_O} \right)}{R_{mem} + R_L} \tag{6.11}$$

The value for the membrane resistance was calculated by a fit to the experimental data shown in Figure 6.2. The STR and TIS models described in Chapter 4 employed an empirical relation for the dependence of the membrane resistance on water activity, but these models were only semi-quantitative and did not account for other internal resistances. The membrane was well hydrated in each experiment, so changes in the membrane resistance with changing water activity were minimized. For the calculations, the value for j in equation (6.11) was set equal to the contribution to the total current from only the area of the MEA under the flow channel, given in equation (6.1). The oxygen partial pressure in the feed was used for P_O. The value of R_{mem} was calculated to be 6.0 Ω cm^{-2}.

The dependence of the current density on the oxygen partial pressure, as given by equation (6.11), is shown in Figure 6.6 (blue curve). At high partial pressures of oxygen (above ~0.5), the current density is fit with a straight line (green curve), with a value of 0.092 A cm^{-2} with pure oxygen. The equation for the linear fit is dependent on the external load resistance, the independent parameter. An increase in load resistance causes the blue curve to shift lower and remain linear to lower partial pressures; a decrease in load resistance has the opposite effect. At low oxygen partial pressures, the numerical solution of equation (6.11) begins to drop off and become unstable as the

current is mass transfer limited; the term $\left(P_O - {}^{j}\!/\!_{\left(4\mathcal{F}\cdot k_O\right)}\right)$ approaches zero and the logarithm becomes negative. The solution to $j = P_O \cdot \left(4\mathcal{F}\cdot k_O\right)$ is used as a linear approximation (red curve) and accurately predicts the value of 0.05 A cm^{-2} at a pressure of 0.21 bar calculated from experimental data. The solution at low partial pressures is not dependent on the load resistance. The linear approximation at the higher partial pressures would introduce some error into the calculations due to the changing current density under the lands invalidating the assumption of a constant current density. However, with oxygen as the feed, the change in oxygen partial pressure and current density is not significant and this is not an issue. The linear approximation at low current densities does not depend on the voltage across the external load resistor and the assumption of a constant current density is still valid.

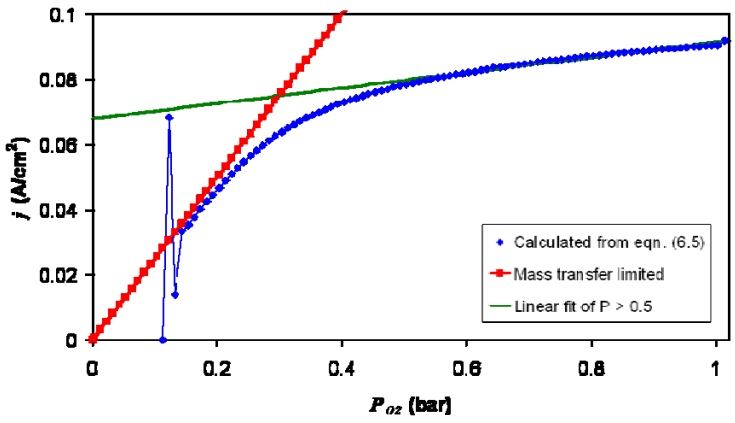

Figure 6.6 Results from equation (6.11). The numerical solution (blue) drops off and becomes unstable at low oxygen partial pressures where the current is mass transfer limited. Two linear fits—one at high partial pressures (green) and one at low partial pressures where the current is mass transfer limited (red)—are acceptable predictions to the exact solution.

The current density under the lands was found from the linear fits shown in Figure 6.6 while the oxygen pressure at the catalyst was a function of *x*, the distance under the

land from the flow channel/land interface. The general mass balance over an element of length *dx* is simply

$$\left(\text{net flux in at } x\right) - \left(\text{net flux out at } x+dx\right) = \begin{pmatrix} \text{rate of reaction} \\ \text{between } x \text{ and } x+dx \end{pmatrix} \tag{6.12}$$

With pure oxygen as the feed, Darcy's law is again used with the same parameters as in Table 6.1. For this simple model, the value of the permeability was not varied for the calculations under the land and under the channel. The maximum difference between the transverse and lateral permeabilities found in the literature was only a factor of two[10] and would not cause a significant change in the following calculations. The mass balance and resulting differential equation are

$$-\frac{\kappa\cdot\left(t_{gdl}l_{gdl}\right)}{\mu}\frac{dP_{O_2}}{dx}\bigg|_{x} + \frac{\kappa\cdot\left(t_{gdl}l_{gdl}\right)}{\mu}\frac{dP_{O_2}}{dx}\bigg|_{x+dx} = \frac{j_{O_2}\cdot l_{gdl}\cdot dx}{4\mathcal{F}\cdot\rho_{O_2}/32} \tag{6.13}$$

$$\frac{d^2P_{O_2}}{dx^2} = \lambda_{O_2} \tag{6.14}$$

$$\lambda_{O_2} = \frac{j_{O_2}\cdot\mu}{4\mathcal{F}\cdot t_{gdl}\kappa\cdot\rho_{O_2}/32} \tag{6.15}$$

The two boundary conditions are the concentration of oxygen at the catalyst under the channel and the no-flux condition at the outer edge of the GDL. The boundary conditions are defined with $x = 0$ at the outer edge and $x = w_{gdl}$ at the channel/land interface to simplify the calculations,

$$\begin{aligned} P_{O_2} &= P_{O_2}^{ch} = 1.013 \text{ bar at } x = w_{gdl} \\ \frac{dP_{O_2}}{dx} &= 0 \text{ at } x = 0 \end{aligned} \tag{6.16}$$

With pure oxygen as the feed, the change in pressure under the lands is very small. The current density is assumed to be constant and equal to the same current density under the

channel, 0.092 A cm^{-2}. The solution for the pressure of oxygen at the catalyst under the land is

$$P_{O_2} = P_{O_2}^{ch} + \frac{\lambda_{O_2}}{2}\left(x^2 - w_{gdl}^2\right) \tag{6.17}$$

With air as the oxidant, the mass balance was very similar to equation (6.13), but dependent on the diffusion coefficient instead of the parameters of Darcy's law (permeability and viscosity). The same tortuosity from Table 6.1 was used in the following calculations; data accounting for the anisotropic structure of the GDL in calculating the tortuosity is not available. The mass balance with air is,

$$-\frac{D_{eff}\cdot\left(t_{gdl}l_{gdl}\right)}{RT}\frac{dP_{O_2,air}}{dx}\bigg|_x + \frac{D_{eff}\cdot\left(t_{gdl}l_{gdl}\right)}{RT}\frac{dP_{O_2,air}}{dx}\bigg|_{x+dx} = \frac{j_{air}}{4\mathcal{F}}\cdot l_{gdl}dx \tag{6.18}$$

The partial pressure of oxygen was much smaller with air, so that the current density could not be assumed constant. Even with the feed partial pressure of 0.21, the current density is mass transfer limited and the equation of the linear fit in Figure 6.6 (red curve), $j_{air} = 0.2508\cdot P_{O_2,air}$, is used. The resulting differential equation is,

$$\frac{d^2P_{O_2,air}}{dx^2} = \left(\lambda_{air}\right)^2 P_{O_2,air} \tag{6.19}$$

$$\lambda_{air} = \left(\frac{0.2508\cdot RT}{4\mathcal{F}\cdot D_{eff}\cdot t_{gdl}}\right)^{1/2} \tag{6.20}$$

The two boundary conditions are the same as with pure oxygen,

$$\begin{aligned} P_{O_2,air} &= P_{O_2,air}^{ch} = 0.212 \text{ bar at } x = w_{gdl} \\ \frac{dP_{O_2,air}}{dx} &= 0 \text{ at } x = 0 \end{aligned} \tag{6.21}$$

The solution for the concentration of oxygen under the land with air as the feed is then

$$P_{O_2,air} = P_{O_2,air}^{ch} \cdot \left[\frac{\cosh\left(\lambda_{air} x\right)}{\cosh\left(\lambda_{air} w_{gdl}\right)} \right] \tag{6.22}$$

The results of equations (6.17) and (6.22) are shown in Figure 6.7. Part (a) gives the calculated oxygen partial pressures as a function of the distance from the middle of the flow channel. There is no noticeable change in the pressure with pure oxygen as the feed. The flux through the pores of the GDL is substantial enough to compensate for the oxygen consumption at the catalyst. The reduced partial pressure of oxygen in the flow channel and the slower flux with air as the feed causes all of the oxygen to be consumed by about 3/16" under the land from the channel/land interface. The difference is also indicated in the λ values; $\lambda_{air} = 3.36$ is over 1000 times greater than $\lambda_{O_2} = 0.0026$.

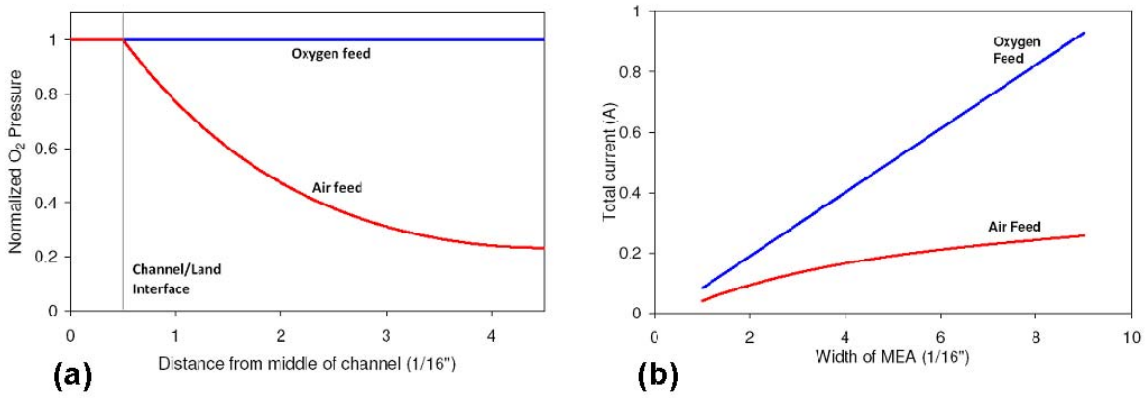

Figure 6.7 Results from modeling the flow of oxygen under the land. With oxygen as the cathode feed, the flux is pressure-driven and modeled by Darcy's law (blue curves).With air as the cathode feed, the flux is driven by diffusion of the oxygen through nitrogen (red curve). **(a)** The calculated oxygen partial pressure as a function of the distance under the land from the middle of the flow channel. The values are normalized by the oxygen pressure at the catalyst layer under the land for clarity, given the large difference between the pressures with an oxygen feed (1.013 bar) and with an air feed (<0.21 bar) **(b)** Calculation of the total current based on the calculated currents with the given partial pressures. The results agree well with Figure 6.2.

Part (b) of Figure 6.7 shows the calculation of the total current versus the total width of the MEA for comparison with Figure 6.2. The calculated results show a good fit

to the experimental data. With a pure oxygen feed, the current continues to increase linearly with MEA width; increasing the width of the MEA would continue to increase the current up to very large widths. With an air feed, the current levels off with increasing MEA width; increasing the width of the MEA under the lands beyond about 6/16" does not increase the current significantly.

Often the complexity of the flow fields found in most fuel cells is justified by the need to evenly distribute the reactants. The results from this and the previous section show that the distribution of reactions is highly dependent on the choice of feed. Air requires wider channels or thinner lands to fully utilize all of the catalyst. The structure properties of the GDL, such as porosity and tortuosity, have a large impact on the distribution of the reactant. The currents with air as the cathode feed are generally lower than with a pure oxygen feed so that larger active areas are required. Pure oxygen flows quickly through the GDL. The channel/land width ratio and GDL properties are much less important. Factors such as fuel cell weight and water removal should determine the optimal flow field design when pure oxygen is used for the cathode feed.

6.2.3 Implications for design

The choice between using oxygen or air for the oxidant has several implications. In order to supply the same amount of oxygen, higher flow rates are needed when using air versus when using pure oxygen. Under hydrated conditions, this can be beneficial as water droplets and slugs will be removed more quickly and have less of an impact on the local current density as they move towards the outlets. On the other hand, if the fuel cell is in a dry state, such as during start-up or when driving a high load, the increased water removal can cause the membrane to dry out and the fuel cell to extinguish. This effect is

amplified by the decreased partial pressure of oxygen with air; the currents are generally lower with air and water is produced at a slower rate.

Independent of the operating conditions is the consideration of flow field design. The catalyst is a very expensive component of the fuel cell and should be completely utilized for optimal operation. Figure 6.2 shows that the optimal flow channel width and spacing is dependent on whether the fuel cell will be operated with oxygen or air. With oxygen, the channels can be farther apart; the pressure difference drives the oxygen well under the lands. All of the catalyst is utilized, at least with the carbon cloth GDL and to the limits of the 9/16" wide MEA possible with the SAPC fuel cell. With the linear increase of the total current with MEA width, the limiting factors will become the ability to remove the water from under the lands and the ability to supply enough reactants. With the diffusion-limited transport with air, increasing the width of the MEA beyond 5/16" (1/8" under each land on either side of the flow channel) to 7/16" allowed for only a small increase in total current. No improvement was observed with an increase to 9/16" total width. Using air as the cathode feed requires channels to be closer together (narrower lands) in order to make full use of the catalyst layer. The diffusion of oxygen through the nitrogen-filled pores is the limiting factor; an increase in feed flow rate or decrease in channel width will not increase the utilization of the catalyst.

The results of equation (6.11) (see Figure 6.6) also show how other factors of the fuel cell design influence the utilization of the catalyst under the lands. The parameter that is explicitly set in the system is the external load resistance (the voltage of the fuel cell is not an independent parameter and is not a variable in equation (6.11)) An increase in the external load resistance lowers the current at high pressures of oxygen and

decreases the pressure where the current becomes mass transfer limited. This can be approximated by the intersection of the two linear fits (red and green curves) in Figure 6.6. The partial pressure of oxygen can also be significantly deceased by the presence of water vapor at elevated temperatures. With consumption of oxygen, especially with the long channels usually employed in fuel cells, the current can become mass transfer limited even with pure oxygen as the feed. This analysis shows a large benefit with using pure oxygen rather than air and indicates that the cost of the catalyst not utilized with air as the feed may be more than the cost of separating the oxygen from the air prior to being fed to the fuel cell. Air is often used for convenience and availability, but the choice of feed needs to be analyzed thoroughly.

6.3 Land surface properties

The complementary issue to lateral flow of gas under the lands is the lateral flow of water produced under the lands to the flow channel. Figure 6.8 shows the three steps of water removal from the fuel cell. First, water is produced at the catalyst layer on the cathode side of the fuel cell. The water accumulates at the catalyst layer until a high enough pressure builds up to overcome the hydrophobic surface tension of the GDL pores. The water then flows through the largest pores where the resistance to flow is minimized. This was discussed extensively in Chapter 5. If the largest pore is under the land, the second step is the flow of water along the contact line between the GDL and land surface, highlighted in red in Figure 6.8. The surface properties of the materials affect the flow of water to the flow channel and are discussed in the following section. If the largest pore is under the channel, the water does not interact with the land surface and the second step is skipped. The third step is the transport of water in the flow channel.

The importance of the fuel cell orientation with respect to gravity and the gas flow rates for the effectiveness of liquid water is removal were discussed in Chapter 3. The transport of water in the flow channel is also determined largely by the interaction of the water with the channel walls, highlighted in green in Figure 6.8. The effects of changing the surface properties of the channel walls are discussed in Section 6.4.

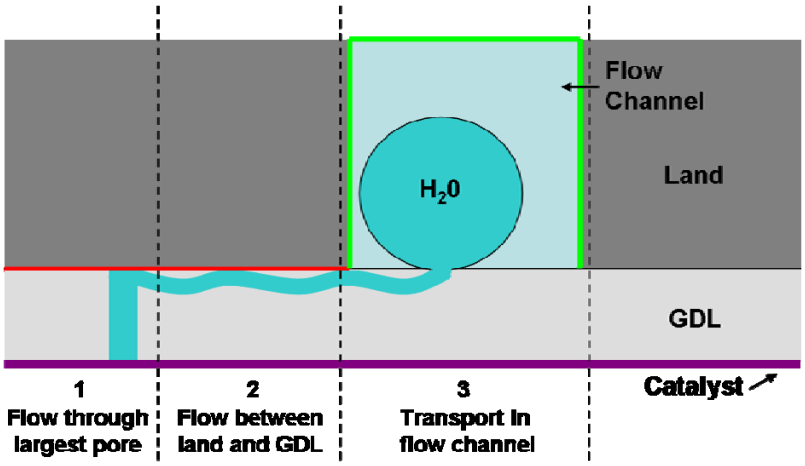

Figure 6.8 Schematic of the three steps of water removal from the fuel cell. 1: The water flows from the cathode catalyst later through the largest pore of the GDL. 2: When the largest pore is under the land, the water flows between the land and GDL surface, highlighted in red. 3: The water flows through the flow channel to the outlets, where it interacts with the flow channel walls, highlighted in green. How effectively the water is removed is determined by the properties of the highlighted surfaces.

With both carbon cloth and carbon paper, the largest pores are in the transverse direction; it is much easier for the water to flow transversely than laterally. When the largest pores are under the land, the water will come into contact with the surface of the electrodes and flow along the interface between the lands and surface of the GDL to reach the flow channel and be removed from the fuel cell. An additional consideration is that the channels are usually carved out of a plate; the material that contacts the GDL is the same as that making up the channel walls. Hydrophilic channel walls may be beneficial to wick water away from the surface of the GDL, but hydrophilic lands may

allow for water to interrupt the electrical conduction path from the GDL through the lands.

The SAPC fuel cell was a unique tool for studying the effects of the material surface properties. Stainless steel was used for the electrodes and polycarbonate made up the back of the flow channel; the surface properties of the lands were separate from those of the flow channel. The changes in the local currents measured with the six different segments gave indications of where liquid water was accumulating in the fuel cell. Additionally, with the ability to change the orientation of the fuel cell, the effects of water accumulation under the lands could be separated from accumulation in the flow channel. Gravity and the gas shear force cause liquid water drops to accumulate and move when in the flow channel. At the interface between the GDL and lands, though, the surface properties of the materials are the larger factor.

The experiments presented in this section are not conclusive, but suggest an array of future experiments. Factors that are not discussed widely in the literature are shown to have large effects on the experimental results. These results show that the surface properties of the electrodes need to be considered between experiments to ensure the correct interpretation of the data.

6.3.1 Experimental results

The effects of changing the surface properties of the lands were investigated with the SAPC fuel cell with both new and used MEAs and with the surface of the electrodes treated to be both more hydrophobic and more hydrophilic. As an MEA is used in multiple experiments—being taken out of the fuel cell, rehydrated, and dried, and put back into the fuel cell—the Teflon coating on the carbon fibers can deteriorate. A new

MEA probably has a more hydrophobic surface than a used MEA (though any systematic measurements of the surface properties of MEAs as a function of running time were not found). The hydrophobicity of the lands was altered by applying either a Rain-x coating (a silicone based material that forms a film over the surface) to make the surface more hydrophobic or an anti-fog surfactant coating (also made by Rain-x) to make the surface more hydrophilic.

The surface properties of the lands and MEA change where water accumulates. Water accumulation has been observed in the flow channels in several previous experiments. The openings of the pores of the GDL can be blocked by liquid water, preventing reactants from flowing to the catalyst layer and causing fluctuations in the local currents. The degree of flooding in the flow channel can be minimized by orienting the fuel cell so that gravity assists in removing the liquid water. Alternatively, water can accumulate under the lands, at the contact line between the land surface and GDL. More hydrophilic lands that allow for the flow of water under the lands leaves the surface of the GDL open for gas flow. The orientation of the fuel cell is much less important in determining the current distribution.

Carbon paper was used for the GDL of each MEA used in the experiments discussed in this section. The conditions were set to maximize liquid water production (load resistance = 0.5 Ω, temperature = 298 K). Untreated electrodes, electrodes treated with a hydrophobic coating, and electrodes treated with a hydrophilic coating were all tested. The new MEAs (having been used in only one or two experiments) were tested only with untreated electrodes. The flow channel walls were not treated and so were slightly hydrophilic. The orientation of the fuel cell was either the “cathode down”

orientation so that gravity made the liquid water droplets detach from the surface of the GDL and fall to the back of the flow channel, or the "cathode up" orientation so that gravity held the water at the surface of the GDL and impeded its removal at the outlets (see Chapter 3). The MEAs were modified by creating a single pore larger than the intrinsic pore sizes in the carbon paper GDL on the cathode side (just as in the experiments discussed in Chapter 5). The large pore was positioned both under the flow channel and under the lands, but was always placed closer to the inlets (3/4" from the end of the GDL). The local and total currents with a reactant feed stoichiometry close to 1 are given in Table 6.2.

Table 6.2 Local and total currents for several configurations of the SAPC fuel cell and varying electrode surface properties.

Orientation	Large pore location	Electrode surface	Segment current (A)						Total current (A)
			1	2	3	4	5	6	
Cathode down	Under land	Untreated	0.1497	0.1775	0.1261	0.1338	0.1474	0.1461	0.8806
		Hydrophobic	0.1824	0.1949	0.1281	0.1044	0.0956	0.0919	0.7974
		Hydrophilic	0.1425	0.1400	0.1345	0.1296	0.1297	0.1094	0.7858
		New MEA	0.1533	0.1726	0.1552	0.1516	0.1444	0.1281	0.9052
	Under channel	Untreated	0.1638	0.1750	0.1427	0.1556	0.1543	0.1693	0.9607
		Hydrophobic	0.1538	0.1622	0.1423	0.1426	0.1465	0.1483	0.8959
		Hydrophilic	0.1375	0.1244	0.1311	0.1394	0.1412	0.1246	0.7981
		New MEA	0.1782	0.1870	0.1616	0.1472	0.1471	0.1442	0.9653
Cathode up	Under land	Untreated	0.1513	0.1833	0.1500	0.1515	0.1415	0.1474	0.9250
		Hydrophobic	0.2290	0.1648	0.0864	0.0479	0.0354	0.0236	0.5871
		Hydrophilic	0.1664	0.1449	0.0866	0.0683	0.0805	0.0873	0.6341
		New MEA	0.1958	0.1329	0.0573	0.0338	0.0223	0.0178	0.4599
	Under channel	Untreated	0.1679	0.1769	0.1392	0.1388	0.1540	0.1769	0.9537
		Hydrophobic	0.1953	0.1950	0.1499	0.1125	0.0942	0.0763	0.8232
		Hydrophilic	0.1871	0.1231	0.0656	0.0598	0.1035	0.1363	0.6754
		New MEA	0.2438	0.1632	0.0683	0.0312	0.0179	0.0120	0.5364

The lowest currents, as low as 0.46 A, are observed with the fuel cell in the "cathode up" orientation and with the large pore under the land. With the other configurations, the total current ranges from 0.79 to 0.96 A. The distribution of the currents gives a better indication of the degree of liquid water accumulation. This was

described more concisely by defining the "spread" of the currents, as described in the next section.

6.3.2 Analysis

The effects of these coatings and the MEA surface properties were measured by the "spread" of the currents caused by liquid water accumulation. Here, spread is defined similar to the standard deviation of the individual segment currents. More precisely, the total current from the fuel cell before any flooding occurred was divided by 6 to give the average stable current. For a given point in time, the absolute value of the deviation of each of the segment currents from the average stable current were summed to give the spread. In an ideal system, the current distribution would be uniform and the spread would equal zero. As flooding occurs, some currents are decreased with the extra mass transfer resistance and others are increased as the currents redistribute, both of which increase the spread. The total current can also be greatly decreased with more severe flooding, further increasing the spread.

Figure 6.9 shows how the spread can change between configurations even though the total currents are almost equivalent. The two curves show the current from each of the six segments for the configuration with the "cathode down" orientation, with the large pore under the land, and with either hydrophobic electrodes (blue curve) or hydrophilic electrodes (red curve). With the hydrophobic electrodes, more water is expelled into the flow channel. Slugs must be formed for the water to be removed, causing the currents to be lower closer to the outlets (segment 6) and higher closer to the inlets (segment 1) after the redistribution. With the hydrophilic electrodes, more water can flow between the surface of the lands and the GDL so that the water has less impact on the flow of

reactants to the catalyst. The current distribution is more uniform. The difference in uniformity between the two current distributions is seen by the distance of each of the points from the average segment current, shown by the dashed gray line. The sum of those distances over the six segments for each curve gives the spread. With the hydrophobic electrodes, the spread is 0.24 A, almost five times greater than that with the hydrophilic electrodes of 0.056 A.

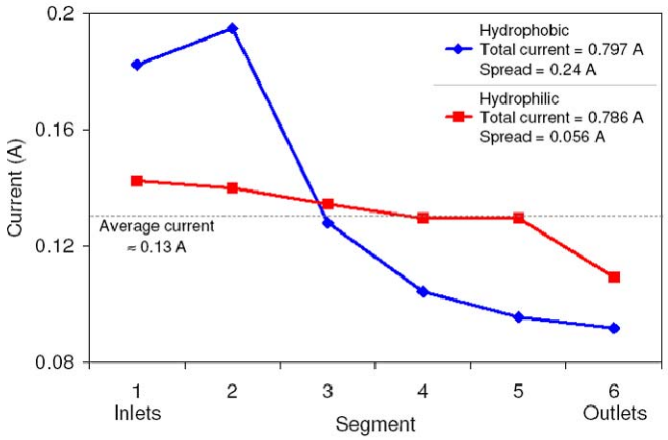

Figure 6.9 Current profile curves for both hydrophobic (blue) and hydrophilic (red) electrodes. The total currents are about the same, but the increased water accumulation with the hydrophobic electrodes causes the currents to be much more widely distributed. The difference in the distribution is captured by the value of the "spread." Experimental parameters: "cathode down" orientation, large pore under the land, load resistance = 0.5 Ω, temperature = 298 K.

Figure 6.10 shows how the spread changes for all of the different configurations of the SAPC fuel cell tested. The values are the steady-state values between any fluctuations in the currents during the starvation stage of the experiment. Error bars are not given but rather the analysis is done to understand why such large differences were seen between multiple experiments.

Again, these experiments are preliminary and need to be followed up with several more experiments with a more tailored experimental setup. Still, there are trends seen in

Figure 6.10 that can offer insights into the impact of the electrode surface properties on the accumulation of liquid water in the fuel cell. The first is that the spread with the "cathode up" orientation is generally greater than the spread with the "cathode down" orientation. This is expected as more water accumulates on top of the GDL and blocks the flow of oxygen to the catalyst with the "cathode up" orientation. This was discussed thoroughly in Chapter 3.

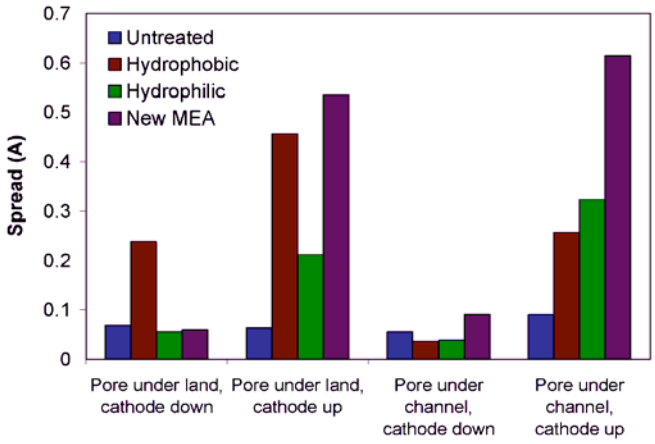

Figure 6.10 Comparison of the spread for several different configurations of the MEA and varying the hydrophobicity of the lands. The MEA was constructed from carbon paper in each case. Experimental parameters: load resistance = 0.5 Ω, temperature = 298 K.

The second main observation is that the largest spreads occur with either the new MEAs or the hydrophobic treated electrodes. The GDL is always hydrophobic, but probably to a larger degree when it is new. In both of those cases, more water is expelled into the flow channel where it can block the flow of reactants from the flow channel into the pores of the GDL and to the catalyst layer. With the electrodes coated to be hydrophilic, high spreads are also observed with the fuel cell in the "cathode up" orientation. The water can flow under the lands, but still must accumulate in the flow channel to form a slug that can then be removed through the outlet tube against gravity.

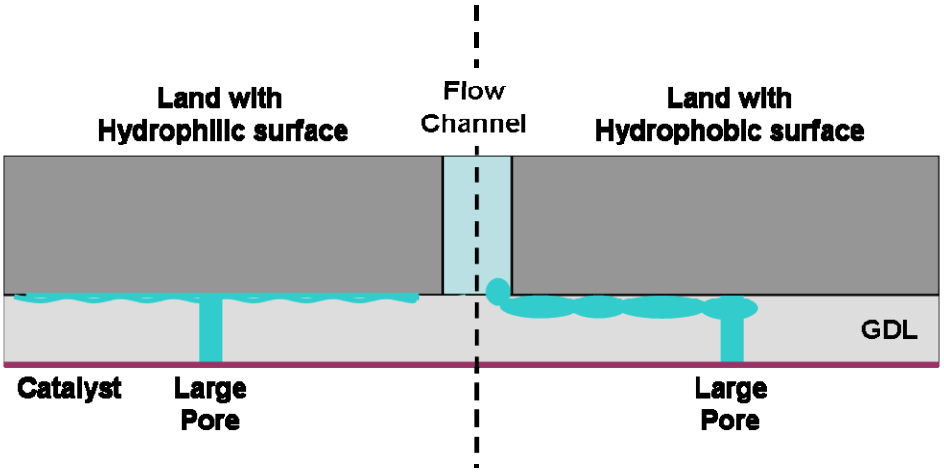

Figure 6.11 Schematic of water flow under the lands with the two different treatments of the electrode surface, either increased hydrophobicity or increased hydrophilicity. A more hydrophilic surface allows the water to flow between the land and GDL. A more hydrophobic surface causes the water to be expelled into the flow channel where it can cause flooding.

A schematic of how the water is thought to flow under the lands with the two different treatments of the electrode surfaces is shown in Figure 6.11. With a more hydrophilic surface, the water can spread out under the lands and not accumulate in the flow channel to block the reactant flow and cause flooding. A hydrophobic surface will repel the water and in combination with the hydrophobic GDL, the water will be expelled into the flow channel. Water accumulation in the flow channel is the cause of flooding that impacts the local current production in the fuel cell.

These results highlight the difficulty in identifying the optimal configuration for a fuel cell system. Flooding may not occur as easily with more hydrophilic lands and with the water forced to flow under the land. Yet, if water does accumulate under the lands, it is not removed as easily. Convection is greatly reduced, so the water must evaporate and diffuse through the GDL to reach the flow channel. At the same time, the effects of gravity are largely negated. This could be beneficial for systems where the orientation of

the fuel cell may change drastically. On the other hand, gravity cannot be exploited to assist in the removal of liquid water.

The possible benefits of using gravity are shown clearly in the third group of Figure 6.10. The results are for the "cathode down" orientation and a large pore was artificially created under the channel; most of the liquid water flowed directly into the channel and was pulled to back of the flow channel by gravity. This configuration of the fuel cell greatly decreased the effects of liquid water accumulation. There were only very little fluctuations (not shown) in the currents and the spread was low. The effects of the surface properties of the lands and hydrophobicity of the MEA were diminished as the water emerged from the surface of the GDL exposed to the flow channel and fell to the back surface.

Future experiments may prove that the surface properties of the materials should be chosen to either increase or decrease the importance of gravity to ensure optimal operation of the fuel cell. Manipulation of the MEA surface properties may also be an option for controlling liquid water flow, but is beyond the scope of this work.

6.4 Flow channel hydrophobicity

In each of the experiments discussed in the previous section, stainless steel plates made up the lands and the two sides of the flow channel. Only the surface contacting the GDL was treated to become more or less hydrophobic. The polycarbonate block into which the plates were pressed made up the back side of the flow channel. The surface of the machined polycarbonate was slightly rough and that caused it to be hydrophilic. It could be chemically polished with dichloro-ethane to make the surface hydrophobic, (the original purpose of chemical polishing was to improve optical clarity). The effect of the

dichloro-ethane on the side walls of the channel (made up of stainless steel) is unclear. The contact of water on the stainless steel did not appear to change after the stainless steel side walls were exposed to the dichloro-ethane (based on simple visualization with the disassembled SAPC fuel cell). This is a factor that can be studied better in future experiments, perhaps with modifications to the flow channel construction.

Figure 6.12 shows how water (dyed red for better visualization) spread out along the back surface of the flow channel when simply added with a pipette. Part (a) is a frame taken from a video when adding a small amount of water to the machined (unpolished) channel; part (b) is with the polished polycarbonate.

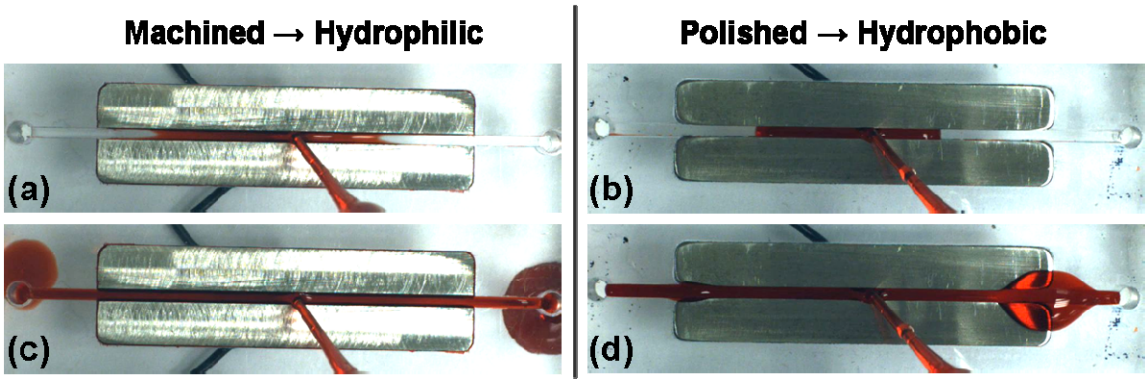

Figure 6.12 Frames from videos showing water being added to the flow channel with the flow channel machined (unpolished) (parts a and c) and chemically polished (parts b and d).

The hydrophilicity of the unpolished channel causes the water to wick along the channel, especially at the corners, and spread out as a thin film (part (a)). This is also indicated by the parabolic curvature at the water/channel interface. As the channel starts to fill up, the water is pushed out through the holes at the ends of the channel where the inlet and outlet tubes would be connected; part (c) shows the water droplets caught by paper placed under the fuel cell after falling out of the outlet holes.

The behavior of the water was significantly different with the polished channel. The hydrophobicity of the polished polycarbonate holds the water together as a large drop that fills the depth of the channel (part b). The water/channel interface is flat with the water not wetting the polished channel. As the channel fills with water and is not pushed by any gas flow, the surface energy keeps the water from flowing out of the holes and it starts to rupture from the top of the flow channel (part d). In an operating fuel cell, this changes how well the water is kept away from the surface of the GDL and eventually removed at the outlets.

Again, the results in this section are not conclusive. The information is intended to show the dramatic effects that changing the surface properties of the channel can have on the fuel cell operation. The flow channels are usually carved into the plates that make up the lands that contact the GDL and provide the electrical conduction path. In the literature, attention is given to the conductivity, cost, and durability of the flow field plates. The effects of the surface properties of the machined channels are not widely discussed.

6.4.1 Experimental results

The effects of changing the surface properties of the flow channel were again investigated with the SAPC fuel cell. The two fuel cells pictured in Figure 6.12—one with a chemically polished channel and one with a freshly machined channel—were used and setup in the same two orientations as in Section 6.3, “cathode down” and “cathode up”.

Carbon paper was used for the GDL of each MEA and the conditions were set to maximize liquid water production (load resistance = 0.5 Ω, temperature = 298 K). The

MEAs were modified by creating a single pore larger than the intrinsic pore sizes in the carbon paper GDL on the cathode side (just as in the experiments discussed in Chapter 5). The large pore was made to be both under the flow channel and under the lands. The pore was introduced 3/4" from the end of the GDL with that end placed either closer to the inlets or closer to the outlets. The local and total currents with a reactant stoichiometry close to 1 are given in Table 6.3. The total currents versus configuration are plotted in Figure 6.13.

Table 6.3 Local and total currents for several configurations of the SAPC fuel cell with both polished and unpolished, machined flow channels.

Orientation	Large pore location	Channel surface	Segment current (A)						Total current (A)
			1	2	3	4	5	6	
Cathode down	Under land, near inlets	Polished	0.1353	0.2111	0.1430	0.1226	0.0507	0.0898	0.7525
		Machined	0.1497	0.1775	0.1261	0.1338	0.1474	0.1461	0.8806
	Under land, near outlets	Polished	0.0069	0.0072	0.0065	0.0062	0.0060	0.0066	0.0394
		Machined	0.1602	0.1668	0.1302	0.1364	0.1424	0.1509	0.8869
	Under channel, near inlets	Polished	0.1052	0.1304	0.0688	0.0431	0.0268	0.0228	0.3971
		Machined	0.1638	0.1750	0.1427	0.1556	0.1543	0.1693	0.9607
	Under channel, near outlets	Polished	0.1178	0.1984	0.1274	0.0834	0.0533	0.0462	0.6264
		Machined	0.1682	0.1892	0.1384	0.1300	0.1431	0.1871	0.9560
Cathode up	Under land, near inlets	Polished	0.1572	0.1303	0.0723	0.0573	0.0708	0.0741	0.5621
		Machined	0.1513	0.1833	0.1500	0.1515	0.1415	0.1474	0.9250
	Under land, near outlets	Polished	0.0057	0.0052	0.0054	0.0053	0.0052	0.0053	0.0321
		Machined	0.1541	0.1759	0.1336	0.1328	0.1454	0.1500	0.8917
	Under channel, near inlets	Polished	0.1100	0.1499	0.0835	0.0524	0.0353	0.0337	0.4649
		Machined	0.1679	0.1769	0.1392	0.1388	0.1540	0.1769	0.9537
	Under channel, near outlets	Polished	0.0050	0.0049	0.0049	0.0047	0.0053	0.0052	0.0300
		Machined	0.2135	0.1463	0.0611	0.0343	0.0221	0.0202	0.4975

The total currents vary much more with changing the channel surface than with changing the electrode surface. The fuel cell actually fails in a few cases, indicated by a total current of <30 mA. Failure occurs with the fuel cell in the "cathode up" orientation with the polished channel and the large pore near the outlets both under the land and under the channel. In the "cathode up" orientation, the water must form a slug in the flow channel to be pushed against gravity through the outlet tubes in order to be removed.

The polished, hydrophobic channel hinders slug formation and causes greater water accumulation in the flow channel.

Failure is also observed in the "cathode down" orientation with the polished channel and the large pore under the land and near the outlets. This was not expected, but probably occurred because of water emerging from under the land, spanning the flow channel, and creating a path for the gas flow between the water and the back of the flow channel.

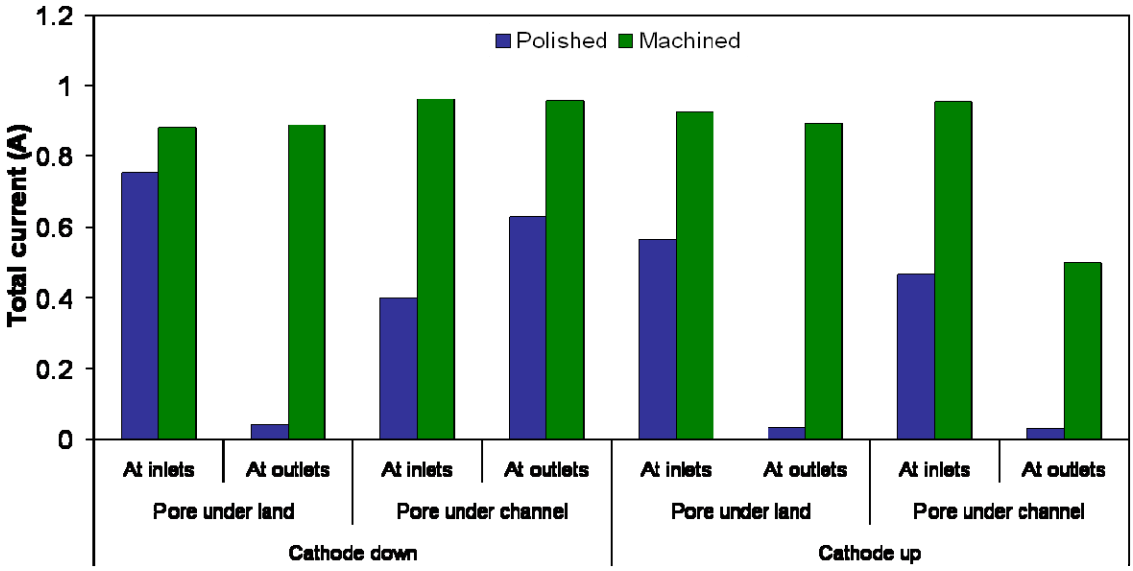

Figure 6.13 Total current versus configuration of the SAPC fuel cell with both polished and unpolished machined channels. A current of about 30 mA indicates complete failure of the fuel cell. Experimental parameters: load resistance = 0.5 Ω, temperature = 298 K.

The currents for the other configurations range from 0.46 to 0.96 A. For a given configuration, the current is always higher with the machined channel than with the polished channel. This suggests that the degree of flooding is consistently increased with a more hydrophobic channel surface.

The fluctuations in the currents are not shown. In every case with the machined channel, the total current changed by no more than 15 mA. With the polished channel, much larger fluctuations were observed without a large dependence on the orientation: 100 – 150 mA fluctuations in the total current with the pore under the land and 60 – 65 mA fluctuations with the pore under the channel. Each setup that resulted in fuel cell failure was with the polished channel and the large pore closer to the outlets.

Calculating the spread of the currents, as in Section 6.3 gives a better and concise way to compare the flooding between the different configurations.

6.4.2 Analysis

The spread of the currents also captures the greater degree of flooding with the polished channel, shown in Figure 6.14. When the fuel cell fails, the currents are much lower than the average current before the failure and the spread is very large, indicating a large degree of flooding. Although the fuel cell does not fail with the other configurations with a polished channel, the spreads are higher than those with the machined channel and the increased flooding is still captured. With the machined channel, the value of the spread shows that introducing the large pore under the channel and close to the outlets causes more flooding than with the pore under the land. This effect is not immediately obvious when only looking at the total current.

Similar to the effects with changing the surface properties of the electrodes, changing the surface properties of the flow channel alters how other factors, such as gravity and GDL properties, control liquid water accumulation and motion. Orientation of the fuel cell is less important when the flow channel is hydrophobic (as seen with the polished channel). With the unpolished machined channel, the orientation is most

significant when the large pore carrying water through the GDL is under the channel. Orientation is less important with hydrophilic channels when placing the water large pore in the GDL under the land.

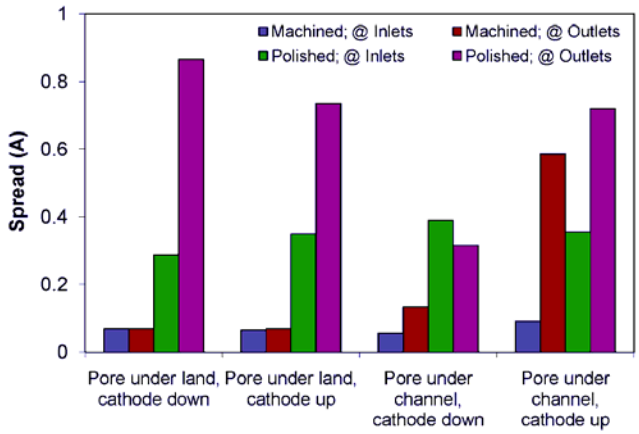

Figure 6.14 Comparison of the spread for several different configurations of the MEA and for the machined and polished flow channels. The MEA was constructed from carbon paper in each case and the lands were not treated. Experimental parameters: load resistance = 0.5 Ω, temperature = 298 K.

The results presented in this chapter extend the experiments discussed in Chapter 5, where the focus was on understanding the influence of making large pores in the GDL to control the path of liquid water. In those experiments, the importance of surface wettability in the gas flow channels was not yet anticipated; the flow channels were polished and the electrodes were not treated in those experiments. The most significant difference between the studies reported in Chapter 5 and here was in the material used for the GDL. The experiments discussed in Chapter 5 all used a carbon cloth GDL whereas those discussed here were all with a carbon paper GDL. Very recent experiments in the Benziger group have shown significant differences with how water flows between the GDL and a plastic surface for the two different materials.[12] With carbon paper, the surface is not as rough and the water can work a path around individual fibers, allowing

for much faster flow from one point into an open plenum. The carbon cloth has a much rougher surface that requires water to be pushed through the bundles of fibers where the spacing is much smaller. The water flow is much more hindered. In an operating fuel cell, this allows water to flow under the lands and over the free surface of the GDL much easier with a carbon paper GDL. Complete failure was observed in several more cases with the experiments discussed in Chapter 6 with carbon paper than when a carbon cloth GDL was used. At the same time, using carbon paper GDLs amplified the effects of the land and channel surface properties.

6.5 Conclusions

The best design of a fuel cell system must take several factors into consideration. Choice of the cathode feed, flow field geometry, land and channel surface properties, and GDL structure all have a large influence on the fuel cell operation. Two separate transport processes must be optimized: the transport of reactants to the catalyst layers and the removal of water out of the fuel cell. Effective transport of water away from the surface of the GDL allows for sustained reactant flow into the GDL from the flow channel. The factors affecting liquid water accumulation are not independent; the surface energies at each of the interfaces, the shear force from the gas flow, the hydrophobic surface tension in the GDL pores, and gravity are all forces that are balanced against each other to determine how well the fuel cell operates.

The SAPC fuel cell was designed to study the accumulation and movement of liquid water in the flow channels and how it affected the local current density. It was also used to begin to study the accumulation and removal of liquid water at the GDL surface, both under the lands or in the flow channel. The experiments presented here have shown

that this is a significant issue; new experiments should be designed and tailored to investigating this problem further. Still, some interesting results were obtained that showed the significance of the land and channel surface properties. There is no single best design, but instead the application of the fuel cell and the different operating parameters should be considered and guide the choice of materials. Stability must be balanced against robustness, just as with the results presented in Chapter 5.

The choice of oxidant is tied in with the issue of water removal as well. The width of the channels and lands should be determined based on how well water will be removed, but also with how well the entire catalyst layer is being utilized. The higher flow rates required with air will remove slugs faster, but will have little effect if the configuration is such that slugs do not readily form. It is possible that the higher flow rates will push more water to the surface of the GDL and lead to failure, an issue that should also be investigated future work.

The interactions between the several factors discussed in this chapter are complex. A thorough understanding of the effects on fuel cell operation requires well designed experiments with both *ex-situ* and model fuel cell setups. The SAPC fuel cell experiments have led to a much better understanding of the physics of the fuel cell operation and can continue to serve as a guide for future work.

6.6 References

1. Wang, Z.H., C.Y. Wang, and K.S. Chen, *Two-phase flow and transport in the air cathode of proton exchange membrane fuel cells.* Journal of Power Sources, 2001. **94**(1): p. 40-50.

2. Weber, A.Z., R.M. Darling, and J. Newman, *Modeling two-phase behavior in PEFCs.* Journal of the Electrochemical Society, 2004. **151**(10): p. A1715-A1727.

3. Mehta, V. and J.S. Cooper, *Review and analysis of PEM fuel cell design and manufacturing.* Journal of Power Sources, 2003. **114**(1): p. 32-53.

4. Ralph, T.R., G.A. Hards, J.E. Keating, S.A. Campbell, D.P. Wilkinson, M. Davis, J. St-Pierre, and M.C. Johnson, *Low cost electrodes for proton exchange membrane fuel cells: Performance in single cells and Ballard stacks.* Journal of the Electrochemical Society, 1997. **144**(11): p. 3845-3857.

5. Wang, L. and H. Liu, *Performance studies of PEM fuel cells with interdigitated flow fields.* Journal of Power Sources, 2004. **134**(2): p. 185-196.

6. Davies, D.P., P.L. Adcock, M. Turpin, and S.J. Rowen, *Stainless steel as a bipolar plate material for solid polymer fuel cells.* Journal of Power Sources, 2000. **86**(1-2): p. 237-242.

7. Wind, J., R. Spah, W. Kaiser, and G. Bohm, *Metallic bipolar plates for PEM fuel cells.* Journal of Power Sources, 2002. **105**(2): p. 256-260.

8. Hermann, A., T. Chaudhuri, and P. Spagnol, *Bipolar plates for PEM fuel cells: A review.* International Journal of Hydrogen Energy, 2005. **30**(12): p. 1297-1302.

9. Feser, J.P., A.K. Prasad, and S.G. Advani, *Experimental characterization of in-plane permeability of gas diffusion layers.* Journal of Power Sources, 2006. **162**(2): p. 1226-1231.

10. Gostick, J.T., M.W. Fowler, M.D. Pritzker, M.A. Ioannidis, and L.M. Behra, *In-plane and through-plane gas permeability of carbon fiber electrode backing layers.* Journal of Power Sources, 2006. **162**(1): p. 228-238.

11. Wang, Y., C.Y. Wang, and K.S. Chen, *Elucidating differences between carbon paper and carbon cloth in polymer electrolyte fuel cells.* Electrochimica Acta, 2007. **52**(12): p. 3965-3975.

12. Gauthier, E., *Personal Communication*. 2009.

7 Conclusions and Future work

Polymer electrolyte membrane fuel cells have the potential to be an important part of an energy portfolio that does not rely on the world's supply of fossil fuels. The development of fuel cells has historically been driven by industry rather than by scientific curiosity. Fuel cell systems are now exceedingly complex due to the implementation of design changes that improved performance on a heuristic basis. A fundamental understanding of the physics of fuel cell operation did not guide design principles. The work presented in this dissertation attempted to offer insights into what factors were significant when running a fuel cell independent of auxiliary components, external controllers, and complex designs.

The SAPC fuel cell was constructed as the simplest two-dimensional fuel cell that could be designed. The segmented anode allowed for current distribution measurements that showed the propagation of ignition and extinction fronts and the sensitivity to the operation parameters, especially the choice of flow pattern. The combination of the segmented anode with the transparent flow channels showed that flooding occurred due to water in the flow channels blocking the pore openings of the GDL while the actual pores remained mostly free of liquid water. The low flow rates, down the point of complete reactant consumption, autonomous operation, and ability to change the orientation of the fuel cell elucidated the importance of gravity in how well the liquid water is removed or builds up. The experimental data fit well with the Tanks-in-series model to allow for prediction of fuel cell performance.

With the increased understanding of the operation of fuel cells with dry feeds and high fuel efficiency, the goal was to use the insights to guide system design. The pore

size distribution of the GDL should be chosen to influence the size of droplets emerging at the surface of the GDL. Droplets can either detach and move down the flow channel with the gas flows and gravity, or can span the channel to form a slug that creates a back pressure in the channel. Knowing that water flows through only largest pores, the path of water through the GDL can be controlled to be anywhere along the flow channel and either under the lands or under the flow channel. The optimal choice for these factors is not a single answer but rather depends on the application of the fuel cell including the required flow rates and orientation.

The construction of the flow fields also affects the removal of liquid water through the surface properties of the flow channel walls and lands. More hydrophobic lands can better expel water into the flow channel, but more hydrophobic channel walls can create more of a build-up of water on the surface of the GDL. Another consideration is the flow of oxygen under the lands. The choice of feed to the cathode—pure oxygen versus air—changes the driving force for flow through the GDL from pressure-driven flow with oxygen to diffusive flux with air. The width of the lands should be chosen to ensure that all the catalyst under the lands is utilized. This is not an issue with oxygen as the feed, but is an important factor with air.

The work presented in this document suggests a few paths for future studies. One approach is to create novel designs to allow for low flow rates and dry feeds while effectively removing excess liquid water. This could be done by creating two sets of channels, one for gas flow and one for water flow, by controlling where the water flows through the GDL and tailoring the surface properties of the flow field. The same effect can be accomplished by creating a path for the water through the GDL so that the water

contacts the side walls of the flow channel. With hydrophilic side walls, the water can wick along the walls down the channel, leaving the surface of the GDL open for oxygen flow to the catalyst. Cost, weight, and ease of manufacturing are important considerations in the design of flow field plates. The feasibility of using different materials or modifications to the materials already commonly used to achieve enough liquid water removal should be investigated.

Another approach for future work should be to define optimal fuel cell designs for specific applications. Large stationary systems will have different requirements than smaller fuel cells for portable use. The dynamics of the power demand, the stability of the system temperature, the stability of the orientation, the required flow rates, and the choice of feed to the cathode will each influence the design of the fuel cell system. The connection of between observations from laboratory experiments and operation of real world systems is still lacking in the literature.

Finally, simulations and experiments should continue to be matched to capture more of the physics of liquid water flow through the fuel cell. The flow of water under the lands at the interface between the land and GDL will depend on the roughness and lateral structure of the GDL along with the surface properties of the lands. The flow of water in the flow channels as slugs or droplets depends on the flow rates, channel dimensions, channel surface properties, channel orientation, and pore sizes of the GDL. Results suggest that too much water accumulation both under the lands and on top of the GDL are detrimental to the fuel cell performance. Whether slug formation is beneficial or the optimal size of the slugs and frequency of formation is still unclear. A much better understanding of these factors would be extremely useful in guiding system design.

It is possible to design fuel cells to operate efficiently with dry feeds and high fuel utilization when properly designed. Different factors are important under these conditions than what has traditionally been investigated and require more work to obtain a better understanding of their affects on fuel cell operation. Assumptions derived from past experiments with complex systems need to be reevaluated and instead based on the fundamental physics.